



University
of Glasgow

Burge, Christina Alice (2012) Particle acceleration in noisy magnetised plasmas. PhD thesis

<http://theses.gla.ac.uk/3588/>

Copyright and moral rights for this thesis are retained by the author

A copy can be downloaded for personal non-commercial research or study, without prior permission or charge

This thesis cannot be reproduced or quoted extensively from without first obtaining permission in writing from the Author

The content must not be changed in any way or sold commercially in any format or medium without the formal permission of the Author

When referring to this work, full bibliographic details including the author, title, awarding institution and date of the thesis must be given.

Particle Acceleration in Noisy Magnetised Plasmas

Christina Alice Burge
MPhys, University of Manchester

Submitted in fulfilment of the requirements for
the degree of Doctor of Philosophy

School of Physics & Astronomy
College of Science & Engineering
University of Glasgow

May 2012

Acknowledgements

The work presented in this thesis could not have been done without the support, help and insight of my supervisors, Dr. Alec MacKinnon and Dr. Giota Petkaki. The combination of Alec's big ideas and Giota's relentless attention to detail has helped me to learn how to bring an idea from a spark to a rigorously thought out theory. In particular, I would like to thank Alec for introducing me to a wide range of mathematical concepts, and never losing patience as he explained new concepts to me. My visits to Giota have always been intensive and useful. Spending an entire working week with your supervisor is a sure way to get things done! I would also like to thank Dr. Mervyn Freeman for useful and stimulating chats, and Prof. Tom Van Doorselaere for suggestions on how to speed up my code.

To the astronomy group at Glasgow, I would like to say thank you for making me very welcome for the past three years. Although solar self-help is now sadly defunct, it proved an invaluable introduction to solar physics for a novice such as myself. I also need to thank the afternoon coffee crew, for caffeinating me and diverting me with a magnificently wide range of conversational topics.

Of course, I could not have remained motivated throughout the past three years without the unwavering support of my wonderful partner, Charis. Thank you for listening to rehearsals of presentations (a riveting way to pass the time, I'm sure), giving me pep talks when I flagged, and generally cheering me on. One day I will find a way to repay you.

Declaration

The work in this thesis is my own work except where it is explicitly indicated in the text.

May, 2012.

Summary

Particle dynamics in the solar corona are of interest since the behaviour of the coronal plasma is important for the understanding of how the solar corona is heated to such high temperatures compared to the photosphere (≈ 1 million Kelvin, compared to a photospheric temperature of ≈ 6 thousand Kelvin). This thesis deals with particle behaviour in various forms of magnetic and electric fields. The method via which particles are accelerated at reconnection regions is of particular interest as particle acceleration at a magnetic reconnection region is the basis for many solar flare models. Solar flares are releases of energy in the solar corona. The amounts of energy released range from the very small amounts released by nanoflares, that cannot be observed individually, to large events such as X-class flares and coronal mass ejections. Chapter one provides background information about the structure of the Sun and about various forms of solar activity, including solar flares, sunspots, and the generation of the solar magnetic field.

Chapter 2 explores various theories of magnetic reconnection. Magnetic reconnection regions are usually characterised as containing a central 'null', a region where the magnetic field is zero, and particles can be freely accelerated in the presence of an electric field, as they decouple from the magnetic field and move non-adiabatically. Chapter 2 gives examples of how such reconnection regions could be formed.

Chapter 3 deals with the construction of a 'noisy' reconnection region. For the purposes of this work, 'noisy' fields were created by perturbing the magnetic and electric fields with a superposition of eigenmode oscillations. The method for the calculation of such eigenmodes, and the creation of the electric and magnetic fields is detailed here.

Chapter 4 details the consequences for particle behaviour in a noisy reconnection region. The behaviour of electrons and protons in such fields was studied. It was found that adding perturbations to the magnetic field caused many smaller nulls to form, which increased the size of the non-adiabatic region. This increased non-adiabatic region led to greater energisation of particles. The X-ray spectra that could be produced by the accelerated electrons were

also calculated. In this chapter I also investigate the consequences of altering the distribution of the spectrum of modes, and altering the value of the inertial resistivity.

In chapter 5, the effects of collisional scattering on particles was also investigated. Collisional scattering was introduced by integrating particle trajectories using a stochastic Runge-Kutta method (which is a form of numerical integration). It was found that adding collisional scattering at a reconnection region causes a significant change in particle dynamics in sufficiently small electric fields. Particles which undergo collisional scattering in the presence of a small electric field gain more energy than those which do not undergo collisional scattering. This effect decreases as the size of the electric field is increased. The correct relativistic expressions for particle collisions were derived. It was found that collisions have a negligible effect on relativistic particles.

Collisional scattering was also used to simulate the drift of particles across magnetic fields. It was found that adding more scattering caused the trajectories of the particles to change from normal gyromotion around the magnetic field, and that particles instead travelled across the magnetic field. I also developed a diffusion coefficient to allow the calculation of a particle's drift across a magnetic field using only 1D equations.

Chapter 6 discusses the findings made in this thesis, and explores how these findings could be built upon in the near future.

Contents

1	The Sun As a Particle Accelerator	21
1.1	Introduction	21
1.2	Particle Acceleration	21
1.2.1	Particle Acceleration Mechanisms	22
1.3	The Dynamic Sun	23
1.4	Solar Flares	26
1.5	Plasma Turbulence	29
1.6	Conclusion	31
2	Magnetic Reconnection	33
2.1	Introduction	33
2.2	What is Magnetic Reconnection?	33
2.3	Steady State Reconnection	34
2.4	Spontaneous Reconnection	36
2.4.1	Tearing Mode	36
2.4.2	Kink Mode	37
2.5	Collisionless Reconnection	38
2.6	The X-Type Neutral Point	39
2.7	Test Particle Studies	43
2.8	Conclusion	44
3	Noisy Electric and Magnetic Fields...	45
3.1	Introduction	45
3.2	Reconnection at an X-type Neutral Point	45
3.3	Normalisations	46
3.3.1	Resistivity	46
3.4	Forms of the Electric and Magnetic Fields	47
3.4.1	Form of the Solution	50
3.4.2	The Hypergeometric Function	52
3.4.3	Explicit Forms of the Electric and Magnetic Fields	54

3.5	Conclusion	63
4	Consequences For Particle Behaviour	65
4.1	Introduction	65
4.2	Particle Behaviour: Protons	65
4.2.1	Equations of Motion	66
4.2.2	Particle Energies & Trajectories	67
4.2.3	Energy Conservation	70
4.2.4	Energy Distributions: Protons	71
4.2.5	Determining the Size of the Non-Adiabatic Region	80
4.2.6	Energy Distributions: Electrons	83
4.2.7	Determining the Size of the Non-Adiabatic Region	90
4.2.8	Magnetic Field Topology	93
4.2.9	Particle Trapping & Pitch Angle	94
4.3	Comparison of Electron & Proton Results	103
4.4	Resulting X-Ray Spectra	104
4.5	Non-Flat Spectrum of Modes	107
4.6	Effect of Varying Resistivity	115
4.7	Conclusions	119
5	Effect of Collisions on Particle Trajectories	121
5.1	Introduction	121
5.2	Collisions in the Solar Corona	121
5.3	Stochastic Integration Methods	123
5.3.1	Deterministic RK4	123
5.3.2	Stochastic RK4	124
5.4	The Test Problem	125
5.5	3D Description of Particle Motion	127
5.5.1	Equations of Motion	127
5.5.2	Different Coordinate Systems	134
5.6	Relativistic Collisional Scattering	135
5.6.1	Slowing-Down Term	135
5.6.2	Change in Pitch Angle	136
5.7	Conversion to Numerical Method	137
5.7.1	Application to Test Problem	137
5.8	Cross-Field Scattering	142
5.8.1	Equations of Motion	143
5.8.2	Perpendicular Diffusion Coefficient	148

5.9	Collisional Scattering At An X-Type Neutral Point	152
5.9.1	The Dreicer Field	153
5.9.2	Equations of Motion	155
5.10	Drift & Diffusion in Polar Co-ordinates	157
5.10.1	The Relativistic Case	163
5.10.2	Application to X-Type Neutral Point	164
5.11	Conclusion	166
6	Conclusions and Future Work	167
6.1	Noisy Electric & Magnetic Fields	167
6.1.1	Consequences for Protons	168
6.1.2	Consequences for electrons	169
6.2	Collisional Scattering	170
6.3	Future Work	172

List of Figures

1.1	Image from the Solar Dynamics Observatory (SDO) showing active regions in the corona at a wavelength of 171Å.	23
1.2	Image showing the various layers of the solar interior and atmosphere, as well as various forms of solar activity. (NASA)	24
1.3	Magnetic flux emergence at the outer layers of the Sun. The label MMF indicates a moving magnetic feature, and the label EB indicates an Ellerman bomb (a small scale magnetic reconnection event,Georgoulis <i>et al.</i> (2002)). Granules are convective cells in the photosphere, the motion of which may drive activity in the corona. A plage is a bright region surrounding a sunspot.(Pariat <i>et al.</i> (2004))	26
1.4	An example of a solar flare time profile at various wavelengths (Benz (2002)). The four stages of the flare are shown.	28
1.5	An example of a solar flare model. HXR indicates areas of hard (i.e. high energy) X-ray emission. SXR indicates areas of soft (i.e. low energy) X-ray emission. The flare is shown extending outwards from the 'limb' (the edge of the solar disk), and electrons are accelerated from the cusp of the flaring loop towards the footpoints. (Aschwanden, 2004b).	29
1.6	Change in plasma energy with wavenumber according to the K41 model (Goldstein, Roberts, and Matthaeus, 1995).	31
1.7	Variation of magnetic power density with frequency in the solar wind, as measured by Cluster (Alexandrova <i>et al.</i> , 2009).	32
2.1	Two sets of oppositely directed magnetic field lines, shown here breaking and reconnecting to form new field lines.	34
2.2	Sweet-Parker reconnection model. Slightly adapted from Zweibel and Yamada (2009). S is the Lundquist number, which is the ratio of the Alfvén timescale to the resistive diffusion timescale.	35
2.3	Petschek reconnection model. Slightly adapted from Zweibel and Yamada (2009).	37

2.4	Chain of magnetic islands, formed from a series of X- and O-type nulls. Figure taken from Birn and Priest (2007).	38
2.5	Collisionless reconnection model, showing ions and electrons moving separately. ω_{pi} is the ion plasma frequency, ω_{pe} is the electron plasma frequency. Zweibel and Yamada (2009).	39
2.6	A 2D X-type neutral point. The left hand pane shows the magnetic field in the x-y plane. The thick grey arrows indicate the direction of inflow and outflow from the $E \times B$ drift. This X-type neutral point does not have any B_z component, and does not vary in the z direction. This is shown in the right hand plane, which shows an arcade in the z-direction. Figure taken from Hannah (2005).	40
2.7	Trajectory of a proton in an unperturbed X-type neutral point.	41
3.1	Form of hypergeometric function for first four eigenmodes. The solid line shows the real part of the function, the dashed line shows the imaginary part.	54
3.2	Electric field variation with distance from the neutral point (where r is normalised to D). Field strength is normalised to the magnetic field strength at the system boundary. The field shown results from different superpositions of eigenmodes, each with a different random phase.	59
3.3	Electric field variation with time at $r = 0$ (where r is normalised to D). Field strength is normalised to the magnetic field strength at the system boundary. The field shown results from different superpositions of eigenmodes, each with a different random phase.	60
3.4	Decay of electric field with time at $r = 0$, for modes 0-4.	61
3.5	Electric field variation with time at $r = 1$ (where r is normalised to D). Field strength is normalised to the magnetic field strength at the system boundary. The field shown results from different superpositions of eigenmodes, each with a different random phase.	61
3.6	Magnetic field perturbation with distance from the neutral point (where r is normalised to D). Field strength is normalised to the magnetic field strength at the system boundary. The field shown results from different superpositions of eigenmodes, each with a different random phase.	62
3.7	Electric field variation with time at $r = 0$ (where r is normalised to D). Field strength is normalised to the magnetic field strength at the system boundary. The field shown results from different superpositions of eigenmodes, each with a different random phase. This is the electric field experienced by the electrons. It has a greater amplitude since electrons are followed for a shorter time.	63

4.1	Comparison of three methods of numerical integration, for the integration of the equation $dy = \sin(4x)dx$. The solid line shows the exact solution of the function.	68
4.2	Orbit of one proton in constant electric and magnetic fields for varying step-sizes.	69
4.3	Distribution of proton energies for constant electric and magnetic fields at $t=5360$ for varying stepsizes.	70
4.4	Distribution of electron energies for constant electric and magnetic fields at $t=2310$ (0.1s) for varying stepsizes.	71
4.5	Energy of an individual ion for cases 1-5 in the absence of an electric field over a period of 1s. It can be seen that energy is well conserved in all cases.	72
4.6	Energy of an individual electron for cases 1-5 in the absence of an electric field over a period of 1s. It can be seen that energy is well conserved in all cases.	73
4.7	Energy distribution of 10000 protons at $t=0$, and at $t=5360$ for different electric and magnetic fields.	74
4.8	Energy distribution of 10000 ions at $t = 0$, and at $t = 5360$ (1 second) for case 5 (electric and magnetic fields perturbed by a superposition of 50 eigenmode oscillations, each with a random phase) and case 5b (electric and magnetic fields perturbed by a superposition of 50 eigenmode oscillations, each with a different random phase).	75
4.9	Energy distribution of 10000 ions at $t = 0$, and at $t = 536$ (0.1 seconds) for different electric and magnetic fields.	76
4.10	Energy distribution of 10000 ions at $t = 0$, and at $t = 2680$ (0.5 seconds) for different electric and magnetic fields.	76
4.11	Energy distribution of 10000 ions at $t = 0$, and at $t = 4824$ (0.9 seconds) for different electric and magnetic fields.	77
4.12	Initial positions of protons for all cases. Dots show the positions (at $t = 0$) of protons which gain less than 100 times their initial energies. Crosses show the positions (at $t = 0$) of protons which gain more than 100 times their initial energies. x and y are given in units of d_p	78
4.13	Final positions of protons for all cases. Dots show the positions (at $t = 5360$) of protons which gain less than 100 times their initial energies. Crosses show the positions (at $t = 5360$) of protons which gain more than 100 times their initial energies. x and y are given in units of d_p	79

4.14	Variation of magnetic moment and energy of high energy protons with distance from the neutral point and time, for case 5. These two particles were chosen as they both gained more than 400 times their original energy. Particle 1 (black) and particle 2 (red) are the same particles in each frame of the figure.	81
4.15	Trajectories of 2 protons in the x-y plane (top) and variation of distance from the neutral point with time (bottom) for case 5. These two particles were chosen as they both gained more than 400 times their original energy. Particle 1 (black) and particle 2 (red) are the same particles in each frame of the figure.	82
4.16	Variation of magnetic moment and energy of high energy protons with distance from the neutral point and time, for case 2. These two particles were chosen as they both gained more than 5 times their original energy. Particle 1 (black) and particle 2 (red) are the same particles in each frame of the figure.	82
4.17	Trajectories of 2 protons in the x-y plane (top) and variation of distance from the neutral point with time (bottom) for case 2. These two particles were chosen as they both gained more than 5 times their original energy. Particle 1 (black) and particle 2 (red) are the same particles in each frame of the figure.	83
4.18	Energy distribution of 10000 electrons at $t = 0$, and at $t = 2310$ (0.1 seconds) for different electric and magnetic fields. The blue curves are the energies of the electrons at the time stated. The black curves are the initial energy distributions.	86
4.19	Energy distribution of 10000 electrons at $t = 0$, and at $t = 231$ (0.01 seconds) for different electric and magnetic fields. The blue curves are the energies of the electrons at the time stated. The black curves are the initial energy distributions.	87
4.20	Energy distribution of 10000 electrons at $t = 0$, and at $t = 1155$ (0.05 seconds) for different electric and magnetic fields. The blue curves are the energies of the electrons at the time stated. The black curves are the initial energy distributions.	88
4.21	Energy distribution of 10000 electrons at $t = 0$, and at $t = 2079$ (0.09 seconds) for different electric and magnetic fields. The blue curves are the energies of the electrons at the time stated. The black curves are the initial energy distributions.	89

4.22 Initial positions of electrons for all cases. Dots show the positions (at $t = 0$) of electrons which gain less than 10 times their initial energies. Crosses show the positions (at $t = 0$) of electrons which gain more than 10 times their initial energies. x and y are given in units of $10 \times d_e$ 90

4.23 Final positions of electrons for all cases. Dots show the positions (at $t = 2310$) of electrons which gain less than 10 times their initial energies. Crosses show the positions (at $t = 2310$) of electrons which gain more than 10 times their initial energies. x and y are given in units of $10 \times d_e$ 91

4.24 Variation of magnetic moment and energy of high energy electrons with distance from the neutral point and time, for case 5. These two particles were chosen as they both gained more than 400 times their original energy. Particle 1 (black) and particle 2 (red) are the same particles in each frame of the figure. 92

4.25 Trajectories of 2 electrons in the x-y plane (top) and variation of distance from the neutral point with time (bottom) for case 5. These two particles were chosen as they travelled reasonably far in r without escaping the system and also gained large amounts of energy. Particle 1 (black) and particle 2 (red) are the same particles in each frame of the figure. 93

4.26 Variation of magnetic moment and energy of high energy electrons with distance from the neutral point and time, for case 2. These two particles were chosen as they travelled reasonably far in r without escaping the system and also gained large amounts of energy. Particle 1 (black) and particle 2 (red) are the same particles in each frame of the figure. 94

4.27 Trajectories of 2 electrons in the x-y plane (top) and variation of distance from the neutral point with time (bottom) for case 2. These two particles were chosen as they travelled reasonably far in r without escaping the system and also gained large amounts of energy. Particle 1 (black) and particle 2 (red) are the same particles in each frame of the figure 95

4.28 Variation of magnetic moment and energy of high energy electrons with distance from the neutral point and time, for case 3. The red line represents a particle which gained 500 times its original energy. The black particle lost energy. Particle 1 (red) and particle 2 (black) are the same particles in each frame of the figure. 96

4.29	Trajectories of 2 electrons in the x-y plane (top) and variation of distance from the neutral point with time (bottom) for case 3. The red line represents a particle which gained 500 times its original energy. The black particle lost energy. Particle 1 (red) and particle 2 (black) are the same particles in each frame of the figure.	96
4.30	Magnetic field contours with a sample proton trajectory overplotted for case 5, for the region $-1 \leq x \leq 1$, $-1 \leq y \leq 1$ (a) for the region $-0.3 \leq x \leq 0.3$, $-0.3 \leq y \leq 0.3$ (b), and (c) for the region $-0.03 \leq x \leq 0.03$, $0.25 \leq y \leq 0.3$, displaying some of the smaller structures formed by the perturbations. Note that the field is plotted at $t = 0.5s$, but the trajectory shown is the path taken by the proton over the whole time of the simulation. However, the central loop that the particle is following remains approximately constant in size and shape throughout the simulation. Panel (d) shows the magnitude of the magnetic field at $x = 0$ for $-0.3 < y < 0.3$. It can be seen that the magnetic field goes to zero (here, the magnetic field is considered to be zero if $ B < 0.01$) 7 times, 6 of which are outside the central null, indicating that the small scale structures seen in panels (b)-(c) of this figure are indeed nulls.	97
4.31	Pitch angle distribution of 10000 protons at $t=0$, and also at $t=5360$ for different forms of the electric and magnetic fields.	98
4.32	Positions at which ion trajectory changes by more than $\pi/2$ for different forms of the electric and magnetic fields. It can be seen that some ‘pitch angle scattering’ events occur even when there are no perturbations present. However, note that these occur at small values of r , and so can be attributed to the fact that the particle is close to the null and is not undergoing regular gyromotion about a field line.	99
4.33	Number of timesteps spent by ions at each value of r for different forms of the electric and magnetic fields.	100
4.34	Pitch angle distribution of 10000 electrons at $t = 0$, and also at $t = 2310$ (0.1s) for different forms of the electric and magnetic fields. The blue histograms indicate particles that stay within the system boundaries. Red histograms indicate particles which left the system, at the time at which they left the system.	101
4.35	Positions at which electron trajectory changes by more than $\pi/2$ for different forms of the electric and magnetic fields.	102
4.36	Number of timesteps spent by electrons at each value of r for different forms of the electric and magnetic fields.	103

4.37	X-ray spectra generated from electron energy distributions at $t = 0.1s$ for cases 1-5.	105
4.38	Example of an observed X-ray spectrum. The red curve shows the fit to the thermal emission. Krucker <i>et al.</i> (2008a).	106
4.39	Electric field for a spectrum of modes with their amplitude distributed as $k^{-5/3}$. The left hand plot shows the variation of the electric field with time at $r = 0$, the middle plot shows the variation of the electric field with time at $r = 1$, and the right hand plot shows the variation of the electric field with r at $t = 0$	109
4.40	Electric field variation with time at $r=0$. The top plot shows the field for a spectrum of modes with their amplitude distributed as $k^{-5/3}$. The bottom plot shows the field for a flat spectrum of modes.	110
4.41	Energy of 10 000 protons at $t = 1s$. The right hand plot shows protons which have been accelerated in fields composed of a flat spectrum of eigenmode oscillations. The left hand plot shows protons which have been accelerated in fields composed of a spectrum of modes with their amplitude distributed as $k^{-5/3}$. For both plots, $a_0 = 0.0001$	111
4.42	Energy of 10 000 protons at $t = 1s$. The right hand plot shows protons which have been accelerated in fields composed of a flat spectrum of eigenmode oscillations. The left hand plot shows protons which have been accelerated in fields composed of a spectrum of modes with their amplitude distributed as $k^{-5/3}$. For both plots, $a_0 = 0.01$	112
4.43	Plots of the variation of the proton's energy with distance from the null, and of the variation of distance from the null with time. The colour of the line identifies a particle with the same initial conditions. For all plots, $a_0 = 0.01$	113
4.44	Plots of positions of protons at $t = 1s$. For all plots, $a_0 = 0.01$. The left hand panel shows the position of protons in the x-y plane, the right hand panel shows position of protons in the x-z plane.	113
4.45	Plots of positions of protons at $t = 1s$. Particles that gain more than 100 000 times their original energy are plotted in red. For all plots, $a_0 = 0.01$	114
4.46	Energies of protons at $t = 1s$. Protons were accelerated in fields composed of a superposition of 50 modes distributed with amplitudes $a_n = a_0 k^{-5/3}$, where $a_0 = 1$ and k is the wavenumber of the mode.	115
4.47	Energy of 1000 protons at $t=1s$ for a superposition of 50 modes. The spectrum of modes is flat, and $a_0 = 0.0001$. The resistivity, $\eta = 3.1724 \times 10^{-10}$ in the left hand plot, and $\eta = 3.1724 \times 10^{-12}$ in the right hand plot.	116

4.48	Magnetic field contours at $t = 0.5s$. The resistivity, $\eta = 3.1724 \times 10^{-10}$ in the left hand plot, and $\eta = 3.1724 \times 10^{-12}$ in the right hand plot.	117
4.49	Magnetic field variation with distance from the null at $t = 0.s$. The resistivity, $\eta = 3.1724 \times 10^{-10}$ in the top plot, and $\eta = 3.1724 \times 10^{-12}$ in the bottom plot.	118
4.50	Electric field variation with time at $r = 0.s$. The resistivity, $\eta = 3.1724 \times 10^{-10}$ in the top plot, and $\eta = 3.1724 \times 10^{-12}$ in the bottom plot.	119
5.1	Comparison of stochastic RK4, Euler integration, and the exact solution evaluated using Legendre polynomials, $t=0.06$	127
5.2	Comparison of stochastic RK4 integrating a set of 6 equations to determine the velocity components of the particles, Euler integration of the same solution reduced to one equation, evaluating the pitch angle of the particle only ; and the exact solution evaluated using Legendre polynomials, $t=0.18$. All three solutions agree closely.	139
5.3	Comparison of the calculation of the slowing down of one electron calculated using stochastic RK4 integrating a set of 6 equations and by evaluating the analytic solution of MacKinnon and Craig (1991). The two solutions agree closely for the stepsize shown, which is 0.0001.	140
5.4	Comparison of the calculation of the slowing down of one electron calculated using stochastic RK4 integrating a set of 6 equations and by evaluating the analytic solution of MacKinnon and Craig (1991). The two solutions agree more closely as the stepsize is decreased.	141
5.5	Comparison of stochastic RK4 integrating a set of 6 equations to determine the velocity components of 100 000 particles, Euler integration of the same solution reduced to one equation, evaluating the pitch angle of the particle only ; and the exact solution evaluated using Legendre polynomials, $t=0.3$. The stepsize used was 0.01 for both numerical integration methods.	142
5.6	Comparison of stochastic RK4 integrating a set of 6 equations to determine the velocity components of 100 000 particles, Euler integration of the same solution reduced to one equation, evaluating the pitch angle of the particle only ; and the exact solution evaluated using Legendre polynomials, $t=0.3$. The stepsize used was 0.001 for both numerical integration methods.	143
5.7	Comparison of stochastic RK4 integrating a set of 6 equations to determine the velocity components of 100 000 particles, Euler integration of the same solution reduced to one equation, evaluating the pitch angle of the particle only ; and the exact solution evaluated using Legendre polynomials, $t=0.3$. The stepsize used was 0.0001 for both numerical integration methods.	144

5.8	Comparison of stochastic RK4 integrating a set of 6 equations to determine the velocity components of 100 000 particles, Euler integration of the same solution reduced to one equation, evaluating the pitch angle of the particle only ; and the exact solution evaluated using Legendre polynomials, $t=0.3$. The stepsize used was 0.00001 for both numerical integration methods. . . .	145
5.9	Tangled magnetic field lines in the solar corona as observed by TRACE (Galloway, Helander, and MacKinnon (2006)). The far left panel shows an example of regular, ordered coronal loops. The middle and right hand panels show more tangled, disordered loops. Galloway, Helander, and MacKinnon (2006) proposed a relationship between the random walk of scattered particles and diffusion across the field lines as a result of this macroscopic tangling.	146
5.10	Slowing down of one electron in the case $A = 1$. There is no electric field, and the magnetic field is 1G in the x direction only	147
5.11	Electron trajectory in the cases $A=0, 10^{-2}, 10^{-1}$ and 1. There is no electric field, and the magnetic field is 1G in the x direction only	148
5.12	Distribution of y position at every half a gyroperiod for different amplitudes of slowing down and scattering terms, i.e. histograms were plotted at $t = 0, 0.5\tau, 1.\tau, 1.5\tau \dots 12\tau, 12.5\tau$, where τ is one gyroperiod. Each histogram is plotted in a different colour. Colours closer to black represent earlier times, colours closer to red represent later times.	149
5.13	Change in the mean y position of the electron distribution with time for different amplitudes of slowing down and scattering terms. The mean y position was plotted every gyroperiod, and the mean y position in the absence of scattering should be zero at the times plotted.	150
5.14	Change in the mean z position of the electron distribution with time for different amplitudes of slowing down and scattering terms. The mean z position was plotted every gyroperiod, and the mean z position in the absence of scattering should be zero at the times plotted.	151
5.15	Change in y with time for different densities. The variance of y was plotted every gyroperiod.	152
5.16	Change in y with time for different values of v_0 . The variance of y was plotted every gyroperiod.	153
5.17	Change in y with time for different values of B . The variance of y was plotted every gyroperiod.	154

5.18	Change in the variance of y with time. The variance of y was plotted every gyroperiod, and is marked with a cross. The solid line is the average displacement as calculated using the diffusion coefficient, D , averaged over the number of electrons being considered (10 000 in this simulation).	155
5.19	Slowing down of one electron at an X-type neutral point. A stepsize of 0.001 was used here. The electric field has magnitude 0. The slowing down in this figure is slightly disappointing, as it is noisier than might be expected from the well-behaved test problem studied at the start of this chapter. This is due to numerical issues which will be avoided by considering the problem in spherical polar coordinates.	157
5.20	Slowing down of 5 electrons with identical starting conditions, including collisional scattering. Three different stepsizes were used. There is no electric field present.	158
5.21	Slowing down of one electron at an X-type neutral point. A stepsize of 0.001 was used here. The electric field has magnitude 0.	159
5.22	Trajectories of 5 electrons for case 1, integrated with and without the addition of collisional scattering. The sample has identical starting conditions for both sets of electrons. The electric field has magnitude 0.001 in our dimensionless units.	160
5.23	Energies at $t=0.015s$ for 10000 electrons whose trajectories have been integrated without the addition of collisional scattering (left) and with collisional scattering (right). The electric field has magnitude 0.001 in our dimensionless units.	161
5.24	Energies at $t = 0.015s$ for 10000 electrons whose trajectories have been integrated without the addition of collisional scattering (left) and with collisional scattering (right). The electric field has magnitude 0.0001 in our dimensionless units.	162
5.25	Energies at $t = 0.015s$ for 10000 electrons whose trajectories have been integrated without the addition of collisional scattering (left) and with collisional scattering (right). The electric field has magnitude 10^{-5} in our dimensionless units.	162
5.26	Energies at $t = 0.015s$ for 10000 electrons whose trajectories have been integrated without the addition of collisional scattering (left) and with collisional scattering (right). The electric field has magnitude 10^{-7} in our dimensionless units.	163

- 5.27 Energies at $t = 0.04s$ for 10000 electrons whose trajectories have been integrated without the addition of collisional scattering (left) and with collisional scattering (right), using the relativistic expressions for collisional scattering and collisional energy loss. The electric field has magnitude 0.001 in our dimensionless units. 165
- 5.28 Energies at $t = 0.04s$ for 10000 electrons whose trajectories have been integrated without the addition of collisional scattering (left) and with collisional scattering (right), using the relativistic expressions for collisional scattering and energy loss. The electric field has magnitude 1×10^{-7} in our dimensionless units. 165

List of Tables

3.1	A selection of values of ω and κ for $\eta = 3.1724 \times 10^{-11}$. The unit t_c is the timescale used in Craig & McClymont's work, where $t_c = v_A D$. \mathbf{D} is the distance from the null at the system boundary, and v_A is the Alven speed at the system boundary.	58
3.2	A selection of values of oscillation time, decay time and period for $\eta = 3.1724 \times 10^{-11}$	59
4.1	Fraction of protons accelerated to above 0.01 MeV with average electric field strength and peak electric field strength in each case.	72
4.2	Number of electrons accelerated to above 0.01 MeV with average electric field strength and peak electric field strength in each case.	87
4.3	Mean temperature of the thermal parts of the X-ray spectra produced from the accelerated electron distributions, and spectral indices of the non-thermal parts of the same distributions.	107
4.4	A selection of values of ω and κ for $\eta = 3.1724 \times 10^{-10}$. The decay and oscillation times for these values of ω and κ are also listed.	116
4.5	A selection of values of ω and κ for $\eta = 3.1724 \times 10^{-12}$. The decay and oscillation times for these values of ω and κ are also listed.	117

1. The Sun As a Particle Accelerator

It is a capital mistake to theorize before one has data. Insensibly one begins to twist facts to suit theories, instead of theories to suit facts.

Sherlock Holmes, *A Scandal In Bohemia*

1.1 Introduction

In this chapter, I will introduce the reader to the various forms of activity that take place in the outer layers of the Sun. In order to do this, I will describe the structure of the Sun, and describe some of the phenomena that occur in active regions on the solar surface. I also briefly explore how such active regions may be formed, by the emergence of magnetic flux from within the solar interior.

I will also provide a brief introduction into the mechanism of solar flares. This is essential, since the much of rest of this work will focus on how particles are accelerated at reconnection regions in the solar corona, and such reconnection regions are to be found in solar flares. Since noisy electric and magnetic fields will be used in later chapters to generate a kind of plasma turbulence, I also provide some explanation of turbulence in plasmas.

1.2 Particle Acceleration

Particle acceleration is a process that energises particles, allowing them to reach non-thermal energies (i.e. energies greater than the ambient energy, that are statistically improbable for particles to reach in the absence of some kind of acceleration mechanism). A major fraction

of energy released in magnetised plasmas takes this form, and accelerated particles transport energy away from the location at which the particles become energised. Accelerated particles produce radiation across a broad range of frequencies; from gamma rays to radio, and these different forms of radiation are an important diagnostic of the properties of the acceleration region. The type of electromagnetic radiation emitted by particles is a function of the particle's energy. Higher energy particles are capable of producing higher frequency radiation. Studies of accelerated particles can also give us an insight into the acceleration mechanism.

Particle acceleration occurs in many situations in our universe. Examples include particle acceleration in solar flares, in the accretion disks of galaxies, and in the solar wind. Solar flares will be discussed in more detail in section 1.3. The solar wind is composed of particles which have been accelerated away from the Sun. These particles can be detected in situ using satellites, or more spectacularly when they interact with the earth's magnetic field to produce the aurorae.

Non-thermal particles can be detected in the halos of galaxies. The particles are detected via the radio, gamma ray and X-ray radiation they emit (Blasi, Gabici, and Brunetti (2007)). Supernova remnants also emit radiation across a spectrum of wavelengths, when particles there are accelerated to high energies by shocks (see e.g., Torres *et al.* (2003)). Such acceleration is thought to be the origin of galactic cosmic rays (see e.g. Hillas (2005)), high energy charged particles which reach the Earth's atmosphere, and which originate within our galaxy. Particle acceleration in energetic plasmas can also be studied in laboratories, in devices called Tokamaks.

1.2.1 Particle Acceleration Mechanisms

There are many different possible mechanisms for particle acceleration. The two most commonly proposed mechanisms are direct electric field acceleration and Fermi acceleration.

Electric field acceleration is simply the acceleration of particles in the presence of an electric field. Such electric fields can be generated in magnetic reconnection events. Fermi acceleration occurs when charged particles are repeatedly reflected, for example by a magnetic mirror. In addition to these two mechanisms, particles may also undergo stochastic acceleration. For example, particles may undergo resonant interaction with electromagnetic waves

1.3 *The Dynamic Sun*

We know that we observe signatures of accelerated particles when we observe the Sun. These particles must be accelerated somehow, by active processes in various regions of the solar plasma. The various forms of solar activity are governed by the sun's magnetic field. This work concerns itself with the coronal magnetic field, which is thought to originate in the solar interior. An image of the active sun taken by the Solar Dynamics Observatory (SDO) can be seen in figure 1.1.

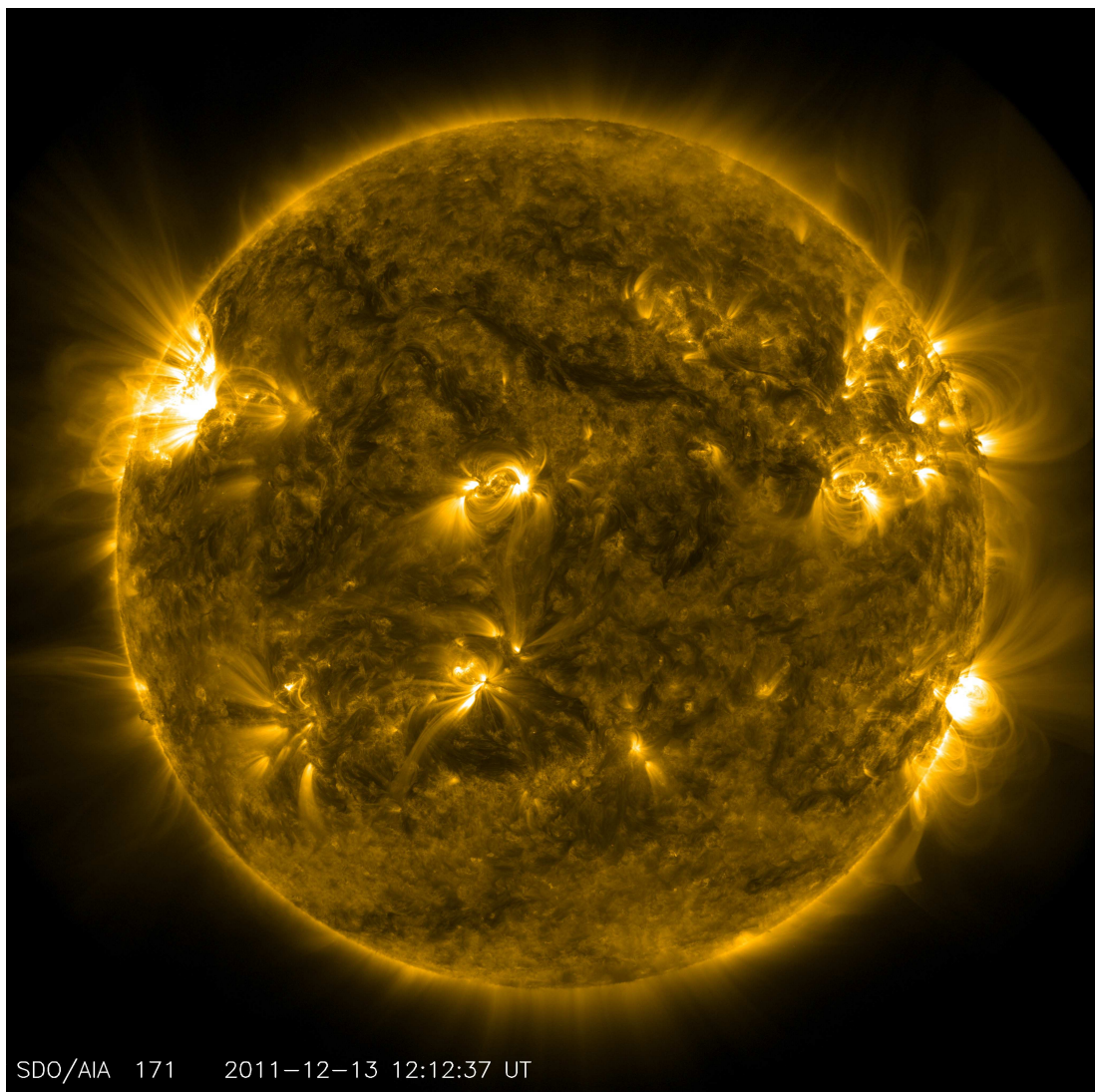


Figure 1.1: Image from the Solar Dynamics Observatory (SDO) showing active regions in the corona at a wavelength of 171\AA .

At this point, it is sensible to take a look at the basic ‘anatomy’ of the sun. A diagram of the solar interior can be seen in figure 1.2. At the very centre of the Sun is the solar core. This is both the hottest and densest part of the Sun, with a temperature of $1.5 \times$

10^7 K. The next two layers are known as the radiative zone and the convective zone. The radiative zone is the zone in which energy is transported towards the solar exterior by means of radiative transport. In the convective zone, energy is transported towards the solar exterior via convection. The convective zone is differentially rotating, whereas the radiative zone is uniformly rotating. The interface between the two layers is called the tachocline, and due to the difference between the rotation of the convective and radiative layers there is a large amount of shear in this region. This shear is thought to play a crucial role in generating the large scale magnetic field of the Sun (see e.g. Jones, Thompson, and Tobias (2010)).

The next layer is called the photosphere. It has a temperature of around 6000K, and forms the solar surface. From the photosphere (the solar surface) downwards, the plasma β (the ratio of the gas pressure to the magnetic pressure) is much greater than 1. This means that the convective motions of the plasma determine the behaviour of the magnetic field.

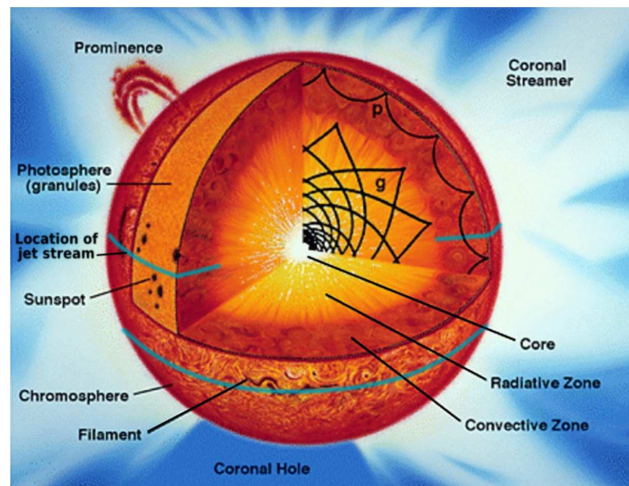


Figure 1.2: Image showing the various layers of the solar interior and atmosphere, as well as various forms of solar activity. (NASA)

In the case of solar flares, particle acceleration takes place in the Sun's tenuous outer atmosphere, the corona. The physical properties of the gas and the role of the magnetic field in the corona then form essential background to understanding how particles are accelerated here. The solar corona is the uppermost layer of the solar atmosphere, lying above the chromosphere. It is composed of an extremely hot plasma (temperature in excess of 10^6 K). The plasma temperature is greatly in excess of that of the lower layers of the solar atmosphere (the chromosphere and photosphere, which has a temperature of approximately 6000K), and the reason for this is not yet understood, although several mechanisms have been proposed, including heating by turbulence, waves, and magnetic reconnection (see e.g. Aschwanden (2001)). In the chromosphere and corona (the outermost layers of the Sun), the plasma β is less than 1, so that the magnetic field now determines the dynamics of the plasma.

The corona is generally thought of as containing ‘active’ regions and ‘quiet’ regions. An active region is made up of magnetic flux tubes which are anchored in the photosphere, and extend upwards through the chromosphere and corona. The number of active regions varies according to the solar cycle, which is approximately 11 years long. Active regions contain signs of magnetic activity, such as sunspots (dark patches on the photosphere, the layer of the Sun below the chromosphere). Sunspots appear dark because they are cooler than the rest of the photospheric surface. The plasma is cooler in these regions because there is a strong magnetic field here which inhibits convective heating of the plasma.

Prominences are another example of an active region phenomenon (with the exception of polar crown prominences; prominences found at the solar poles, away from active regions). Prominences are areas where plasma is confined in a structure which extends away from the solar surface. The plasma confined in prominences is cooler and denser than the surrounding coronal plasma. Active regions also play host to dynamic events such as solar flares and coronal mass ejections (CMEs). The proposed mechanism behind solar flares is described in more detail in section 1.4. A coronal mass ejection is a large and highly energetic release of plasma from the solar corona. It is sometimes accompanied by a solar flare.

The magnetic field emerges into the corona via a process known as flux emergence, which is not yet well understood. Flux emergence is a process whereby magnetic field loops from below the photosphere rise into the chromosphere and corona. These loops can then interact with the coronal magnetic field (Heyvaerts, Priest, and Rust (1977)). A simplified illustration of flux emergence can be seen in figure 1.3. This figure also shows the layers of the solar atmosphere. Also seen in this figure are granules, convective cells in the photosphere which may drive the motion of the magnetic field (Berger and Title (1996)).

It is the emergence of magnetic flux that produces active regions (regions in which features such as sunspots and solar flares originate). Convection below the photosphere can produce regions of twisted and tangled magnetic flux. Such tangled and twisted flux stores a lot of magnetic energy. This tangled flux is produced by photospheric convection causing the movements of the footpoints of magnetic structures in the corona. This is known as direct current (DC) heating. Free energy is built up in the coronal magnetic field. This energy is then released via magnetic reconnection. (See chapter 2.)

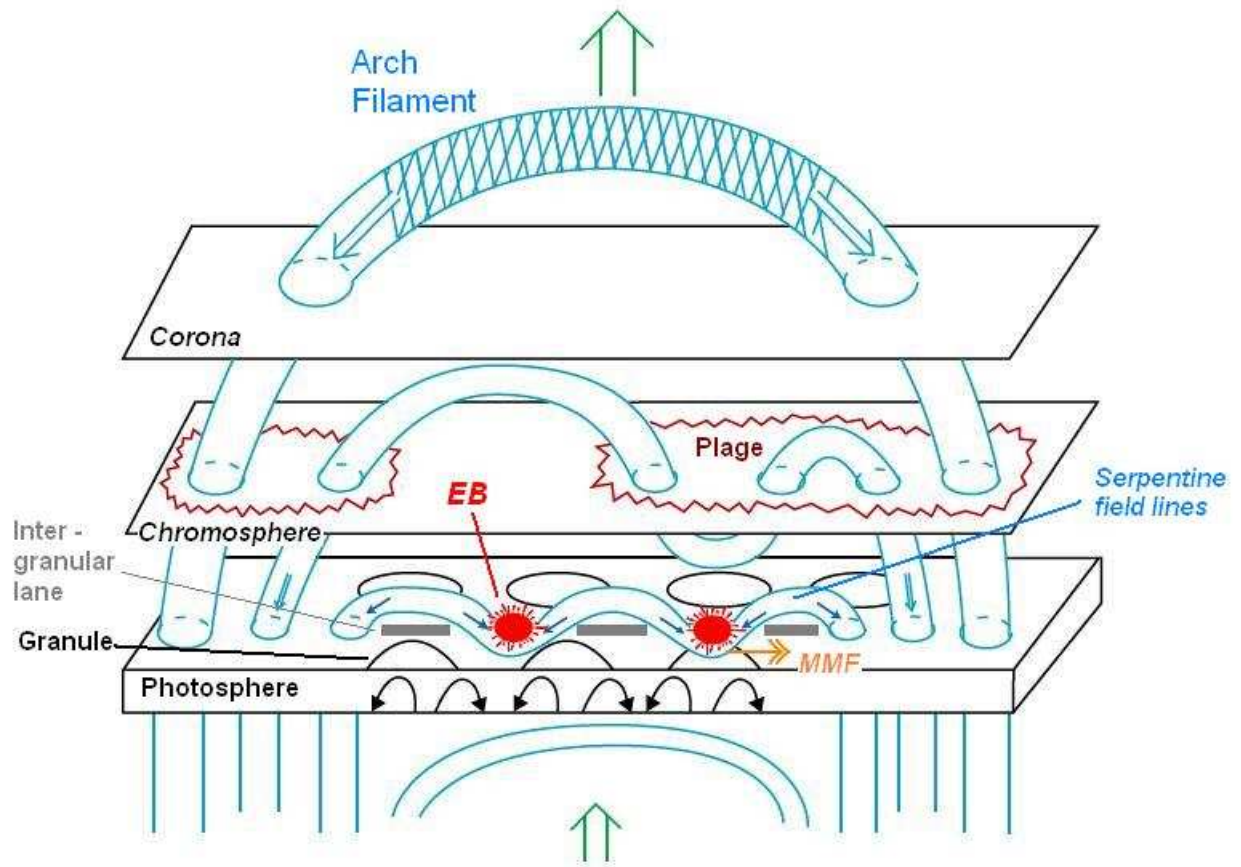


Figure 1.3: Magnetic flux emergence at the outer layers of the Sun. The label MMF indicates a moving magnetic feature, and the label EB indicates an Ellerman bomb (a small scale magnetic reconnection event, Georgoulis *et al.* (2002)). Granules are convective cells in the photosphere, the motion of which may drive activity in the corona. A plage is a bright region surrounding a sunspot. (Pariat *et al.* (2004))

1.4 Solar Flares

The evidence for energetic particles can be seen in radiation signatures across the electromagnetic spectrum, from radio bursts to X-rays and gamma rays. How do such particles gain high energies? Solar flares give a particularly well-studied example, with their impulsive phase hard X-ray, γ -ray and radio signatures (e.g. Lin *et al.*, 2003; White *et al.*, 2011). The high energies of the emitting particles appear to be consequences of magnetic reconnection, in which energy is released rapidly from the non-potential component of the magnetic field via a change in field line connectivity (e.g. Priest and Forbes, 2000). The physical processes by which this can happen remain unclear, but it is proposed (e.g. Miller *et al.* (1997a)) that during a magnetic reconnection event particles become decoupled from the magnetic field

and are accelerated by the electric field. Shocks and high energy plasma jets can also form, which also accelerate particles.

The details of magnetic reconnection will be discussed further in chapter 2. A solar flare is an event in which a large amount of energy is released on short time scales, generally on the order of tens of seconds (Miller *et al.* (1997b)). In a flare, the total energy content of accelerated electrons (according to the cold thick target interpretation of the hard X-rays (HXR)) is $10^{28} - 10^{34}$ ergs, on time scales ranging from under a second to tens of minutes (Miller *et al.* (1997a)). The cold thick target model (CTTM) is a model which seeks to explain how accelerated particles produce HXR. The model describes a situation in which particles from the corona enter the chromosphere, which is much cooler and also much denser (i.e. it is collisionally thick). Because of this, the particles slow down, causing them to emit X-rays via Bremsstrahlung.

The evolution of a solar flare can be broadly divided into four stages (Benz (2008)), which can be seen in figure 1.4 below.

- **Preflare stage.** During this stage there is a small increase in EUV (extreme ultra violet) and SXR (soft X-ray) flux, but very little change in observations at other wavelengths.
- **Impulsive phase,** where bursts of HXR are seen, as well as bursts in EUV and across a range of radio wavelengths. The SXR flux also increases during this time.
- **Main phase,** where the $H\alpha$ and SXR fluxes peak.
- **Gradual phase.** The HXR, microwave and decimetric radio fluxes fall off quickly, whilst the observed SXR, EUV and $H\alpha$ flux decays more slowly.

In order to produce the observed HXR in the impulsive phase, particles must be accelerated to the non-thermal (i.e. high) energies. Each phase is typically longer in duration than the last. The preflare and impulsive phases have lengths of the order of a few minutes for a large flare. The main phase then lasts a few tens of minutes, and the decay phase is typically a few hours long (Benz (2008)).

Many different flare models exist. A typical example of such a model is shown in figure 1.5. This model shows many features common to flare models. The magnetic field is modelled as a loop. The magnetic field loop has two 'footpoints' which are at the interface between the corona and the chromosphere. At these footpoints, hard (photon energy above 20keV) X-rays are produced as electrons are decelerated when they enter the denser chromosphere

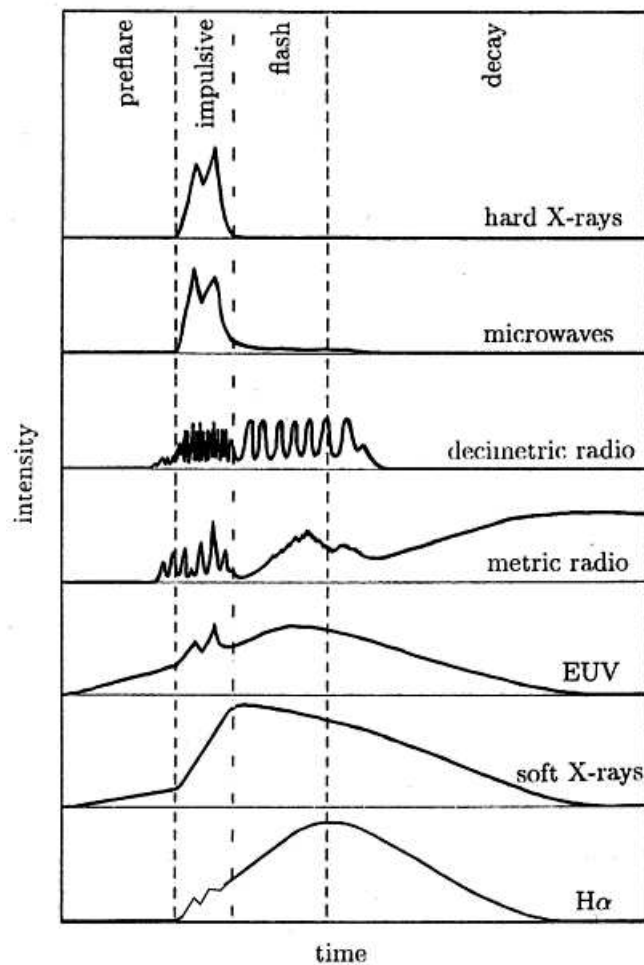


Figure 1.4: An example of a solar flare time profile at various wavelengths (Benz (2002)). The four stages of the flare are shown.

(Brown, 1971). The point at which these electrons are accelerated is typically situated at the cusp of the flaring loop, although some models postulate the existence of many smaller re-acceleration sites along the loop length (e.g. Brown *et al.* (2009)). Soft (photon energy below 20 keV) X-rays are produced by thermal electrons along the loop length. The flare loop is modelled as a magnetic flux tube which confines the coronal plasma.

Although the typical picture of a solar flare places the regions of HXR emission at the flare footpoints, regions of HXR emission have also been observed at the loop top, initially and most famously by Masuda *et al.* (1994a). Such observations require that particles are accelerated to high energies at the loop top, and that collisions occur there (Krucker *et al.* (2008b)). This acceleration region is often modelled as an X-type neutral point (e.g. Fletcher and Petkaki (1997)). The X-type neutral point is defined and further discussed in chapter 2.

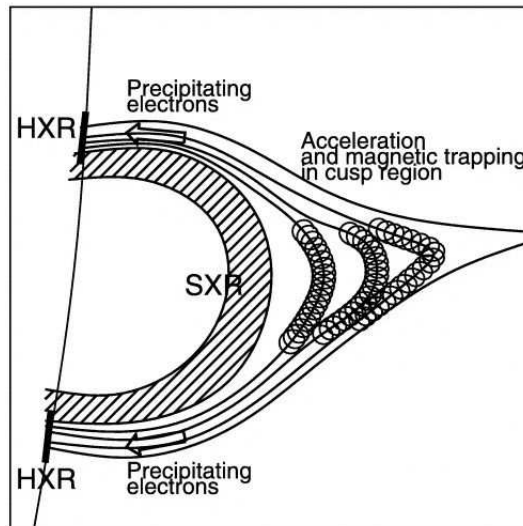


Figure 1.5: An example of a solar flare model. HXR indicates areas of hard (i.e. high energy) X-ray emission. SXR indicates areas of soft (i.e. low energy) X-ray emission. The flare is shown extending outwards from the 'limb' (the edge of the solar disk), and electrons are accelerated from the cusp of the flaring loop towards the footpoints. (Aschwanden, 2004b).

Hard X-rays place particularly stringent requirements on the flare particle accelerator. In order for the chromospheric X-ray fluxes seen in flares to be achieved, electrons must flow through the acceleration region at a rate $\geq 10^{37}$ electrons/s (Vlahos, Krucker, and Cargill (2009)). This requires all of the electrons in a coronal volume of $\approx 10^{30} \text{cm}^3$ to be accelerated over a few minutes, unless the electrons can somehow re-encounter the acceleration region. Since the volume of a solar flare is $\approx 1.8 \times 10^{26} \text{cm}^3$ (Aschwanden (2004a)), it seems inevitable that particles will either have to re-enter the acceleration region, or remain trapped there.

1.5 Plasma Turbulence

The plasma being considered in this thesis is the coronal plasma, which is of course highly dynamic. However, even well-controlled laboratory plasmas will contain some degree of turbulence. Turbulence can be thought of as a superposition of ripples and disturbances

in the plasma which (at least at small amplitude) may be viewed as a superposition of the natural wave modes of the plasma. In the vicinity of energy release, e.g. during magnetic reconnection, such turbulence may become a major component of the plasma.

It has been suggested that the process of magnetic reconnection generates plasma turbulence due to the plasma outflows from the reconnection region (e.g. Liu *et al.* (2008); Petrosian and Liu (2004)). When a magnetised plasma is perturbed by wave mode oscillations, this produces a form of turbulence, which can accelerate electrons to energies which reproduce the spectra seen in electron-dominated flares (Park, Petrosian, and Schwartz (1997)).

Kolmogorov (1941) proposed that the transfer of energy from large scales to small results in a steady situation where energy is distributed over wavenumber as a broken power law. This so called 'K41 turbulence' can be seen in figure 1.6. Broadly speaking, the spectrum is divided into three parts. On the very largest scales, the energy spectrum has a spectral index of -1. On intermediate scales, the spectral index is $-5/3$. This is the range in which particles within the plasma can become energised (Frisch (1995)). On the very smallest scales, this energy is transferred into heat.

The $-5/3$ spectral index is arrived at via dimensional considerations. Kolmogorov postulated that the energy variation per unit wavenumber should depend only on the wavenumber (k), and the rate of energy distribution per unit volume (ψ), as follows

$$E(k, \psi) \approx k^\alpha \psi^\beta. \quad (1.1)$$

It is known that k has units of $1/\text{length}$, ψ has units of $\text{length}^2/\text{temperature}^3$, and E has units of $\text{length}^3/\text{temperature}^2$. Some trivial algebra then gives the result that the index α in equation 1.1 takes the value $-5/3$.

This $-5/3$ power law has been seen in in-situ measurements of the solar wind, an example of which is given in figure 1.7 (which is taken from Alexandrova *et al.* (2009), see also e.g. Matthaeus and Goldstein (1982)). The K41 model was originally used to describe unmagnetised plasmas. However, the appearance of a K41 power law in the solar wind suggests that the application of such models to magnetised plasmas in the solar wind and solar corona is possible. Indeed, a $-5/3$ power law can be used to model turbulence due to Alfvén waves in the solar corona (e.g. Cranmer and van Ballegoijen (2003)), and it is expected (e.g. Liu *et al.* (2008)) that turbulence will be associated with magnetic reconnection events. Magnetohydrodynamic (MHD) turbulence was modelled as wave turbulence roughly 20 years after

K41 turbulence was first proposed (Iroshnikov (1963); Kraichnan (1965)). However, these models require that the energy cascade be isotropic in Fourier space, a caveat which has met with criticism (e.g. Cho, Lazarian, and Vishniac (2002)). An anisotropic cascade was first modelled by Goldreich and Sridhar (1995), who developed a model of MHD turbulence which has an energy spectrum with a spectral index of $k^{-5/3}$, the spectral index that K41 gives for turbulence on intermediate scales.

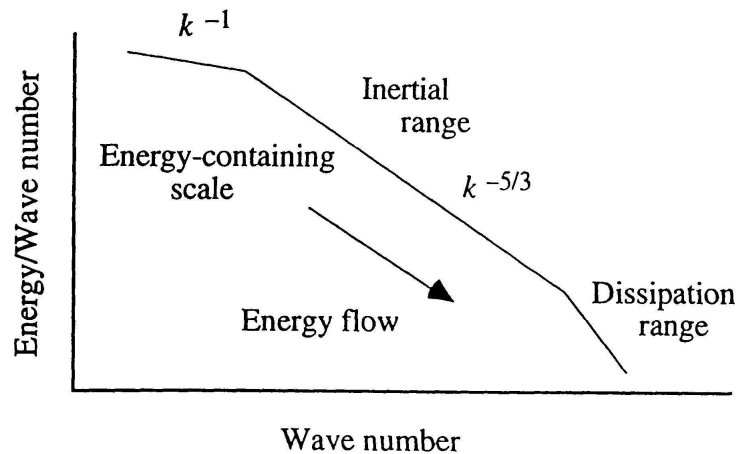


Figure 1.6: Change in plasma energy with wavenumber according to the K41 model (Goldstein, Roberts, and Matthaeus, 1995).

In this work, I will seek to introduce a superposition of disturbances into a simulation of a coronal plasma via creating noisy electric and magnetic fields in which the behaviour of test particles is then studied. The creation of these fields is discussed in detail in chapter 3.

1.6 Conclusion

This chapter formed a brief introduction to activity in the outer layers of the Sun. We have seen that active regions are created by magnetic flux that emerges from the solar interior. This flux is thought to be generated by shear at the tachocline, caused by differences in the rotation of the radiative zone and the convective zone. Such flux emerges due to convection, and forms active regions where it emerges.

Phenomena associated with active regions include CMEs, sunspots, prominences and solar flares. Solar flares are important for the work in this thesis, as they can accelerate particles. Such acceleration regions are likely to be turbulent, so we also briefly explored the concept of plasma turbulence.

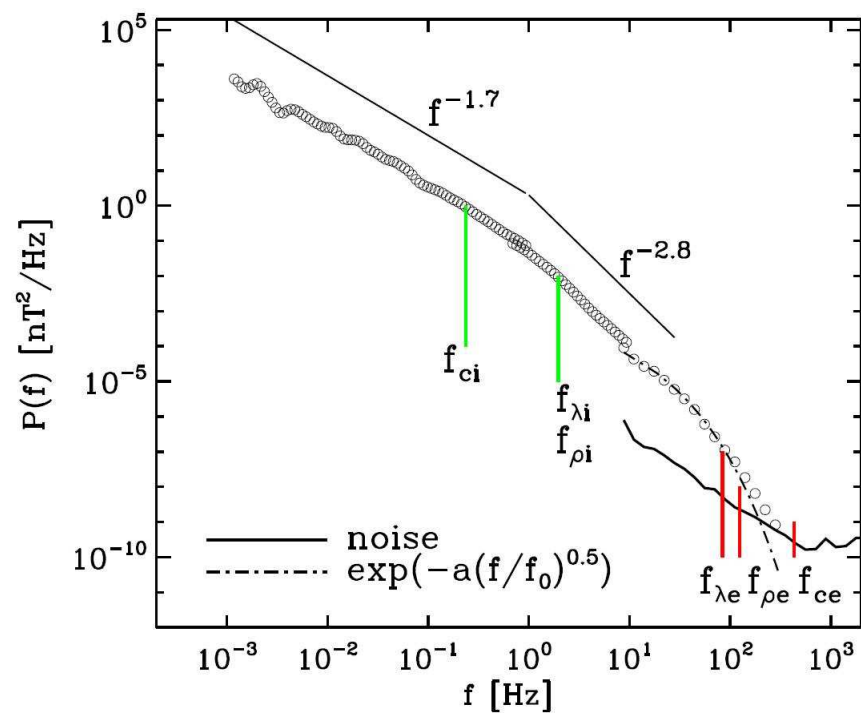


Figure 1.7: Variation of magnetic power density with frequency in the solar wind, as measured by Cluster (Alexandrova *et al.*, 2009).

2. Magnetic Reconnection

2.1 Introduction

In this chapter, I will detail a few examples of mechanisms via which magnetic reconnection can occur. These examples will include steady state models (Sweet-Parker and Petschek) as well as the spontaneous kink mode and tearing mode models. I also discuss collisionless reconnection, and how this can occur if the concept of an inertial resistivity is introduced. Finally, I describe an X-type neutral point, and how this can be used to model an acceleration region in the solar corona.

2.2 What is Magnetic Reconnection?

Magnetic reconnection can be simply described as a change in the structure of the magnetic field due to plasma flows (see e.g. Priest and Forbes (2000)). There is a change in the topology of the magnetic field due to magnetic field lines breaking and reconnecting so that stored energy can be released. A change in magnetic field structure can be described in terms of the induction equation. The induction equation is derived from Maxwell's equations, Faraday's law, Ohm's law and Ampere's law. The displacement current term of Ampere's law can be neglected if one makes the assumption that the fluid velocities are much smaller than the speed of light, and that the oscillation timescale of the electric field is much longer than the timescale of the system (Jackson (1965)). Assuming a uniform resistivity, this gives

$$\frac{\partial \mathbf{B}}{\partial t} = \nabla \times (\mathbf{u} \times \mathbf{B}) + \frac{c\eta}{4\pi} \nabla^2 \mathbf{B}. \quad (2.1)$$

η is the plasma resistivity, and \mathbf{u} is the fluid velocity. The first term on the r.h.s. describes changes in the magnetic field due to advection of the plasma. The second term describes changes due to diffusion. The ratio of the two terms is called the magnetic Reynolds number,

which is very large in the solar corona ($\approx 10^8$). This means that the magnetic field is 'frozen in', i.e. as the plasma moves, the magnetic field is carried with it. When two regions of oppositely directed field (see figure 2.1) are forced together by plasma flows (Gorbachev and Somov (1989)), a large current will arise at the boundary between two regions of oppositely directed field, in accordance with Ampere's law:

$$\nabla \times \mathbf{B} = \frac{1}{c} \left(4\pi \mathbf{J} + \frac{\partial \mathbf{E}}{\partial t} \right) \quad (2.2)$$

where \mathbf{J} is the current density. This current is opposed by the electric resistivity of the plasma, and plasma diffuses through the domain boundary from both sides. Since the field is frozen in to the plasma, magnetic flux is then pulled into a region of oppositely directed flux, resulting in reconnection.

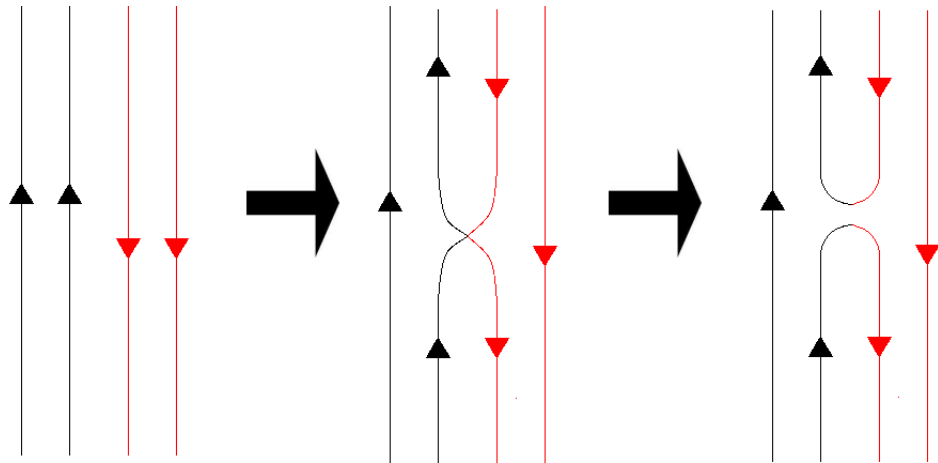


Figure 2.1: Two sets of oppositely directed magnetic field lines, shown here breaking and reconnecting to form new field lines.

There are many theories describing reconnection. All models propose a mechanism whereby the magnetic field is simplified post-reconnection, and that stored energy is released as the magnetic field re-configures following reconnection.

2.3 *Steady State Reconnection*

The first models of reconnection were steady state in character and were constructed by Sweet (1958a) and Parker (1957). The Sweet-Parker model proposes that plasma flows could cause two oppositely directed magnetic fields to be pushed together, creating a current sheet. The two flows are assumed to be antiparallel, of equal strength, incompressible and of uni-

form density. There is a steady inflow of plasma into the current sheet and an outflow of reconnected field from the narrow edges of the current sheet, as shown in figure 2.2.

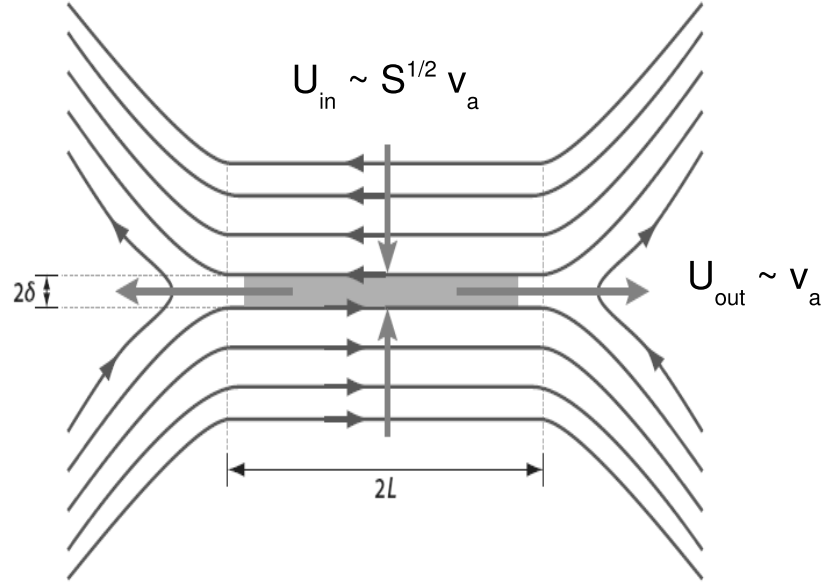


Figure 2.2: Sweet-Parker reconnection model. Slightly adapted from Zweibel and Yamada (2009). S is the Lundquist number, which is the ratio of the Alfvén timescale to the resistive diffusion timescale.

It can be seen in figure 2.2 that plasma flows in to the long side of the current sheet ($2L$) with speeds much smaller than the Alfvén speed, and is ejected from the narrow edge of the current sheet (2δ) at around the Alfvén speed. Sweet-Parker reconnection produces a reconnection rate that is much faster than resistive diffusion, but much slower than the reconnection rates inferred from solar flares. The reconnection rate (defined as U_{in}/U_{out}) can be derived as follows. Using ideal Ohm’s law and the assumptions previously stated (that the two flows are assumed to be antiparallel, of equal strength, incompressible and of uniform density), and expression for the out of plane electric field, E_z , is given by

$$E_z = U_{in} B_{in}, \quad (2.3)$$

where U_{in} is the inflow speed and B_{in} is the upstream magnetic field strength. If displacement current is neglected, an expression for the out of plane current (J_z) can be obtained using Ampere’s law, so that

$$J_z \approx \frac{B_{in}}{\mu_0 \delta}, \quad (2.4)$$

where δ is half of the current sheet thickness. If the electric field outside the sheet is matched with the resistive electric field (given by $\mathbf{E} = \eta \mathbf{J}$, where η is the resistivity) inside the sheet, then the inflow speed is given by

$$U_{in} \approx \frac{\eta}{\mu_0 \delta} \quad (2.5)$$

Conservation of mass gives the relationship between the inflow (U_{in}) and outflow (U_{out}) speeds as

$$U_{out} \delta = U_{in} L. \quad (2.6)$$

The inflow speed is very small because it is inversely proportional to the magnetic Reynolds number, which is $\approx 10^8$ in the corona. This means that reconnection necessarily proceeds very slowly.

Petschek (1964a) proposed a reconnection model which contained standing slow mode shock waves in the inflow region. This creates a current sheet where the inflow and outflow area are of comparable sizes, allowing for a faster reconnection rate (figure 2.3). The inflow speed for Petschek reconnection is inversely proportional to the logarithm of the magnetic Reynolds number (in the Sweet-Parker case, the reconnection rate is inversely proportional to the square root of the magnetic Reynolds number), meaning that reconnection can proceed more quickly.

2.4 Spontaneous Reconnection

2.4.1 Tearing Mode

Steady state reconnection is driven by large scale plasma flows. Furth, Killeen, and Rosenbluth (1963) proposed that small perturbations to the magnetic field could cause the field to become unstable, causing reconnection to occur. The tearing mode instability is an instability in which arises when the resistivity is non-zero, though the plasma is stabilised against

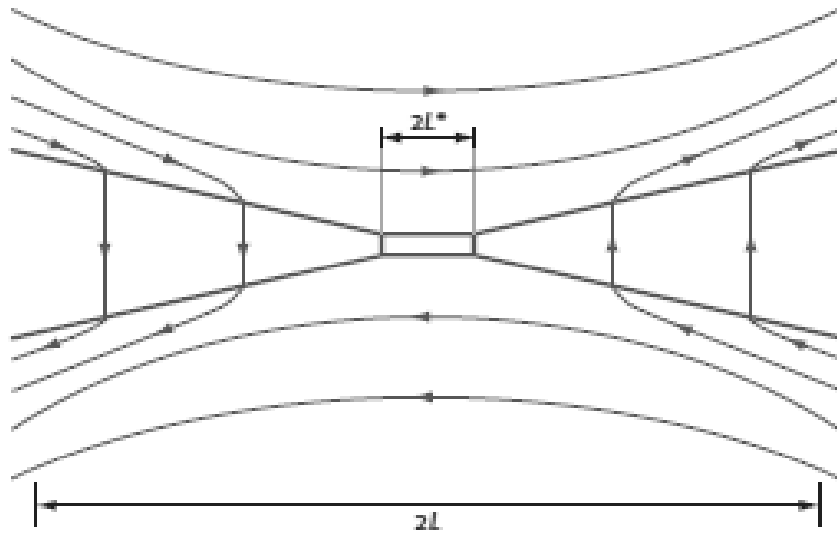


Figure 2.3: Petschek reconnection model. Slightly adapted from Zweibel and Yamada (2009).

the tearing mode when the resistivity is zero. A tearing mode instability is generated when a plasma with a non-uniform current density is subject to perturbations. The perturbation length scale must be greater than the length scale of the current density gradient in order for an instability to form. The tearing mode is associated with the formation of small-scale magnetic structures, called magnetic islands (see e.g. Fitzpatrick (1993)). Magnetic islands are a series of linked X- and O-type nulls, an example of a chain of magnetic islands is shown in figure 2.4. The structure of an X-type neutral point is described in section 2.6. An O-type null is a magnetic field structure formed from a series of concentric elliptical field lines. At the centre of the structure, the magnetic field strength is zero.

2.4.2 Kink Mode

Another example of an instability that can lead to reconnection is the kink mode. The kink mode instability occurs in a flux tube which has a strong axial current. If the magnetic forces on one side of the tube are greater than those on the other side, a kink develops in the tube. The instability becomes self-sustaining as the forces on either side of the flux tube are increasingly imbalanced. Waelbroeck (1989) showed that if such an instability is in a

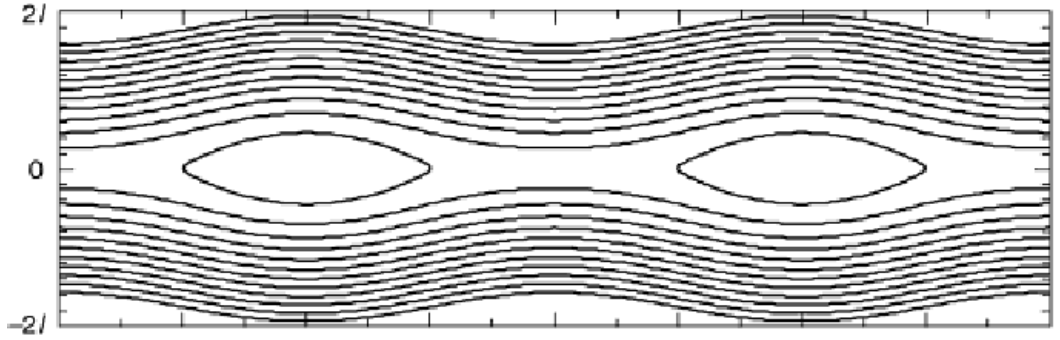


Figure 2.4: Chain of magnetic islands, formed from a series of X- and O-type nulls. Figure taken from Birn and Priest (2007).

non-linear state, a helical current sheet develops which can reconnect as a series of magnetic islands are formed.

2.5 Collisionless Reconnection

Collisionless reconnection in particular has been extensively studied in recent years (e.g. McClements, Shah, and Thyagaraja (2006)). Collisionless reconnection is a type of MHD (magnetohydrodynamic) reconnection in which the Hall effect is included. Ohm's law says that in a steady state the force on particles is balanced by the force due to collisions. The generalised Ohm's law states that:

$$\mathbf{E} = -\frac{1}{c}[\mathbf{v} \times \mathbf{B}] + \eta \mathbf{j} + \frac{\mathbf{j} \times \mathbf{B}}{n_e e c}. \quad (2.7)$$

The final term on the r.h.s. is the Hall term, which had been neglected in the reconnection models previously described. However, in collisionless reconnection, this term dominates. This creates a spatial scale associated with the Hall term, which is given by:

$$d_i = \frac{c}{\omega_{pi}}, \quad (2.8)$$

where ω_{pi} is the ion plasma frequency. At distances less than d_i from the neutral line, ions decouple from electrons, leading to a thinner diffusion layer than in collisional reconnection as the electrons continue to flow inwards, (figure 2.5). This in-plane current generated by the electrons also creates a quadrupolar out of plane magnetic field, which can also be seen in

figure 2.5. The collisionless approach is appropriate when considering acceleration regions in the solar corona since the mean free path of the particles is much larger than the size of the acceleration region (Martens (1988)).

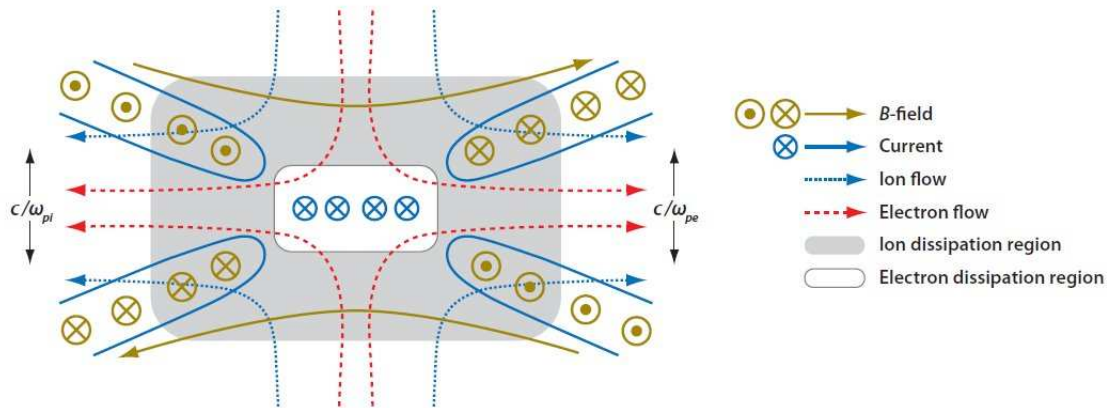


Figure 2.5: Collisionless reconnection model, showing ions and electrons moving separately. ω_{pi} is the ion plasma frequency, ω_{pe} is the electron plasma frequency. Zweibel and Yamada (2009).

In the case of collisionless reconnection, the resistivity of the plasma cannot, of course, be due to collisions. It was therefore thought that reconnection could not occur in the absence of collisions, as there would be no resistivity in the system. However, Speiser (1970) showed that one can calculate an inertial resistivity, which is a function of the amount of time particles spend in the diffusion region. It is this inertial resistivity which I use for my calculations in chapters 3 and 4. The precise manner in which this is calculated is detailed in section 3.3.1.

2.6 The X-Type Neutral Point

An X-type neutral point is a type of magnetic field which contains a central point at which the magnetic field goes to zero and which is divided into four regions of different connectivity, divided by separatrices. A 2D X-type neutral point can be seen in figure 2.6.

Such a field is described in 2D by the equations

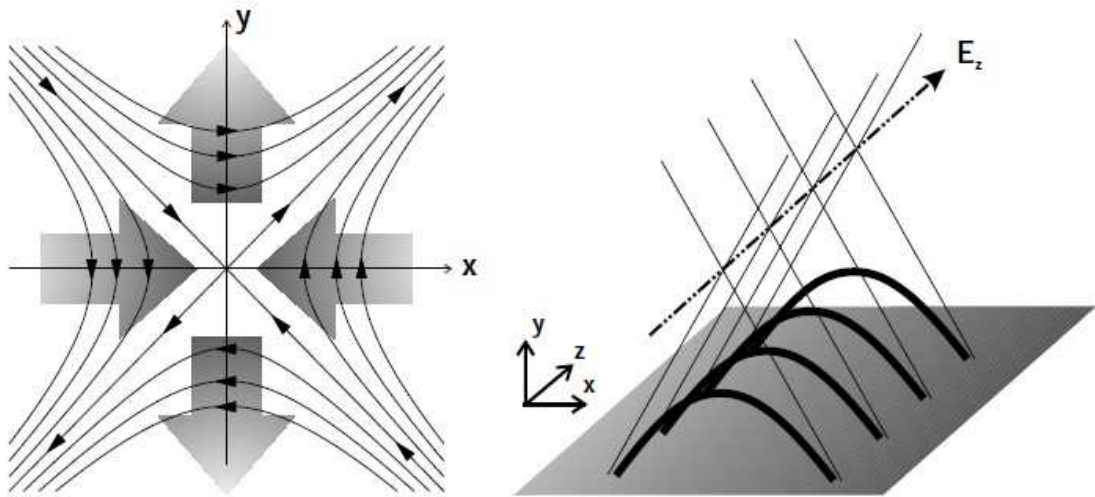


Figure 2.6: A 2D X-type neutral point. The left hand pane shows the magnetic field in the x - y plane. The thick grey arrows indicate the direction of inflow and outflow from the $\mathbf{E} \times \mathbf{B}$ drift. This X-type neutral point does not have any B_z component, and does not vary in the z direction. This is shown in the right hand plane, which shows an arcade in the z -direction. Figure taken from Hannah (2005).

$$B_x = \frac{B_0}{D}y \quad (2.9)$$

$$B_y = \frac{B_0}{D}x \quad (2.10)$$

B_0 is the field strength at $r=D$, where \mathbf{D} is the size of the region. At the centre of the region, (i.e. at the neutral point) particles decouple from the magnetic field and are freely accelerated by any electric field present (i.e. in this region the particle moves non-adiabatically, meaning that they are able to gain or lose kinetic energy). Particles are able to move non adiabatically near the null as they become demagnetised and can gain energy if an electric field is present. The radius of the non-adiabatic region is the point at which the particle's gyroradius is the same size as the scale length of the magnetic field. Such magnetic field configurations are therefore often considered when modelling reconnection regions in the solar corona. The X-type field is a highly idealised configuration but its simplicity means that essential features of reconnection may be studied. If an electric field is imposed in the z -direction, an $\mathbf{E} \times \mathbf{B}$ drift results. This will tend to move particles closer to the null by moving them in the x -direction. The particles are then expelled from the null in the y -direction. When particles enter the non-adiabatic region, they decouple from the magnetic field lines, and are freely accelerated in the z -direction, parallel to the electric field. A sample proton trajectory can be seen in figure 2.7. It can be seen that the particle spirals around the field lines, and mirrors back and

forth. As distance from the neutral point increases, the particle's gyroradius decreases, and it is more tightly tied to the field lines. Closer to the null, the particle decouples from the field lines.

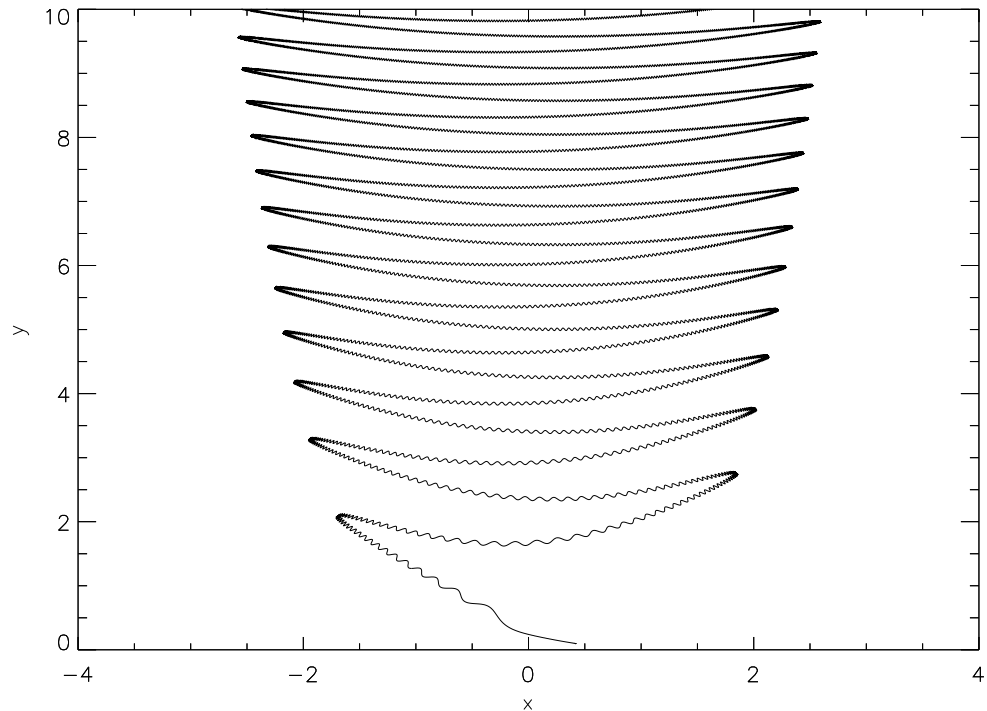


Figure 2.7: Trajectory of a proton in an unperturbed X-type neutral point.

As yet, no model exists which accounts for all of the observed properties of the energy release in solar flares. As has been discussed, early reconnection models (e.g. Sweet (1958b), Parker (1963)) considered the formation of current sheets by resistive diffusion. However, these models gave reconnection rates that were much too slow. Petschek (1964b) suggested that higher outflow speeds can be reached if a central region dominated by wave propagation is introduced.

Bulanov and Syrovatskii (1980) were the first to propose that such waves could be magneto-hydrodynamic in nature, and considered an X-type neutral point perturbed by harmonic fast waves that are azimuthally symmetric. They considered a 2D cylindrically symmetric geometry, and perturbed the system at the system boundary. They found that these perturbations became azimuthally symmetric as they approached the null. Initially, this prescribed symmetry meant that it was unclear if this result was applicable more generally. However, Craig and co-authors (Craig and McClymont (1991), Craig and McClymont (1993), Craig and Watson (1992)) found that reconnection can only occur if the wave modes perturbing the neutral point have azimuthal symmetry.

This thesis deals with following test particles in the presence of electric and magnetic fields calculated by a similar formalism to Craig and McClymont (1991). Test particle calculations allow us to follow the behaviour of individual particles without considering the effect that the particles themselves may have on the fields they move in, so the behaviour of the particles can potentially be studied using a different approach to that which was used to calculate the electric and magnetic fields. Whilst this approach neglects the effect of the particles on the fields they move in (and the effect of particles on one another), the inclusion of such effects would make the calculations considerably more complicated and increase the computation time to an impractical extent.

Petkaki and MacKinnon (1997),(2007) considered an X-type neutral point being perturbed by single eigenmode oscillations, similar to those studied in Craig and McClymont's work, and found that such oscillation increased the efficiency of the neutral point as a particle accelerator. Petkaki and MacKinnon (2007) found that certain frequencies were more effective at accelerating particles than others, and it was thought that this was due to resonant interactions, since particles were observed to gain energy outside of the central diffusion region.

This work seeks to extend these models by examining the effects of weak turbulence on the reconnection region and on particle behaviour. This turbulence will be introduced by considering a superposition of MHD eigenmodes. It is likely that a viable solution to the problem must be time dependent. This is because steady state solutions cannot adequately deal with the large scale advection of the plasma as well as the small scale diffusion region around the neutral point. Since this project focusses on the reconnection region specifically, a time-dependent solution is necessary.

The motivation for introducing this time dependence via a time-dependent electric field into this picture comes from the idea of linear reconnection as laid down by Craig and McClymont (1991). The structure and evolution of the reconnection region implies the form of the electric field which I use to accelerate particles in these simulations. It is hoped that the superposition of modes will lead to particle scattering, allowing the particles to re-encounter the diffusion region many times, leading to particles reaching high energies. It is also predicted that such a superposition of modes will lead to repeated resonant interactions by the particles, which will also enable them to become highly energised. A combination of these effects should create an effective method for particle acceleration in the corona.

2.7 Test Particle Studies

The test particle approach is widely used in the study of accelerated particles, see e.g. Wood and Neukirch (2005), Dalla and Browning (2005), Gordovskyy and Browning (2011), Zharkova and Agapitov (2009). Test particle studies can be divided into two groups: 3D and 2D simulations. For 2D simulations such as those in this thesis, the magnetic field has no B_z component. These studies generally assume a magnetic field in the x-y plane, with an imposed electric field component (see e.g. Petkaki and MacKinnon (1997), Vekstein and Browning (1997), Petkaki (1996)). These studies show that the effectiveness of the acceleration mechanism varies depending on the initial position of the particles being accelerated, as well as on the strength of the electric field and the size of the null (i.e. the size of the region in which particles can be freely accelerated).

In 3D simulations, a B_z component is included. In many 3D simulations, the magnetic field takes the form of a ‘spine and fan’ field, where the ‘fan’ part is very similar to a 2D x-point, and is the field in the x-y plane. The ‘spine’ is a B_z component which extends from the centre of the x-y plane (see e.g. Dalla and Browning (2008); Browning *et al.* (2010)).

I will consider particles in linearly reconnecting fields (see also e.g. Hamilton *et al.* (2005)). Other research has made use of more sophisticated numerical models of reconnection to provide the fields in which the particles move (e.g. Gordovskyy, Browning, and Vekstein (2010b), Gorbachev and Somov (1989), Wood and Neukirch (2005)). In this work, I will be considering particle motion around a null point, rather than in a current sheet. The electric and magnetic fields are also time-dependent. Crucially, a unique feature of this work is the attempt to construct electric and magnetic fields that are both ‘noisy’ and realistic. The fields are constructed from a superposition of eigenmodes appropriate to this spatially inhomogeneous situation. The dynamic character of the field is essential to this.

It is also common practice in this kind of work to follow particles in the guiding centre approximation (e.g. Karlický and Bárta (2006); Gordovskyy, Browning, and Vekstein (2010a); Browning *et al.* (2010)). This means that only the centre of the particle’s gyromotion is followed. This simplifies the equations of motion, and allows particles to be followed for longer times than I was able to do in this work. However, this work focuses on effects that result near the null from non-adiabatic behaviour, which wouldn’t be properly described in the guiding centre approximation. I will therefore calculate particle trajectories by considering their motion in x, y and z .

2.8 Conclusion

In this chapter, I have established what is meant by magnetic reconnection. I have also looked at a selection of different methods via which magnetic reconnection can occur. We have seen that early steady state models give reconnection rates that are too slow when compared with rates inferred from observations. I also introduced the concept of collisionless reconnection, and the inertial resistivity that I will use in the construction of the magnetic fields in the following chapter. I looked at the X-type neutral point, which is the basic model of an acceleration region that I will be using in the following chapters. Finally, I discussed previous test particle studies, since I will be using a test particle approach to study particle behaviour.

3. Noisy Electric and Magnetic Fields Near A Magnetic Null Point

3.1 *Introduction*

In this chapter, I will calculate the form of the electric and magnetic fields that will be used in chapter 4. These fields will be created from a superposition of cold plasma eigenmode oscillations. The electric and magnetic fields associated with these eigenmodes will be calculated, and noisy electric and magnetic fields will be constructed from a superposition of the fields for each of the eigenmodes. In this chapter, I will use the word ‘noisy’ to indicate fields which contain superpositions of oscillations, meaning that they vary both spatially and temporally. I use the word ‘noisy’ rather than the word ‘turbulent’, as these fields are still too well ordered to be considered truly turbulent. In section 3.4 I reproduce the results and calculations of Petkaki (1996) in order to do this. The spatial dependence of these fields will be introduced via the hypergeometric function, so a fast, accurate method of calculating the hypergeometric function for each electric and magnetic field mode will be developed.

3.2 *Reconnection at an X-type Neutral Point*

The simplicity of the X-type neutral point field and the associated description of linear reconnection provide a prototypical picture in which particle acceleration may be studied. Petkaki and MacKinnon (1997),(2007) considered an X-type neutral point being perturbed by single eigenmode oscillations, similar to those studied in Craig and McClymont’s work, and found that such oscillation increased the efficiency of the neutral point as a particle accelerator. This was shown to be due to the finite width of the nonadiabatic region close to the neutral point which allows particles to gain or lose energy randomly resulting in a Fermi-type stochastic acceleration. Furthermore Petkaki and MacKinnon (2007, 2011) found that certain frequencies were more effective at accelerating particles than others, possibly through resonant interactions, since some particles were observed to gain energy outside of the cen-

tral diffusion region. (See also Guo *et al.* (2010) and the analytical discussion of Litvinenko (2003)).

This work seeks to extend these models by examining the effects of weak turbulence on the reconnection region and on particle behaviour. This turbulence will be introduced by considering a superposition of magnetohydrodynamic (MHD) eigenmodes. It is likely that a viable solution to the problem must be time-dependent. This is because steady state solutions cannot adequately deal with the large-scale advection of the plasma as well as the small scale diffusion region around the neutral point. The motivation for introducing this time dependence via a time-dependent electric field into this picture comes from the idea of linear reconnection as laid down by Craig and McClymont (1991). The structure and evolution of the reconnection region implies the form of the electric field which I use to accelerate particles in these simulations. The introduction of multiple scale lengths could produce a form of turbulence in the corona, and allow the reproduction of the scale-free behaviour seen in solar flares.

3.3 Normalisations

In order to investigate the motion of particles at an X-type neutral point, it is wise to normalise the problem variables to sensible length and time scales. The equations of motion are made dimensionless in the same manner as the equations of motion in Petkaki and MacKinnon (1997). Specifically, distances are normalised to $d_i = \left(\frac{c^2 m_i}{e B_0}\right)^{1/2}$, where $i = e$ or p for electrons or protons, and $B_0 = B/D$ (the magnetic field at distance D). The velocities then are normalized to the speed of light which is appropriate for the relativistic equations of motion. The normalising time is derived from these to quantities such that $\tau_p = 1.87 \times 10^{-4} s$. I normalise masses to the particle rest mass. If $B = 100G$ and D is a typical coronal length scale of $10^9 cm$ then $d_p = 5.6 \times 10^6 cm$. The electric field is normalised to $B_0 d_i$, as is the magnetic field.

3.3.1 Resistivity

A rough estimate of inertial resistivity is given by considering the time (t) a thermal particle takes to cross the non-adiabatic region, i.e.:

$$\eta = \frac{1}{4\pi\sigma\tau_p} \quad (3.1)$$

and

$$\sigma = \frac{ne^2t}{m_e}, \quad (3.2)$$

where τ_p is the normalising time. By using the time (t , in seconds) taken for a 1keV proton to travel a distance equal to twice the size of the non-adiabatic region, one can obtain an approximate value for the inertial resistivity (Speiser (1965)). The dimensionless resistivity is therefore $\eta = 3.1724 \times 10^{-11}$. Converting η to c.g.s units gives $\eta = 5.9324 \times 10^{-15}$ s. By way of comparison, the collisional resistivity is 2.2×10^{-13} in these units, or 4.16×10^{-17} s. This is comparable to a typical coronal value, which is usually taken to be around 10^{-16} (e.g. Litvinenko (2006)). In Craig and McClymont (1991) increased resistivity leads to a larger diffusion region. Increased resistivity could be due to enhanced inertial or anomalous effects (e.g. Petkaki and Freeman (2008) shows that an increased electron drift velocity leads to increased resistivity).

Changing the value of the resistivity will lead to changes in the magnetic field. Specifically, the size of the non-adiabatic region r_{ad} varies with η . The values of the decay and oscillation times for the cold plasma eigenmodes also depend on η , so the precise form of the perturbations to the electric and magnetic fields will also change. If I believed I knew the value of η from other considerations, I could rewrite 3.1 to estimate r_{ad} . However 3.3 provides only a first estimate of η . Other physical processes (e.g. ion-acoustic turbulence) might contribute to it and I cannot assume that changes in this parameter will be mirrored in the behaviour of test particles.

3.4 *Forms of the Electric and Magnetic Fields*

Following Craig and McClymont (1991) and Petkaki and MacKinnon (1997) I study the behaviour of test particles in a system with translational invariance in the z -direction. Then the magnetic field may be written:

$$\mathbf{B} = \nabla \times (\psi(x, y, t)\hat{\mathbf{z}}). \quad (3.3)$$

\mathbf{B} will be calculated in a 2D cold plasma model.

Following the method outlined in Petkaki (1996), I will look for eigenfunctions of the potential, ψ . I will use a superposition of these eigenfunctions to create noisy electric and magnetic fields.

In order to demonstrate how these eigensolutions are obtained, I will reproduce the calculations outlined in Petkaki (1996). Some intermediate steps in the algebra will be omitted.

In our dimensionless units, the induction equation is given by

$$\frac{\partial \mathbf{B}}{\partial t} = \nabla \times (\mathbf{v} \times \mathbf{B}) + \eta \nabla^2 \mathbf{B}, \quad (3.4)$$

where η is the dimensionless resistivity and v is the fluid velocity. If equation 3.3 is substituted into the above equation, after using the appropriate vector identities and integrating over the surface S ,

$$\frac{\partial \psi}{\partial t} + \mathbf{v} \cdot \nabla \psi = \eta \nabla^2 \psi. \quad (3.5)$$

is obtained. Using the Lagrangian time derivative, this can be written as

$$\frac{D\psi}{Dt} = \eta \nabla^2 \psi. \quad (3.6)$$

In our dimensionless units, the fluid momentum equation in the absence of an electric field is given by

$$\frac{d\mathbf{v}}{dt} = \mathcal{A} \nabla \times \mathbf{B} \times \mathbf{B}, \quad (3.7)$$

where \mathcal{A} is a constant which converts from our dimensionless units to those of Craig and McClymont;

$$\mathcal{A} = \frac{u_a^2 d_p^2}{c^2 D^2}, \quad (3.8)$$

where u_A is the Alfvén speed at the system boundary, \mathbf{D} is the size of the system (10^9 cm), c is the speed of light and d_p is the normalising length for protons.

If the current density and vector potential are substituted into equation 3.7, this gives

$$\frac{D\mathbf{v}}{Dt} = -\mathcal{A}\nabla^2\psi\nabla\psi. \quad (3.9)$$

I now want to make linear expansions of equations 3.6 and 3.9. I therefore write ψ and v as

$$\psi = \psi_0 + \psi_1 \quad (3.10)$$

$$v = v_0 + v_1, \quad (3.11)$$

where ψ_1 and v_1 are first-order terms. The system starts from equilibrium so that $v_0=0$. Using the following:

$$\frac{\partial\psi}{\partial t} = 0 \quad (3.12)$$

$$\nabla^2\psi = 0, \quad (3.13)$$

the time derivative of equation 3.6 can be written as

$$\frac{\partial^2\psi_1}{\partial t^2} + (v_1 \cdot \nabla)\psi_0 = \eta\nabla^2\dot{\psi}_1. \quad (3.14)$$

Rewriting and linearly expanding equation 3.9 gives

$$\frac{\partial v_1}{\partial t} = -\mathcal{A}\nabla^2\psi_1\nabla\psi_0. \quad (3.15)$$

Combining equations 3.14 and 3.15 gives (after some algebra)

$$\frac{\partial^2 \psi}{\partial t^2} - \eta \nabla^2 \dot{\psi} = \mathcal{A} r^2 \nabla^2 \psi, \quad (3.16)$$

where $r^2 = x^2 + y^2$ and the subscript 1 has been dropped so that ψ is now the perturbed potential.

3.4.1 Form of the Solution

I will look for solutions of the form:

$$\psi = e^{\lambda t} f(r) e^{im\phi} \quad (3.17)$$

Here λ and $f(r)$ are complex. The quantity m is an integer which is taken to be zero, since these are the only solutions via which reconnection can occur (Craig and McClymont (1991)). Evaluating $\dot{\psi}$, $\nabla^2 \dot{\psi}$ and $\nabla^2 \psi$, and combining their solutions gives

$$r(rf')' = \left(\frac{\lambda^2}{\mathcal{A} + \frac{\eta\lambda}{r^2}} \right) f(r). \quad (3.18)$$

At this point, it is expedient to make a change of variable such that

$$z = -\frac{\mathcal{A}r^2}{\eta\lambda}. \quad (3.19)$$

Taking and combining the first and second derivatives of f with respect to r gives

$$z(1-z)\frac{d^2 f}{dz^2} + (1-z)\frac{df}{dz} = -\frac{\lambda^2}{4\mathcal{A}}f(z). \quad (3.20)$$

This has the same form as the general form of the hypergeometric equation, which is

$$z(1-z)\frac{d^2 f}{dz^2} + (c - (\alpha + \beta + 1)z)\frac{df}{dz} = \alpha\beta f(z). \quad (3.21)$$

By inspection, it can be seen that

$$c = 1, \quad (3.22)$$

$$\alpha + \beta + c = 1, \quad (3.23)$$

$$\alpha\beta = -\frac{\lambda^2}{4\mathcal{A}}, \quad (3.24)$$

$$\alpha = -\beta. \quad (3.25)$$

The quantities α, β and λ are all complex, so that

$$\alpha = \rho + i\xi, \quad (3.26)$$

$$\beta = -\rho - i\xi, \quad (3.27)$$

$$\lambda = \kappa + i\omega. \quad (3.28)$$

If these expressions for α, β and λ are substituted into equation 3.24, after some algebra one obtains

$$\alpha = -\frac{\kappa}{2\sqrt{\mathcal{A}}} + i\frac{\omega}{2\sqrt{\mathcal{A}}}, \quad (3.29)$$

$$\beta = \frac{\kappa}{2\sqrt{\mathcal{A}}} - i\frac{\omega}{2\sqrt{\mathcal{A}}}. \quad (3.30)$$

The solution is therefore

$$f(r) = {}_2F_1(a, b; c; z) = f_{\Re}(r) + if_{\Im}(r). \quad (3.31)$$

The complex eigenvalues λ are written $\lambda = -\kappa + i\omega$ so that the real numbers ω and κ are frequency and decay rate respectively. Then the eigenvalues λ_n are fixed by the boundary conditions for the real (\Re) and imaginary (\Im) parts of the hypergeometric function at $r = 1$:

$$\Im(f(1)) = 0 = \Re(f(1)) = 0$$

This choice of boundary condition ‘freezes in’ the field, meaning that these perturbations are standing modes. Since the perturbation vanishes at the boundary, no flux enters or leaves the system (see Craig and McClymont (1991)). A different choice of boundary condition could produce travelling waves, but I do not study those here. I will then use these perturbations (recall that these are calculated in the manner of Petkaki (1996)) to produce electric and magnetic fields.

Numerically, I found the eigenvalues λ_n using Broyden’s method (Press *et al.*, 1992; Petkaki, 1996), with the analytical estimates of Craig and McClymont (1991) as first guesses. The hypergeometric function will be discussed further in section 3.4.2. This work follows particles in the presence of a 2D magnetic field. It has been shown (Litvinenko (1996), Hamilton *et al.* (2003)) that the addition of a B_z component can cause particles to become trapped within the current sheet as they become tied to the magnetic field in the z -direction. As particles follow these field lines, they are moving parallel to the electric field, leading to them gaining high energies. This means that the energies gained by particles in these simulations are likely to be at the lower end of the energy range that could be achieved with a 3D geometry.

3.4.2 The Hypergeometric Function

The Gauss hypergeometric function ${}_2F_1(a, b; c; z)$ is given by (Abramowitz and Stegun (1965))

$${}_2F_1(a, b; c; z) = \sum_{i=0}^{\infty} \frac{(a)_i (b)_i}{(c)_i} \frac{z^i}{i!}, \quad (3.32)$$

where $(x)_n = x(x+1)(x+2)\dots(x+n-1)$. Equation (3.32) converges only for $|z| < 1$. Since I would also like to consider $|z| > 1$, I must use a transformation formula in order to consider this region, which is given by (Abramowitz and Stegun (1965))

$$\begin{aligned}
{}_2F_1(a, b; c; z) &= \frac{\Gamma(c)\Gamma(b-a)}{\Gamma(b)\Gamma(c-a)}(-z)^{-a}{}_2F_1(a, 1-c+a; 1-b+a; \frac{1}{z}) \\
&+ \frac{\Gamma(c)\Gamma(a-b)}{\Gamma(a)\Gamma(c-b)}(-z)^{-b}{}_2F_1(b, 1-c+b; 1-a+b; \frac{1}{z}). \tag{3.33}
\end{aligned}$$

Recalling equation 3.31, I now have a solution for the hypergeometric function $f(r)$, since $f(r) = {}_2F_1(a, b; c; z(r))$ (Petkaki (1996)). I could also solve the hypergeometric function in this region by solving the hypergeometric equation (Press *et al.* (1992)), however this takes a long time to solve numerically, and for these purposes it is not practical. The analytic continuation method detailed above allowed these simulations to run approximately 2 orders of magnitude faster than when using the method detailed by Press *et al.* (1992). In order to obtain a smooth function at $|z| = 1$, the method of Press *et al.* (1992) (which is valid for all z) was used to between bridge the gap between the two solutions. The region of z for which the Press solution was used was from $|z| = 0.9$ to $|z| = 2.5$. This range was determined empirically, and is the smallest such region that gives a smooth solution.

Recall that for the problem being considered, the parameters a, b, c and z are complex and given by (Petkaki (1996))

$$a = -\frac{\kappa}{2} + i\frac{\omega}{2}$$

$$b = \frac{\kappa}{2} - i\frac{\omega}{2}$$

$$c = 1$$

$$z = -\frac{\mathcal{A}r^2}{\eta\lambda},$$

where $\lambda = -\kappa + i\omega$ and η is the dimensionless resistivity.

Figure 3.1 shows the form of the hypergeometric function for the modes $n = 0 : n = 3$. As n increases, there are more oscillations present, and the oscillations are closer together.

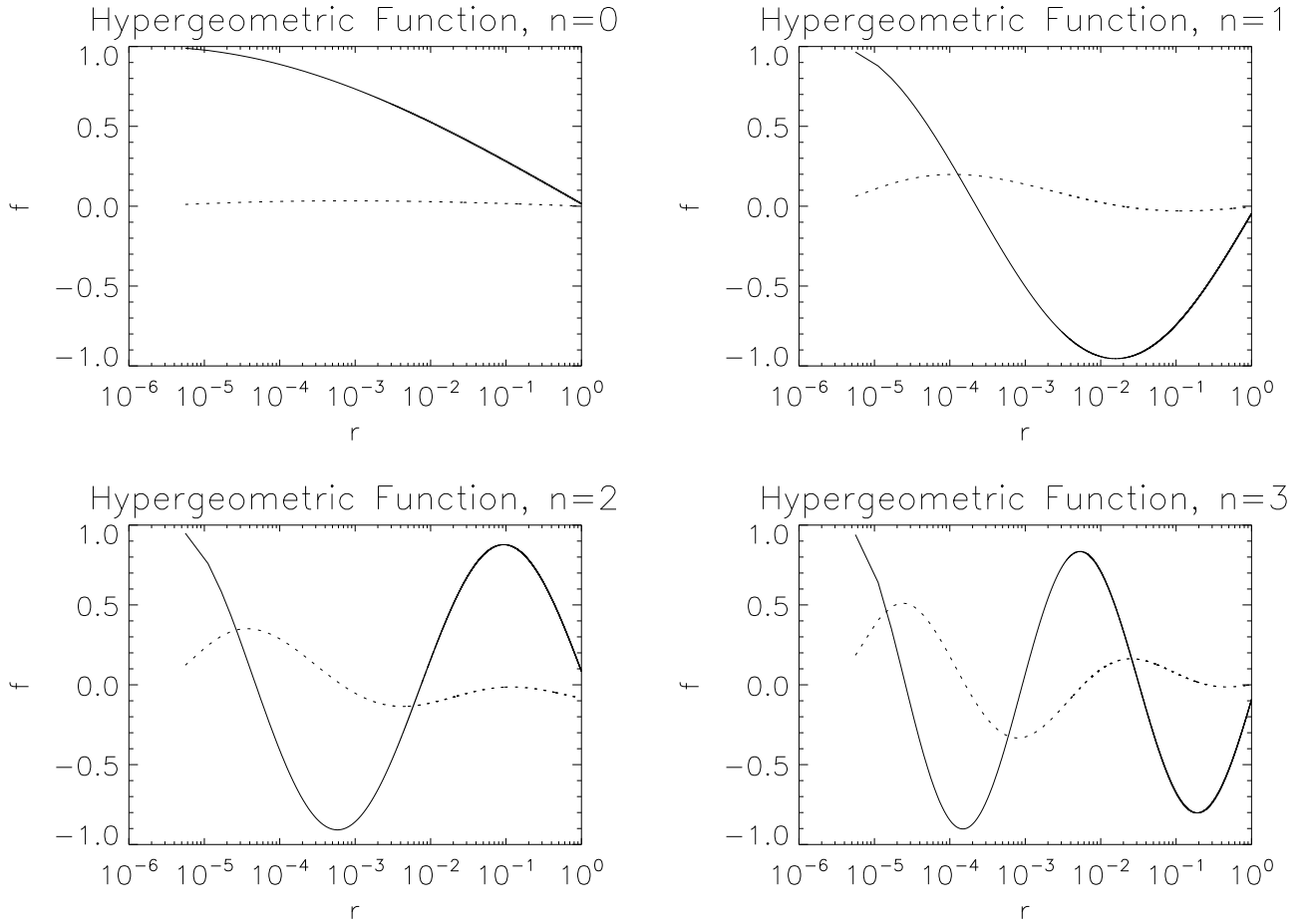


Figure 3.1: Form of hypergeometric function for first four eigenmodes. The solid line shows the real part of the function, the dashed line shows the imaginary part.

For the calculation of the magnetic field perturbation, the derivative of the hypergeometric function is used, which is given by Abramowitz and Stegun (1965) as

$$\frac{d}{dz} {}_2F_1(a, b; c; z) = \frac{ab}{c} {}_2F_1(a+1, b+1; c+1; z).$$

3.4.3 Explicit Forms of the Electric and Magnetic Fields

Because I am interested in a superposition of eigenmode solutions, the form of the vector potential is given by

$$\psi(x, y, t) = \psi_0(x, y) + \frac{1}{n} \sum_{n=1}^{n_{max}} a_n e^{(\lambda_n t + \phi_n)} f_n(r), \quad (3.34)$$

where $n = 0, 1, 2, \dots$, a_n is the amplitude of the perturbation, λ_n is the complex eigenvalue of the solution, ϕ_n is a random phase between 0 and 2π and $f_n(r)$ is the hypergeometric function. Below I experiment with values of n_{max} up to 49, a large enough number of eigenmodes to produce disordered, noisy fields without excessive computational effort. Eigenfunctions were all normalised to unity at $t = 0$. In the absence of a more detailed model for partition of energy between modes, and to highlight the potential role of turbulence I adopted a flat spectrum, $a_n = a_0 = 10^{-4}$ for all n .

The magnetic field is given by

$$\mathbf{B} = \nabla \times (\psi(x, y, t)\hat{\mathbf{z}}). \quad (3.35)$$

Therefore the electric field is

$$\mathbf{E} = -\frac{1}{c} \frac{\partial \psi}{\partial t} \hat{\mathbf{z}}. \quad (3.36)$$

The background field includes an X-type null point at $x = y = 0$, increases in strength linearly with r and is given by

$$\psi_0(x, y) = \frac{1}{2} (y^2 - x^2).$$

Here lengths have been normalised to the size D (taken to be 10^9 cm) of the system (so the outer boundary is at $r = 1$) and field strengths to the value on the boundary. I will have to use a different set of dimensionless units, however, to describe particle orbits.

The rest of ψ sums over the first n_{max} of the cold plasma eigenmodes calculated above, and which were originally constructed in Hassam (1992), Craig and McClymont (1991) and Petkaki and MacKinnon (1997) (see also Petkaki (1996)). These eigenmodes have a wavelike character far from the null and take on a resistive character at small r (i.e. they dissipate as they approach the null). The resistive character is modelled using the plasma resistivity η which is a parameter controlling the size of the diffusion region (Petkaki and MacKinnon, 1997). I include only the azimuthally symmetric eigenmodes that dissipate reconnectively (Craig and McClymont, 1991, 1993; Craig and Watson, 1992).

With randomly chosen phases ϕ_n , such a superposition simulates turbulence involving the eigenmodes appropriate to this inhomogeneous situation, and pays attention to the dissipation that takes place via reconnection at small r (see also McLaughlin, Hood, and de Moortel, 2011).

The following electric and magnetic fields were calculated for each mode (Petkaki and MacKinnon (1997)). These fields are time dependent, and evolve over the duration of the particle simulation.

$$E = a_n [\exp(-\kappa t) [\kappa (\cos(\omega t) f_{\Re} \sin(\omega t) f_{\Im}) + \omega (\cos(\omega t) f_{\Im} + \sin(\omega t) f_{\Re})]] \quad (3.37)$$

$$\overline{B_x} = \overline{y} [1 + a_n \frac{1}{2\eta} \exp(-\kappa t) [\kappa (\cos(\omega t) f'_{\Re} - \sin(\omega t) f'_{\Im}) + \omega (\sin(\omega t) f'_{\Re} + \cos(\omega t) f'_{\Im})]] \quad (3.38)$$

$$\overline{B_y} = \overline{x} [1 - a_n \frac{1}{2\eta} \exp(-\kappa t) [\kappa (\cos(\omega t) f'_{\Re} - \sin(\omega t) f'_{\Im}) + \omega (\sin(\omega t) f'_{\Re} + \cos(\omega t) f'_{\Im})]], \quad (3.39)$$

where f_{\Re} is the real part of the hypergeometric function, and f_{\Im} is the imaginary part. The values κ and ω are the real and imaginary parts of the eigenvalues of the perturbation. These give the decay and oscillation terms of the electric and magnetic fields. η is the dimensionless resistivity. Each eigenfunction was normalised so that its square norm was unity at $t = 0$ before multiplying by the amplitudes discussed above. Each perturbation was also given a random phase between 0 and 2π .

I therefore need to calculate

$$\int_0^{2\pi} \int_0^1 \psi \psi^* r dr d\phi = 1.$$

Given

$$\psi \psi^* = e^{\lambda t} f(r) e^{im\phi} e^{\lambda t} f(r)^* e^{-im\phi} = e^{2\lambda t} (f_{\Re}^2 + f_{\Im}^2), \quad (3.40)$$

this gives (at $t = 0$)

$$\int_0^1 (f_{\Re}^2 + f_{\Im}^2) r dr = \frac{1}{2\pi}. \quad (3.41)$$

Therefore, the perturbation for each mode is normalised to 1 at $t = 0$. For these superpositions of several modes, the sum of modes is divided by the number of modes being considered, so that this normalisation is preserved.

Particles will be followed in the presence of 5 different electric and magnetic fields, composed for ions as follows:

- Case 1: $E = 1 \times 10^{-4}$, $B_x = y$, $B_y = x$. The electric field in this case is constant, and is the same everywhere.
- Case 2: Perturbation for the $n = 0$ mode only. The perturbation has amplitude 1×10^{-4} .
- Case 3: Perturbation for a superposition of modes $n = 0 - n = 4$. Each perturbation has amplitude 1×10^{-4} .
- Case 4: Perturbation for a superposition of modes $n = 0 - n = 19$. Each perturbation has amplitude 1×10^{-4} .
- Case 5: Perturbation for a superposition of modes $n = 0 - n = 49$. Each perturbation has amplitude 1×10^{-4} .

Each mode is also given a random phase at $t = 0$. These phases then remain constant for the rest of the simulation, so that each particle sees the same fields. These five cases have been chosen to represent a progression in the degree of turbulence, more generally ‘noise’, in the reconnection region. Case 1 represents the steady reconnection region whose study dates back to Speiser (1956) while the other four cases become progressively more dynamic and irregular. As described earlier a normalisation is adopted to ensure that electric field amplitudes remain comparable and that differences in accelerated particle distributions really result from the different degrees of variability and spatial structure.

For electrons, the fields have the same composition, except that the perturbations in cases 2-5 and the constant electric field in case 1 all have amplitude 1×10^{-3} . This is because I only follow electrons for 0.1s due to the long computation times required for electrons, so a higher electric field is needed to accelerate particles over this time frame. The electric field experienced by the electrons at $r = 0$ can be seen in figure 3.7.

A sample of the eigenvalues for $\eta = 3.1724 \times 10^{-11}$ (used in calculating the fields) can be seen in Table 3.1. The oscillation and decay times that these values give can be seen

in table 3.2. These decay and oscillation times compare favourably with those seen in De Moortel, Ireland, and Walsh (2000) (which gives an oscillation time ≈ 180 to ≈ 420 s), Aschwanden *et al.* (1999) (which gives an oscillation time ≈ 300 s), Verwichte *et al.* (2009) (which gives an oscillation time 630 ± 30 s and a decay time 1000 ± 300 s) and De Moortel *et al.* (2002) (oscillation time ≈ 180 to ≈ 300 s). These times were inferred from observations of coronal loops, however they give us an idea of the kind of timescales on which disturbances propagate in the corona.

n	$\kappa (t_c)$	$\omega (1/t_c)$
0	0.007224	0.117742
1	0.023451	0.367979
2	0.048197	0.621554
3	0.057407	0.880324
4	0.071435	1.137985
5	0.090700	1.396334
10	0.178909	2.700797
15	0.234672	4.073513
20	0.364947	5.372426
25	0.435492	6.731654
30	0.556102	8.101894
35	0.658314	9.481737
40	0.800338	10.83539
45	0.981808	12.15455
49	1.184325	13.20617

Table 3.1: A selection of values of ω and κ for $\eta = 3.1724 \times 10^{-11}$. The unit t_c is the timescale used in Craig & McClymont's work, where $t_c = v_A D$. D is the distance from the null at the system boundary, and v_A is the Alven speed at the system boundary.

Magnetic and electric fields for a superposition of eigenmodes were generated by simply calculating the magnitude of the field at each mode and adding the modes together. a_n is the amplitude given to each mode. I chose a flat spectrum of modes ($a_n = 1$).

The variation of the electric field with r (where r is normalised to D) at $t = 0$ for can be seen in figure 3.2. Figure 3.6 shows the variation of the perturbation of the magnetic field.

The variation of the electric field with time at two different values of r (where r is normalised to D) can be seen in figures 3.3 and 3.5.

The field for case 2 is almost constant, as the $n = 0$ mode decays very slowly. The field for case 3 actually increases over the time of the simulation. However, this is merely an effect of the choice of end point for the simulation, as higher order modes do oscillate, causing the field to increase and decrease. Over a longer time, the field for case 3 also decays. Recall

n	Decay time (s) ($\frac{1}{\kappa}$)	Period(s) ($\frac{2\pi}{\omega}$)	Frequency(Hz)
0	634.0	244.0	0.0041
1	194.4	77.9	0.0128
2	94.6	46.1	0.0217
3	79.4	32.6	0.0307
4	63.8	25.2	0.0397
5	50.3	20.5	0.0488
10	25.5	10.6	0.0943
15	19.4	7.0	0.1429
20	12.5	5.3	0.1887
25	10.5	4.3	0.2326
30	8.2	3.5	0.2857
35	6.9	3.0	0.3333
40	5.7	2.6	0.3846
45	4.6	2.4	0.4167
49	3.9	2.2	0.4545

Table 3.2: A selection of values of oscillation time, decay time and period for $\eta = 3.1724 \times 10^{-11}$.

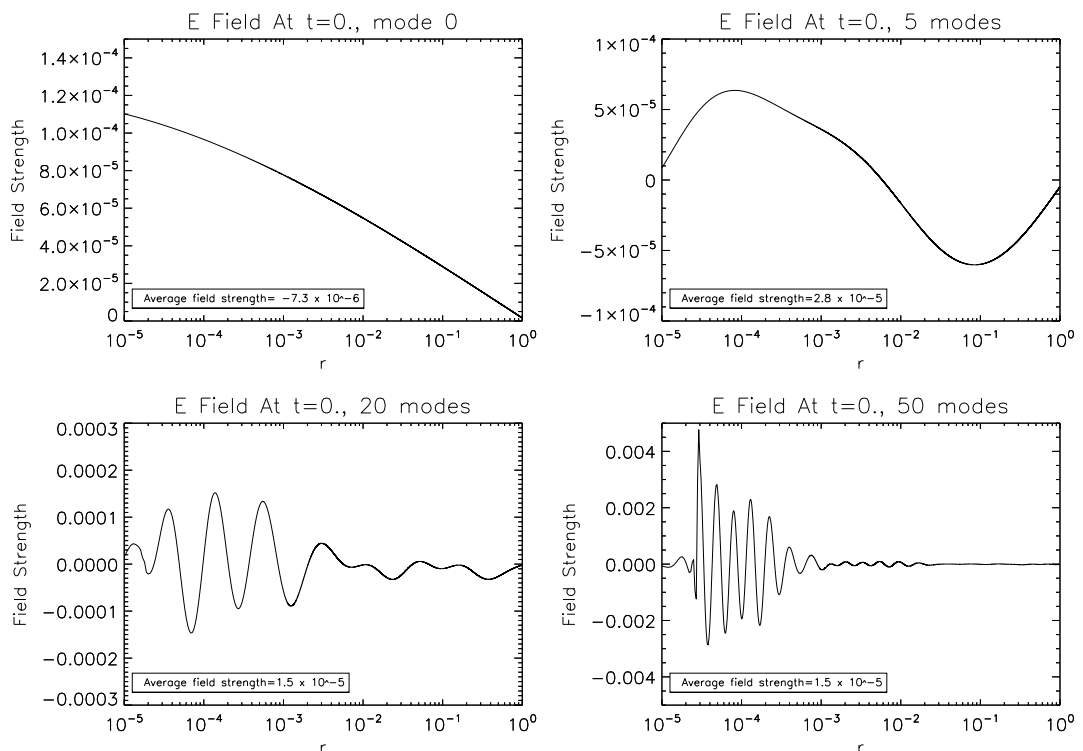


Figure 3.2: Electric field variation with distance from the neutral point (where r is normalised to D). Field strength is normalised to the magnetic field strength at the system boundary. The field shown results from different superpositions of eigenmodes, each with a different random phase.

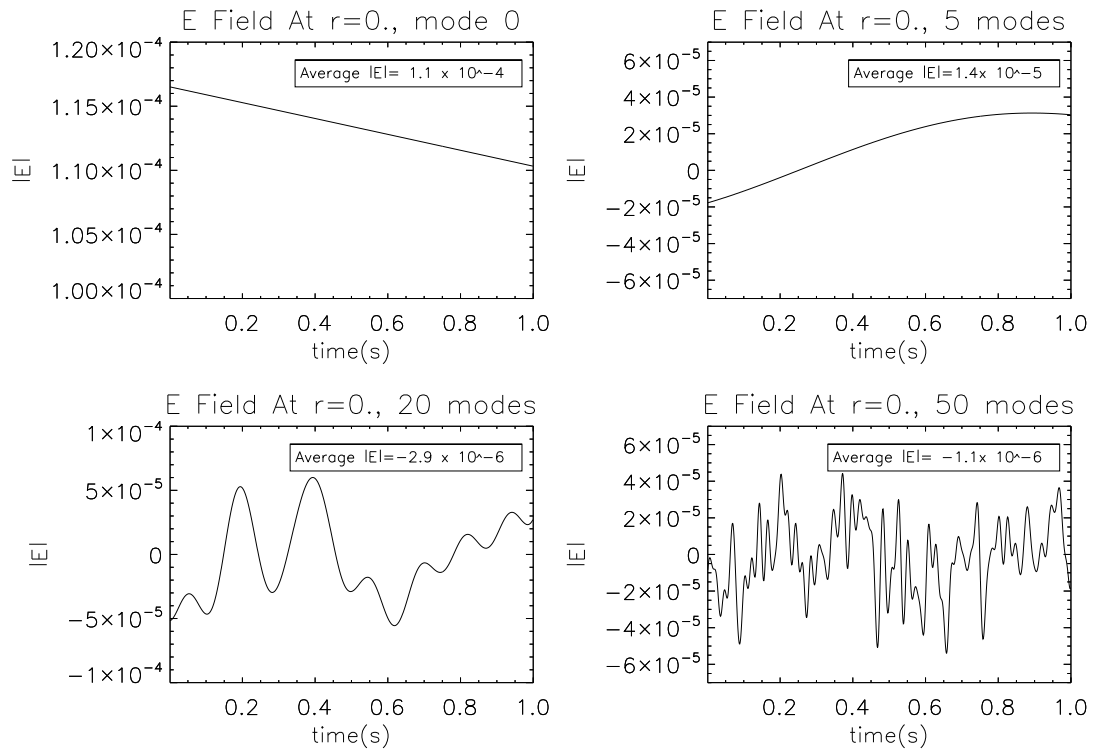


Figure 3.3: Electric field variation with time at $r = 0$ (where r is normalised to D). Field strength is normalised to the magnetic field strength at the system boundary. The field shown results from different superpositions of eigenmodes, each with a different random phase.

that each mode has also been given a random phase, which will also affect the evolution of the electric and magnetic fields. The fields for cases 4 and 5 appear noisier, although they will also decay over time. The higher order modes will decay first, leaving progressively simpler fields. This can be seen in figure 3.4, which also shows the forms of the electric field for modes 0 to 4. It can be seen that the number of oscillations in a given time increases with the number of the mode being considered, and that each mode has been normalised to have the same initial amplitude. Figure 3.5 shows once again that the field for case 2 is almost constant. In this case, the field for case 3 does decrease over the time of the simulation. The fields for cases 4 and 5 once again appear the noisiest. The average field is smaller (as would be expected) than at $r = 0$ in all cases

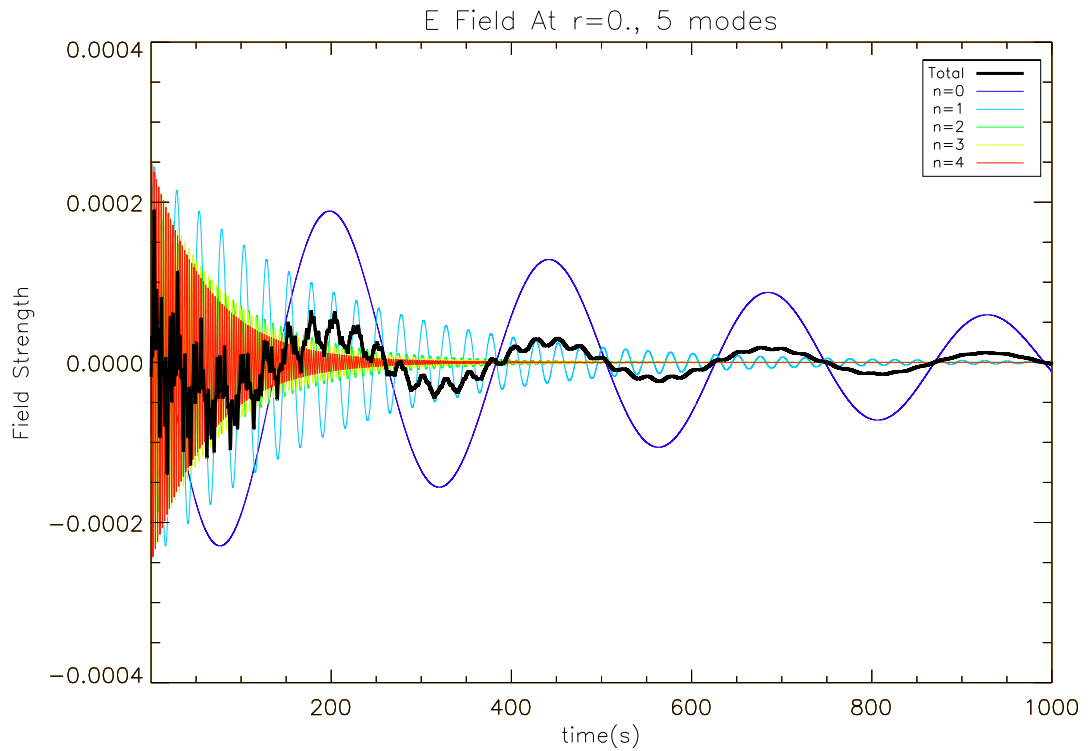


Figure 3.4: Decay of electric field with time at $r = 0$, for modes 0-4.

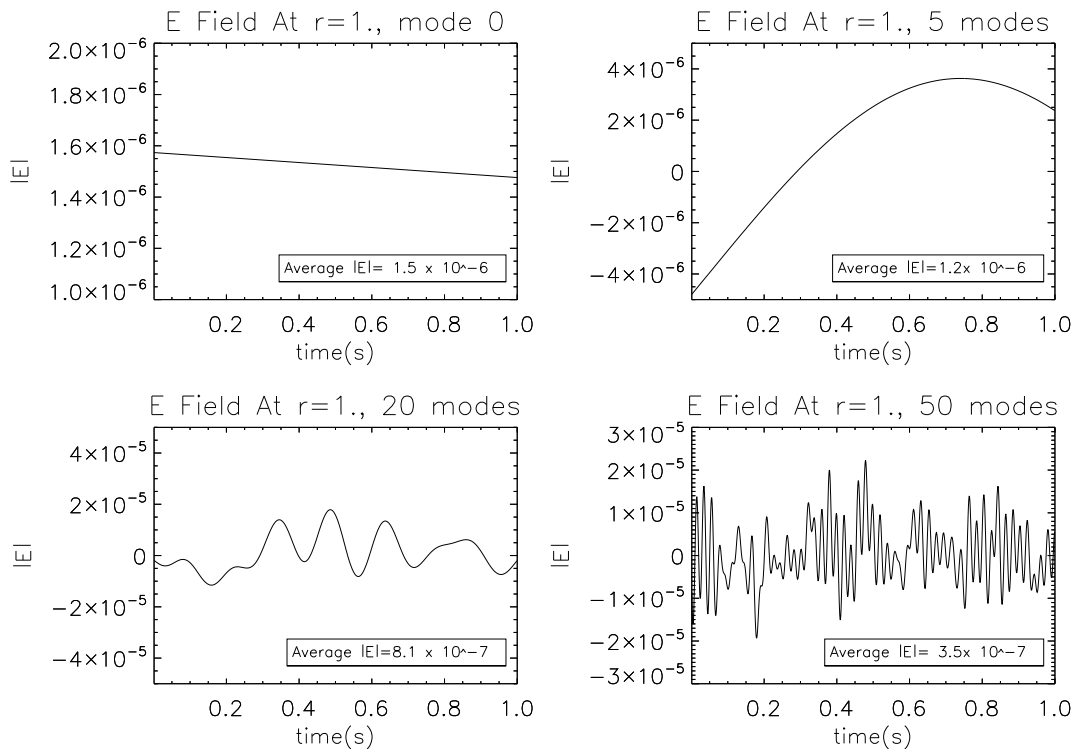


Figure 3.5: Electric field variation with time at $r = 1$ (where r is normalised to D). Field strength is normalised to the magnetic field strength at the system boundary. The field shown results from different superpositions of eigenmodes, each with a different random phase.

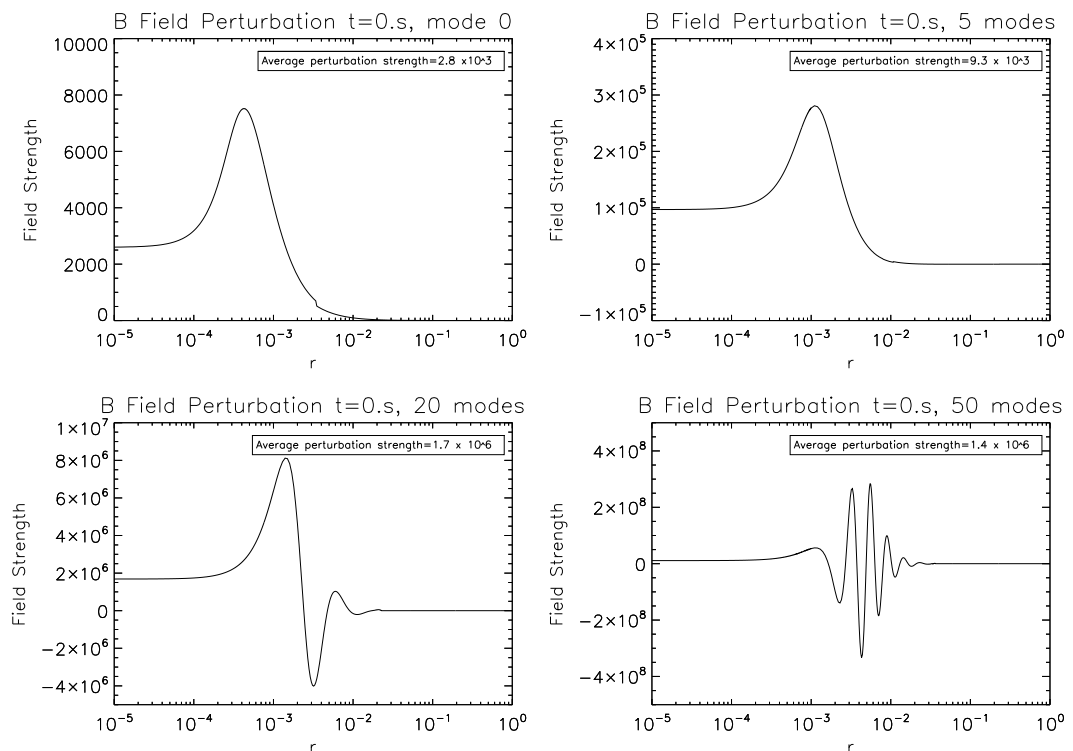


Figure 3.6: Magnetic field perturbation with distance from the neutral point (where r is normalised to D). Field strength is normalised to the magnetic field strength at the system boundary. The field shown results from different superpositions of eigenmodes, each with a different random phase.

The electric and magnetic fields for the $n = 0$ mode have previously been plotted in Petkaki (1996). My plots for the $n = 0$ case (case 2) reproduce these plots. I chose the superpositions of 5, 20 and 50 modes (cases 3, 4 and 5) to produce progressively noisier fields.

The electric fields that the electrons were subjected to in each case can be seen in figure 3.7, which shows the electric field at $r = 0$ for a flat spectrum of different numbers of modes, each with amplitude 10^{-3} . The electrons were followed for 0.1 s, so the field is plotted for this time only.

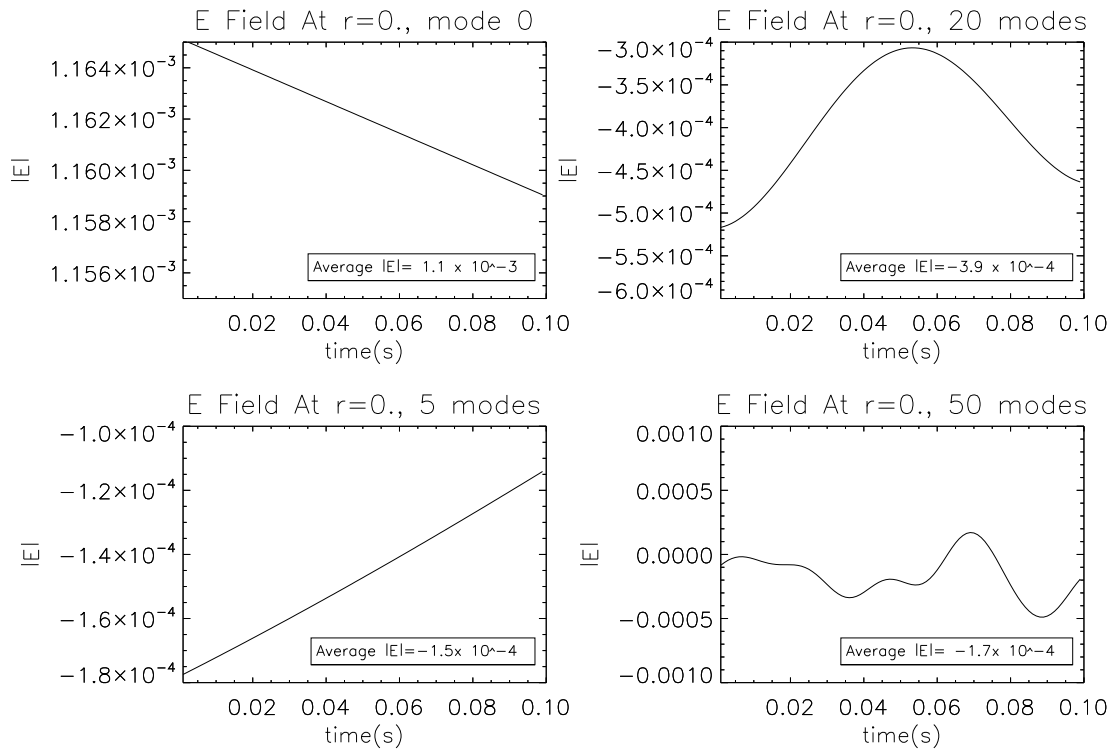


Figure 3.7: Electric field variation with time at $r = 0$ (where r is normalised to D). Field strength is normalised to the magnetic field strength at the system boundary. The field shown results from different superpositions of eigenmodes, each with a different random phase. This is the electric field experienced by the electrons. It has a greater amplitude since electrons are followed for a shorter time.

Figure 3.7 shows that over this short time scale, the electric field is much less noisy, therefore the fields experienced by electrons will be less noisy. Of course, this is only because of the different simulation times, as the actual fields calculated are identical. The fields for cases 2 and 3 are now very similar in character. The field for cases 4 and 5 oscillate much more smoothly over 0.1s than they do over 1s. The average magnitude of the field is progressively smaller in each case.

3.5 Conclusion

In this chapter, I have constructed the noisy electric and magnetic fields that will be used in the next chapter. I have done this by considering a perturbed potential, and finding the eigenmodes of this perturbation. The electric and magnetic fields for each eigenmode were then calculated, and noisy fields were created from a superposition of the fields for each

eigenmode, with each mode being given a random phase. I created 5 different cases to be studied: one in which there are no eigenmode oscillations, one for the $n = 0$ mode only, one for a superposition of modes 0 to 4, one for a superposition of modes 0 to 19 and one for a superposition of modes 0 to 49.

In order to calculate the electric and magnetic fields, I needed to calculate an appropriate value of the inertial resistivity. This was done by considering the time taken for a proton to cross the non-adiabatic region. The spatial dependence of the electric and magnetic fields was introduced via the hypergeometric function. This therefore had to be calculated this quickly and accurately, and for $r > 1$. This was done using an analytic continuation method.

4. Consequences For Particle Behaviour

4.1 Introduction

In this chapter, I will use noisy electric and magnetic fields to accelerate protons and electrons. In the previous chapter, I introduced a set of dimensionless units which make it easier to do this. I have already developed five different cases for the electric and magnetic fields, and I will study the consequences for electrons and protons in each case. In particular, I wish to know if noisier fields are more efficient at accelerating particles, and if so, why? Accelerated electrons will produce X-ray bremsstrahlung, so the X-ray spectra produced by the accelerated electrons will be calculated.

I will also investigate the consequences of varying the distribution of the amplitudes of the eigenmodes to better reflect a turbulent spectrum, as well as investigating the consequences of varying the value of the inertial resistivity.

4.2 Particle Behaviour: Protons

Here I follow test particles in the presence of model electric and magnetic fields. Test particle calculations study the behaviour of individual particles while neglecting the self-fields of these same particles. This approach allows us to employ reduced (e.g. MHD) descriptions for the electromagnetic fields and thus to explore a very large parameter space with reasonable computational effort. The huge disparity of spatial scales involved probably renders a complete description of the plasma impractical for the foreseeable future. This approach allows us to investigate the gross properties that the reconnection must have if it is to actually account for observed particle distributions.

The equations of motion of a charged particle in the presence of a magnetic field are:

$$\frac{d\mathbf{r}}{dt} = \frac{\mathbf{p}}{m\gamma} = \mathbf{v} \quad (4.1)$$

$$\frac{d\mathbf{p}}{dt} = q \left(\mathbf{E} + \frac{1}{c} (\mathbf{v} \times \mathbf{B}) \right), \quad (4.2)$$

where \mathbf{p} is the relativistic momentum of a particle, \mathbf{v} is the particle velocity, m is the particle mass and γ is the Lorentz factor. A charged particle in a uniform magnetic field where electric field is equal to zero will travel along a magnetic field line, spiralling around the field line with a gyroradius given by $r_g = \frac{m\mathbf{v}_\perp}{|q|\mathbf{B}}$. When the gyroradius of the particle becomes comparable to the scale length of the field, the particle will decouple from the field lines, and can gain energy in the presence of an electric field.

4.2.1 Equations of Motion

Although the magnetic field is 2D, the system has translational invariance in the z -direction, and hence the particles were allowed to move around in 3D. I will integrate the equations of motion numerically, and use the noisy electric and magnetic fields as $\overline{\mathbf{E}}$ and $\overline{\mathbf{B}}$ (the normalised electric and magnetic fields).

According to Petkaki and MacKinnon (1997), the equations of motion of a particle for our normalisations for protons can be written as

$$\frac{dx}{dt} = v_x \quad (4.3a)$$

$$\frac{dy}{dt} = v_y \quad (4.3b)$$

$$\frac{dz}{dt} = v_z \quad (4.3c)$$

$$\frac{dp_x}{dt} = -B_y v_z \quad (4.3d)$$

$$\frac{dp_y}{dt} = B_x v_z \quad (4.3e)$$

$$\frac{dp_z}{dt} = (E + (B_y v_x - B_x v_y)). \quad (4.3f)$$

In our dimensionless units

$$p = \gamma v,$$

where $\gamma = (1 + p_x^2 + p_y^2 + p_z^2)^{1/2}$.

4.2.2 Particle Energies & Trajectories

In order to investigate the behaviour of charged particles in the turbulent fields, 10000 ions were released into electric and magnetic fields of the kind shown above, at positions distributed randomly within $0 \leq x \leq 1, 0 \leq y \leq 1$, in the plane $z = 0$. Their starting energies were chosen randomly from a Maxwellian distribution of temperature $5 \times 10^6 K$, a typical coronal temperature. This temperature is equivalent to the thermal energy $W_{th} = k_B T$, where k_B is Boltzmann's constant and T is the temperature in Kelvin. This energy is equivalent to a thermal speed of $0.05c$ for protons. The direction of the velocity was chosen randomly using the FORTRAN code GASDEV (Press *et al.* (1992)). Note that these speeds are thermal speeds, and that the particles are not undergoing any kind of drift at the start of the simulation.

Numerics

The differential equations 4.3 were solved numerically via discretisation according to the 4th order Runge-Kutta scheme (Press *et al.* (1992)). At this point, it is worth discussing the differences between different methods of numerical integration.

Euler integration is the simplest method of numerical integration. Adopting a stepsize h , the Euler method approximates the solution of the ODE $dy/dx = f(x, y)$ at a set of points x_n via the algorithm

$$y_{n+1} = y_n + f(x_n, y_n)h. \quad (4.4)$$

Accuracy can be improved by using a smaller stepsize, but taking many steps may mean that the function takes a long time to evaluate computationally.

The midpoint method is more accurate. Each step is broken in half, and the derivative of the function is evaluated at the midpoint.

RK4 is a refinement of the midpoint method. At each step, the derivative of the function is evaluated at the start of the step, as well as at two trial midpoints and a trial endpoint. All of this information is then used to evaluate the function at the end of the step. A comparison of the three methods outlined here can be seen in figure 4.1, which shows the solution of the equation $dy = \sin(4x)dx$.

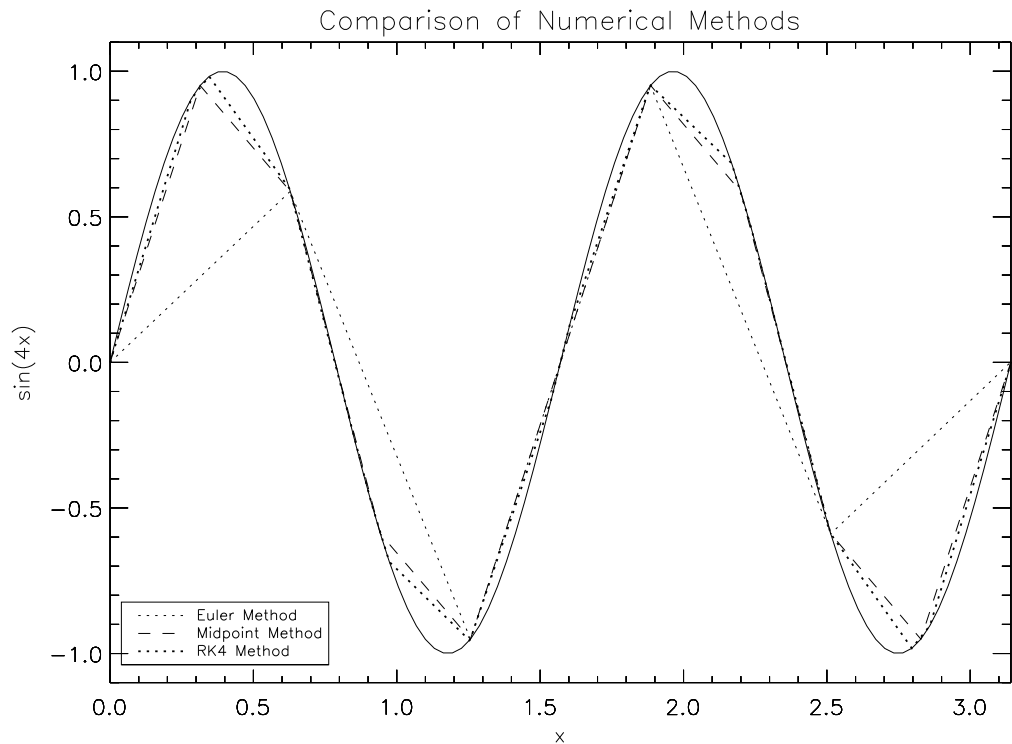


Figure 4.1: Comparison of three methods of numerical integration, for the integration of the equation $dy = \sin(4x)dx$. The solid line shows the exact solution of the function.

It can be seen that each refinement of the integration method brings the solution closer to the analytical solution. The Euler method produces a result which is very different from the true solution of $dy = \sin(4x)dx$, and I concluded from this that it would be a very inaccurate method for following particles whose equations of motion are more complicated than this simple function, unless a very small stepsize was used. The midpoint method and the RK4 method both reproduce the analytical solution reasonably well, however the error associated with the midpoint method is greater than that associated with RK4. The midpoint method has an associated error $O(h^2)$, whereas RK4 has an associated error $O(h^5)$, where h is the stepsize.

Of course, more accurate methods are possible. One such method is the Bulirsch-Stoer method, which uses a varying stepsize in order to adapt to the rate of change of the function. Such a method was used to follow particle trajectories in Petkaki (1996) and Petkaki and MacKinnon (1997). However, such methods take more computation time than is practical for the number of particles that I wish to follow. I chose to use RK4 for this problem as it is accurate enough (see the discussion on shadowing theorems, below) to follow the gyration of particles without taking too long to compute their trajectories.

I want to consider particles in the presence of a magnetic null point. The gyroradius of such particles can vary widely throughout the simulation. Close to the null, the gyroradius becomes very big as particles are no longer tied to the magnetic field lines. Away from the null, particles will have small orbits, and follow the magnetic field lines closely. Clearly, the integrator used must be able to deal with a variety of spatial scales accurately. Care must therefore be taken to choose a timestep that is appropriate to the problem. Smaller stepsizes clearly give more accurate results, but at the expense of longer running times for the simulation. In order to determine an acceptable stepsize for these simulations, I first examined the orbits of individual protons calculated using different stepsizes. These orbits can be seen in figure 4.2.

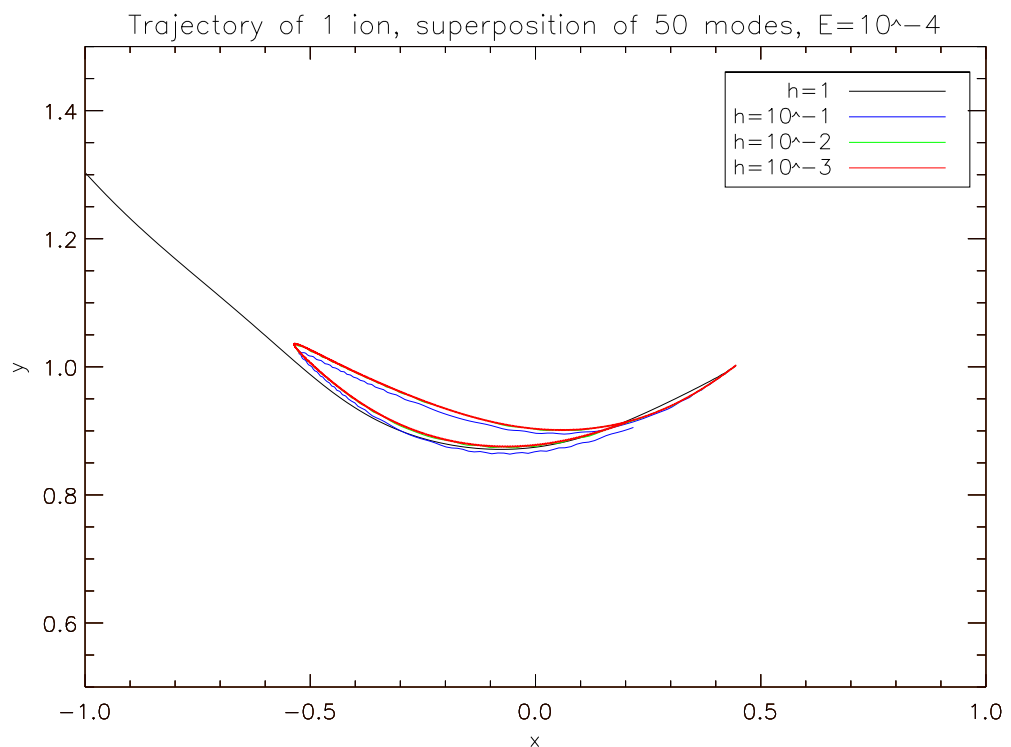


Figure 4.2: Orbit of one proton in constant electric and magnetic fields for varying stepsizes.

Figure 4.2 shows that the orbits differ slightly for different stepsizes. However, as long as each individual orbit is a reasonable orbit, for a distribution of particles these slight differences should not be important. To test this, 10 000 protons were followed in the presence of constant electric and magnetic fields until $t=5360$ (1s for our normalisations for ions if $B_0 = 10^{-7}$) for a variety of stepsizes. The distribution of their final energies can be seen in figure 4.3.

Figure 4.3 shows that the distributions for stepsizes 10^{-1} and 10^{-2} are identical, even though the individual particle trajectories differ. This is because although the individual trajectories

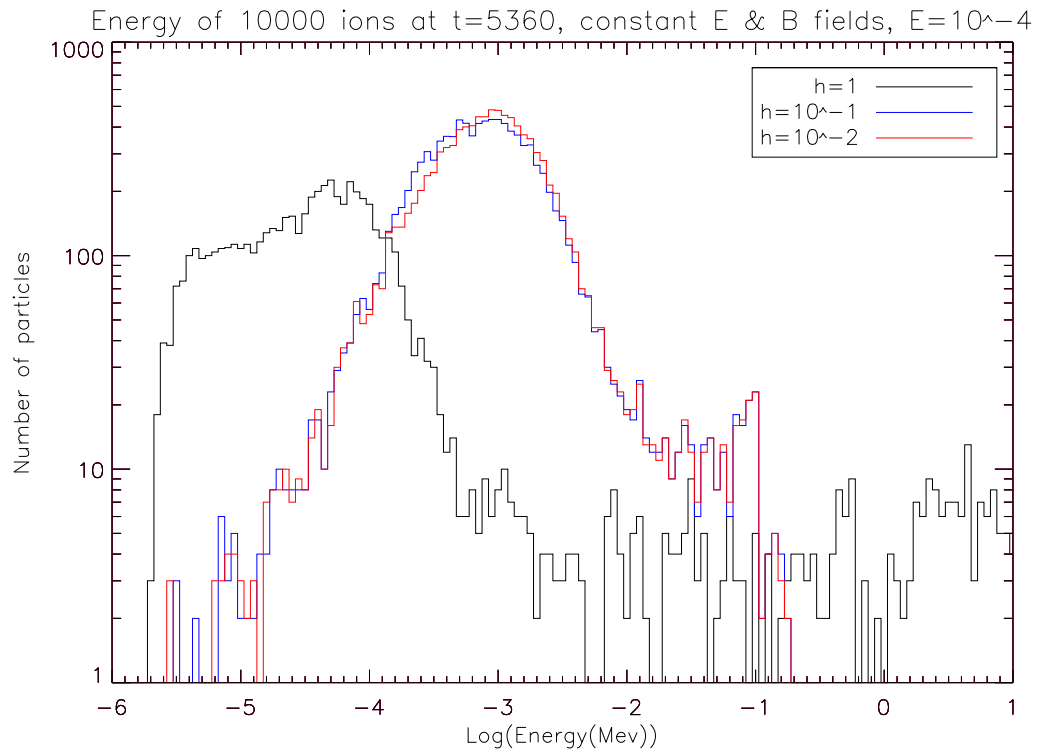


Figure 4.3: Distribution of proton energies for constant electric and magnetic fields at $t=5360$ for varying stepsizes.

of the particles are not followed accurately, there exists another particle with slightly different initial conditions for which the trajectory in question would be the true trajectory. This property of a system is known as the shadowing property (e.g. Ott (2002)).

It was therefore found (by inspection of figures 4.2 and 4.3) that a stepsize of 10^{-1} was sufficiently accurate for the purpose of following protons. To integrate electron trajectories, a smaller stepsize was used. Figure 4.4 shows distributions of 10 000 electrons at $t = 2310$, (0.1s for our normalisations for electrons). From these distributions, the largest accurate stepsize for electrons (3×10^{-3}) was chosen.

4.2.3 Energy Conservation

In the absence of an electric field, the kinetic energy of an individual particle should be conserved. This was tested for each simulation by plotting the change in energy at each step as a fraction of the particle's original energy. The electric field was set to zero in all cases, but the magnetic fields were still allowed to evolve with time, in order to test energy conservation of the code in a variety of different magnetic field structures. Changing magnetic fields of course result in an electric field, so these simulations are clearly very artificial, and are useful only as numerical tests. The results for cases 1-5 for ions can be seen in figure 4.5. It can

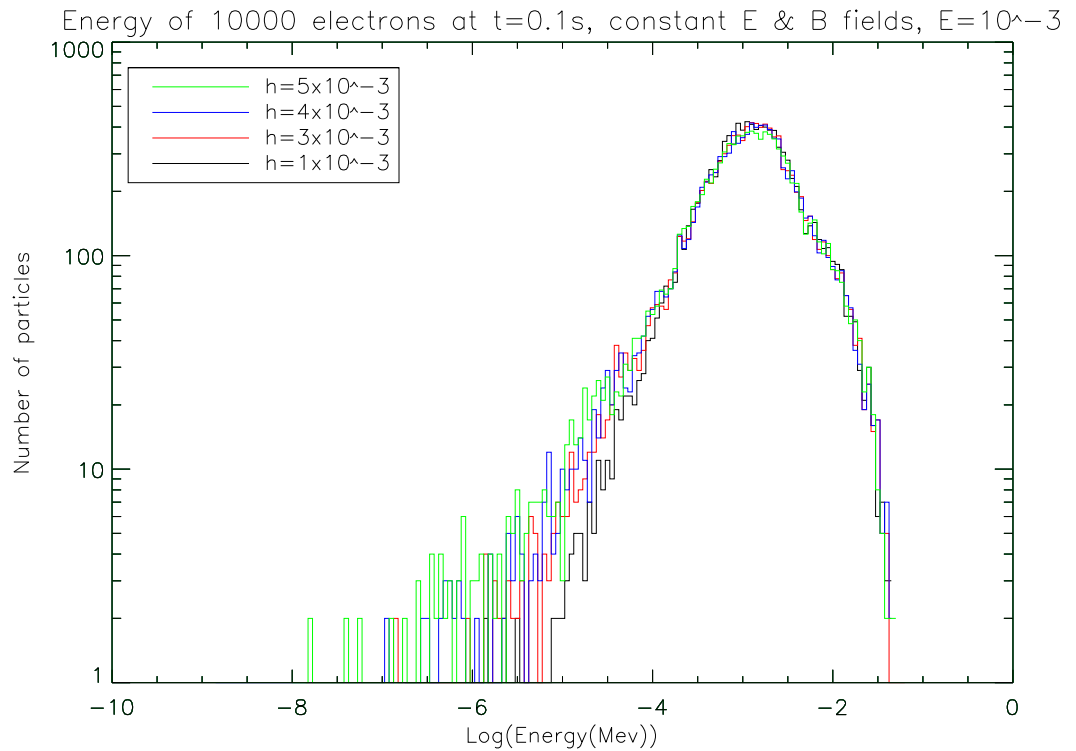


Figure 4.4: Distribution of electron energies for constant electric and magnetic fields at $t=2310$ (0.1s) for varying stepsizes.

be seen that energy is well conserved (to within one part in 10^{-6}) in all cases. In all cases (except for case 1), there are several sharp spikes, of equal size in each case, where the particle's energy was not conserved. The origin of these spikes is not clear, but as they are very small (less than one part in 10^{-6}), they were not thought to present significant problems to the simulations.

The results for cases 1-5 for electrons can be seen in figure 4.6. It can be seen that energy is well conserved (to within one part in 10^{-6}) in all cases. In case 1, the same small spikes can be seen as were seen for cases 2-5 in the proton simulations. As these spikes are also very small, they were also discounted.

4.2.4 Energy Distributions: Protons

Protons were followed until $t = 5360$, which is equivalent to 1s if $B_0 = 10^{-7}$. Particles which left the simulation boundary ($x = y = 178, z = 17.8$ in units of d_p) were discarded. These boundaries were chosen to give a system boundary in the x-y plane of 10^9 cm (Craig and McClymont (1991)), and to satisfy the condition that the system width should be around a tenth of its size in the x-y plane (Aschwanden and Nightingale (2005), which placed observational constraints on the length and width of coronal loops using measurements from the

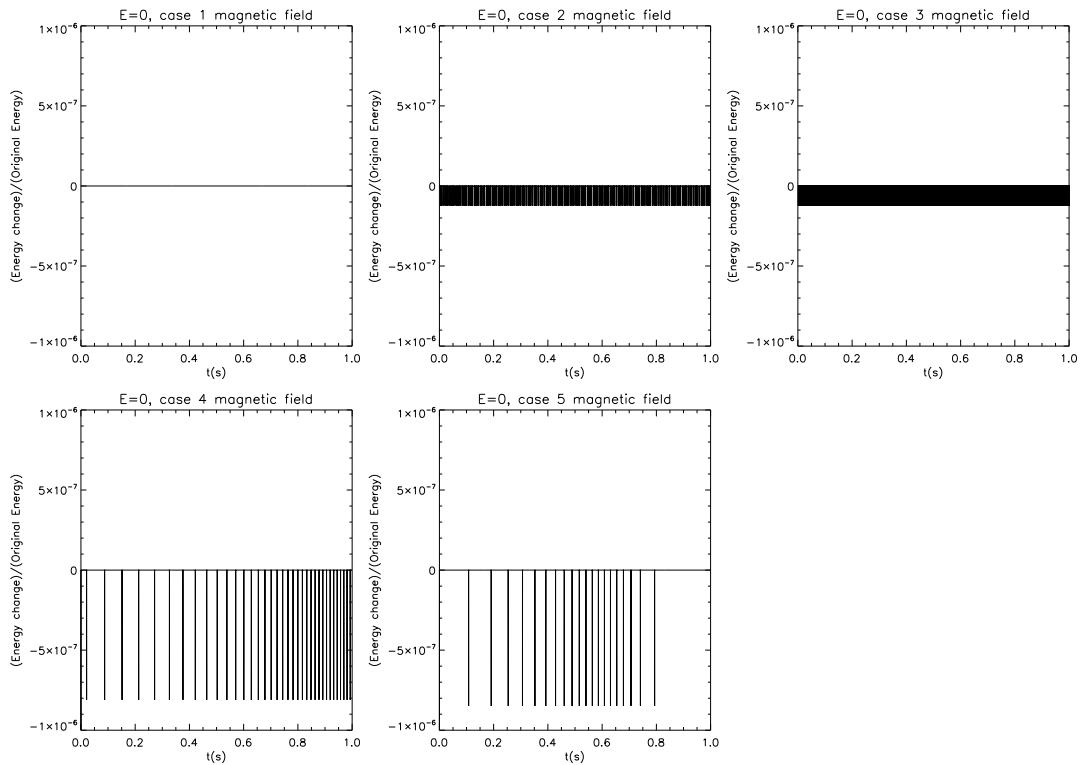


Figure 4.5: Energy of an individual ion for cases 1-5 in the absence of an electric field over a period of 1s. It can be seen that energy is well conserved in all cases.

TRACE (Transition Region And Coronal Explorer) archive). These conditions meant that 11 particles (of 10000) from case 3 and 3 particles from case 5 were discarded. The resulting energy distribution is shown in figure 4.7.

Figure 4.7 compares the initial energy distribution of the ions with distributions at $t=1s$ for the static X-type neutral point, for the $n=0$ mode of oscillation, and for superpositions of 5, 20 and 50 modes.

Case	Average $ E $ At $r = 0$	Peak $ E $ At $r = 0$	% of Protons $> 0.01MeV$ at $t=1s$
1	$1. \times 10^{-4}$	$1. \times 10^{-4}$	3.1
2	1.1×10^{-4}	1.2×10^{-4}	1.6
3	1.4×10^{-5}	1.9×10^{-4}	0.3
4	2.8×10^{-6}	6.0×10^{-5}	1.2
5	1.1×10^{-6}	5.4×10^{-5}	16.9

Table 4.1: Fraction of protons accelerated to above 0.01 MeV with average electric field strength and peak electric field strength in each case.

Cases 1 and 2 produce similar-looking energy distributions, although fewer particles were accelerated to energies above 0.01MeV in case 2. In case 1, 3.1% of particles achieved energies above 0.01MeV. In case 2, only 1.6%, achieved these energies, although the average

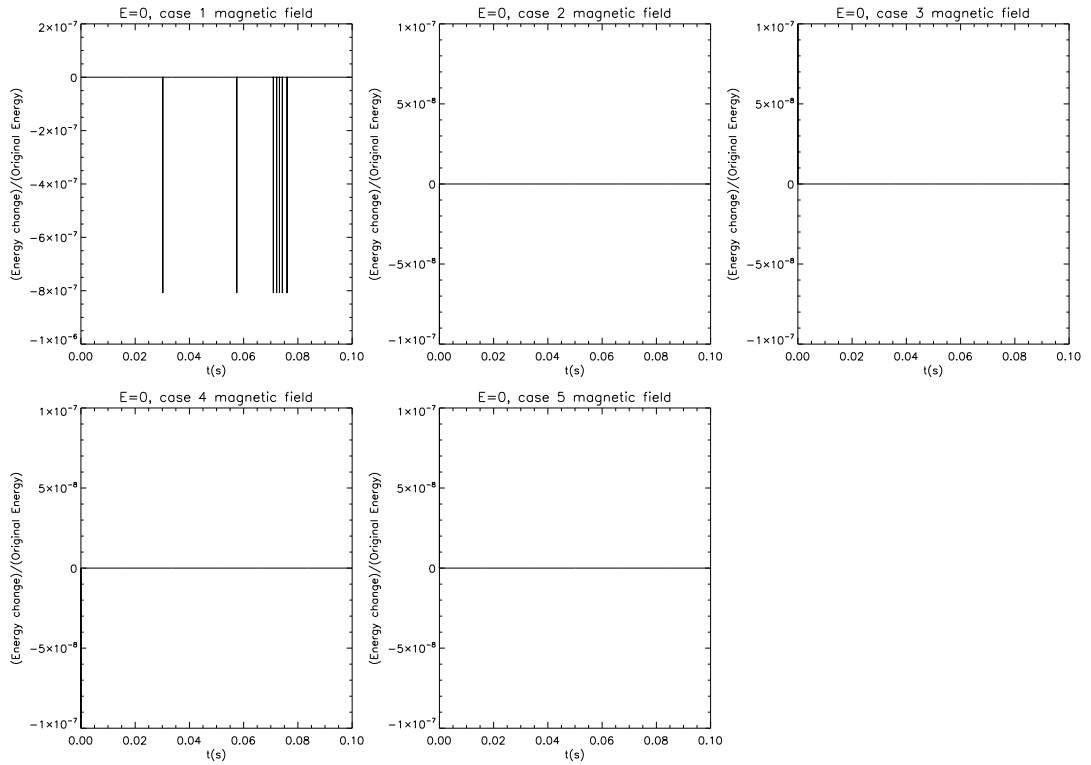


Figure 4.6: Energy of an individual electron for cases 1-5 in the absence of an electric field over a period of 1s. It can be seen that energy is well conserved in all cases.

electric field strength in these cases is roughly the same. In case 3, 0.3% of particles were accelerated to above 0.01MeV. However the average field strength in this case was also approximately a tenth of that in case 1. Case 4 accelerates 1.2% of particles to above 0.01MeV, around half the number in case 1, but it does so using an average electric field that is almost 40 times smaller than that in case 1. By case 5, a second Maxwellian-type distribution of high energy particles is produced, with a temperature of $\approx 7.3 \times 10^8$ K. This temperature was obtained by considering the mean energy of the particles in this second distribution. 16.9% of particles have energies higher than 0.01MeV. In this case, the average electric field, and the peak amplitude of the electric field are the smallest of any case. The average electric field here is 100 times smaller than that in case 1.

Of course, I want to be satisfied that the increased energies of particles in case 5 are not simply due to some special property of the phase differences I have chosen for the eigenmode perturbations. Let us choose a different set of random phases and calculate the resulting electric and magnetic fields for a superposition of 50 modes. I will call this case 5b. Figure 4.8 compares the energy distributions of protons at $t = 1$ s for cases 5 and 5b. It can be seen that the energy distributions are very similar for both cases (in that they both contain two Maxwellian-type distributions, each with approximately the same width and peak value,

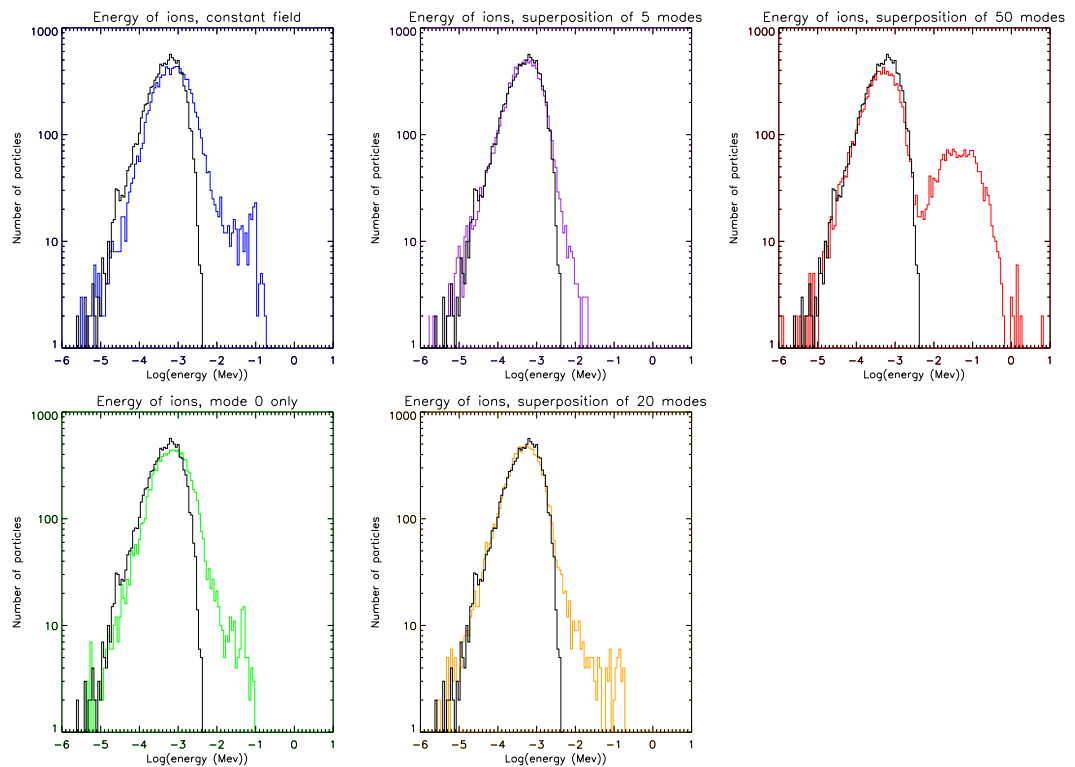


Figure 4.7: Energy distribution of 10000 protons at $t=0$, and at $t=5360$ for different electric and magnetic fields.

although there are slight differences between the shapes of the two graphs), so that the ‘noisy’ fields are not merely more efficient for a particular set of phases, but are consistently better than unperturbed fields at accelerating particles. Other sets of random phases were studied, and were also found to produce the same results.

In order to investigate how the particle energy distributions evolve over time, the energy distributions in each case were plotted at 0.1s (figure 4.9), 0.5s (figure 4.10) and 0.9s (figure 4.11). These figures show that the particles in all cases (except for case 4) are energised quickly. The particle energy distributions do not change very much after $t = 0.5s$. The exception to this is case 4, where the particles are energised steadily throughout the duration of the simulation, and are still gaining significant energy between 0.9s and 1s. Recalling figures 3.3 and 3.5 (which showed the variation of the electric field with time at $r = 0$ and $r = 1$ respectively), one possible explanation for this could be that electric field for case 4 is still generally increasing after 0.5s, whereas the electric field in cases 2 is decreasing, the electric field in case 3 is approaching a steady value and the electric field in case 5 both increases and decreases rapidly. The consequences for protons accelerated in the electric and magnetic fields of case 2 were investigated in Petkaki and MacKinnon (1997), and my distributions at $t = 1s$ agree with their findings.

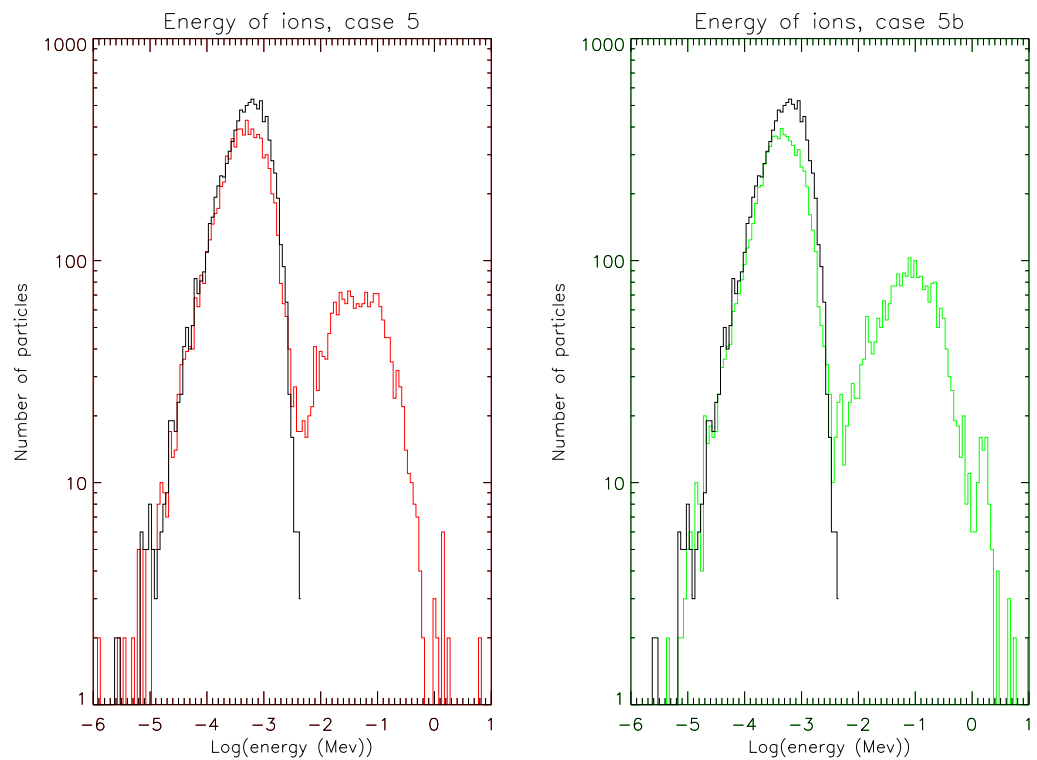


Figure 4.8: Energy distribution of 10000 ions at $t = 0$, and at $t = 5360$ (1 second) for case 5 (electric and magnetic fields perturbed by a superposition of 50 eigenmode oscillations, each with a random phase) and case 5b (electric and magnetic fields perturbed by a superposition of 50 eigenmode oscillations, each with a different random phase).

It is known that in order to produce gamma ray radiation, protons must have an energy of at least 2 MeV (Vilmer, MacKinnon, and Hurford (2011)). None of the protons in any of the cases studied here achieves such an energy. However, many medium-sized flares do not produce gamma ray radiation. Protons will of course be present in the coronal plasma, but it is not easy to say anything about the role they play if they do not produce observable radiation.

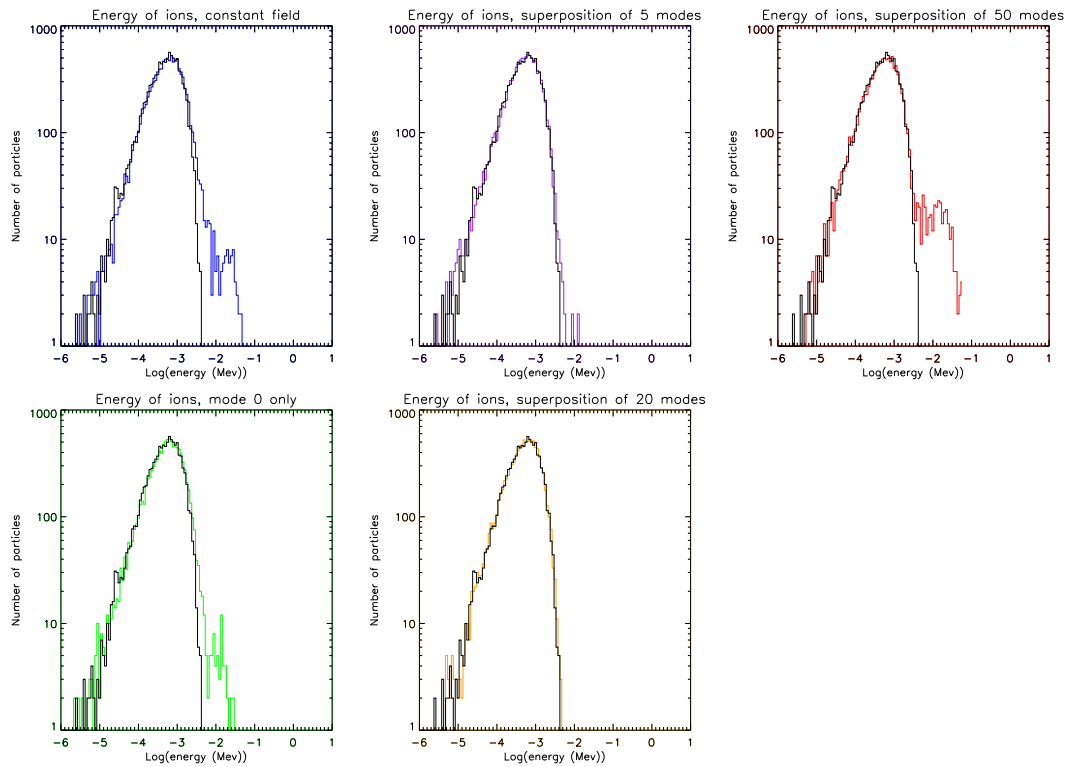


Figure 4.9: Energy distribution of 10000 ions at $t = 0$, and at $t = 536$ (0.1 seconds) for different electric and magnetic fields.

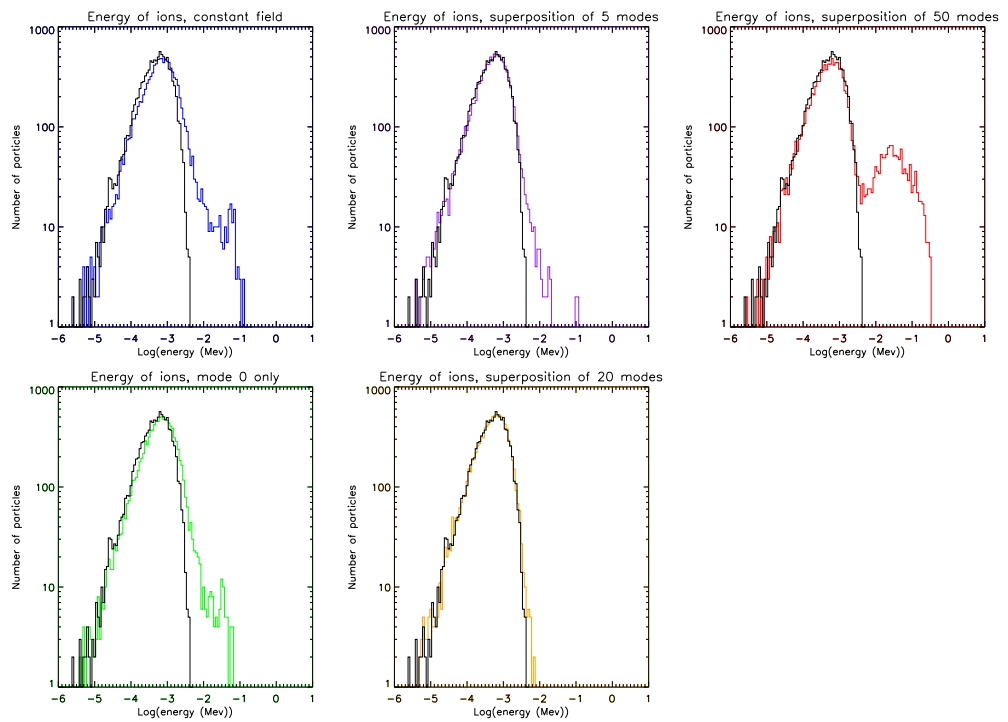


Figure 4.10: Energy distribution of 10000 ions at $t = 0$, and at $t = 2680$ (0.5 seconds) for different electric and magnetic fields.

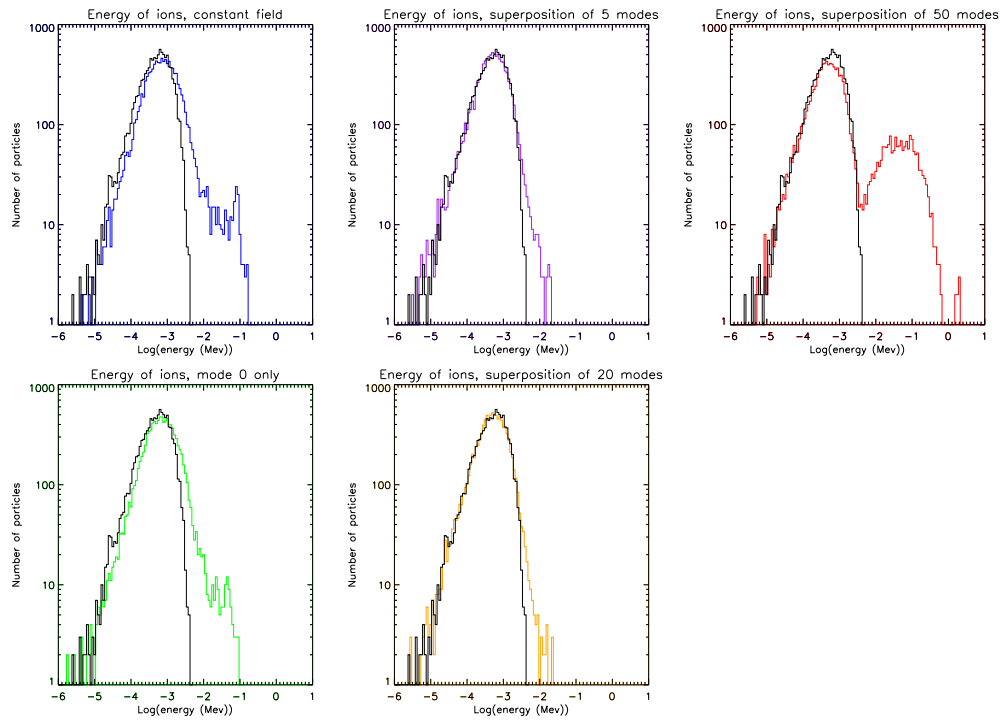


Figure 4.11: Energy distribution of 10000 ions at $t = 0$, and at $t = 4824$ (0.9 seconds) for different electric and magnetic fields.

For our normalisations, an electric field, $\overline{E} = 0.0001$ corresponds to an electric field of ≈ 1.8 V/m. My weakest average electric field (case 5) is therefore ≈ 0.018 V/m, yet it is able to accelerate particles to energies of almost 1MeV. Recall that the electric field for case 5 is made up of a superposition of perturbations of 50 eigenmodes. As this field is so noisy, on average it is very small. However, the peak amplitude of the for case 5 is still only around half that for case 1, indicating that it is the fluctuations in the electric and/or magnetic fields that produce the high energy tail of particles.

Dalla and Browning (2005) found that in a 3D static X-type neutral point, electric fields of 1.5kV/m were required to reach these energies (in a system where particles were allowed to move equal distances in x , y and z). The electric field strength in solar flares and erupting prominences has been measured to be in the region of 1kV/m (Somov, Oreshina, and Kovalenko (2008) and Foukal, Little, and Gilliam (1987) respectively), around 1000 times bigger than the peak value in case 5, which is ≈ 1 V/m. However, solar flare protons with energies in the GeV range, much greater than the energies achieved with this small field, have been observed (e.g. Wang and Wang (2006); Kanbach *et al.* (1993); Vilmer *et al.* (2003)). The noisy fields in case 5 seem to be very efficient at accelerating particles. In order to dis-

cover the reason behind this acceleration, a sample of particles must be examined in more detail.

High Energy Particles

In the X-type neutral point model, particles become energised as they pass through the non-adiabatic region around the null, if an electric field is present. I must therefore determine whether particles achieve higher energies for the superpositions of modes because they spend more time in this region, or if there is some other cause. In order to investigate this, the initial positions of all 10 000 protons were plotted for each of the simulations.

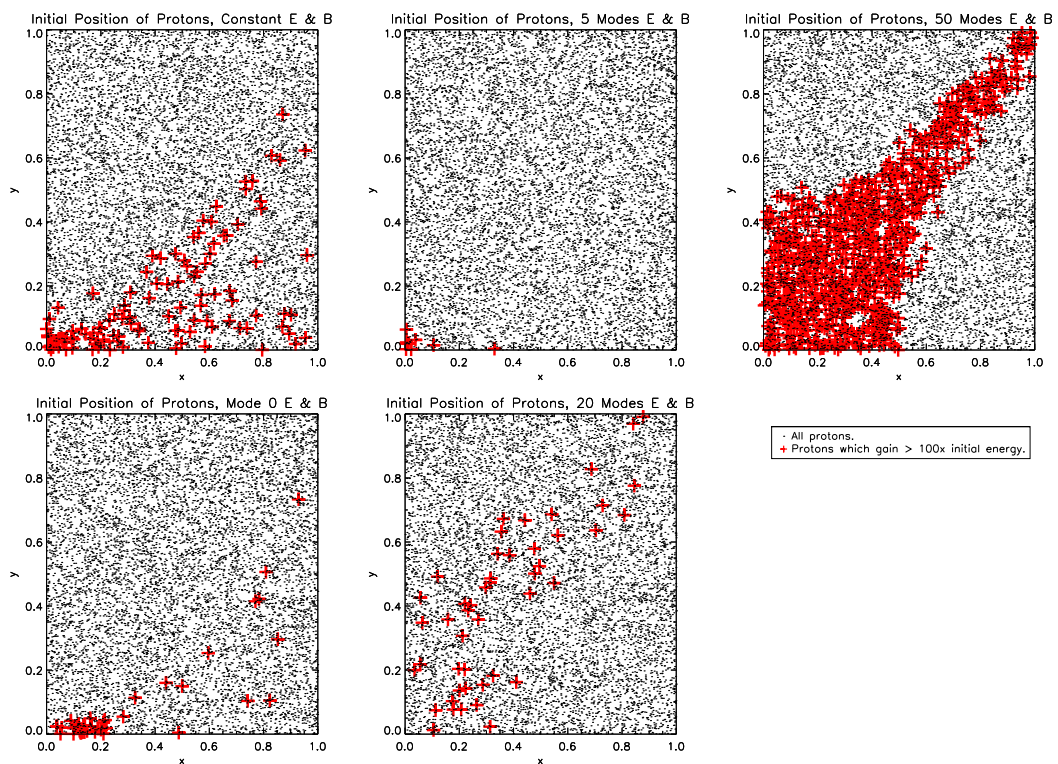


Figure 4.12: Initial positions of protons for all cases. Dots show the positions (at $t = 0$) of protons which gain less than 100 times their initial energies. Crosses show the positions (at $t = 0$) of protons which gain more than 100 times their initial energies. x and y are given in units of d_p .

Figure 4.12 shows that the size of the region where highly energised particles originate changes as more modes are added. In case 4, it can be seen that high energy particles can originate from a much wider region compared to cases 1-3. In case 5, high energy particles can originate from an extended central region, and from a region along the separatrices.

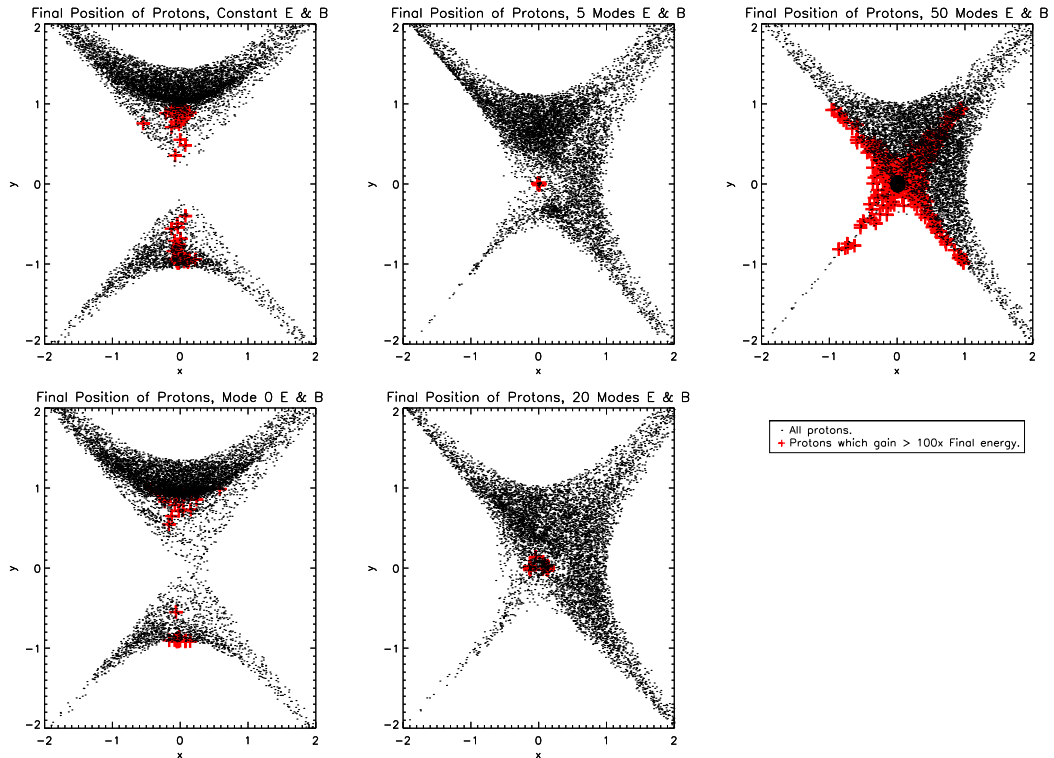


Figure 4.13: Final positions of protons for all cases. Dots show the positions (at $t = 5360$) of protons which gain less than 100 times their initial energies. Crosses show the positions (at $t = 5360$) of protons which gain more than 100 times their initial energies. x and y are given in units of d_p .

Figure 4.13 shows the final positions of protons in all cases. In cases 1 and 2, high energy protons are ejected from the X-point into regions at $x \approx 0$, $|y| \approx 1$. Recall figure 2.6, which shows the direction of the $\mathbf{E} \times \mathbf{B}$ drift at an X-type neutral point. Since high energy particles are those which undergo this $\mathbf{E} \times \mathbf{B}$ drift, the initial location of these particles now makes sense, as these are the particles which can most readily drift along the x-axis.. In cases 3 and 4, high energy protons end the simulation at the null point, with more such particles being found in case 4. In case 5, high energy particles are clustered inside a region of $r \approx 0.5$, as well as along the separatrices. There is also a concentration of lower energy particles around the null.

The final positions of the protons is not symmetrically distributed for cases 3, 4 and 5. This is because particles began the simulation in the quadrant $0 \leq x \leq 1$, $0 \leq y \leq 1$. When the magnetic fields are simple, this is not important for the final positions of the protons, as their motion is governed by $\mathbf{E} \times \mathbf{B}$ drift. This causes particles to travel towards the central null, and they are then expelled from this region in the y -direction, with approximately equal numbers of particles travelling in the positive and negative y direction. As more modes are added, $\mathbf{E} \times \mathbf{B}$ drift is no longer the dominant effect on the motion of the particles. The change

in the magnetic field topology, and the noisier electric field cause particles to follow different trajectories, so that their final positions are no longer symmetrically distributed. This could be due to trapping by newly-created structures within the magnetic field, or due to small scale changes in the electric field causing changes in the particles' trajectories.

Clearly, adding more modes changes the way in which particles are energised. In cases 1 and 2, particles appear to be energised via being drawn into the X-point via $\mathbf{E} \times \mathbf{B}$ drift, and being expelled from it. When more modes are added, high energy particles tend to remain in a central region of increasing size. Could this be due to particle trapping?

4.2.5 Determining the Size of the Non-Adiabatic Region

When the motion of the particle is adiabatic, its magnetic moment is conserved. For our normalisations, the magnetic moment is given by (e.g.Chen and Torreblanca (1984))

$$\mu = \frac{v_{\perp}^2}{|B|}. \quad (4.5)$$

In regions where a particle's magnetic moment varies, the motion is non-adiabatic and in the presence of an electric field a change in energy will occur. Figure 4.14 shows this relationship. At times and positions where the particle's magnetic moment changes, so does its energy. These large magnetic moment variations occur within $r \approx 0.5$, as do large changes in the particle's energy. This finding is supported by figure 4.12, which shows that high energy particles can originate from a central region with radius ≈ 0.5 . Compare this with figure 4.16, which shows variation in magnetic moment and energy with time and position for case 2. The particles shown do not gain such high energies, and their magnetic moment changes significantly only within $r \approx 0.2$, so any large energy change takes place within a smaller region, meaning that the non-adiabatic region in case 2 is smaller than that in case 5.

Ideally, I would like to find particles whose magnetic moment changes and which travel large distances in r . These particles proved difficult to find, as it would appear that particles that encounter such regions do not travel great distances, suggesting that they become trapped within a small local region.

Is an increase in the size of the non-adiabatic region solely responsible for the greater energies reached by particles? High energies can also be achieved by multiple crossings of the non-adiabatic region. However, when a high energy particle returns to the non-adiabatic region, it spends less time in this region as it is travelling faster. Therefore the energy gained in

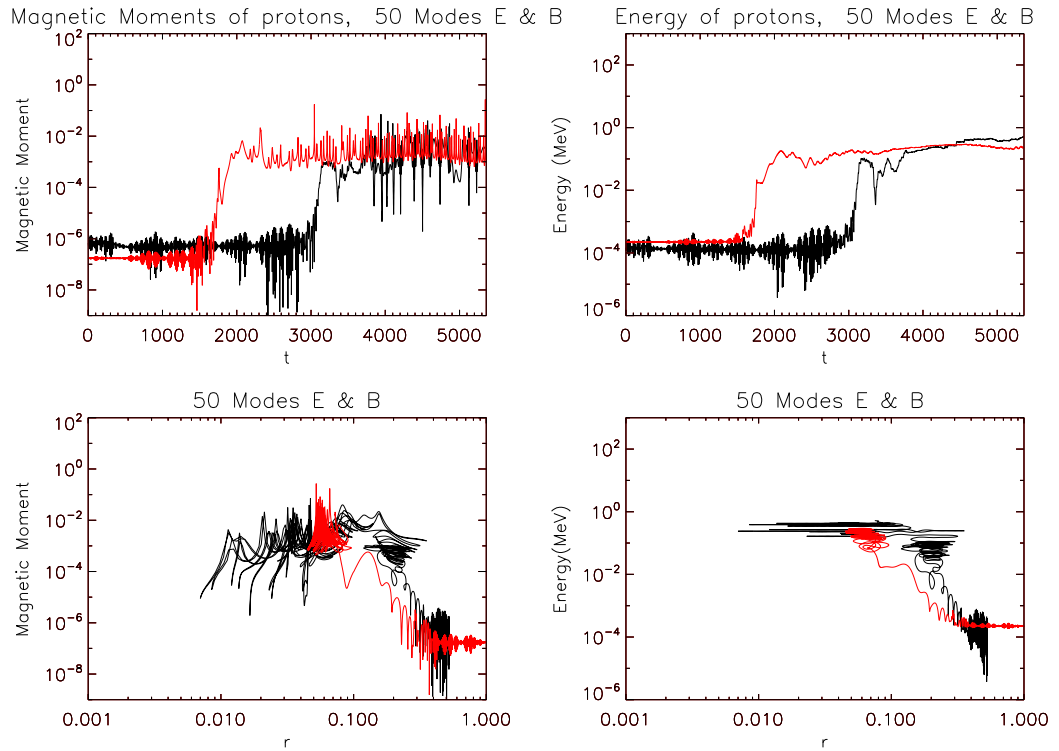


Figure 4.14: Variation of magnetic moment and energy of high energy protons with distance from the neutral point and time, for case 5. These two particles were chosen as they both gained more than 400 times their original energy. Particle 1 (black) and particle 2 (red) are the same particles in each frame of the figure.

the non-adiabatic region decreases with successive crossings (Litvinenko (2003)). This leads me to the conclusion that measurement of a particle's magnetic moment is not an especially robust method of determining the size of the non-adiabatic region, as only a few particles can be examined individually. A better method could be the measurement of the particle's gyroradius relative to the magnetic field scale length. If the particle's gyroradius is larger than the magnetic field scale length, the particle is moving non-adiabatically. However, the scale length of the magnetic field can be difficult to determine for the cases with more disordered fields.

Figure 4.15 shows the trajectories in the x-y plane of the 2 protons shown in figure 4.14, as well as the variation of their distance from the neutral point with time. It can clearly be seen that the particles spend most of their time orbiting the null at small values of r . The same plot for case 2 (figure 4.17) shows that particles are free to move to large distances from the neutral point when only one eigenmode is present, and that such particles orbit the field lines of a typical X-point geometry. The two particles shown in figure 4.17 move between $r \approx 0.1$ and $r \approx 1$ over the time period of the simulation. The two particles in figure 4.14 stay at approximately the same distance from the neutral point for over half the simulation time,

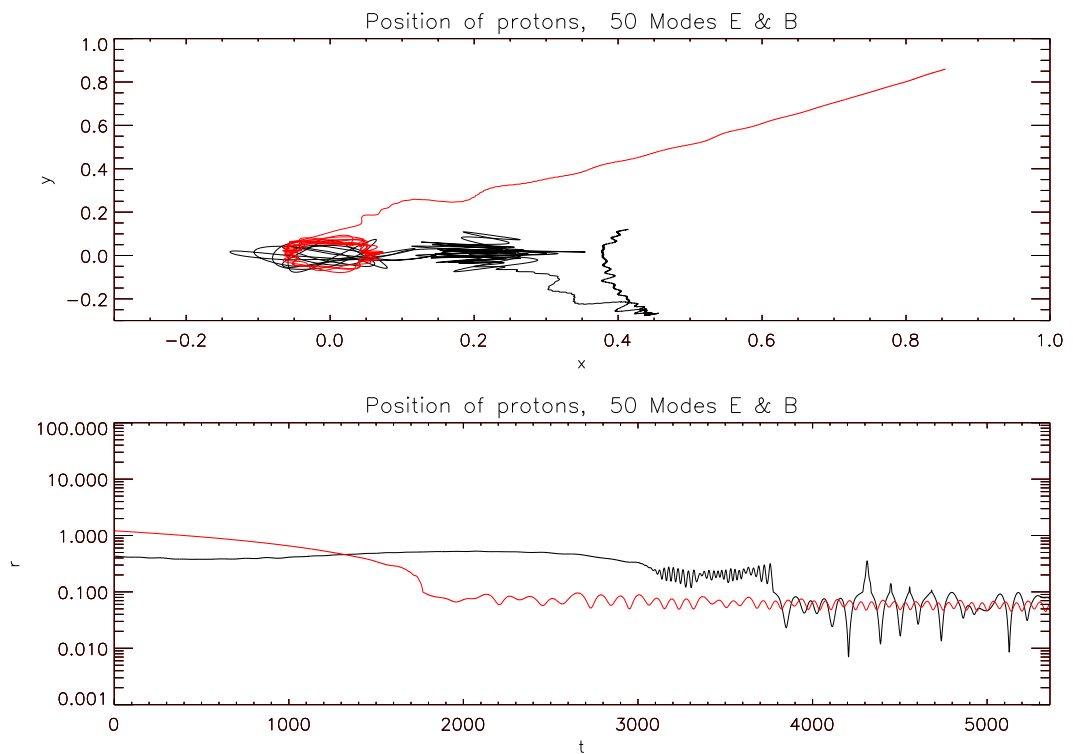


Figure 4.15: Trajectories of 2 protons in the x-y plane (top) and variation of distance from the neutral point with time (bottom) for case 5. These two particles were chosen as they both gained more than 400 times their original energy. Particle 1 (black) and particle 2 (red) are the same particles in each frame of the figure.

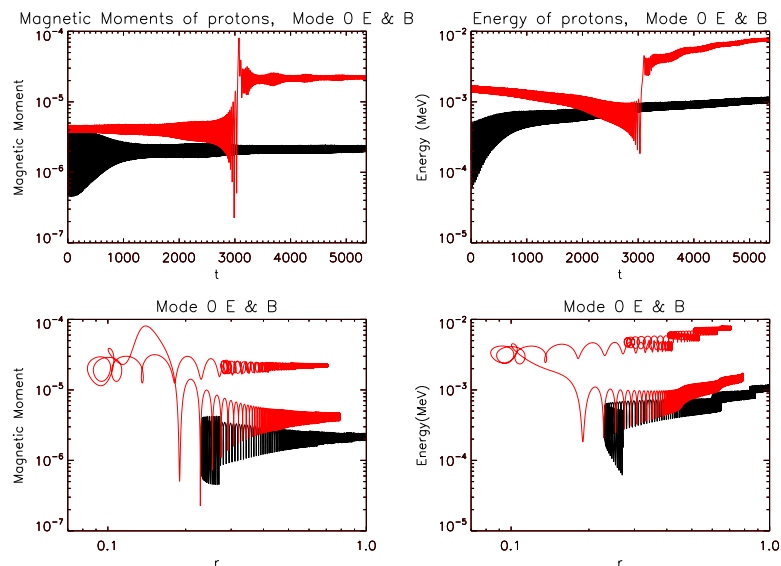


Figure 4.16: Variation of magnetic moment and energy of high energy protons with distance from the neutral point and time, for case 2. These two particles were chosen as they both gained more than 5 times their original energy. Particle 1 (black) and particle 2 (red) are the same particles in each frame of the figure.

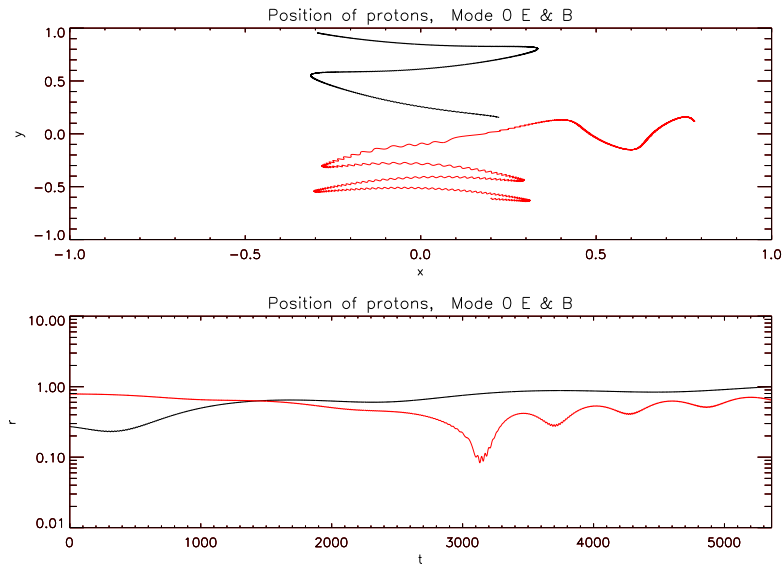


Figure 4.17: Trajectories of 2 protons in the x-y plane (top) and variation of distance from the neutral point with time (bottom) for case 2. These two particles were chosen as they both gained more than 5 times their original energy. Particle 1 (black) and particle 2 (red) are the same particles in each frame of the figure

indicating that particles in case 5 gain large amounts of energy due to becoming trapped at favourable locations within the magnetic field.

4.2.6 Energy Distributions: Electrons

In section 3.3 I set out the form of my dimensionless units. These units are dependent on the particle species. For electrons, I will take a normalising length of ten times d_e . This is to reduce computation times to a more practical length. This gives $d_e = 1.3 \times 10^6$ cm and $t_e = 4.33 \times 10^{-5}$ s. For the same reason I also take a particle mass of $10m_e$. This reduces the computation time because the normalising length depends on the particle mass. Since the normalising speed is taken to be c , this defines an intrinsic timescale to the problem, which also depends on the particle mass. Therefore by increasing the particle mass we can increase the timescale associated with the problem, thus decreasing the computation time required to follow particles until a specific physical time. Because of the normalisations I have chosen for the mass of the electrons, the equations of motion must be altered as set out below.

In c.g.s units, (for the rate of change of the x component of the particle's momentum):

$$\frac{dp_x}{dt} = \frac{-q}{c} B_y v_z \quad (4.6)$$

Let us choose some normalising length, d_n , and a normalising time t_n . Let's normalise speed to c , so that $d_n/t_n = c$. I will normalise the magnetic field so that the dimensionless magnetic field, \tilde{B} is given by

$$\tilde{B} = \frac{B}{B_0 d_n}, \quad (4.7)$$

where

$$B_0 = \frac{B}{D}. \quad (4.8)$$

B is the magnetic field strength at $r = D$, where D is the size of the system. I will take B to be 100G, and D to be $10^9 cm$.

Making quantities dimensionless, this gives

$$\frac{d\tilde{p}_x}{d\tilde{t}} = -\frac{q d_n^2 B_0}{m_e \mathbf{D} c^2} \tilde{B}_y \tilde{v}_z. \quad (4.9)$$

In the calculations of Petkaki and MacKinnon, and previously in this chapter, the normalising length (d_n) is chosen so that

$$\frac{q d_n^2 B_0}{m_e \mathbf{D} c^2} = 1. \quad (4.10)$$

I will call this value of the normalising length d_e , which is a very short length ($1.3 \times 10^5 cm$). This means that the normalising times for electrons will be correspondingly short, so the integration times will be very long. If the normalising length is increased to $10d_e$, the running time of the simulation is correspondingly reduced. At this point, I also increase the electron mass to $10m_e$, which gives

$$\frac{q 100 d_e^2 B_0}{10 m_e \mathbf{D} c^2} = 10. \quad (4.11)$$

The equations of motion now look like this (where I have dropped the tildes, and all quantities are dimensionless)

$$\frac{dx}{dt} = v_x \quad (4.12a)$$

$$\frac{dy}{dt} = v_y \quad (4.12b)$$

$$\frac{dz}{dt} = v_z \quad (4.12c)$$

$$\frac{dp_x}{dt} = 10B_y v_z \quad (4.12d)$$

$$\frac{dp_y}{dt} = -10B_x v_z \quad (4.12e)$$

$$\frac{dp_z}{dt} = -(10E + (10B_y v_x - 10B_x v_y)). \quad (4.12f)$$

Electrons were followed until $t = 2310$, which is equivalent to $0.1s$ if $B_0 = 10^{-7}$. Because the simulation was stopped at $0.1s$, the average electric fields experienced by the electrons will be slightly different than those experienced by the protons, which were followed for $1s$. Particles which left the simulation boundary ($x = y = 769., z = 76.9$ in units of $10 \times d_e$) were noted. These boundaries were chosen to give the same system boundaries as for protons. The resulting energy distribution is shown in figure 4.18.

Figure 4.18 compares the initial energy distribution of the electrons with distributions at $t = 0.1s$ for the static X-type neutral point, for the $n = 0$ mode of oscillation, and for superpositions of 5, 20 and 50 modes. It can be seen that cases 1 and 2 look broadly similar, as they did for ions. The bulk distribution of electrons is energised, although no high energy tail is produced. This means that the electrons have been heated, rather than accelerated. The average temperature that electrons are heated to in cases 1 and 2 is $\approx 1.8 \times 10^7$ K. This is approximately the temperature to which the coronal plasma is heated during a solar flare (Lin *et al.* (1981); Tsuneta *et al.* (1992); Tsuneta (1996)). In both cases, no electrons leave the system. In case 1, more electrons gain high energies than in case 2, and more electrons lose energy in case 2.

In case 3, there is a tail of low energy electrons, as well as a small high energy tail. There is a higher maximum energy than in cases 1 and 2. Again, no particles leave the system. The low energy tail is likely to be caused by particles which are decelerated as they attempt to move against an electric field directed against their direction of motion. In case 4 more high energy particles are seen and very few particles are decelerated. By case 5, a low energy tail of decelerated particles is not seen, but we do see an increased high energy tail, as well as the highest peak energy of any of the cases. However, we do not see any significant bulk

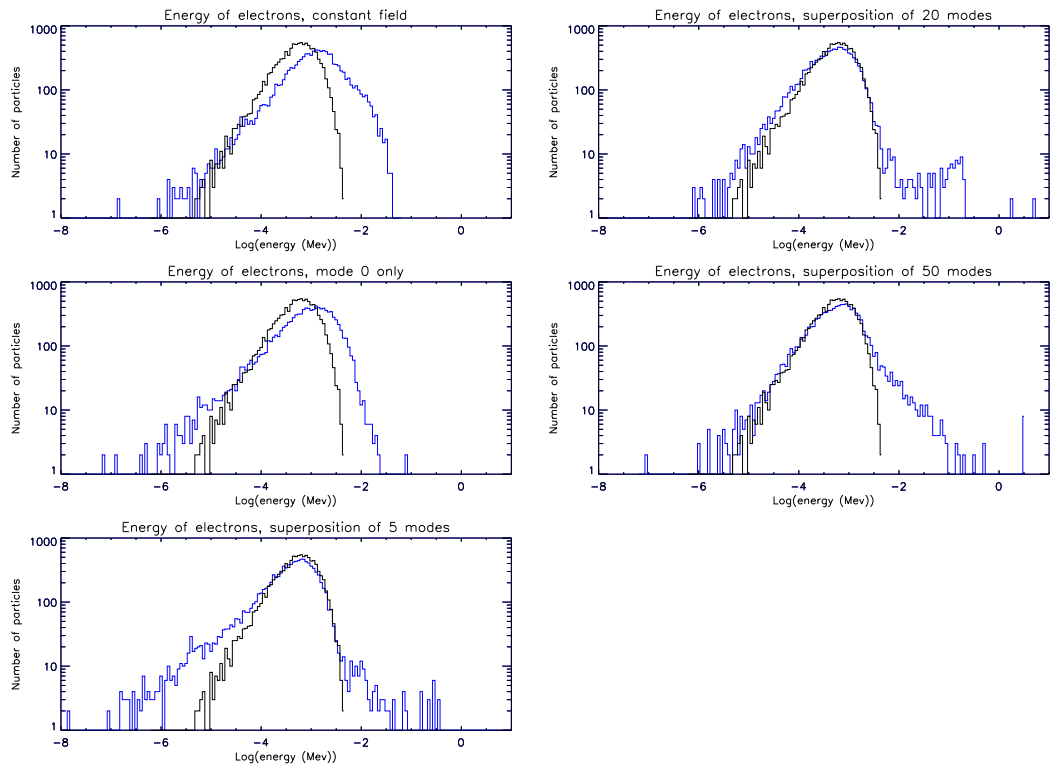


Figure 4.18: Energy distribution of 10000 electrons at $t = 0$, and at $t = 2310$ (0.1 seconds) for different electric and magnetic fields. The blue curves are the energies of the electrons at the time stated. The black curves are the initial energy distributions.

heating. This is probably because the mean electric field is too low. No particles leave the system in any case.

I therefore conclude that cases 2 and 3 are less efficient at accelerating particles than the constant field of case 1. Cases 4 and 5 see fewer particles with energies over 0.01 MeV than in case 1, but greater maximum energies are achieved. The peak electric field in cases 4 and 5 is also roughly half that in case 1, meaning that these fields are more efficient at energising electrons.

Comparing figure 4.18 with figure 4.9, which shows the energy distributions for ions at 0.1s, it can be seen that electrons are indeed more easily energised than protons. In 0.1s, only a few tens of protons are energised.

As I did for protons, I will plot the energy distributions for electrons at a selection of times in order to study the evolution of the distribution. The energy distributions for $t = 0.01s$ (4.19), $t = 0.05s$ (4.20) and $t = 0.09s$ (4.21) were plotted. It can be seen that the distributions change throughout the duration of the simulation, so that the electrons are still gaining

Case	Average $ E $ At $r = 0$	Peak $ E $ At $r = 0$	% of Electrons $> 0.01\text{MeV}$ at $t=0.1\text{s}$
1	$1. \times 10^{-3}$	$1. \times 10^{-3}$	4.84
2	1.1×10^{-3}	1.2×10^{-3}	0.54
3	1.5×10^{-4}	1.8×10^{-4}	0.85
4	3.9×10^{-4}	5.2×10^{-4}	1.34
5	1.6×10^{-4}	4.9×10^{-4}	2.34

Table 4.2: Number of electrons accelerated to above 0.01 MeV with average electric field strength and peak electric field strength in each case.

energy at the end of the simulation, and a steady state has not been reached. In cases where deceleration occurs, the deceleration occurs more quickly than the acceleration.

It can be seen that electrons in case 3 reach high energies very quickly (within 0.01s), but that as the simulations progress, more electrons achieve higher energies in cases 4 and 5.

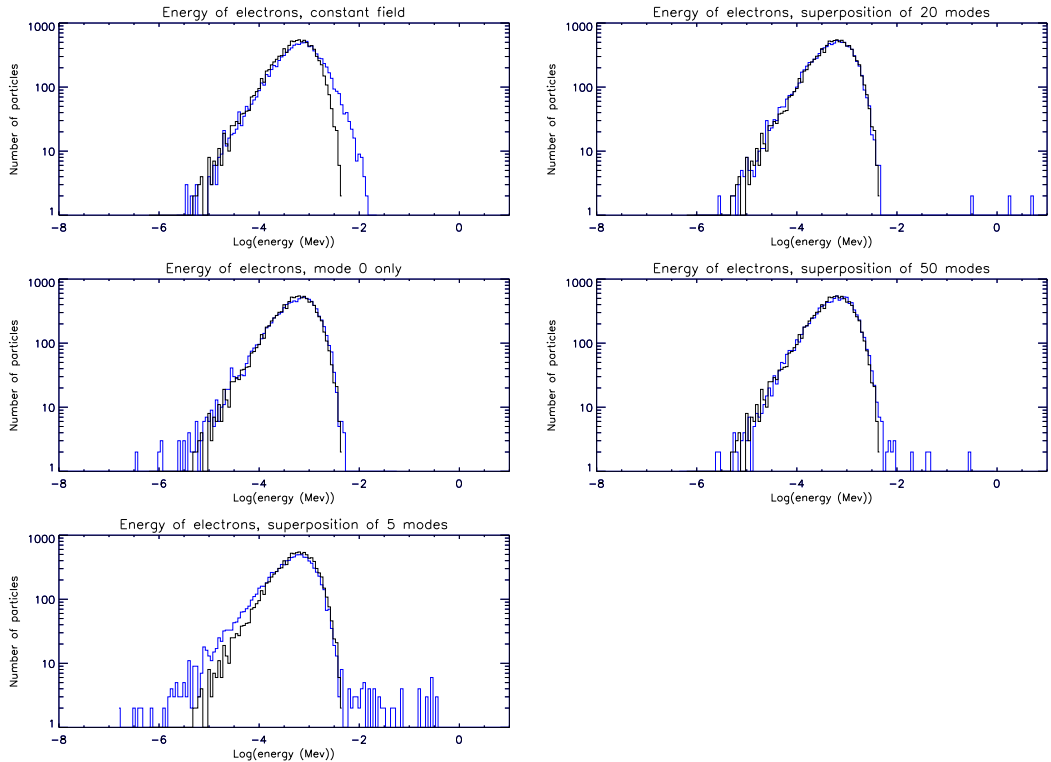


Figure 4.19: Energy distribution of 10000 electrons at $t = 0$, and at $t = 231$ (0.01 seconds) for different electric and magnetic fields. The blue curves are the energies of the electrons at the time stated. The black curves are the initial energy distributions.

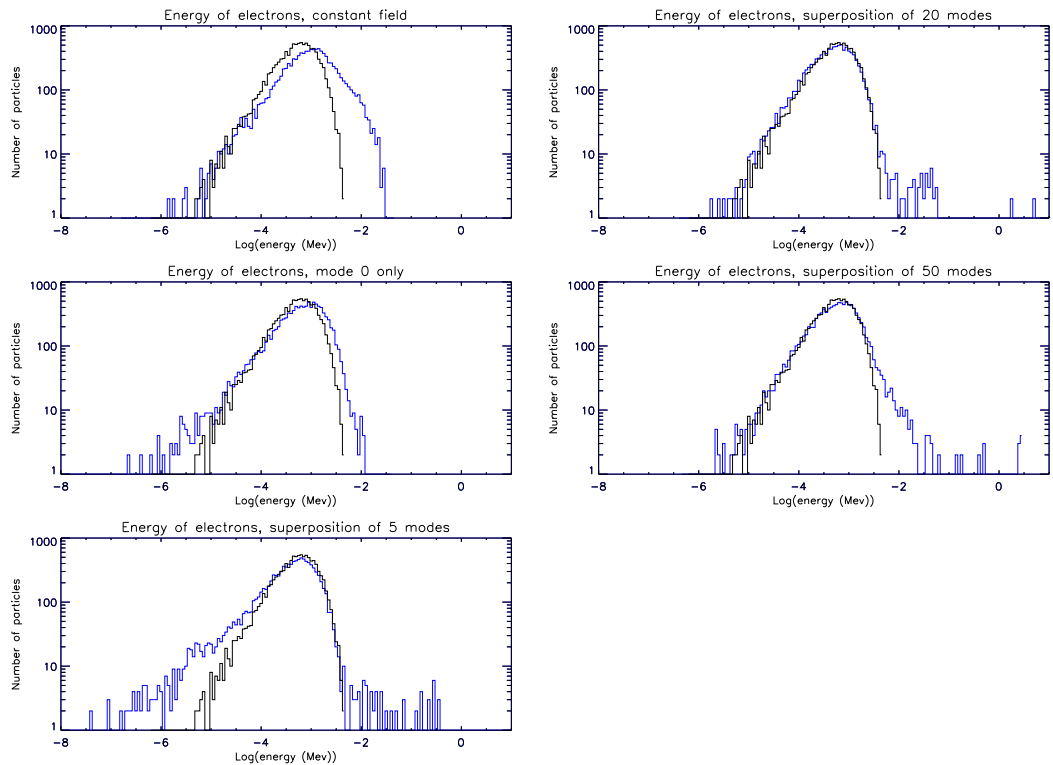


Figure 4.20: Energy distribution of 10000 electrons at $t = 0$, and at $t = 1155$ (0.05 seconds) for different electric and magnetic fields. The blue curves are the energies of the electrons at the time stated. The black curves are the initial energy distributions.

High Energy Particles

In order to investigate how the particles become energised, and why in this case adding more modes does not necessarily make a more efficient accelerator, the initial and final positions of all 10 000 electrons were plotted for each case.

Figure 4.22 shows that the locations of the origin of high energy electrons are quite different in each case. In case 1, high energy electrons mainly originate within $r \approx 0.2$, or in the half of the region below the $x = y$ line. In case 2, very few high energy electrons are seen. Those which are seen originate either very close to $r = 0$, or at $r \approx 1$. For case 3, we see a very defined region within $r \approx 0.4$ where high energy particles originate as well as a region at $r \approx 1$. In case 4, two concentric circles are seen where high energy particles originate, as well as a few high energy particles scattered at larger values of r . Case 5 is similar to case 4; concentric circles of high energy particles are seen, with more such particles than in case 4. I speculate that these concentric rings arise from the cylindrically symmetric character of the eigenmode disturbances. High energy particles could originate from energetically

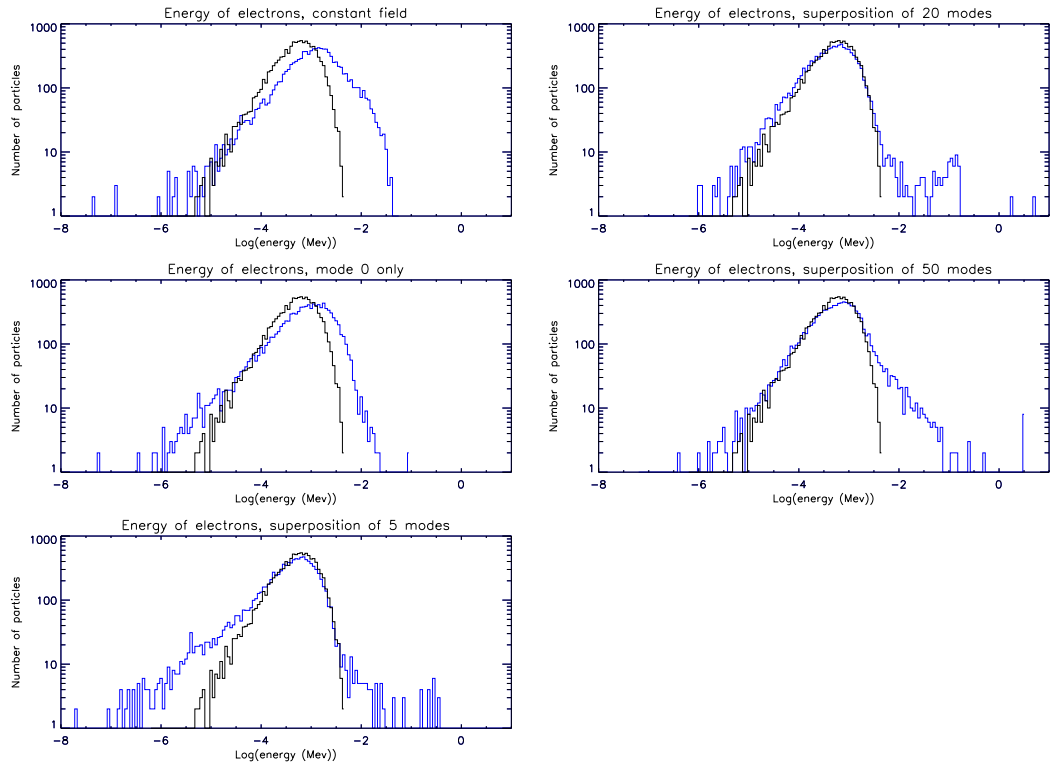


Figure 4.21: Energy distribution of 10000 electrons at $t = 0$, and at $t = 2079$ (0.09 seconds) for different electric and magnetic fields. The blue curves are the energies of the electrons at the time stated. The black curves are the initial energy distributions.

favourable positions in this cylindrically symmetric geometry, so that regions where high energy particles originate form concentric rings.

Figure 4.23 shows the locations of high energy particles at $t = 0.1s$. In case 1, the electrons are ejected from the central region. High energy electrons end up at $x \approx 0, y \approx |2|$. As for protons, electrons are drawn via $\mathbf{E} \times \mathbf{B}$ drift into the null along the x-axis, and are expelled along the y-axis. Since high energy particles are those which undergo this $\mathbf{E} \times \mathbf{B}$ drift, the initial location of these particles now makes sense, as these are the particles which can most readily drift along the x-axis. In case 2, the majority of electrons end up in a circular region within $r \approx 1$. Some electrons are expelled in a similar fashion to those in case 1. High energy particles are found in both regions.

In case 3 there are high energy particles at $x \approx 0, y \approx |2|$. Low energy particles form a well defined central circle with $r \approx 1$, as well as two symmetric arcs at $y \approx |1|$. For case 4, high energy particles also end up within $r \approx 1$. Lower energy particles form two concentric circles are formed with radii ≈ 1 and 2 . In case 5, the low energy particles form a circular central region, as well as two symmetric arcs. The majority of high energy particles are found either at the centre, or in an extended region on the right hand side.

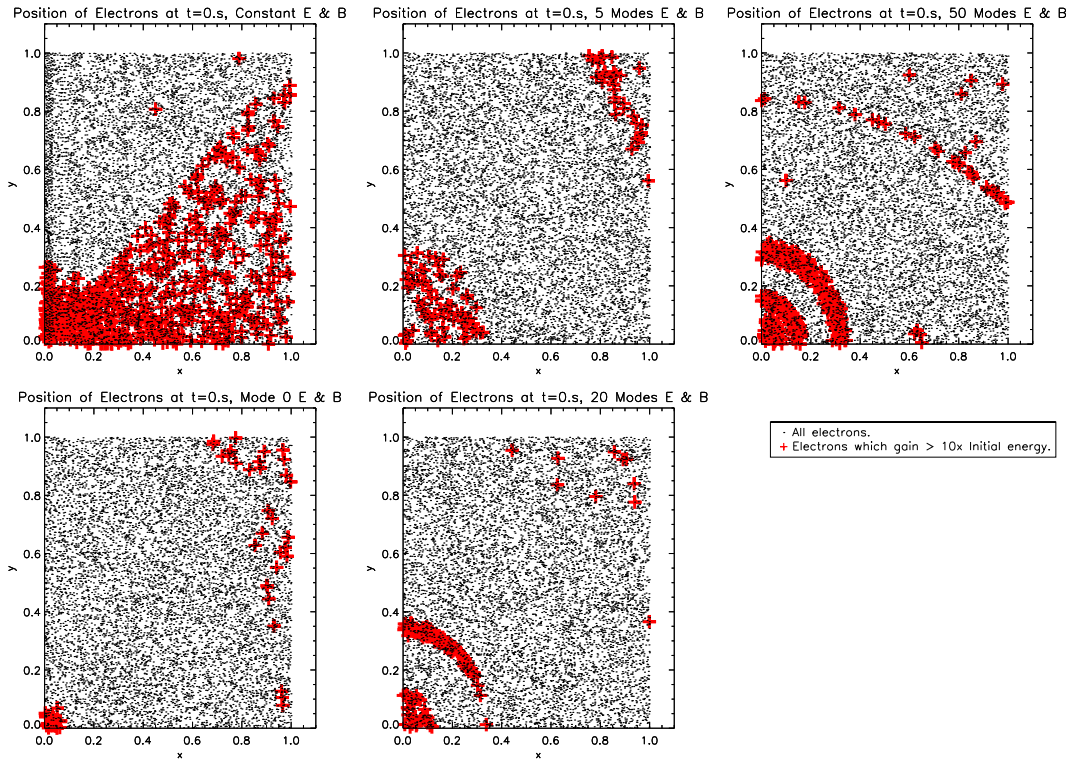


Figure 4.22: Initial positions of electrons for all cases. Dots show the positions (at $t = 0$) of electrons which gain less than 10 times their initial energies. Crosses show the positions (at $t = 0$) of electrons which gain more than 10 times their initial energies. x and y are given in units of $10 \times d_e$.

Clearly, these two figures show that electrons behave very differently when more perturbations are added to the electric and magnetic fields. Instead of particles being drawn into the null and then expelled, they are drawn to specific spatial locations where they can be energised. These may possibly represent the nodes of the oscillations, or a magnetic field topology which results in particle trapping.

4.2.7 Determining the Size of the Non-Adiabatic Region

Using the same arguments as in section 4.2.5, the size of the non-adiabatic region for electrons was established by calculating the magnetic moment of the electrons.

Figure 4.24 shows the variation of particle magnetic moment with time and distance from the neutral point for two electrons in case 5. It can be seen that the particle magnetic moment changes substantially between $r \approx 0.1 - 0.2$, after which any changes are small until $r \approx 0.5$. Figure 4.25 shows the trajectory of the particles in the x - y plane, and the variation in distance from the null point with time. It can be seen that the electrons mainly follow the field lines created by the eigenmode disturbances. The two electrons in question also spend significant

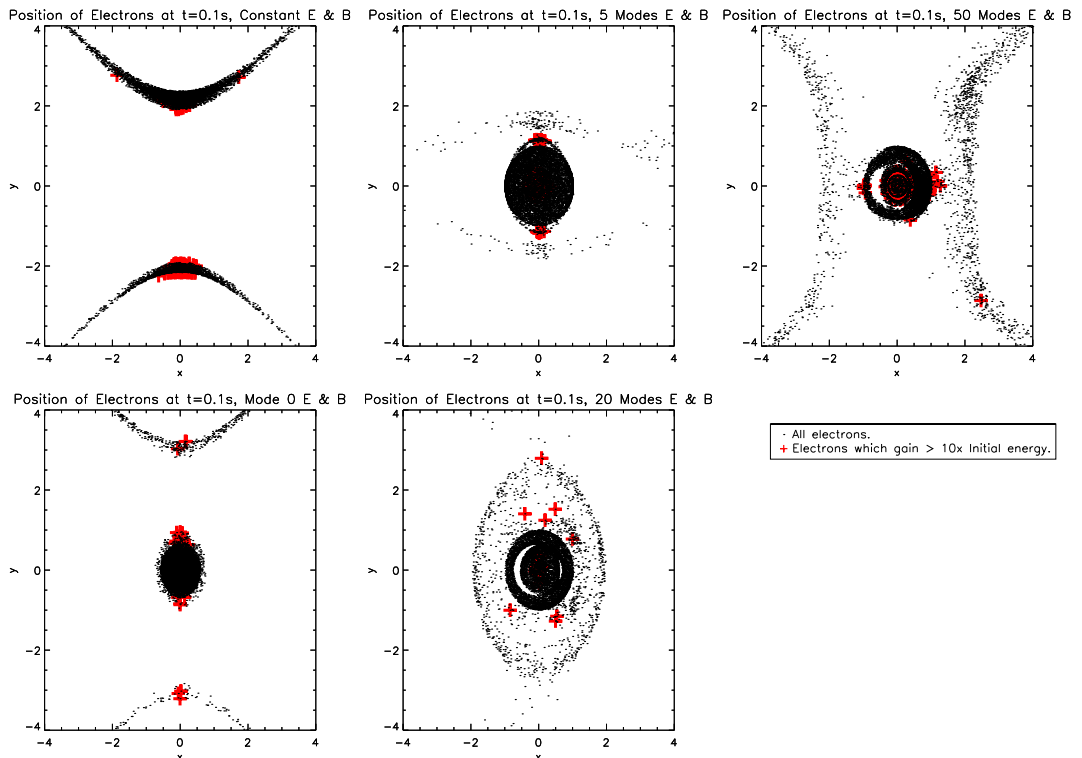


Figure 4.23: Final positions of electrons for all cases. Dots show the positions (at $t = 2310$) of electrons which gain less than 10 times their initial energies. Crosses show the positions (at $t = 2310$) of electrons which gain more than 10 times their initial energies. x and y are given in units of $10 \times d_e$.

amounts of time trapped at the radii at which the particle's magnetic moment can vary, i.e. in regions where they can gain energy.

Figure 4.26 shows how the magnetic moment of electrons varies in case 2. In case 2, particles which gain energy tend to remain close to the null, and I was unable to identify particles which gained large amounts of energy and travelled to large r . It can be seen that magnetic moment of the electrons undergoes large changes within $r \approx 0.1$. Figure 4.27 shows that these particles follow circular orbits within this radius, moving to smaller radii as the simulation progresses.

Figure 4.28 shows how the magnetic moment of electrons varies in case 3. As for case 2, particles which gain energy tend to remain close to the null, and I was unable to identify particles which gained large amounts of energy and travelled to large r . It can be seen that the particles in figure 4.28 remain trapped at approximately the distance from the neutral point at which they began the simulation, and that their magnetic moment varies at these locations, i.e. they are moving non-adiabatically. Figure 4.29 shows that these particles follow circular

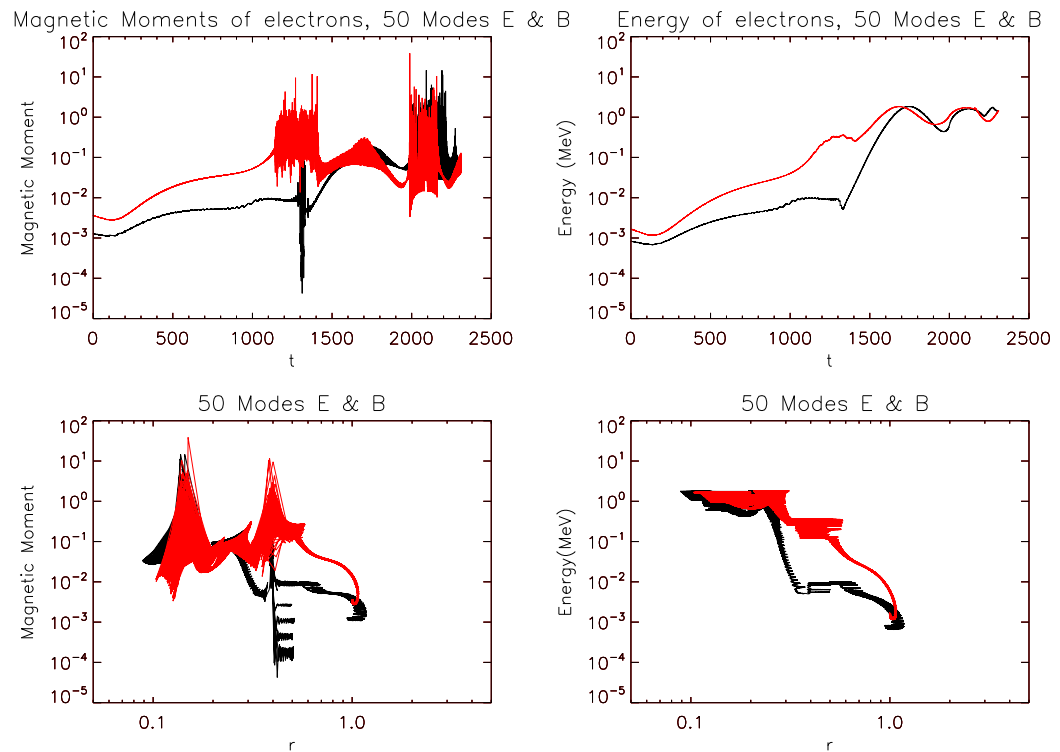


Figure 4.24: Variation of magnetic moment and energy of high energy electrons with distance from the neutral point and time, for case 5. These two particles were chosen as they both gained more than 400 times their original energy. Particle 1 (black) and particle 2 (red) are the same particles in each frame of the figure.

orbits at these radii, remaining at a roughly constant distance from the neutral point as the simulation progresses.

In attempting to plot the variation in distance from the null for electrons in cases 3, 4 and 5, it was consistently difficult to find particle which gained large amounts of energy and travelled large distances from the null. I wished to find such particles in order to explore the variation in magnetic moment of particles as they travelled throughout the x-y plane.

For each of the cases 3, 4 and 5, particles which travelled large distances from the null did not gain very much energy (they typically gained less than their initial energy). Since magnetic moment should be conserved when a particle is moving adiabatically, particles which do not gain very much energy will not change their magnetic moment much. This means that such particles are not very useful indicators of the variation of the magnetic moment throughout the x-y plane. Particles which did experience large changes in magnetic moment did not travel very far in the x-y plane, and so could only provide information about the variation of magnetic moment within a small region.

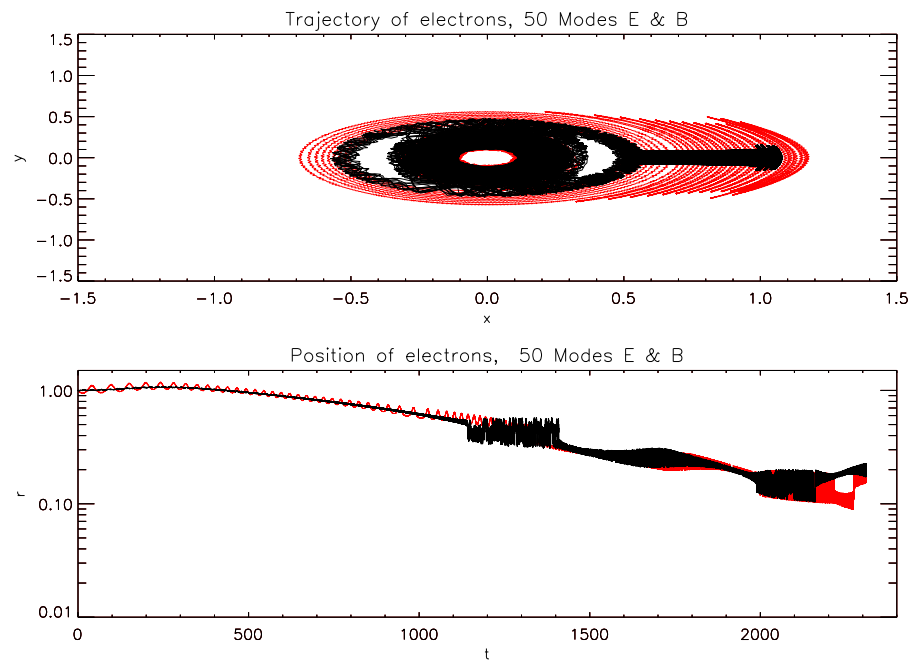


Figure 4.25: Trajectories of 2 electrons in the x - y plane (top) and variation of distance from the neutral point with time (bottom) for case 5. These two particles were chosen as they travelled reasonably far in r without escaping the system and also gained large amounts of energy. Particle 1 (black) and particle 2 (red) are the same particles in each frame of the figure.

4.2.8 Magnetic Field Topology

Why do some of the particles studied stay so close to the null? Figure 4.30 shows the shape of the magnetic field close to the null for case 5. It can be seen that for the superposition of modes the centre of the field is significantly altered from a standard X-type neutral point. The field for case 5 contains a region of closed magnetic field (an O-type neutral point) at its centre where the particle can become trapped. Since these closed regions are within $r \approx 0.5$, where the particles can move non-adiabatically, particles which become trapped in these regions can gain significant amounts of energy. The trajectory of one such particle (a proton) is shown, and the particle is seen to be approximately following one of the central circular field lines. Note that the field is plotted at $t = 0.5s$, but the trajectory shown is the path taken by the proton over the whole time of the simulation. However, the central loop that the particle is following remains approximately constant in size and shape throughout the simulation. Near the null, one also sees the development of many smaller X-type and O-type points, which will also be regions of particle demagnetisation, and therefore give rise to acceleration in the presence of an electric field. Such magnetic structures are reminiscent of those caused by a tearing mode instability when a plasma with finite conductivity (such

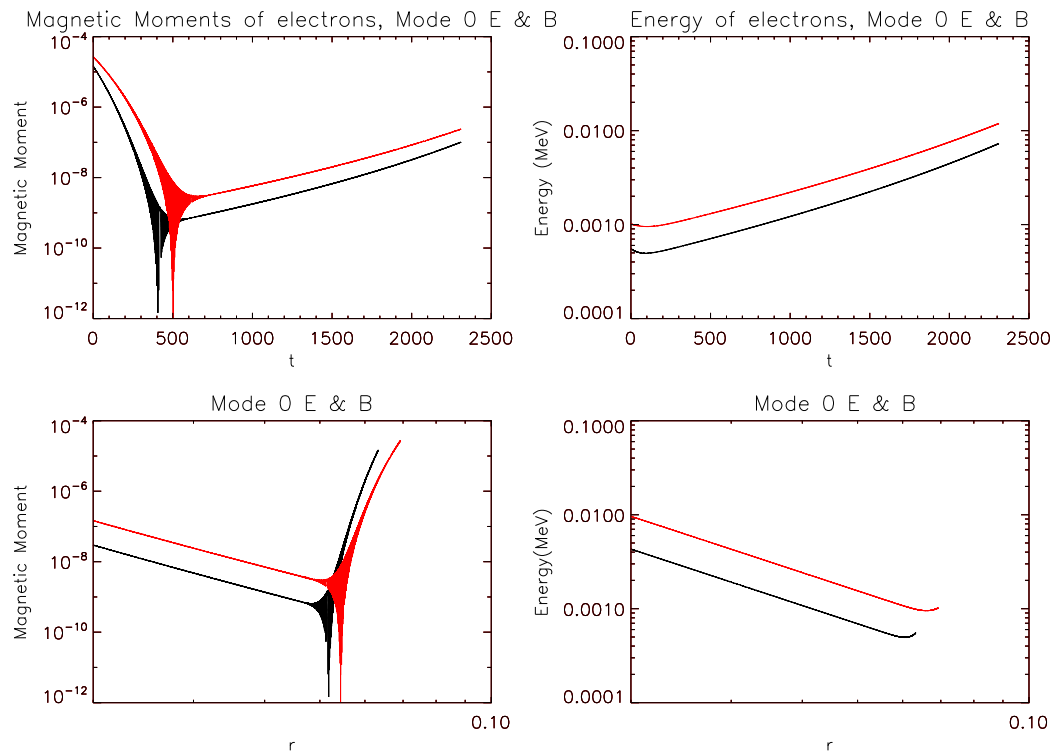


Figure 4.26: Variation of magnetic moment and energy of high energy electrons with distance from the neutral point and time, for case 2. These two particles were chosen as they travelled reasonably far in r without escaping the system and also gained large amounts of energy. Particle 1 (black) and particle 2 (red) are the same particles in each frame of the figure.

as the plasma I simulate) is perturbed at an X-type point (Furth, Killeen, and Rosenbluth (1963)).

4.2.9 Particle Trapping & Pitch Angle

As we have seen, adding more perturbations to the magnetic field causes many smaller structures to form. What effect do these structures have on the particle pitch angle?

Protons

Figure 4.31 shows the distribution of proton pitch angles at $t = 5360$ (1 second) for all cases. The black histograms indicate the initial pitch angles of the particles, an approximately flat distribution. The distributions for cases 1, 3 and 3 look broadly similar. The distribution is symmetric about a peak at zero, and there are two smaller peaks at ± 1 , indicating particles travelling parallel to the magnetic field. It can be seen that adding more modes causes the distribution of pitch angles at $t = 5360$ to become flatter, meaning that adding more modes

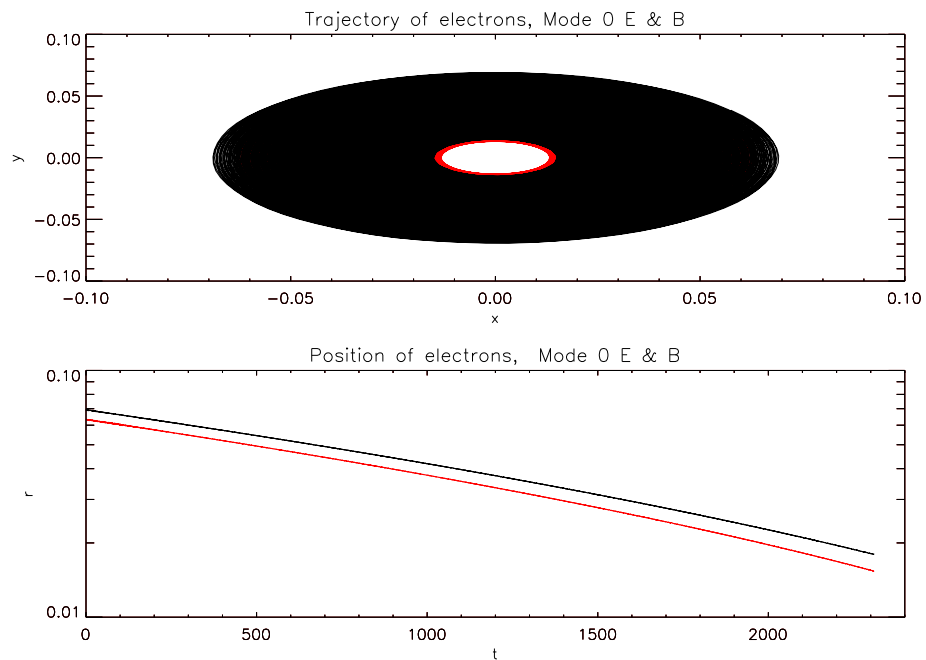


Figure 4.27: Trajectories of 2 electrons in the x-y plane (top) and variation of distance from the neutral point with time (bottom) for case 2. These two particles were chosen as they travelled reasonably far in r without escaping the system and also gained large amounts of energy. Particle 1 (black) and particle 2 (red) are the same particles in each frame of the figure

causes greater scattering in pitch angle. In this chapter, I will define scattering as simply being any process which causes the pitch angle of the particle to change. As more modes are added, many more particles with pitch angles parallel to the magnetic field are also seen. If particles are travelling parallel to the magnetic field, they will be following magnetic field lines very closely (possibly as a result of a magnetic mirror force, i.e. as the particles travel into an area of decreasing magnetic field, the magnetic mirror force will cause their pitch angles to decrease), which could lead to particles travelling more easily to areas of the magnetic field where they can gain energy.

What effect does this pitch angle scattering have on the behaviour of particles? An obvious answer is that pitch angle scattering causes particles to change their trajectories. Figure 4.32 shows the locations at which the pitch angle of the particle changes by more than $\pi/2$, in other words, the locations at which the particle's direction of motion is reversed. If a particle's pitch angle had changed by more than $\pi/2$ in 0.1s, a 'pitch angle scattering event' was determined to have occurred. It can be seen that large changes in pitch angle mainly occur closest to the neutral point in all cases. As more modes are added, more such changes occur. For cases 1 and 2 and, around the same number of large changes occur. As more modes are added, this figure increases, such that by case 5 around six times as many large

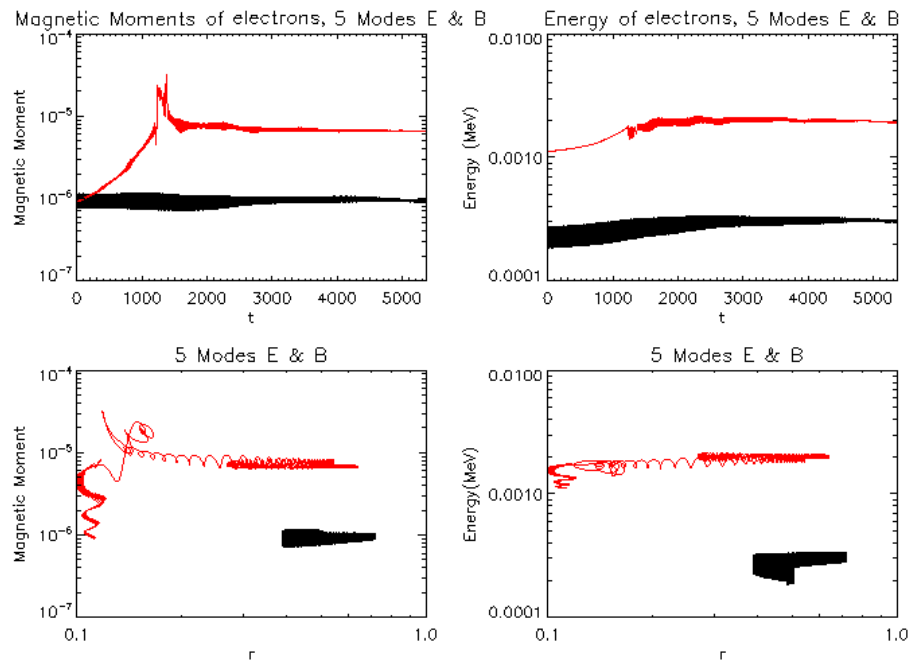


Figure 4.28: Variation of magnetic moment and energy of high energy electrons with distance from the neutral point and time, for case 3. The red line represents a particle which gained 500 times its original energy. The black particle lost energy. Particle 1 (red) and particle 2 (black) are the same particles in each frame of the figure.

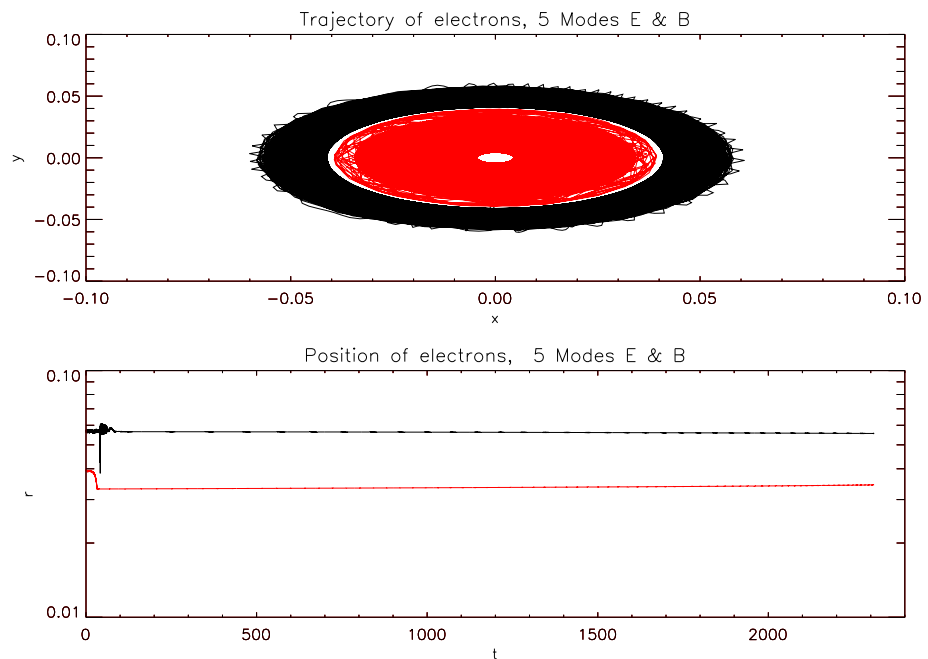


Figure 4.29: Trajectories of 2 electrons in the x-y plane (top) and variation of distance from the neutral point with time (bottom) for case 3. The red line represents a particle which gained 500 times its original energy. The black particle lost energy. Particle 1 (red) and particle 2 (black) are the same particles in each frame of the figure.

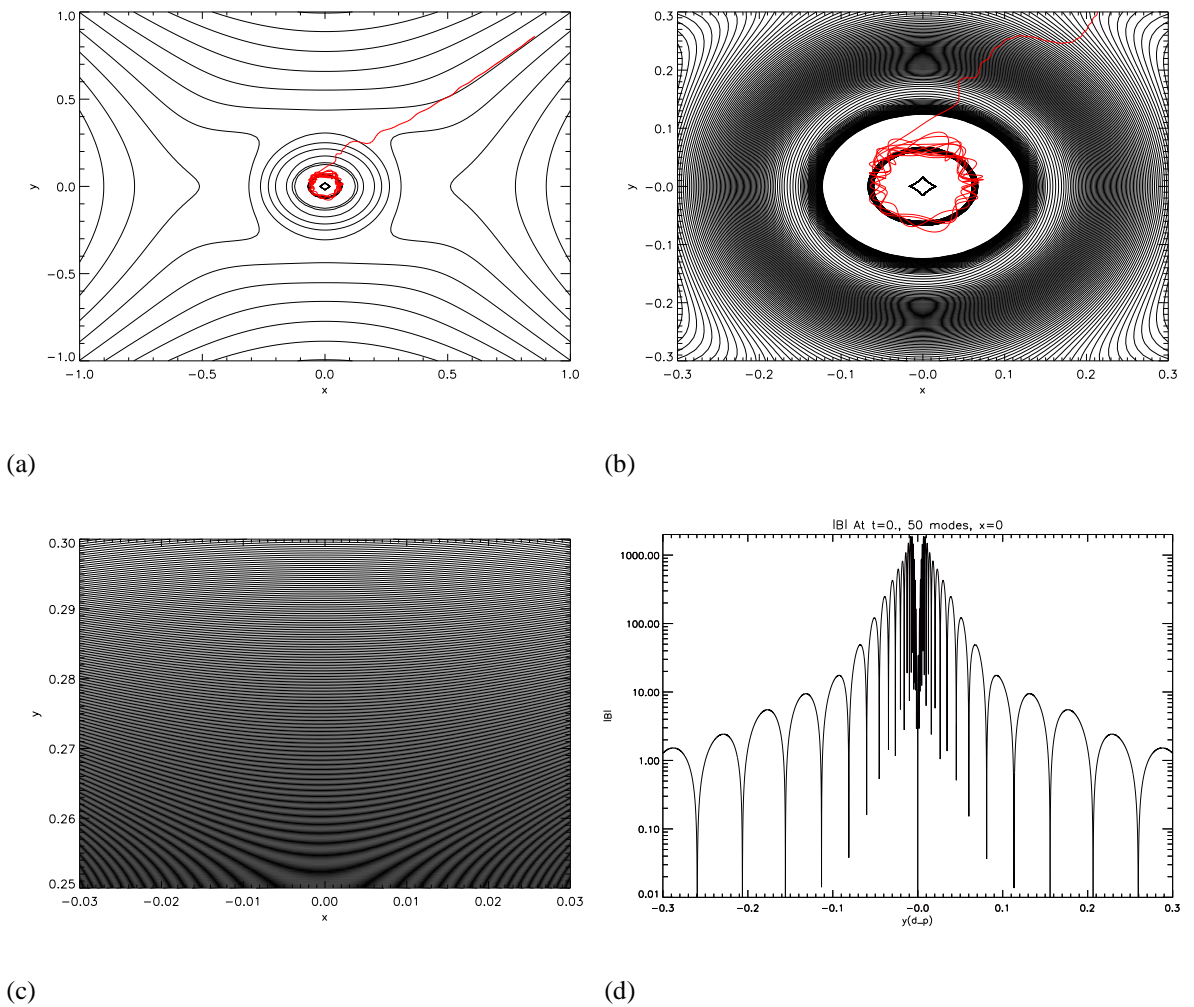


Figure 4.30: Magnetic field contours with a sample proton trajectory overlotted for case 5, for the region $-1 \leq x \leq 1$, $-1 \leq y \leq 1$ (a) for the region $-0.3 \leq x \leq 0.3$, $-0.3 \leq y \leq 0.3$ (b), and (c) for the region $-0.03 \leq x \leq 0.03$, $0.25 \leq y \leq 0.3$, displaying some of the smaller structures formed by the perturbations. Note that the field is plotted at $t = 0.5s$, but the trajectory shown is the path taken by the proton over the whole time of the simulation. However, the central loop that the particle is following remains approximately constant in size and shape throughout the simulation. Panel (d) shows the magnitude of the magnetic field at $x = 0$ for $-0.3 < y < 0.3$. It can be seen that the magnetic field goes to zero (here, the magnetic field is considered to be zero if $|B| < 0.01$) 7 times, 6 of which are outside the central null, indicating that the small scale structures seen in panels (b)-(c) of this figure are indeed nulls.

changes in particle direction are made as for cases 1 and 2. For case 5, the size of the region where the particle's trajectory can be reversed also increase greatly. For cases 1 to 4 all such changes occur within $r = 1$. It should be noted that these changes are recorded every $0.1s$.

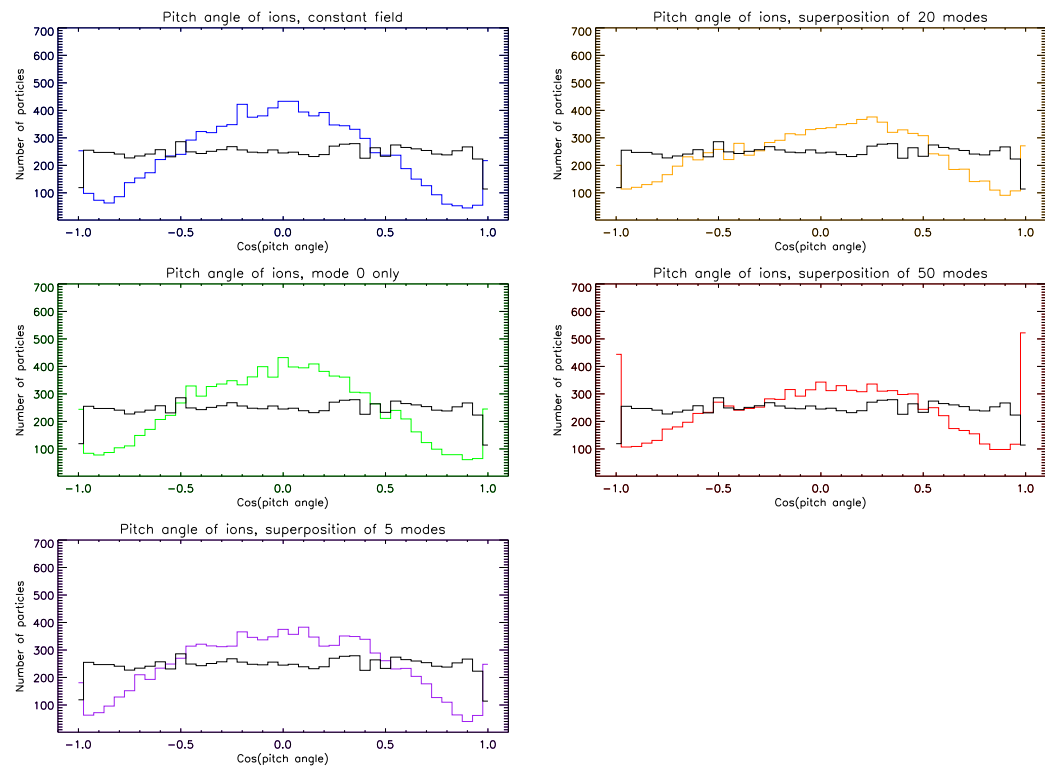


Figure 4.31: Pitch angle distribution of 10000 protons at $t=0$, and also at $t=5360$ for different forms of the electric and magnetic fields.

Therefore, I can say that adding more perturbative modes causes the pitch angle of the protons to change more often. I speculate that this ‘pitch angle scattering’ is caused by the development of small scale structures within the magnetic field. In that sense, adding more perturbations to the electric and magnetic fields causes a sort of pitch angle scattering to occur.

Do these changes in the particles’ trajectories mean that the particles will spend more time in the non-adiabatic region? Figure 4.33 shows the number of timesteps spent at each value of r . It can be seen that adding more modes causes particles to spend more time at small r . The plots for cases 1 and 2 again look very similar. As more modes are added, the peak of the distribution broadens, and more particles spend time at lower values of r . By cases 5, there is a sharp peak at $r < 0.2$, suggesting that particles become trapped there. It seems likely that the increase in occurrences of large changes in pitch angle causes particles to spend more time at $r < 1$. The ‘scattering’ caused by adding more perturbative modes causes particles to change direction, and they may become trapped in regions where they can move non-adiabatically and gain energy.

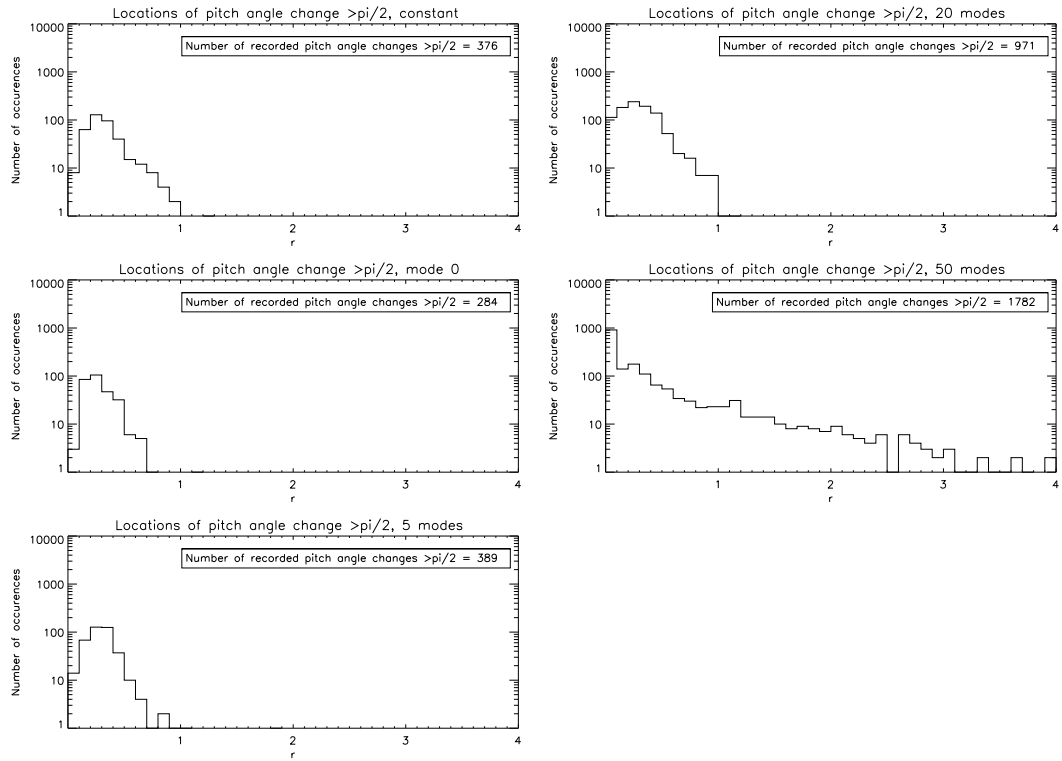


Figure 4.32: Positions at which ion trajectory changes by more than $\pi/2$ for different forms of the electric and magnetic fields. It can be seen that some ‘pitch angle scattering’ events occur even when there are no perturbations present. However, note that these occur at small values of r , and so can be attributed to the fact that the particle is close to the null and is not undergoing regular gyromotion about a field line.

Electrons

Electrons are lighter, so any process which causes changes in pitch angle will have a greater effect on electrons. This is because the small mass of the electron gives it a small gyroradius, meaning that the electron is able to interact with smaller scale structures than protons can interact with. Therefore electrons will be more susceptible to small scale changes in the electric and magnetic fields. Figure 4.34 shows the distribution of pitch angles in all cases at $t = 0.1s$. It can be seen that in all cases, particles start out with a flat distribution of pitch angles. In case 1, the cosine of the pitch angle of particles then evolves to a symmetric distribution centred on 0.

In case 2, the distribution is symmetric, with particles tending to have pitch angles parallel to the magnetic field. This could account for the high and low energy tails, since some particles will travel away from the null, meaning that they will not be accelerated, whereas other particles will be transported directly to the null. Recall also that the low energy tail could be caused by particles moving in the opposite direction to the electric field.

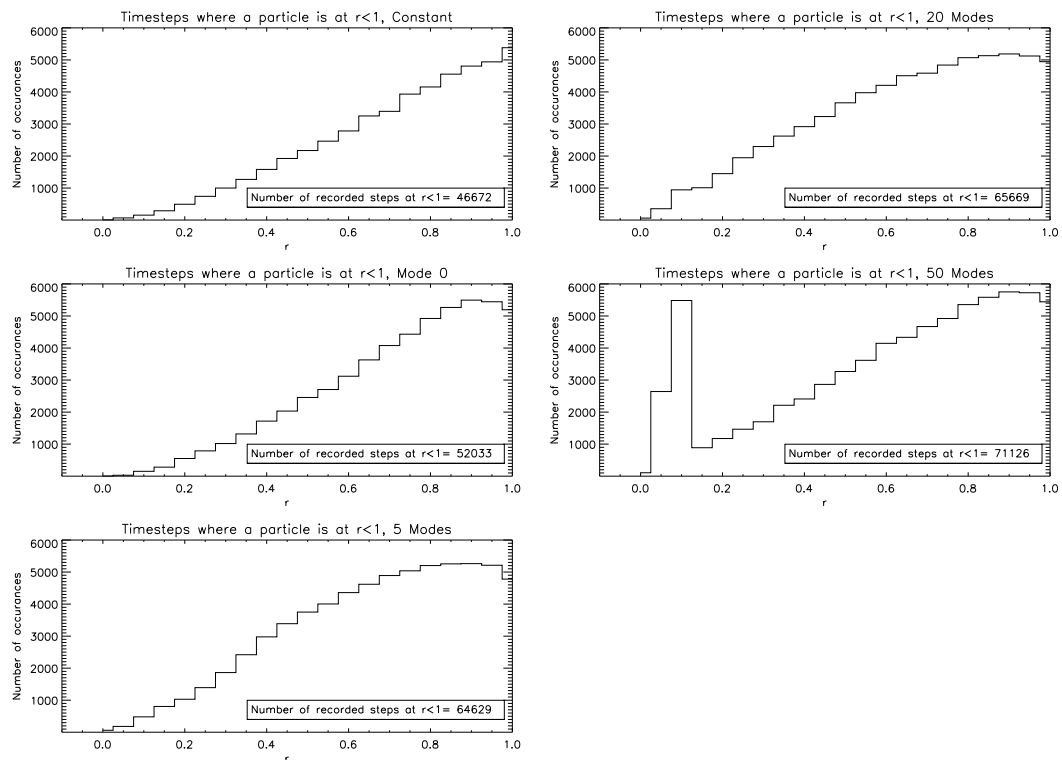


Figure 4.33: Number of timesteps spent by ions at each value of r for different forms of the electric and magnetic fields.

In case 3, the distribution of pitch angles is much flatter, although there are slightly more particles travelling parallel to the magnetic field. Again, this could account for the high and low energy tails, since some particles will travel away from the null, meaning that they will not be accelerated, whereas other particles will be transported directly to the null. The high and low energy tails in this case are bigger than in case 2. This could reflect the effect of eigenmode oscillations on the topology of the magnetic field, which could result in particle trapping.

In case 4, the distribution of pitch angles is on average unchanged. Particles have a range of pitch angles, distributed fairly evenly. This could either mean that the particles do not do much at all, or that the ‘scattering’ effect affects all particles equally, so that the distribution of pitch angles is unchanged.

In case 5, the distribution of pitch angles is also unchanged, and the distribution looks similar to that in case 4, except that there is a slight peak in particles travelling perpendicular to the magnetic field, i.e. parallel to the electric field. Of course, these particles are following the magnetic field lines in the x-y plane, so they travel parallel to the electric field merely when their trajectories intersect this plane.

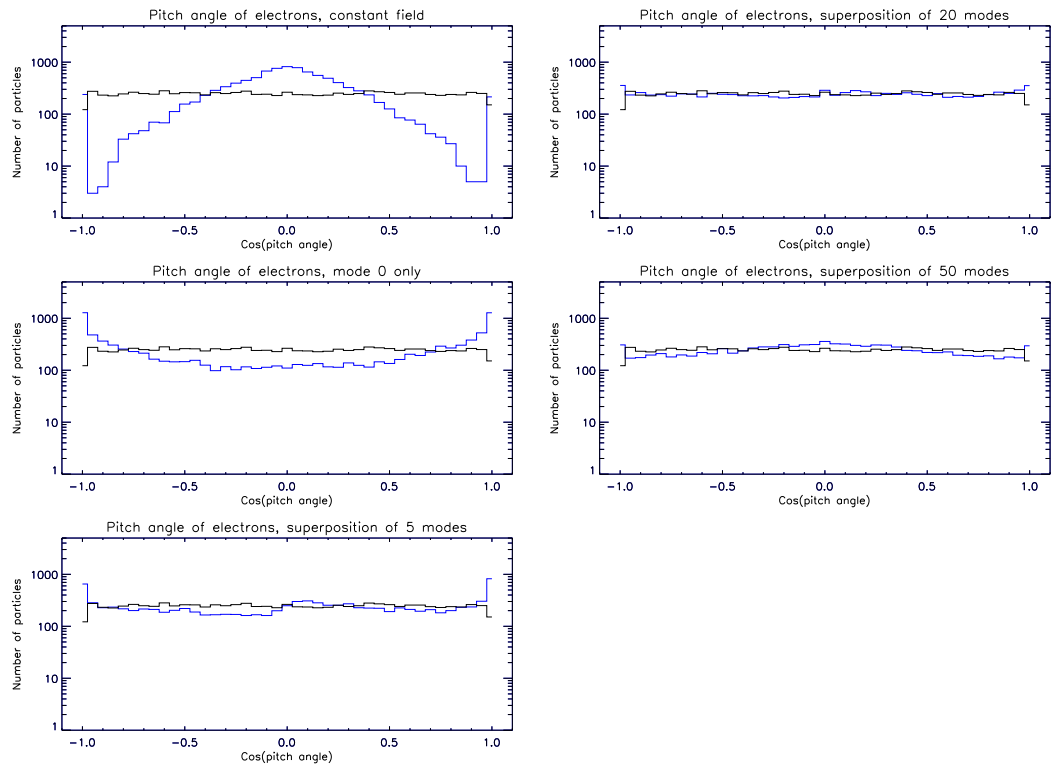


Figure 4.34: Pitch angle distribution of 10000 electrons at $t = 0$, and also at $t = 2310$ (0.1s) for different forms of the electric and magnetic fields. The blue histograms indicate particles that stay within the system boundaries. Red histograms indicate particles which left the system, at the time at which they left the system.

What can this information tell us about the behaviour of particles? Are the distributions for cases 3, 4 and 5 flat because the pitch angles don't change, or because they change a lot, so that the net effect of the changes is zero? Figure 4.35 shows the locations at which the pitch angle of the particle changes by more than $\pi/2$. It should be noted that these changes are recorded every $0.01s$. It can be seen that the electrons have most large pitch angle changes in case 1. This is perplexing, since one might expect that pitch angle changes are due to the interaction of the electrons with small scale changes in the electric and magnetic fields. This high number of pitch angle changes may be because electrons in case 1 are moving more quickly as they experience a higher average electric field, and so their pitch angle evolves more rapidly. In case 2, the number of large pitch angle changes drops by over two thirds. These changes also tend to occur further away from the null, and there is a strong dip in the number of changes at $r \approx 2$. Case 3 has very few pitch angle changes. The majority occur between $r = 1$ and $r = 2$. Cases 4 and 5 are broadly similar in character. There are fewer pitch angle changes than for case 1, but more than for cases 2 and 3. Most pitch angle changes occur closer to the null, with the number of such changes decreasing with increasing r . The distributions of pitch angle seen in figure 4.34 for cases 4 and 5 are

therefore flat because there are many changes in pitch angle, with no particular direction being favoured. Overall, there are many more changes in pitch angle for electrons than for ions, which is to be expected since electrons are much lighter, and so are more affected by scattering-type events.

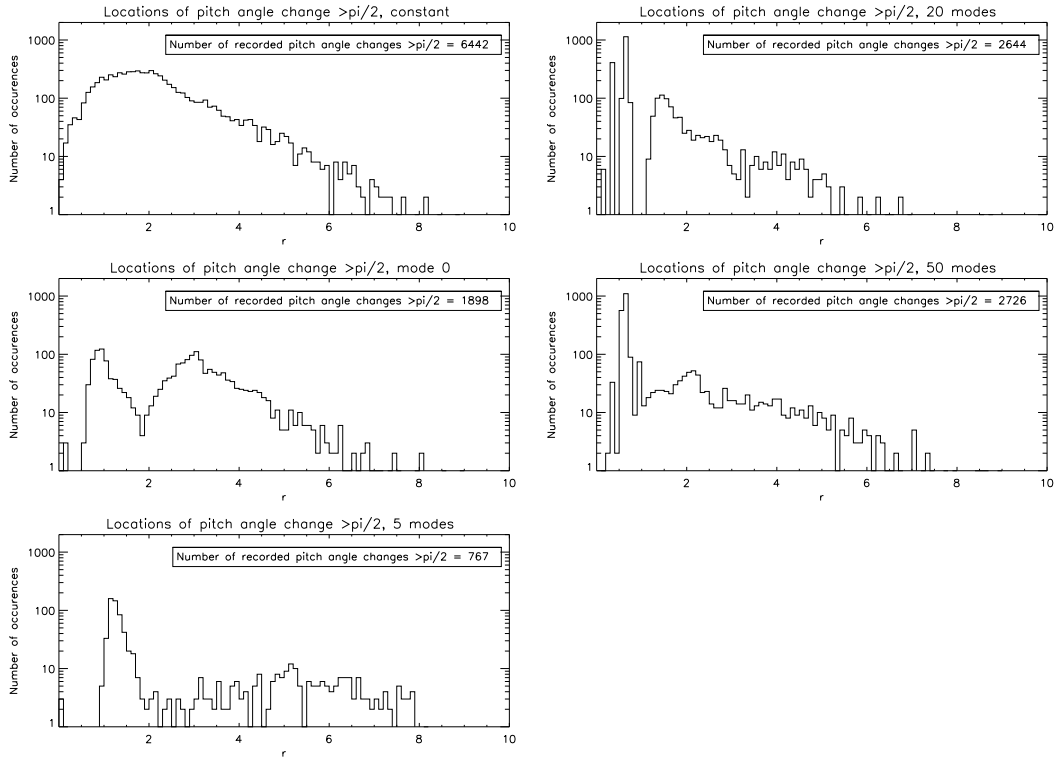


Figure 4.35: Positions at which electron trajectory changes by more than $\pi/2$ for different forms of the electric and magnetic fields.

As we did for ions, we must ask if these changes in pitch angle cause electrons to spend more time in the nonadiabatic region. Figure 4.36 shows the number of timesteps spent at each value of r . For cases 1, 3, 4 and 5, the form of the distribution is the same: a very small number of steps are spent very close to $r = 0$, and the number of steps spent at each radius increases relatively smoothly up to $r = 1$. For case 2 however, there is a very different distribution. The number of steps spent at each radius increases very quickly up to $r \approx 0.2$. It then decreases as r goes to 1. This appears to indicate a region where particles can become trapped, although this is clearly not a region where particles can become highly energised, since such significant trapping would surely cause particles to become highly energised if the region was one in which particles could move non-adiabatically.

Fewer particles spend times at $r < 1$ in cases 4 and 5 than in case 3. Therefore, adding more modes does not cause more trapping at small r . However, the creation of many nulls means

that there are more areas in which the particles can move non-adiabatically, so that particles do not need to be trapped at very small r in order to gain energy.

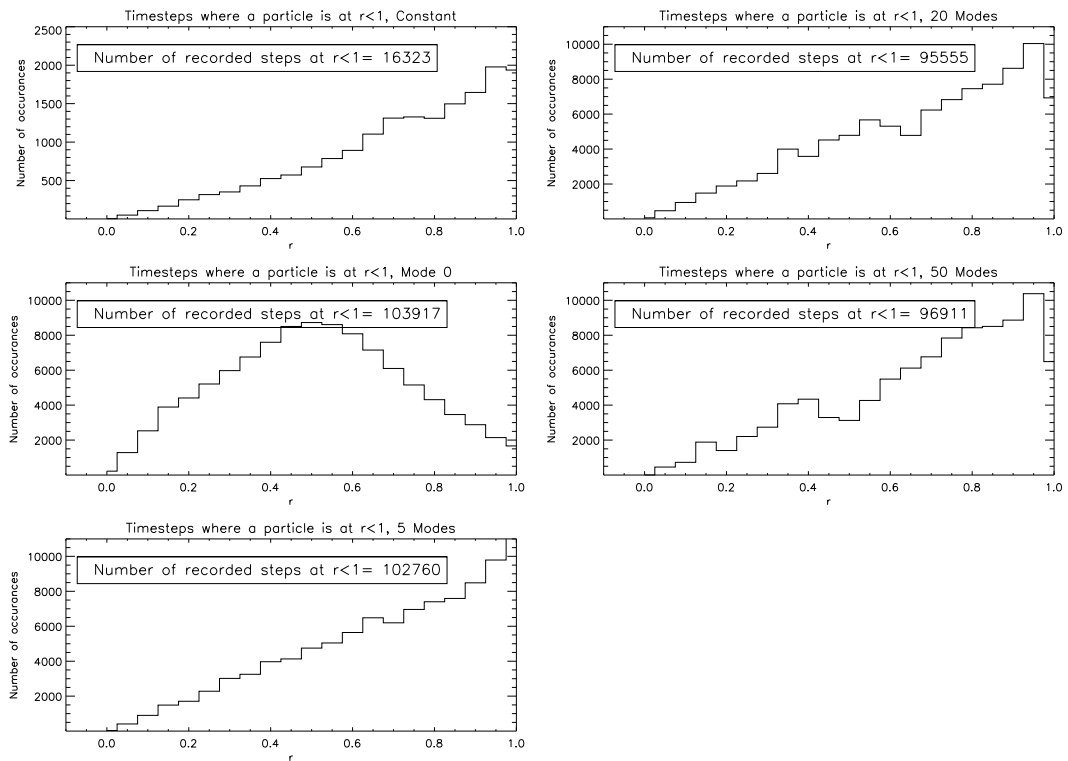


Figure 4.36: Number of timesteps spent by electrons at each value of r for different forms of the electric and magnetic fields.

4.3 Comparison of Electron & Proton Results

At this point, it is sensible to compare the effect of the ‘noisy’ fields on electrons with the effect on protons. Tables 4.1 and 4.2 show that electrons are subjected to electric fields which are around an order of magnitude greater than the electric fields that protons are exposed to. This is true for all cases. However, electrons are followed for 0.1s, whereas protons are followed for 1s. I can therefore make meaningful comparisons between the final distributions for both species of particle.

For protons, the energy distribution develops a high energy part at the end of the simulation in all cases, although the precise character of this varies. In cases 1-4, the high energy part of the distribution looks like a high energy ‘tail’ (although in case 3 the tail is very small). In case 5, the high energy part of the spectrum looks like a second Maxwellian-type distribution. By contrast, the distributions for electrons at the end of the simulation look quite different. In

cases 1 and 2, the distribution is subject to bulk heating, and no high energy tail is developed. A high energy tail develops by case 3, the size of which increases in cases 4 and 5.

In the case of electrons, the energy distributions continue to evolve over the whole simulation, in contrast to the energy distributions for protons, which do not change much after $t = 0.5s$. I speculate that this is because electrons are followed for a shorter time, and so there are more small-scale perturbations present in the electric and magnetic fields (as these perturbations decay fastest, their effect diminishes with time). Electrons, being less massive, are more affected by such small-scale changes. This can also be seen when one considers the initial and final positions of the particles. The initial and final positions of electrons form symmetric, circular patterns, consistent with the fact that the eigenmode disturbances in these simulations are cylindrically symmetric. The initial and final positions of protons do not form such patterns, and the initial and final position of protons owes more to the overall X-point geometry.

It can therefore be said that both electrons and protons are more efficiently accelerated by ‘noisier’ fields, but that electrons are more affected by the exact nature of this ‘noise’.

4.4 Resulting X-Ray Spectra

Since energy spectra for the electrons have now been obtained, the resulting X-ray photon fluxes can be calculated. Since I am considering electrons at an acceleration region, it is assumed that these X-rays are a result of thin target bremsstrahlung. This is because the region in which the electrons are accelerated is of comparatively low density, and hence it is collisionally thin. The thin target X-ray flux is calculated in c.g.s. units using the expression (e.g. Schrijver and Siscoe (2010))

$$S(E_{ph}) = \frac{n_p V}{4\pi R^2} \int_{E_{ph}}^{\infty} \sigma_{E_{ph}}(E_e) v(E_e) N(E_e) d(E_e), \quad (4.13)$$

where E_e is the energy of the electron, E_{ph} is the energy of the photon, v is the velocity of the electron, N is the number density of the electrons n_p is the number density of the protons, R is the distance from the source at which the emission is observed, V is the volume of the system and σ is the bremsstrahlung cross section. Since some of the electrons reach relativistic energies, the cross section given in Haug (1997) is used. There is a slight caveat here: the electrons I have used are ‘heavy electrons’, where $m = 10m_e$. This means that the

X-ray spectra shown here are merely indicative of the potential real X-ray spectra. The X-ray spectra obtained can be seen in figure 4.37. If such spectra are compared with an observed X-ray spectrum (figure 4.38, Krucker *et al.* (2008a)), we can see how realistic these spectra are.

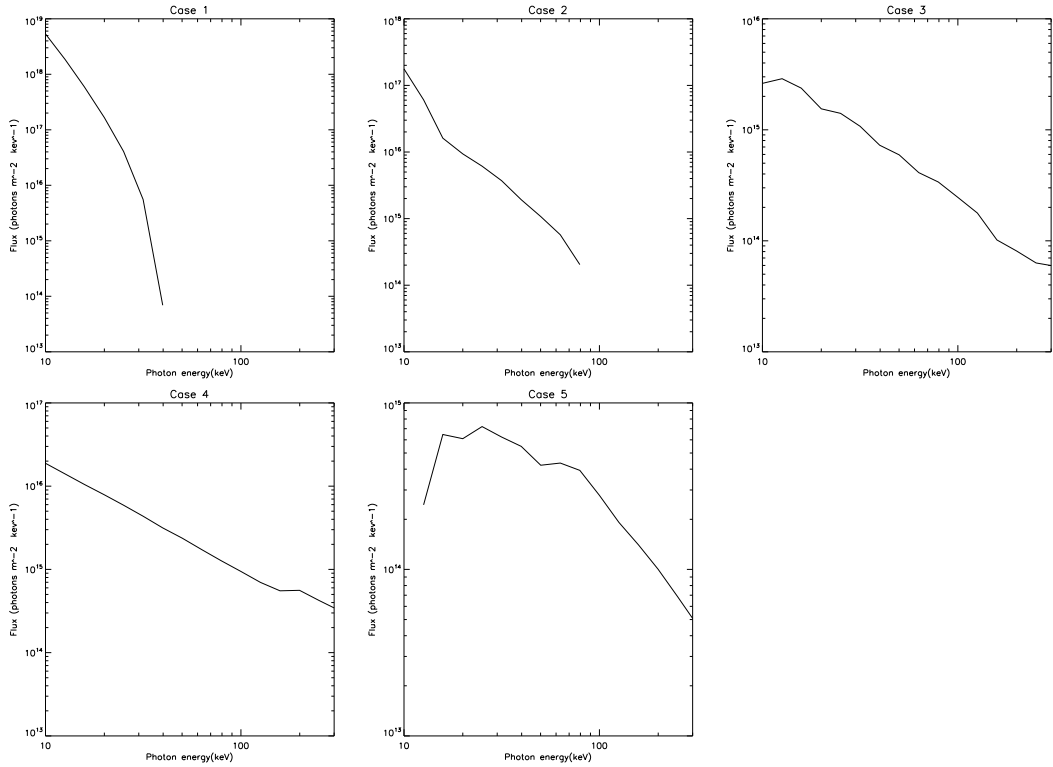


Figure 4.37: X-ray spectra generated from electron energy distributions at $t = 0.1s$ for cases 1-5.

Figure 4.38 (from Krucker *et al.* (2008a)) shows a typical flare hard X-ray photon spectrum together with the major components used in fitting it: a thermal spectrum (shown in red) at energies below about 20keV, plus a non-thermal power-law tail extending to higher energies. These components occur in the synthesised spectra to varying degrees. Most of our studied cases produce power-law components that are rather too hard (i.e. flat) compared with most flare spectra (i.e. photon spectral index γ in the range 1 - 2), in common with many other reconnection test particle calculations (e.g. Turkmani *et al.* (2006)). Case 2, however, involves a combination of a steeper power-law tail plus thermal component that is more similar to observations. The spectral index γ can be calculated using the relation

$$\gamma = \frac{-\log(I(E_2)/I(E_1))}{\log(E_2/E_1)} \quad (4.14)$$

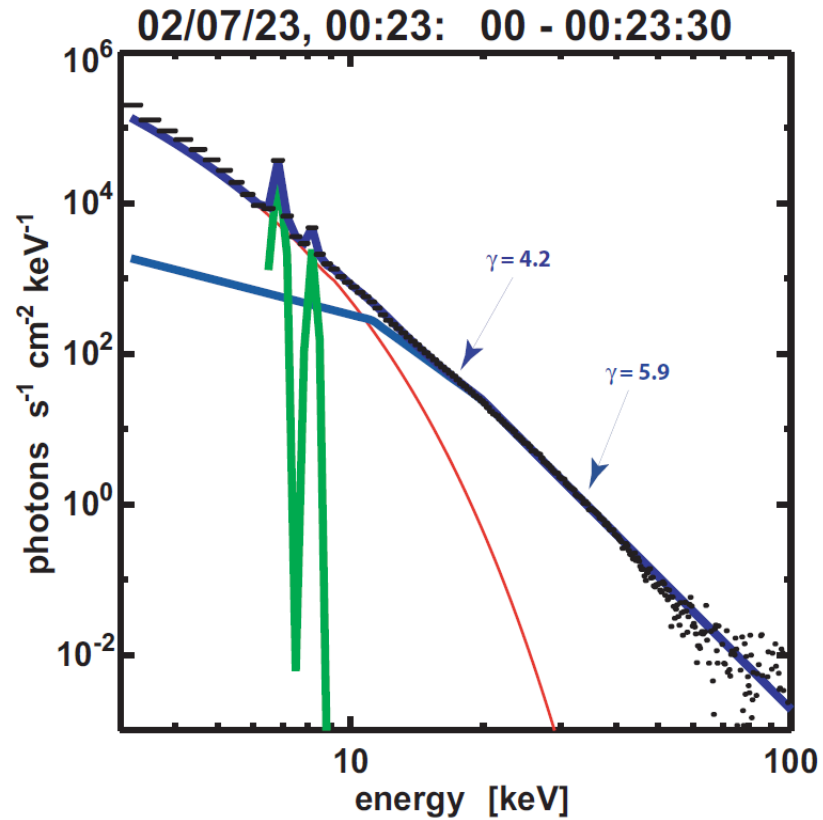


Figure 4.38: Example of an observed X-ray spectrum. The red curve shows the fit to the thermal emission. Krucker *et al.* (2008a).

where $I(E_1)$ is the photon flux at energy E_1 , and $I(E_2)$ is the photon flux at energy E_2 . Values for E_2 and E_1 were selected by taking the maximum and minimum values of the energy of the part of the spectrum being considered. For the thermal part of the spectrum, a spectral index was not taken, but instead the mean temperature (T) of the spectrum was calculated using the relation

$$T = \frac{E}{k_B}, \quad (4.15)$$

where E is the mean energy of the thermal part of the spectrum (in Joules), and k_B is Boltzmann's constant.

The spectral indices of the non-thermal part of the X-ray spectra produced in each case can be seen in table 4.3, as well as the mean temperature of the thermal part of each spectrum. It can be seen that the mean temperature of the thermal component increases as more modes are added.

Case	Mean Temperature (K) (Thermal Radiation)	Spectral Index (Non-Thermal Radiation)
1	$(1.1 \pm 0.5) \times 10^8$	Not applicable
2	$(1.1 \pm 0.5) \times 10^8$	2.7 ± 0.2
3	$(1.6 \pm 0.5) \times 10^8$	0.4 ± 0.2
4	$(2.0 \pm 0.5) \times 10^8$	1.5 ± 0.2
5	$(3.3 \pm 0.5) \times 10^8$	1.5 ± 0.2

Table 4.3: Mean temperature of the thermal parts of the X-ray spectra produced from the accelerated electron distributions, and spectral indices of the non-thermal parts of the same distributions.

Case 1, involving a steady electric field and no turbulence, does not result in an extended power-law tail but to a thermal type distribution with a higher temperature than assumed initially. In the X-type null model, turbulence evidently plays an important role in the development of power-law electron tails. It could be speculated that the emergence of a ‘superhot’ spectral component late in a flare (Lin *et al.* (1981)) reflects the development of a state of steady reconnection with most turbulence having decayed. Sturrock *et al.* (1984) suggested such steady reconnection as the explanation of the flare gradual phase. The suspected coronal origin of the superhot component (Krucker *et al.*, 2008a) would be consistent with my thin target calculation, concentrating on the vicinity of the energy release region.

4.5 Non-Flat Spectrum of Modes

So far in this work, the amplitude of the eigenmode disturbance was the same for each mode (i.e. a flat spectrum). In order to better model turbulence in the manner of Kolmogorov (1941), the amplitudes of the modes could be distributed as a power law with a spectral index of $-5/3$, as discussed in section 1.5. Perturbations on a variety of scales could be produced by convective motions in the photosphere causing oscillations in the coronal plasma. Large scale explosive events such as solar flares or coronal mass ejections, as well as smaller scale reconnection events could also produce disturbances in the coronal magnetic field. A cascade of energy from large to small scales could also be used to explain the unexpectedly high temperature of the solar corona. Particles become energised on intermediate scales, and this energy is converted to heat at the smallest length scales (in the dissipation range).

It is known (Kolmogorov (1941)) that turbulence on intermediate scales can be modelled as a power law with a spectral index of $-5/3$. It is also known (Alexandrova *et al.* (2009)) that such a power law is observed in the solar wind. Let us investigate consequences for ions if the amplitude of the eigenmode oscillations follows such a distribution. I will distribute the

amplitude of the modes according to the wavenumber of the mode such that the amplitude will be

$$a_n = a_0 k_n^{-5/3}, \quad (4.16)$$

where k is the wavenumber of the mode, and a_0 is a constant which can be fixed to have any amplitude. For these simulations, I chose $a_0 = 0.0001$, which was the amplitude of each mode for the flat spectrum of modes. The eigenmodes in this inhomogeneous situation are not described by a single wavenumber. This is because the form of the waves varies with r . For the purposes of distributing energy across modes as in K41 a rough wavenumber can be calculated at $r = 0$. This can be estimated using

$$k \approx \frac{d^2 E}{dx^2} \frac{1}{E}. \quad (4.17)$$

I will calculate the total electric and magnetic fields in the same manner as in previous simulations: by calculating the field for each mode and adding the fields together, then dividing by the number of modes. The eigenfunctions are still normalised so that their square norms are unity at $t = 0$. The form of the electric field generated by such a spectrum of modes can be seen in figure 4.39. It can be seen that, unlike the electric field for a flat spectrum, the electric field for this distribution decreases with time (over the simulation time). The variation of the electric field with r is the same as for the flat spectrum of modes. The average field strength is greater than for the flat modes at $r = 0$, but is smaller at other values of r .

The electric field for the $k^{-5/3}$ spectrum decays more quickly than the electric field for the flat spectrum if the simulation is stopped at $t = 1s$. If the simulation is run for longer times, this effect disappears. This can be seen in figure 4.40, which also shows that the electric field for the flat spectrum of modes is much larger and noisier than that for the $k^{-5/3}$ spectrum.

The effect of these new electric and magnetic fields on protons can be seen in figure 4.41. It can be seen that these new fields do not accelerate particles, probably because they are too small.

In order to better study the consequences for particle acceleration, I will increase the magnitude of a_0 to 0.01, for both spectra of modes. The energy distributions (at $t = 1s$) of protons that have been accelerated in these fields can be seen in figure 4.42. For the flat spectrum of

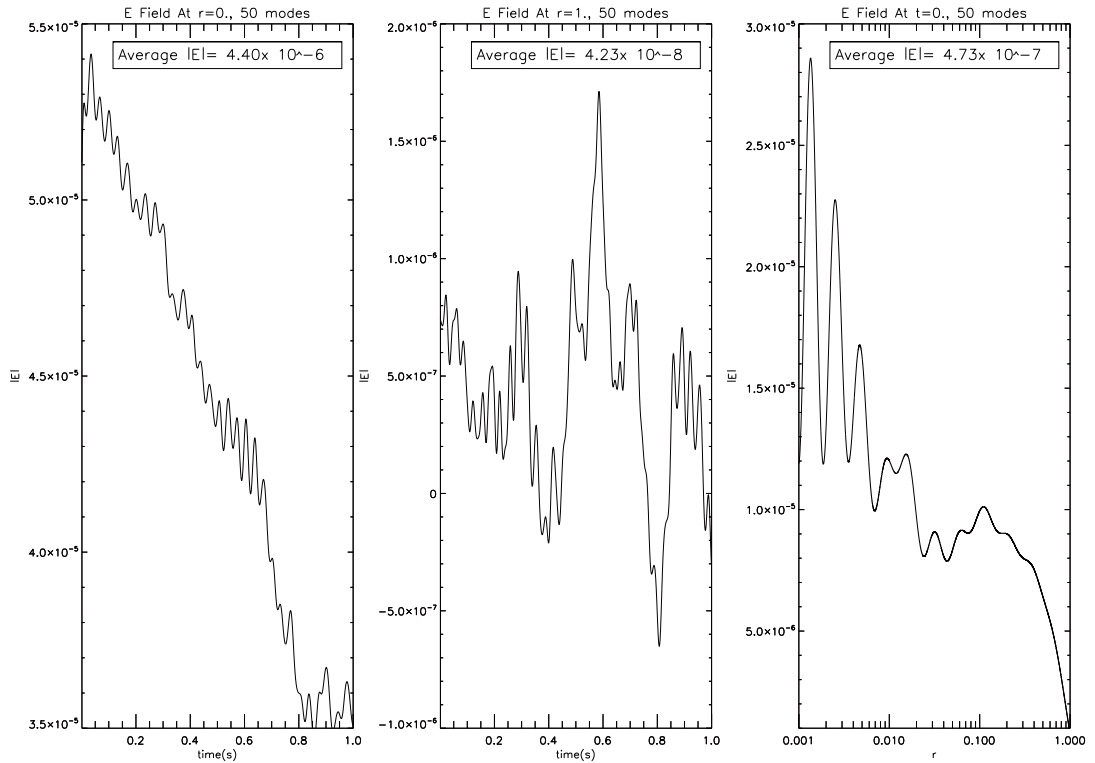


Figure 4.39: Electric field for a spectrum of modes with their amplitude distributed as $k^{-5/3}$. The left hand plot shows the variation of the electric field with time at $r = 0$, the middle plot shows the variation of the electric field with time at $r = 1$, and the right hand plot shows the variation of the electric field with r at $t = 0$.

modes, this creates an average electric field at $r = 0$ of $\approx 1.8V/m$. For the $k^{-5/3}$ spectrum, the average electric field at $r = 0$ is $\approx 10V/m$. The average electric field strength in a solar flare is $\approx 1000V/m$ (Somov, Oreshina, and Kovalenko (2008), in which the electric field strength is calculated from the motion of the flare ribbons). It can be seen that whilst the flat spectrum of modes accelerates particles to higher energies, the $-5/3$ spectrum produces a more realistic looking high energy tail of protons (more similar to observed proton energy distributions, see e.g. Van Hollebeke, Ma Sung, and McDonald (1975), in which data from 185 solar flare events was analysed).

In order to understand why the protons are accelerated to such high energies for the flat spectrum of modes, the behaviour of a sample of ten protons was studied in more detail. These protons were selected randomly. The evolution of the particle's distance from the null with time, and the variation of the particle's energy with distance from the null are both plotted, and can be seen in figure 4.43. It can be seen that for the flat spectrum of modes, particles gain most energy at $r < 1$. Some particles remain trapped at small r ($r \approx 0.1$). The majority of particles (around 6000) leave the system (that is, they move to distances in x or y that are greater than $178d_p$, or distances in z that are greater than $17.8d_p$), and their

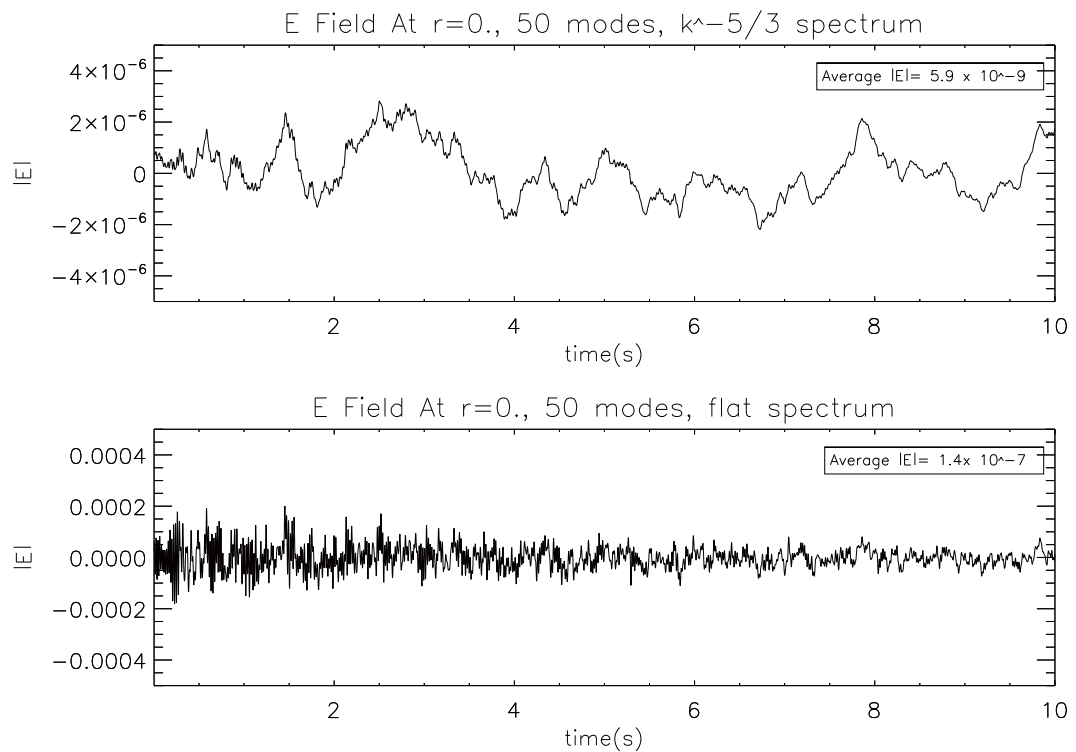


Figure 4.40: Electric field variation with time at $r=0$. The top plot shows the field for a spectrum of modes with their amplitude distributed as $k^{-5/3}$. The bottom plot shows the field for a flat spectrum of modes.

energies are not plotted in figure 4.42. For the $k^{-5/3}$ distribution, particles move steadily to larger r as the simulation progresses, and gain energy at a variety of values of r . The final position of protons at $t = 1$ is shown in figure 4.44. This figure clearly shows that for the flat spectrum of modes, a lot of particles leave the system. For the $k^{-5/3}$ distribution, particles remain within the system.

Finally, the final positions of protons in the flat spectrum case were plotted on a logarithmic scale. The results of this can be seen in figure 4.45, which shows that the protons clearly split into two populations. One population stays close to the null, and moves a large distance in z . The other moves a large distance in the x - y plane. It can be seen that the particles which gain a lot of energy (plotted in red) either stay close to the null or are ejected to very large distances. Recall that for a flat spectrum of modes there are large oscillations in the electric field at small r (see figure 3.2). These oscillations are much larger than those that the $k^{-5/3}$ spectrum gives at small r , hence the flat spectrum energises particles much more if the protons are at small values of r .

The expected energy gain of a particle can be calculated if we recall that kinetic energy in SI units is

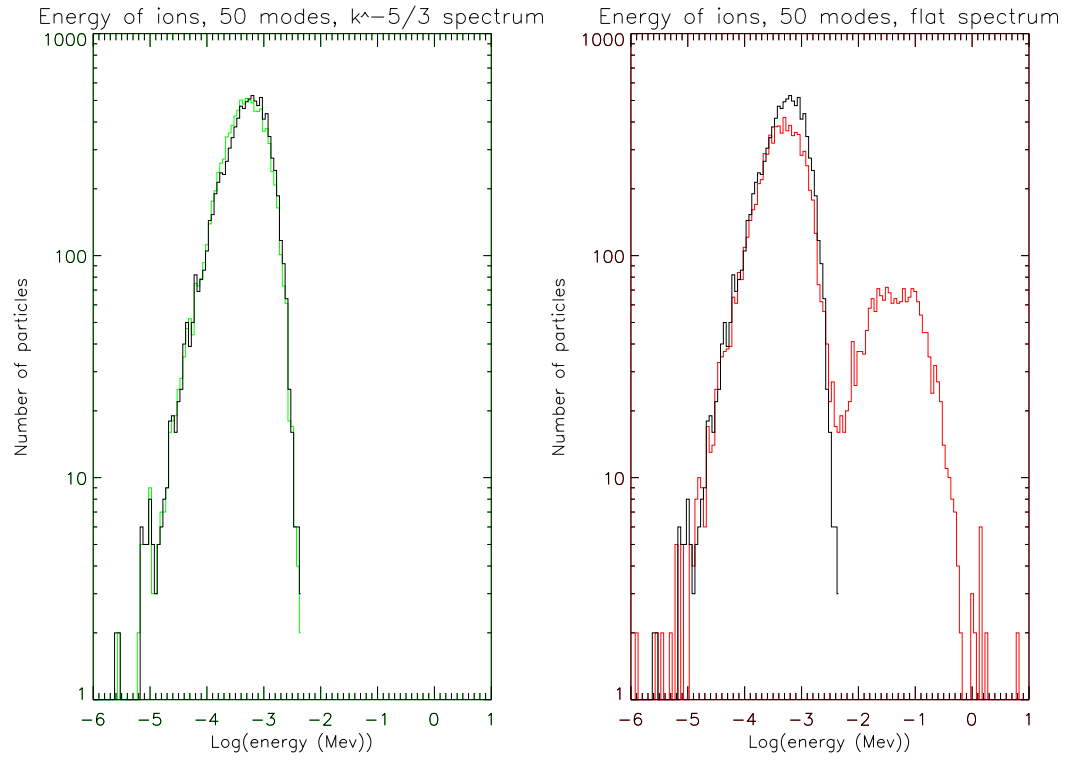


Figure 4.41: Energy of 10 000 protons at $t = 1s$. The right hand plot shows protons which have been accelerated in fields composed of a flat spectrum of eigenmode oscillations. The left hand plot shows protons which have been accelerated in fields composed of a spectrum of modes with their amplitude distributed as $k^{-5/3}$. For both plots, $a_0 = 0.0001$

$$E_k = \frac{1}{2} m \mathbf{v}^2, \quad (4.18)$$

which means that

$$\frac{dE_k}{dt} = m \mathbf{v} \cdot \frac{d\mathbf{v}}{dt}. \quad (4.19)$$

Since $\mathbf{v} \times \mathbf{B}$ is always perpendicular to \mathbf{v} then

$$m \mathbf{v} \cdot \frac{d\mathbf{v}}{dt} = e \mathbf{v} \cdot \mathbf{E}. \quad (4.20)$$

To convert the energy into eV, drop e (the charge of the particle) from the equation above. Since the code is run for $1s$ the maximum energy gain is

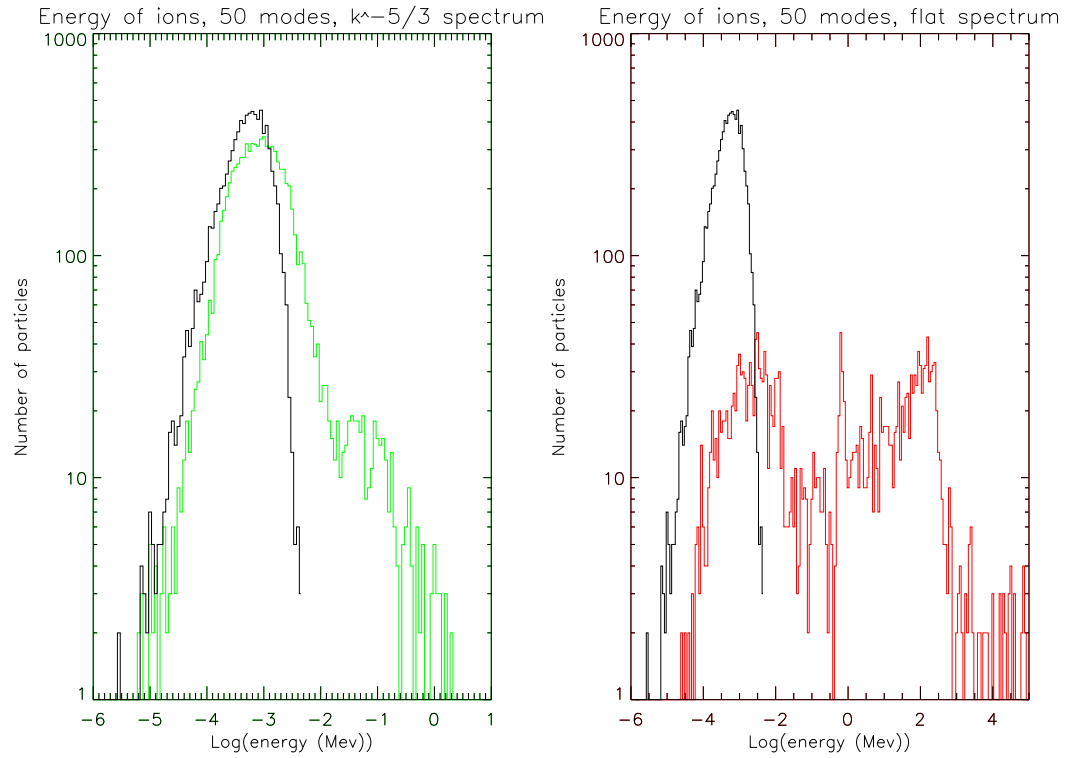


Figure 4.42: Energy of 10 000 protons at $t = 1s$. The right hand plot shows protons which have been accelerated in fields composed of a flat spectrum of eigenmode oscillations. The left hand plot shows protons which have been accelerated in fields composed of a spectrum of modes with their amplitude distributed as $k^{-5/3}$. For both plots, $a_0 = 0.01$

$$cE = 3 \times 10^8 E. \quad (4.21)$$

The maximum electric field anywhere in the system at $t = 0$ is $\approx 10\,000$ V/m for the flat spectrum of modes (this peak field is at $r \approx 0.0001$). This gives a possible energy gain of 2.6×10^6 MeV for protons which encounter these high electric field strengths. By contrast, the peak electric field strength in the system at $t = 0$ for the $k^{-5/3}$ spectrum of modes is ≈ 55 V/m. This gives a possible energy gain of 1.6×10^4 MeV for protons, much lower than the possible energy gain for the flat spectrum of modes. The electric field strength also decays more quickly than for the flat spectrum of modes (over the simulation time), meaning that particles do not experience these peak field strengths for as long.

It should be noted that the energies achieved by particles for the flat spectrum of modes are artificially high, and the distribution in figure 4.42 is oddly shaped. This could be an effect of the fact that I increased the magnitude of the electric field for the flat spectrum (in order to better compare the effects of the flat spectrum and the $k^{-5/3}$ spectrum), meaning that the

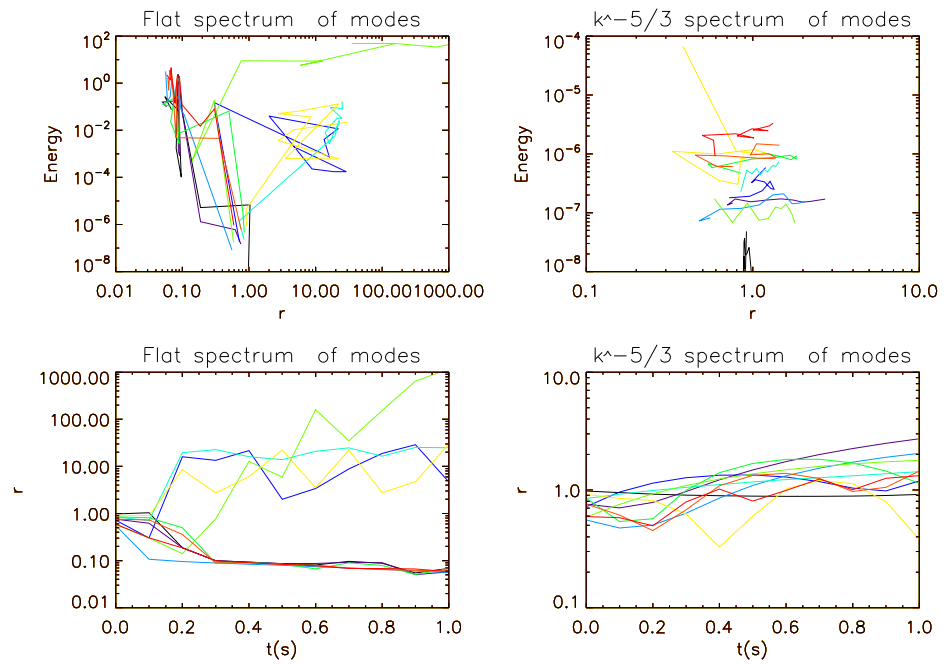


Figure 4.43: Plots of the variation of the proton’s energy with distance from the null, and of the variation of distance from the null with time. The colour of the line identifies a particle with the same initial conditions. For all plots, $a_0 = 0.01$

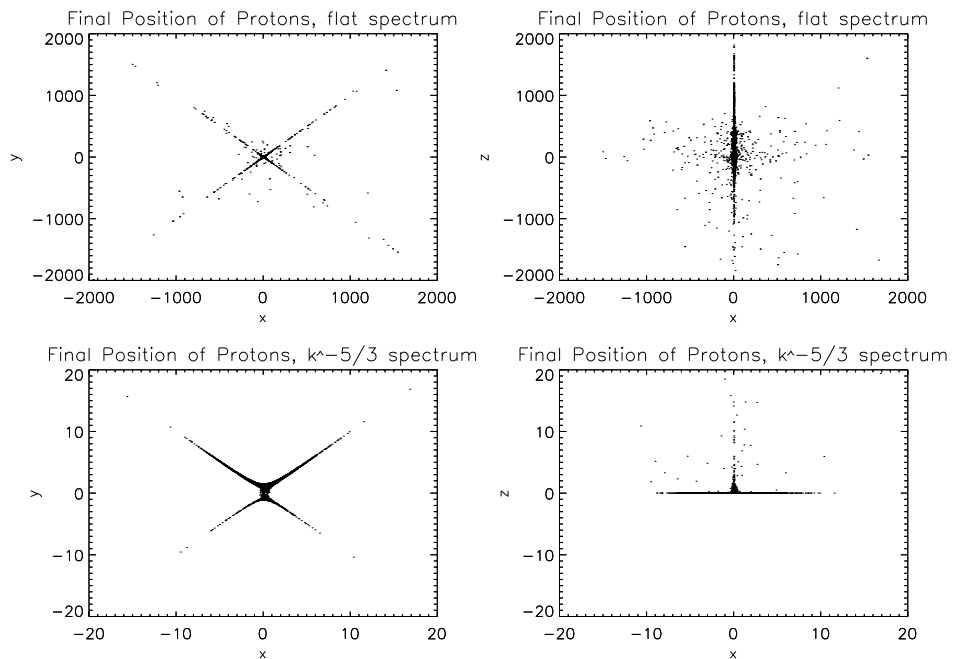


Figure 4.44: Plots of positions of protons at $t = 1s$. For all plots, $a_0 = 0.01$. The left hand panel shows the position of protons in the x-y plane, the right hand panel shows position of protons in the x-z plane.

peak electric field is artificially high (around ten times the typical electric field strength in a solar flare).

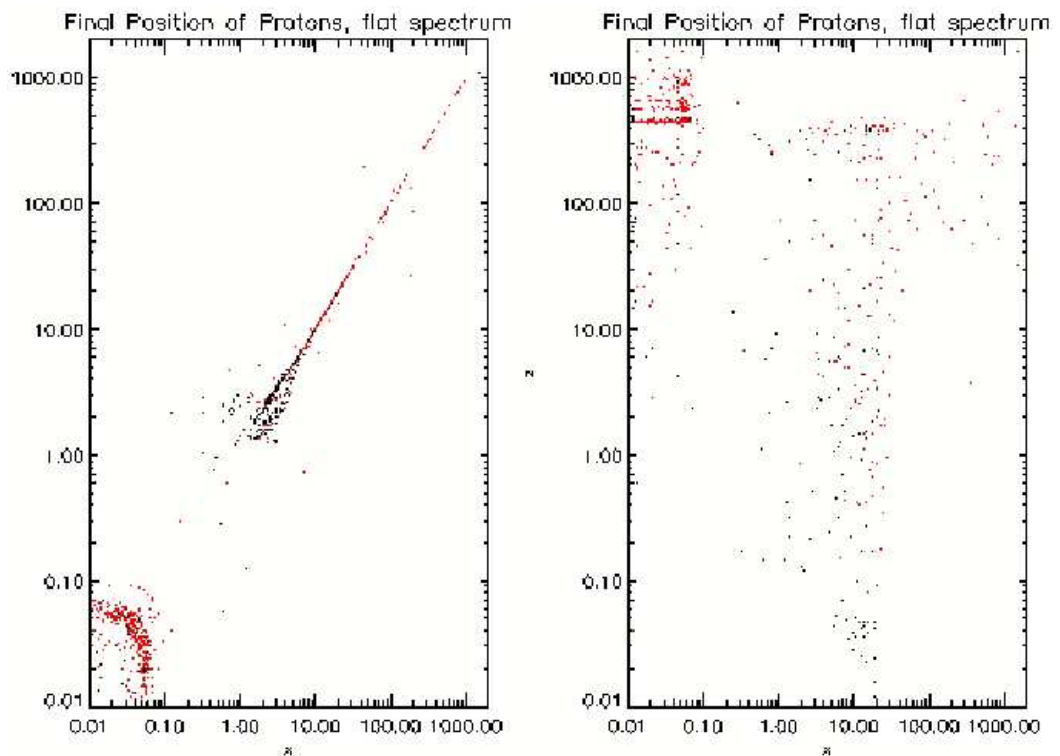


Figure 4.45: Plots of positions of protons at $t = 1s$. Particles that gain more than 100 000 times their original energy are plotted in red. For all plots, $a_0 = 0.01$

In order to test this, the behaviour of particles in an electric field with $a_0 = 1$, and the modes distributed as $k^{-5/3}$ was studied. Here, the average electric field strength at $r = 0$ is $\approx 1000V/m$, a typical electric field strength for a solar flare. The peak field strength anywhere in the system is $\approx 5000 V/m$ at $t = 0$.

Figure 4.46 shows the resulting energy distributions at $t = 1s$ for protons accelerated in such fields. Protons which travelled further than $178d_p$ in the x or y direction, or further than $17.8d_p$ in the z direction were discarded, as they had left the simulation region. This meant that around a quarter of the protons studied were discarded. It can be seen that some protons gain energies well in excess of 1000 GeV. Even very high energy solar flares do not produce protons with such high energies (e.g Wang and Wang (2006)). My previous calculations showed that the highest energy that particles will achieve is anticipated to be around 100 MeV. This is for particles in an electric field of 10 000 V/m, for our values of the initial energy. I therefore conclude that the magnetic field configuration is having a large effect on the ability of particles to become highly energised.

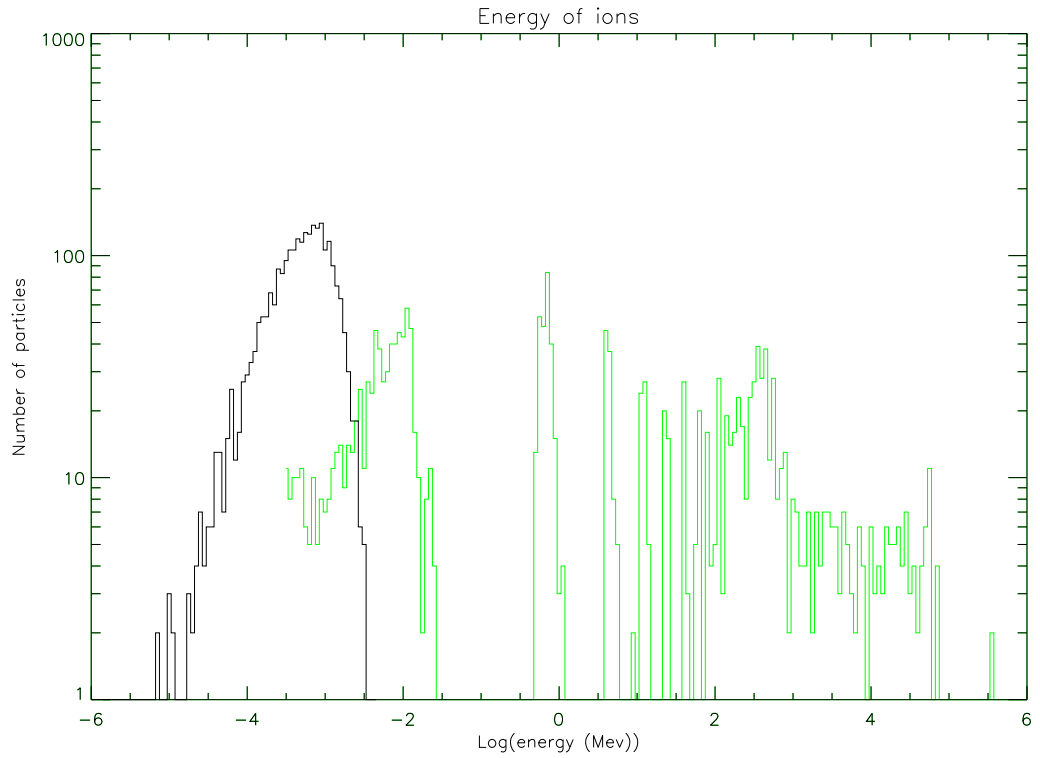


Figure 4.46: Energies of protons at $t = 1s$. Protons were accelerated in fields composed of a superposition of 50 modes distributed with amplitudes $a_n = a_0 k^{-5/3}$, where $a_0 = 1$ and k is the wavenumber of the mode.

4.6 Effect of Varying Resistivity

In the above simulations, I have used the value $\eta = 3.124 \times 10^{-11}$ for the dimensionless resistivity. It has been seen (in section 3.3.1) that varying the resistivity causes the size of the non-adiabatic region to vary. How does varying the resistivity affect particles in the case of a superposition of 50 modes? Here, I return to a flat spectrum of modes, with $a_0 = 0.0001$. I will investigate particle behaviour for two values of resistivity, $\eta = 3.124 \times 10^{-10}$ and $\eta = 3.124 \times 10^{-12}$. Recall that the collisional resistivity for this plasma is 2.2×10^{-13} . The resulting values of κ (decay) and ω (oscillation) can be seen in tables 4.4 and 4.5.

Particle Behaviour

Let us now examine the consequences for particle behaviour in fields constructed using these modes and resistivities. The energy distribution of 1000 protons at $t = 1s$ for different values of resistivity can be seen in figure 4.47. It can be seen that particles are accelerated to higher energies for lower values of resistivity.

n	κ	ω	Decay Time (s)	Period (s)
0	0.007231	0.117742	633.36	244.44
1	0.040132	0.623374	114.12	46.17
2	0.056878	0.880324	80.52	32.69
3	0.066333	1.138055	69.05	25.29
4	0.094551	1.396227	48.44	20.61
5	0.123517	1.915506	37.08	15.03
10	0.209239	3.487320	21.89	8.25
15	0.318289	5.099938	14.39	5.64
20	0.437758	6.728753	10.46	4.28
25	0.587363	8.373390	7.80	3.44
30	0.713287	10.03532	6.42	2.87
35	0.869951	11.77654	5.26	2.52
40	1.009341	13.95606	4.54	2.20
45	1.429638	18.77579	3.20	1.53
49	2.000738	16.38633	2.38	1.76

Table 4.4: A selection of values of ω and κ for $\eta = 3.1724 \times 10^{-10}$. The decay and oscillation times for these values of ω and κ are also listed.

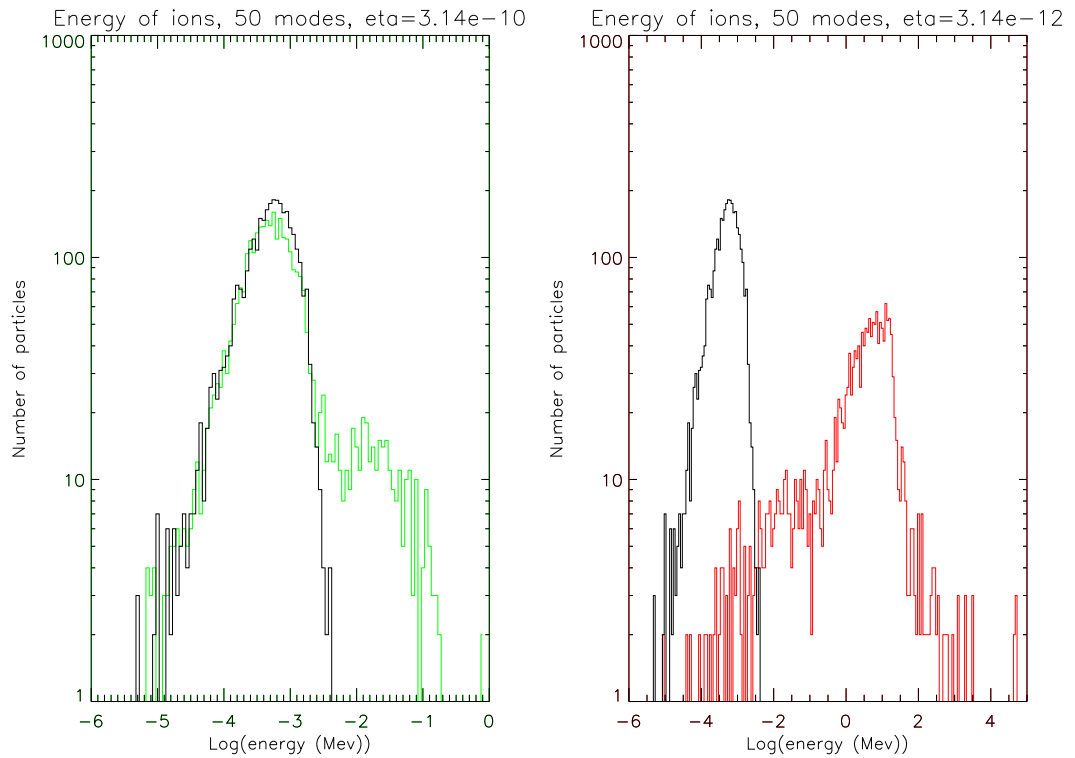


Figure 4.47: Energy of 1000 protons at $t=1s$ for a superposition of 50 modes. The spectrum of modes is flat, and $a_0 = 0.0001$. The resistivity, $\eta = 3.1724 \times 10^{-10}$ in the left hand plot, and $\eta = 3.1724 \times 10^{-12}$ in the right hand plot.

Since the values for the eigenmodes κ and ω have changed slightly, the forms of the electric and magnetic fields will also have changed slightly. This will alter the topology of the mag-

n	κ	ω	Decay Time (s)	Period (s)
0	0.007227	0.117752	633.76	244.43
1	0.023451	0.367979	195.30	78.21
2	0.040132	0.623374	114.12	46.17
3	0.056887	0.880318	80.51	32.69
4	0.056878	0.880328	80.52	32.69
5	0.073724	1.137993	62.12	25.29
10	0.161704	2.438449	28.32	11.80
15	0.204973	3.495437	22.34	8.23
20	0.304888	4.561388	15.02	6.31
25	0.384146	5.643078	11.92	5.10
30	0.436674	6.729363	10.49	4.28
35	0.540241	7.826324	8.48	3.68
40	0.619834	8.928312	7.39	3.22
45	0.698822	10.03623	6.55	2.87
49	0.812018	11.15022	5.64	2.58

Table 4.5: A selection of values of ω and κ for $\eta = 3.1724 \times 10^{-12}$. The decay and oscillation times for these values of ω and κ are also listed.

netic field. It is known that the size of the central null changes with η , but what about the many smaller nulls created by the superposition of modes?

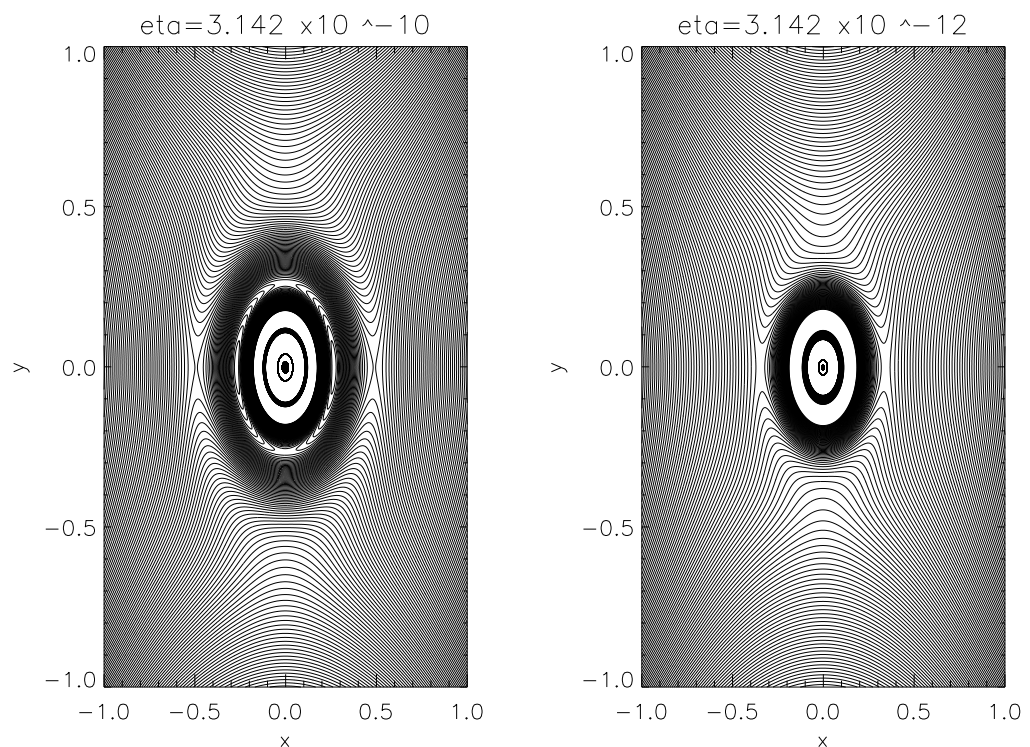


Figure 4.48: Magnetic field contours at $t = 0.5s$. The resistivity, $\eta = 3.1724 \times 10^{-10}$ in the left hand plot, and $\eta = 3.1724 \times 10^{-12}$ in the right hand plot.

The magnetic field topology for two different values of η can be seen in figure 4.48. It can be seen that for smaller η , the form of the small-scale nulls changes slightly. Slightly more small nulls are formed at $r > 0.5$. These could also cause particles to become highly energised. The form of the magnetic field is also changed near the centre of the region; the field becomes less complex when the resistivity is decreased. The variation of the magnitude of the magnetic field with r at $t = 0$ can be seen in figure 4.49. Here, the magnetic field is considered to have fallen to zero if $|B| \leq 0.01$. By this definition three nulls are created for $\eta = 3.1724 \times 10^{-10}$, whilst eight are created for $\eta = 3.1724 \times 10^{-12}$, so that more non-adiabatic regions (sites of particle acceleration) have been created for lower resistivity.

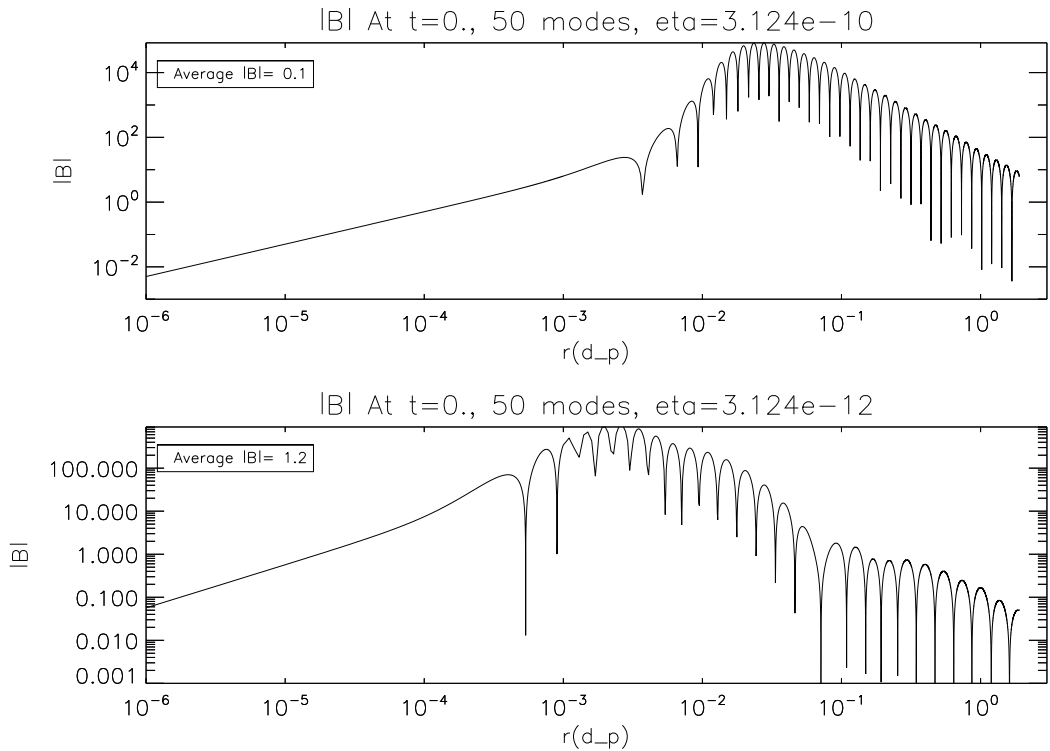


Figure 4.49: Magnetic field variation with distance from the null at $t = 0.s$. The resistivity, $\eta = 3.1724 \times 10^{-10}$ in the top plot, and $\eta = 3.1724 \times 10^{-12}$ in the bottom plot.

Changing the decay time and period of the eigenmode oscillations also causes changes in the electric field. The change in decay time does not affect particles over the time of this simulation, since particles are only followed for 1s, and the decay times of all of the modes (for both values of η) are longer than this. However, decreasing η does make the electric field less noisy, as can be seen in figure 4.50. It can therefore be concluded that it is not the noisier electric field that causes particles to become more highly energised in the comparisons of cases 1 to 5. Rather, it is the creation of further acceleration sites within the magnetic field.

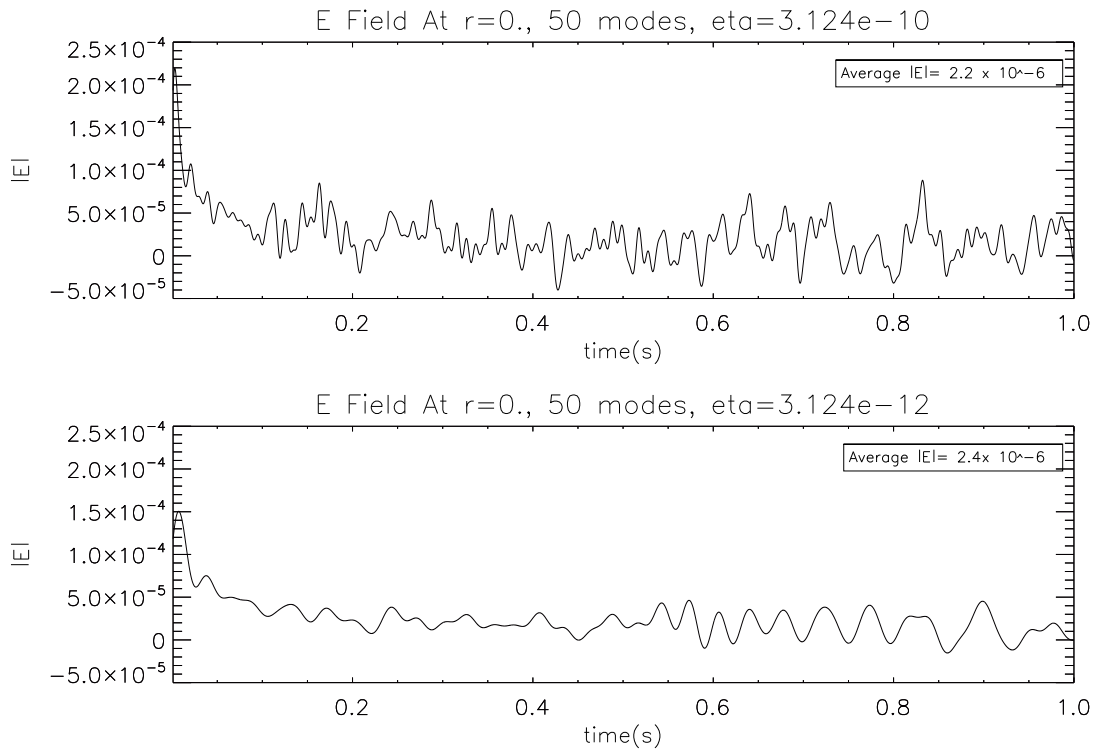


Figure 4.50: Electric field variation with time at $r = 0.s$. The resistivity, $\eta = 3.1724 \times 10^{-10}$ in the top plot, and $\eta = 3.1724 \times 10^{-12}$ in the bottom plot.

4.7 Conclusions

In this chapter, I have investigated the behaviour of protons and electrons in noisy magnetic and electric fields. We have seen that adding more perturbative modes to the fields causes particles to gain higher energies. The reasons for this are twofold: the perturbations change the form of the magnetic field such that more nulls are created, and the particles become trapped. There are therefore more regions where particles can become energised, and particles spend longer in these regions. Since electrons are lighter, they are more affected by perturbations, and so are energised more quickly. The results for protons have been presented in Burge, Petkaki, and MacKinnon (2012). I have also calculated the thin target X-ray bremsstrahlung for the distributions of electron energies at $t = 0.1s$. We have seen that adding more modes produces more realistic X-ray spectra. If the electric and magnetic fields are static, the spectrum produced is composed of thermal emission. When modes are added, we see non-thermal emission being produced.

Other work on test particle simulations of 2D reconnection regions (e.g. Petkaki and MacKinnon (2011)), show identical results for the energy distributions for electrons and protons in the case where there are no perturbations (using the same initial conditions as used in this

thesis). Initially, it was hoped that the use of a spectrum of perturbative modes would significantly enhance acceleration due to resonant-type interactions. This was because Petkaki and MacKinnon (2007) found that certain frequencies preferentially accelerated different parts of an initial proton spectrum, therefore it was proposed that a spectrum of frequencies would accelerate all parts of the distribution. In Petkaki and MacKinnon (2007), certain frequencies produced bimodal distributions of proton energies, similar in character to the energy distribution for case 5 at $t = 1s$. This makes the distribution for case 5 surprising, as these protons were accelerated by fields perturbed by a superposition of 50 modes. It is possible that one of the frequencies used was especially effective at accelerating particles, thus producing a distribution similar in character to those seen for single frequency disturbances. If this is the case, we know that the eigenmode in question must be in the $n = 20$ to $n = 49$ range, since this effect is not seen in any of the other cases.

I also investigated the consequences of using a different distribution of eigenmode oscillations to compose the electric and magnetic fields. The amplitude of the modes was distributed according to a $k^{-5/3}$ spectrum, where k is the wavenumber of the eigenfunction. It was found that such a distribution did not accelerate particles as efficiently as a flat spectrum of modes, probably because the field produced were smaller. However, when the amplitude of the field is sufficiently high, the $k^{-5/3}$ spectrum produces a high energy tail of particles that is more realistic than the energy distribution produced by the flat spectrum of modes. For the flat spectrum of modes, many particles leave the simulation as they travel large distances in the z -direction.

I have also investigated the consequences of changing the value of the inertial resistivity. A decrease in the value of the inertial resistivity meant that the fields were more efficient at accelerating particles. Decreasing resistivity leads to changes in the formation of the small-scale nulls, so that more such nulls are created away from the very centre of the region. Since there are more sites of particle acceleration, particles can become more highly energised.

5. Effect of Collisions on Particle Trajectories

5.1 Introduction

In this chapter I will describe work aimed at including the effects of binary collisions in test particle calculations. I start by recalling Honeycutt's (1992) extension of the RK4 method to stochastic differential equations. I will apply this method to the 1D problem described by MacKinnon and Craig (1991), verifying that it reproduces analytical results for the distribution function, at least as well as simpler numerical methods. The 1D Fokker-Planck (FP) description is only valid when electrons move adiabatically so I will next recast the description of scattering in terms of all three velocity components. As a further check I will confirm that the 3D description applied to the 1D problem reproduces the 1D results. As a first application of this method I will study collisional cross-field scattering of suprathermal electrons. Finally, with confidence in the code established, I will use it to study the modifications to electron acceleration near null points.

5.2 Collisions in the Solar Corona

The test particle calculations carried out in Chapter 4 considered particles in a collisionless plasma. However, it seems obvious that particles in a real plasma will undergo collisions. It is also known that in order for hard X-rays (HXR) to be emitted, particles must undergo collisions. Therefore, in order to account for coronal HXR sources (e.g. Masuda *et al.* (1994b)), collisions must be introduced into the acceleration mechanism. Because protons are heavier than electrons, collisions will have a greater impact on electron trajectories.

Masuda *et al.* (1994b) suggested that a coronal HXR source could be created by a very high temperature plasma at the top of a flaring loop. However, as Fletcher (1995) pointed out, a HXR source created by heating should be seen to increase in size as the plasma expands. The fact that this is not seen would then require some kind of plasma confinement at the

top of the loop (e.g. Fletcher and Martens (1998) found that a magnetic bottle could be formed by the geometry of the current sheet). If instead the loop top source is a result of non-thermal particles that are created by transport effects, no source of thermal emission is required.

Hamilton *et al.* (2003) developed a method of including collisions when following particle trajectories, but their method included only energy change, not collisional scattering. If pitch angle scattering via collisions is taken into account when considering the trajectories of particles at an X-type neutral point, it is hoped that particles will return to the non-adiabatic region more frequently, leading to particles attaining higher energies. In this chapter, I will address scattering due to binary collisions, a process whose statistical character is well understood.

The inclusion of collisions means that the random forces which these collisions generate must be modelled. This is done by describing the particle's motion using stochastic differential equations, which are easier to solve computationally. Stochasticity can be modelled by the inclusion of a Gaussian random noise process in the system of differential equations. This can be done by using a Wiener process (a continuous-time stochastic process) of the required mean and variance to calculate a new value of the Gaussian noise component each time it is required. Then the envelope of the particle trajectories is governed by a Fokker-Planck (FP) equation (e.g. Gardiner 1983).

The general form of a FP equation with $n + 1$ independent variables $(t, x_1, x_2, \dots, x_n)$ is given by

$$\frac{df}{dt} + A \frac{df}{dx} + \frac{D}{2} \frac{d^2 f}{dx^2} = 0, \quad (5.1)$$

where f is the distribution function being considered. According to Gardiner (1985), a FP equation can be written as a stochastic differential equation of the form

$$d\mathbf{x} = \mathbf{A}(\mathbf{x}, t)dt + \mathbf{D}(\mathbf{x}, t)^{1/2}d\mathbf{W}(t). \quad (5.2)$$

The first term of (5.2) is a slowing down term. The second term will be evaluated by using a stochastic RK4. \mathbf{x} is the vector (x_1, x_2, \dots, x_n) , $\mathbf{W}(t)$ is an n -variable Wiener process, \mathbf{D} gives the amplitude of the scattering term.

In 1D, the non-relativistic FP equation is (see e.g. MacKinnon and Craig (1991))

$$\frac{\partial f}{\partial t} + \mu v \frac{\partial f}{\partial z} - C \frac{\partial}{\partial v} \left(\frac{f}{v^2} \right) - \frac{C}{v^3} \frac{\partial}{\partial \mu} \left((1 - \mu^2) \frac{\partial f}{\partial \mu} \right) = 0, \quad (5.3)$$

f is the distribution function of the electrons, $C = 4\pi e^4 \Lambda n / m_e^2$, where Λ is the Coulomb logarithm, usually taken to be 25 in the solar corona. μ is the cosine of the pitch angle of the particle, and z is the distance that the particle has travelled along the magnetic field line. This equation is valid for the case where the gyroradius is very small and particles are tied to field lines. Under these circumstances, the motion of an electron can be described using just its pitch angle and velocity. In a cold medium, the electrons slow down deterministically. Later, this will be generalised this to a 3D description, where the evolution of v_x , v_y and v_z will be followed.

MacKinnon and Craig (1991) examined how a FP equation could be replaced by a set of stochastic differential equations which can be integrated numerically using Euler integration. However, in order to integrate particle trajectories in oscillating electric and magnetic fields, a more accurate method of numerical integration was chosen, a stochastic fourth-order Runge-Kutta (RK4) method. The stochastic RK4 method has the major benefit of reducing to the deterministic RK4 methods used in the previous chapter in the absence of noise.

5.3 Stochastic Integration Methods

5.3.1 Deterministic RK4

In the original Runge-Kutta method (Press *et al.* (1992)):

$$x(\Delta t) = x_0 + \frac{\Delta t}{6} \left(k_1 + 2k_2 + 2k_3 + k_4 \right), \quad (5.4)$$

where x is the variable being considered, (which in this case is v_x , v_y or v_z), Δt is the timestep being used, and

$$k_1 = \Delta t f(t_0, x_0)$$

$$k_2 = \Delta t f\left(t_0 + \frac{\Delta t}{2}, x_0 + \frac{k_1}{2}\right)$$

$$k_3 = \Delta t f\left(t_0 + \frac{\Delta t}{2}, x_0 + \frac{k_2}{2}\right)$$

$$k_4 = \Delta t f\left(t_0 + \frac{\Delta t}{2}, x_0 + \frac{k_3}{2}\right).$$

At $t = 0$, $t = t_0$, x_0 is the value of the solution (x) at $t = t_0$ and f is the function being considered. Equation 5.4 provides a numerical estimate of x at $t = \Delta t$. This gives a solution of the equation being considered with an associated error of the order of Δt^5 .

5.3.2 Stochastic RK4

Honeycutt (1992) considered the one-variable additive noise equation

$$dx = f(x)dt + \mathbf{D}d\mathbf{W}(t). \quad (5.5)$$

$\mathbf{W}(t)$ is a Wiener process which scales as $(\Delta t)^{1/2}$. If this is integrated from 0 to Δt , and the Taylor expansion of f is taken, an expression for $x(\Delta t)$ is obtained which includes a stochastic term, $R(\Delta t)$. The full form of $R(\Delta t)$ is very lengthy, and can be seen in Honeycutt (1992). The stochastic RK4 that is developed must have the same statistical properties as $x(\Delta t)$ for the deterministic part, and $R(\Delta t)$ for the stochastic part. In order to develop a stochastic integrator, Honeycutt (1992) considered the equation

$$\frac{dx}{dt} = F(x). \quad (5.6)$$

The algorithm for integrating this via second order Runge-Kutta integration is

$$x(\Delta t) = x_0 + \frac{\Delta t}{2}(F_1 + F_2), \quad (5.7)$$

where

$$F_1 = f(x_0)$$

$$F_2 = f(x_0 + \Delta t F_1).$$

However, this algorithm cannot be used to integrate equation 5.5 directly, due to the presence of a stochastic term. Instead, let $F(x) = f(x)$ and introduce the stochasticity as part of the integration algorithm.

$$x(\Delta t) = x_0 + \frac{\Delta t}{2}(F_1 + F_2) + (2\mathbf{D}\Delta t)^{\frac{1}{2}}\psi \quad (5.8)$$

ψ is a random number with $\langle \psi \rangle = 0$ and $\langle \psi^2 \rangle = 1$. \mathbf{D} is the amplitude of the stochastic term. For purely mathematical problems the amplitude of this can be varied arbitrarily. For physical problems, care must be taken to select an appropriate value of \mathbf{D} (e.g. via comparison with the FP equation governing the distribution). This can then be extended to a fourth-order Runge-Kutta via comparison with the usual deterministic RK4 method found in Press *et al.* (1992):

$$x(\Delta t) = x_0 + \frac{\Delta t}{6}(F_1 + 2F_2 + 2F_3 + F_4) + (2D\Delta t)^{\frac{1}{2}}\psi, \quad (5.9)$$

where

$$F_1 = f(x_0)$$

$$F_2 = f(x_0 + \Delta t F_1 + (2D\Delta t)^{\frac{1}{2}}\psi)$$

$$F_3 = f(x_0 + \Delta t F_2 + (2D\Delta t)^{\frac{1}{2}}\psi)$$

$$F_4 = f(x_0 + \Delta t F_3 + (2D\Delta t)^{\frac{1}{2}}\psi)$$

5.4 The Test Problem

In order to develop and test an RK4 algorithm, I will consider a problem which already has a known solution. The problem used was that considered in MacKinnon and Craig (1991), which dealt with pitch-angle scattering of particles in a non-magnetised medium. The FP equation for this problem also has a known analytical solution (for the spatially homogeneous case) which is given in terms of the Legendre polynomials, which acts as a further check for the stochastic RK4 solution. MacKinnon and Craig (1991) developed a stochastic system for

calculating the variation in particle pitch angle that makes use of the Ito form of a stochastic differential equation.

The FP equation can be replaced by a system of stochastic differential equations (s.d.e.s). As shown by MacKinnon and Craig (1991) this general equivalence in this particular case means that μ evolves according to the s.d.e.

$$d\mu = -\frac{2\mu}{v(t)^3}dt + \left[\frac{(1-\mu^2)}{v(t)^3}\right]^{1/2} r(t)dt, \quad (5.10)$$

where $r(t)$ is a Gaussian random noise process. The initial distribution is monoenergetic. Speeds are normalised to the initial speed (v_0), distances are normalised to $(v_0^4 nm_e^2)/(4\pi e^4 \lambda)$ and times are normalised to $(v_0^3 nm_e^2)/(4\pi e^4 \lambda)$, where n is the density of the plasma and λ is the Coulomb logarithm. It should be noted here that v is also evolving with time; the particles are slowing down monotonically. This can be integrated using the Euler method or by using stochastic RK4 with a noise term

$$D = \left[\frac{(1-\mu^2)}{v^3}\right]. \quad (5.11)$$

Here, D is chosen by directly comparing equations (5.9) and (5.10). This means that in the FORTRAN code for the stochastic RK4 method, when integrating an s.d.e, all of the r.h.s. of equation 5.10 is not evaluated. Instead, only the first term of the r.h.s is integrated, and the second (stochastic term) is included as part of the integrator itself. I carried out a comparison of the 2 methods. A particular example is shown in figure 5.1, at $t = 0.06$ (the stopping time for these particles is $t = 1/3$). This shows that all three solutions are in close agreement. Similarly good agreement is found for later times. This apparently simple process, of adding a Wiener noise term to each of the RK4 iterates, is justified in detail by Honeycutt (1992).

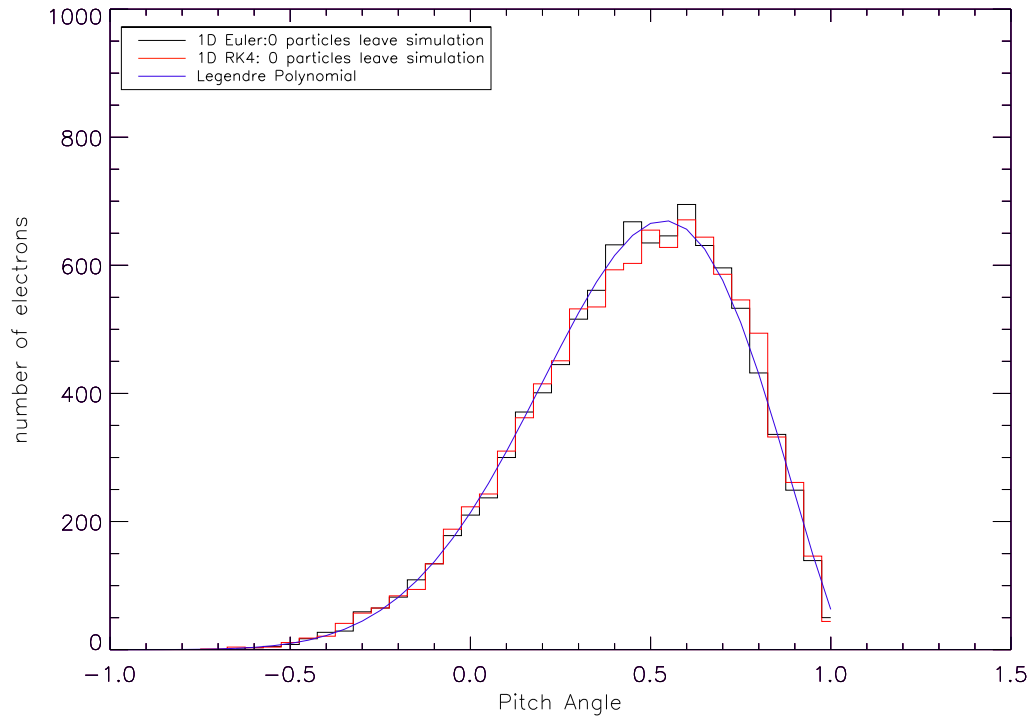


Figure 5.1: Comparison of stochastic RK4, Euler integration, and the exact solution evaluated using Legendre polynomials, $t=0.06$.

5.5 3D Description of Particle Motion

5.5.1 Equations of Motion

MacKinnon and Craig (1991) is applicable if particles are tied tightly to field lines and do not drift across the field. If particles are no longer tied tightly to field lines, e.g. near a null, a more general 3D description is needed. In order to make the test problem more generally applicable, I will now consider how to re-cast it in the form of a set of o.d.e.s such as those given in equations (4.3). I want to introduce collisional scattering by extending (4.3) to include stochastic terms. It should be noted that this solution is merely a generalisation of that given in MacKinnon and Craig (1991). Such a generalisation should be made in order to follow the evolution of the particles in v_x , v_y and v_z . Once this is known, the behaviour of particles in the presence of electric and magnetic fields can also be considered. In the first instance I am considering a problem in which no electric or magnetic fields are present. Equations (4.3) are therefore rewritten as

$$\frac{dx}{dt} = v_x \quad (5.12a)$$

$$\frac{dy}{dt} = v_y \quad (5.12b)$$

$$\frac{dz}{dt} = v_z \quad (5.12c)$$

$$dp_x = -A(\mathbf{x}, t)_x dt + (\mathbf{D}^{1/2} d\mathbf{W})_x \quad (5.12d)$$

$$dp_y = -A(\mathbf{x}, t)_y dt + (\mathbf{D}^{1/2} d\mathbf{W})_y \quad (5.12e)$$

$$dp_z = -A(\mathbf{x}, t)_z dt + (\mathbf{D}^{1/2} d\mathbf{W})_z. \quad (5.12f)$$

The drift $\mathbf{A}(\mathbf{x}, t)$ and diffusion terms \mathbf{D} will now be determined by exploring how the distribution function of the particles evolves, and using this information to develop drift and diffusion terms for the behaviour of a single particle. I will do this by drawing on the known velocity diffusion coefficients in a FP description (Trubnikov (1965)) and the equivalence between FP and s.d.e. descriptions. Once the coefficients of the first- and second-order terms in the FP equation are known, \mathbf{A} and \mathbf{D} immediately follow.

According to Trubnikov (1965), the effect of collisions ($\mathbf{C}^{\alpha/\beta}$, where $\mathbf{C}^{\alpha/\beta}$ is the sum of the drift $\mathbf{A}(\mathbf{x}, t)$ and diffusion terms \mathbf{D}) on a particle, α , moving through a medium of particles of type β is given by

$$\mathbf{C}^{\alpha/\beta} = (-\nabla_v \mathbf{j}^{\alpha/\beta}), \quad (5.13)$$

where

$$\mathbf{j}^{\alpha/\beta} = \frac{1}{m_\alpha} F_i^{\alpha/\beta} f_\alpha - D_{ik}^{\alpha/\beta} \nabla_k f_\alpha. \quad (5.14)$$

The first term on the r.h.s is the slowing down term. The second term on the r.h.s is the scattering term. When equation 5.14 is inserted into equation 5.13, the first term on the r.h.s of equation 5.14 turns out to be analagous to the first term on the r.h.s. of equation 5.2. Similarly, the second term on the r.h.s of equation 5.14 turns out to be analagous to the second term on the r.h.s. of equation 5.2. The subscript $i = (x, y, z)$, as does the subscript k and f_α is the distribution function of particles of type α and

$$F_i^{\alpha/\beta} = \frac{m_\alpha^2}{m_\beta} \frac{\partial}{\partial v_k} D_{ik}^{\alpha/\beta} \quad (5.15)$$

$$D_{ik}^{\alpha/\beta} = K^{\alpha/\beta} \frac{v^2 \delta_{ik} - v_i v_k}{v^3}. \quad (5.16)$$

$$K^{\alpha/\beta} = \frac{\lambda n_\beta}{4\pi} \left(\frac{4\pi e_\alpha e_\beta}{m_\alpha} \right)^2,$$

Here λ is the Coulomb logarithm, which is usually taken to be 25 in the solar corona, and n_β is the number density of β particles, which is 10^9 cm^{-3} in a typical flare loop (Aschwanden and Benz (1997)). It should be noted that the velocity of the field particles is taken to be zero, since in this case the behaviour of a particle with a velocity much greater than the thermal velocity is being studied.

I want to obtain an expression for the slowing-down term ($\mathbf{A}(\mathbf{x}, t)$), so equation 5.15 must be rewritten. To evaluate $\frac{\partial}{\partial v_k} D_{ik}^{\alpha/\beta}$ must be rewritten as

$$\frac{\partial}{\partial v_k} D_{ik}^{\alpha/\beta} = K^{\alpha/\beta} \left(\frac{\partial}{\partial v_x} \left(\frac{v^2 \delta_{ix} - v_i v_x}{v^3} \right) + \frac{\partial}{\partial v_y} \left(\frac{v^2 \delta_{iy} - v_i v_y}{v^3} \right) + \frac{\partial}{\partial v_z} \left(\frac{v^2 \delta_{iz} - v_i v_z}{v^3} \right) \right). \quad (5.17)$$

One can then write the first term of the R.H.S as:

$$\frac{\partial}{\partial v_x} \left(\frac{v^2 \delta_{ix} - v_i v_x}{v^3} \right) = \frac{\partial}{\partial v_x} \left(\frac{v^2 \delta_{xx} - v_x^2}{v^3} + \frac{v^2 \delta_{yx} - v_y v_x}{v^3} + \frac{v^2 \delta_{zx} - v_z v_x}{v^3} \right),$$

which equals

$$\frac{\partial}{\partial v_x} \left(\frac{v^2 \delta_{xx} - v_x^2}{v^3} + \frac{v^2 \delta_{yx} - v_y v_x}{v^3} + \frac{v^2 \delta_{zx} - v_z v_x}{v^3} \right) = \frac{\partial}{\partial v_x} \left(\frac{v^2 - v_x^2 - v_y v_x - v_z v_x}{v^3} \right).$$

Evaluating the above, for the first term of (5.17) gives:

$$\frac{\partial}{\partial v_x} \left(\frac{v^2 - v_x^2 - v_y v_x - v_z v_x}{v^3} \right) = \frac{1}{v^5} (3v_x^2 (v_x + v_y + v_z) - v^2 (3v_x + v_y + v_z)).$$

And similarly, the second and third terms of (5.17) are

$$\frac{\partial}{\partial v_y} \left(\frac{v^2 - v_y^2 - v_x v_y - v_z v_y}{v^3} \right) = \frac{1}{v^5} (3v_y^2 (v_x + v_y + v_z) - v^2 (v_x + 3v_y + v_z)),$$

$$\frac{\partial}{\partial v_z} \left(\frac{v^2 - v_z^2 - v_x v_z - v_y v_z}{v^3} \right) = \frac{1}{v^5} (3v_z^2 (v_x + v_y + v_z) - v^2 (v_x + v_y + 3v_z)),$$

which gives

$$\frac{\partial}{\partial v_k} D_{ik}^{\alpha/\beta} = K^{\alpha/\beta} \frac{-(v_x + v_y + v_z)}{v^3}.$$

There is also a first-order term which is obtained from the collision term. When this is added in, and recalling that the slowing-down term is given by

$$\mathbf{A}(\mathbf{x}, t) = -K^{\alpha/\beta} \frac{m_\alpha}{m_\beta} \frac{\partial}{\partial v_k} D_{ik}^{\alpha/\beta}, \quad (5.18)$$

a slowing-down term of the form

$$\mathbf{A}(\mathbf{x}, t) = K^{\alpha/\beta} \left(\frac{m_\alpha}{m_\beta} + 2 \right) \left(-\frac{v_x}{v^3}, -\frac{v_y}{v^3}, -\frac{v_z}{v^3} \right) \quad (5.19)$$

can be obtained. I now wish to sum over interactions with both electrons and protons. The particle α is always an electron. This because ions do not scatter very much collisionally in pitch angle. The particle that it is colliding with (β) can be an electron or a proton. Summing over collisions with electrons and protons gives

$$\mathbf{A}(\mathbf{x}, t) = K^{\alpha/\beta} \left(\frac{m_e}{m_e} + \frac{m_e}{m_p} + 2 \right) \left(-\frac{v_x}{v^3}, -\frac{v_y}{v^3}, -\frac{v_z}{v^3} \right). \quad (5.20)$$

Since protons are so much heavier than electrons ($m_p/m_e = 1836$), the term $\frac{m_e}{m_p}$ can be neglected. This gives a slowing down term

$$\mathbf{A}(\mathbf{x}, t) = -3K^{\alpha/\beta} \left(\frac{v_x}{v^3}, \frac{v_y}{v^3}, \frac{v_z}{v^3} \right). \quad (5.21)$$

Therefore

$$A(\mathbf{x}, t)_x = -3 \frac{K^{\alpha/\beta} v_x}{v^3} \quad (5.22a)$$

$$A(\mathbf{x}, t)_y = -3 \frac{K^{\alpha/\beta} v_y}{v^3} \quad (5.22b)$$

$$A(\mathbf{x}, t)_z = -3 \frac{K^{\alpha/\beta} v_z}{v^3}. \quad (5.22c)$$

A physically correct value of \mathbf{D} must now be determined for this problem. This can be obtained by considering the interaction of a test particle with a field of 'background' particles. According to Trubnikov (1965), the diffusion term can be written as

$$D_{ik}^{\alpha/\beta} = K^{\alpha/\beta} \frac{\partial}{\partial v_i} \left(\frac{v^2 \delta_{ik} - v_i v_k}{v^3} \cdot \frac{\partial f_\alpha}{\partial v_k} \right). \quad (5.23)$$

I therefore need to evaluate

$$\frac{\partial}{\partial v_i} \left(\frac{v^2 \delta_{ik} - v_i v_k}{v^3} \cdot \frac{\partial f_\alpha}{\partial v_k} \right). \quad (5.24)$$

Expanding this gives

$$\frac{\partial}{\partial v_i} \left(\frac{v^2 \delta_{ik} - v_i v_k}{v^3} \cdot \frac{\partial f_\alpha}{\partial v_k} \right) = \frac{\partial}{\partial v_i} \left(\frac{v^2 \delta_{ix} - v_i v_x}{v^3} \cdot \frac{\partial f_\alpha}{\partial v_x} + \frac{v^2 \delta_{iy} - v_i v_y}{v^3} \cdot \frac{\partial f_\alpha}{\partial v_y} + \frac{v^2 \delta_{iz} - v_i v_z}{v^3} \cdot \frac{\partial f_\alpha}{\partial v_z} \right) \quad (5.25)$$

Evaluating the first term

$$\begin{aligned} & \frac{\partial}{\partial v_i} \left(\frac{v^2 \delta_{ix} - v_i v_x}{v^3} \cdot \frac{\partial f_\alpha}{\partial v_x} \right) = \\ & \frac{v^2 - v_x^2}{v^3} \frac{\partial^2 f}{\partial v_x^2} - \frac{3v_x(v^2 - v_x^2)}{v^5} \frac{\partial f}{\partial v_x} \\ & + \frac{v_x}{v^3} \left(\frac{3v_y^2}{v^2} \frac{\partial f}{\partial v_x} - v_y \frac{\partial f}{\partial v_y \partial v_x} - \frac{\partial f}{\partial v_x} \right) \\ & + \frac{v_x}{v^3} \left(\frac{3v_z^2}{v^2} \frac{\partial f}{\partial v_x} - v_z \frac{\partial f}{\partial v_z \partial v_x} - \frac{\partial f}{\partial v_x} \right). \end{aligned}$$

Similarly, the second term of (5.25) equals:

$$\frac{\partial}{\partial v_i} \left(\frac{v^2 \delta_{ix} - v_i v_y}{v^3} \cdot \frac{\partial f_\alpha}{\partial v_y} \right) =$$

$$\begin{aligned}
& \frac{v_y}{v^3} \left(\frac{3v_x^2}{v^2} \frac{\partial f}{\partial v_y} - v_x \frac{\partial f}{\partial v_x \partial v_y} - \frac{\partial f}{\partial v_y} \right) \\
& + \frac{v^2 - v_y^2}{v^3} \frac{\partial^2 f}{\partial v_y^2} - \frac{3v_y(v^2 - v_y^2)}{v^5} \frac{\partial f}{\partial v_y} \\
& + \frac{v_y}{v^3} \left(\frac{3v_z^2}{v^2} \frac{\partial f}{\partial v_y} - v_x \frac{\partial f}{\partial v_z \partial v_y} - \frac{\partial f}{\partial v_y} \right).
\end{aligned}$$

And the third term of (5.25) equals

$$\begin{aligned}
& \frac{\partial}{\partial v_i} \left(\frac{v^2 \delta_{ix} - v_i v_z}{v^3} \cdot \frac{\partial f_\alpha}{\partial v_z} \right) = \\
& \frac{v_z}{v^3} \left(\frac{3v_x^2}{v^2} \frac{\partial f}{\partial v_z} - v_x \frac{\partial f}{\partial v_x \partial v_z} - \frac{\partial f}{\partial v_z} \right) \\
& + \frac{v_z}{v^3} \left(\frac{3v_y^2}{v^2} \frac{\partial f}{\partial v_z} - v_y \frac{\partial f}{\partial v_y \partial v_z} - \frac{\partial f}{\partial v_z} \right) \\
& + \frac{v^2 - v_z^2}{v^3} \frac{\partial^2 f}{\partial v_z^2} - \frac{3v_z(v^2 - v_z^2)}{v^5} \frac{\partial f}{\partial v_z}.
\end{aligned}$$

Bringing the 3 terms together, this can be written as the matrix

$$\mathbf{D} = \frac{1}{v^3} \begin{bmatrix} v_z^2 + v_y^2 & -v_x v_y & -v_x v_z \\ -v_x v_y & v_x^2 + v_z^2 & -v_y v_z \\ -v_x v_z & -v_y v_z & v_x^2 + v_y^2 \end{bmatrix} \quad (5.26)$$

plus a first order term, which will be added into the slowing down term

$$\text{First order part of } D_{ik} = -\frac{2v_x}{v^3} \frac{\partial f}{\partial v_x} - \frac{2v_y}{v^3} \frac{\partial f}{\partial v_y} - \frac{2v_z}{v^3} \frac{\partial f}{\partial v_z}. \quad (5.27)$$

Recall that the stochastic term is given by $((2K^{\alpha/\beta} \mathbf{D})^{1/2} \cdot \mathbf{r})_x dt^{1/2}$, where \mathbf{r} is a vector containing the random numbers by which $\mathbf{D}^{1/2}$ will be multiplied ($\mathbf{r}) dt^{1/2} = d\mathbf{W}$), thus obtaining the noise term in the stochastic RK4 method. I therefore want to know the ‘square root’ of the matrix \mathbf{D} . According to standard theory, every $n \times n$ matrix can be written $\mathbf{V}\mathbf{L}\mathbf{V}^{-1}$. \mathbf{L} is a matrix whose diagonal values are the the eigenvalues of the matrix, and whose other values

are 0. \mathbf{V} is a matrix whose columns are the unit eigenvectors of the original matrix. The matrix $\mathbf{D}^{1/2}$ is therefore constructed as

$$\mathbf{D}^{1/2} = \mathbf{V}\mathbf{E}\mathbf{V}^{-1}, \quad (5.28)$$

where \mathbf{V} is a matrix whose columns are the unit eigenvectors of \mathbf{D} , and \mathbf{V}^{-1} is its inverse. \mathbf{E} is a matrix whose diagonal values are the square roots of the eigenvalues of \mathbf{D} , and whose other values are 0. The eigenvalues λ of a 3×3 matrix \mathbf{M} are calculated as follows.

$$\det(\mathbf{M} - \lambda\mathbf{I}) = 0, \quad (5.29)$$

where \mathbf{I} is the identity matrix and \det indicates the matrix determinant. The eigenvalues, λ of \mathbf{D} were found using Mathematica, and are given by

$$\lambda_1 = \frac{1}{v} \quad (5.30)$$

$$\lambda_2 = \frac{1}{v} \quad (5.31)$$

$$\lambda_3 = 0. \quad (5.32)$$

The corresponding eigenvectors (\mathbf{x}) are found using the relation

$$\mathbf{D}\mathbf{x} = \lambda\mathbf{x}. \quad (5.33)$$

That is, the eigenvector is the vector which, when multiplied by the corresponding eigenvalue, returns an answer which is equal to the product of the original matrix and its eigenvector. The eigenvectors (\mathbf{x}) of \mathbf{D} are

$$x_1 = \begin{bmatrix} \frac{-v_z}{v_x} \\ 0 \\ 1 \end{bmatrix} \quad (5.34)$$

$$x_2 = \begin{bmatrix} \frac{-v_y}{v_x} \\ 1 \\ 0 \end{bmatrix} \quad (5.35)$$

$$x_3 = \begin{bmatrix} \frac{v_x}{v_z} \\ \frac{v_y}{v_z} \\ 1 \end{bmatrix} \quad (5.36)$$

$\mathbf{D}^{1/2}$ can then be calculated, and turns out to be:

$$\mathbf{D}^{1/2} = \frac{1}{v^{5/2}} \begin{bmatrix} v_z^2 + v_y^2 & -v_x v_y & -v_x v_z \\ -v_x v_y & v_x^2 + v_z^2 & -v_y v_z \\ -v_x v_z & -v_y v_z & v_x^2 + v_y^2 \end{bmatrix} \quad (5.37)$$

At energies below the thermal speed, diffusion in particle energy becomes important. However, this is not included here as this approach assumes that particle energies are much greater than the thermal speed.

5.5.2 Different Coordinate Systems

It is sometimes numerically expedient to use polar coordinates in order to study the stochastic behaviour of a particle. For example, it will be seen in Section 5.9.2 that when considering the motion of particles at an X-type neutral point, it is more accurate to use polar coordinates since numerical errors arise when modelling the slowing down of a particle if Cartesian coordinates are used.

If we change variables from v_x, v_y, v_z to v, μ, θ , the Fokker-Planck equation describing a particle undergoing drift and diffusion becomes:

$$F = -\frac{D}{v^2} \frac{\partial f}{\partial v} - \frac{D}{v^3} \left[\frac{\partial}{\partial \mu} \left(\sin^2(\phi) \frac{\partial f}{\partial \mu} \right) + \frac{1}{\sin^2(\phi)} \frac{\partial^2 f}{\partial \theta^2} \right], \quad (5.38)$$

where $D = \frac{n\lambda^4\pi e^4}{m_e^2}$ and $\mu = \cos(\phi)$ (ϕ is the particle's pitch angle and θ is its azimuthal angle). The energy loss and scattering terms can be readily chosen from equation 5.38, and the form of the stochastic differential equations obtained for the motion of an electron can be seen in Section 5.10.

5.6 Relativistic Collisional Scattering

5.6.1 Slowing-Down Term

As has been noted, the above approach is not valid for relativistic particles, that is for particles with energies greater than ≈ 160 keV. Leach and Petrosian (1981) discussed collisions in the relativistic case and found that the energy change due to collisions is given by

$$\frac{dE}{dt} = \frac{4\pi r_0^2 cn\Lambda}{\beta} \quad (5.39)$$

where n is the number density of the plasma and r_0 is the classical electron radius, which is given by $r_0 = e^2/(m_e c^2)$. The factor $\beta = v/c$.

Since, in c.g.s units $E = (\gamma - 1)mc^2$,

$$\frac{d\gamma}{dt} = \frac{4\pi e^4 cn_i \lambda}{m_e v}. \quad (5.40)$$

It is known that

$$\frac{d\beta}{dt} = \frac{1}{\beta\gamma^3} \frac{d\gamma}{dt}, \quad (5.41)$$

and

$$\frac{dv}{d\beta} = c. \quad (5.42)$$

Therefore

$$\frac{dv}{dt} = \frac{d\beta}{dt} \frac{dv}{d\beta} = \frac{c}{\beta\gamma^3} \frac{d\gamma}{dt}, \quad (5.43)$$

which means (substituting from 5.40):

$$\frac{dv}{dt} = \frac{1}{\gamma^3} \frac{4\pi e^4 n \lambda}{m_e^2} \frac{1}{v^2}. \quad (5.44)$$

The non-relativistic slowing-down rate is

$$\frac{dv}{dt} = -\frac{4\pi e^4 n \lambda}{m_e^2} \frac{1}{v^2}. \quad (5.45)$$

It can be seen that the only difference between the above equation and the slowing-down rate given by Leach and Petrosian (1981) is a factor of $1/\gamma^3$. Therefore in order for the equations of motion to be relativistic, a factor of $1/\gamma^3$ must be included in the slowing-down term.

5.6.2 Change in Pitch Angle

According to MacKinnon and Craig (1991), the non-relativistic term giving change in pitch angle is given by

$$\frac{\partial f}{\partial t} = \frac{4\pi e^4 n \lambda}{m_e^2 v^3} \frac{\partial f}{\partial \mu} \left((1 - \mu^2) \frac{\partial f}{\partial \mu} \right). \quad (5.46)$$

Leach and Petrosian (1981) give a relativistic pitch angle term which has the form

$$\frac{\partial f}{\partial t} = \frac{\pi e^4 n \lambda}{m_e^2 v^3} \frac{3 + \gamma}{\gamma^2} \frac{\partial f}{\partial \mu} \left((1 - \mu^2) \frac{\partial f}{\partial \mu} \right). \quad (5.47)$$

It can readily be seen that equation 5.47 is equal to equation 5.46 for $\gamma \approx 1$. Therefore in order to make the scattering term relativistic, the ‘noise strength’ in the stochastic RK4 becomes

$$\mathbf{D} = (K^{\alpha/\beta} \frac{3 + \gamma}{4\gamma^2} \mathbf{B})^{1/2} \cdot \mathbf{r}. \quad (5.48)$$

5.7 Conversion to Numerical Method

Since the stochastic differential equations have now been written out, they must be solved numerically using the stochastic RK4. The scattering terms of (5.12) are therefore taken and used to determine a value of the noise strength, \mathbf{D} .

The stochastic term looks like:

$$D_{ik} = ((2K^{\alpha/\beta}\mathbf{D})^{1/2} \cdot \mathbf{r})_x dt^{1/2}.$$

Recall that for the stochastic RK4

$$x(\Delta t) = x_0 + \frac{\Delta t}{6}(F_1 + 2F_2 + 2F_3 + F_4) + (2D\Delta t)^{\frac{1}{2}}\psi,$$

where ψ is a random variable and the stochastic element of the integrator is contained within the final term. Comparing the previous two equations therefore gives

$$D = (K^{\alpha/\beta}\mathbf{D})^{1/2} \cdot \mathbf{r}. \quad (5.49)$$

This gives a 1 x 3 matrix of values for \mathbf{D} . I will extend the 1D approach of Honeycutt to 3D without further formal development. Inspection of her argument suggests that her 1D description should be straightforwardly extensible to 3D. The algorithm for stochastic RK4 can therefore be written as

$$\begin{aligned} F_1 &= f(x_0 + (2\Delta t)^{1/2}D) \\ F_2 &= f(x_0 + \Delta t F_1 + (2\Delta t)^{1/2}D) \\ F_3 &= f(x_0 + \Delta t F_2 + (2\Delta t)^{1/2}D) \\ F_4 &= f(x_0 + \Delta t F_3 + (2\Delta t)^{1/2}D). \end{aligned} \quad (5.50)$$

5.7.1 Application to Test Problem

In order to test this approach, the Mackinnon & Craig test problem is recast as a system of 6 o.d.e.s, as follows

$$\frac{dx}{dt} = v_x \quad (5.51a)$$

$$\frac{dy}{dt} = v_y \quad (5.51b)$$

$$\frac{dz}{dt} = v_z \quad (5.51c)$$

$$dv_x = -3\frac{\tilde{K}v_x}{v^3}dt + ((\tilde{K}\Delta t\mathbf{D})^{1/2}d\mathbf{W})_x \quad (5.51d)$$

$$dv_y = -3\frac{\tilde{K}v_y}{v^3}dt + ((\tilde{K}\Delta t\mathbf{D})^{1/2}d\mathbf{W})_y \quad (5.51e)$$

$$dv_z = -3\frac{\tilde{K}v_z}{v^3}dt + ((\tilde{K}\Delta t\mathbf{D})^{1/2}d\mathbf{W})_z. \quad (5.51f)$$

K has units cms^{-2} , and is made dimensionless in accordance with the units of MacKinnon and Craig (1991), so that

$$\tilde{K} = \frac{K^{\alpha/\beta}\tau}{v_0^3} = \frac{4\pi e^4\lambda v_0^3 n m_e^2}{m_e^2 4\pi e^4\lambda v_0^3} = 1, \quad (5.52)$$

where τ is the normalising time for this problem. Again, only the first term on the r.h.s of equations 5.51d to 5.51f is evaluated. The second term on the r.h.s. is incorporated directly into the stochastic RK4 as the form of the noise term, \mathbf{D} .

I have recast the differential equations describing particle motion in terms of Cartesian coordinates to allow combination of Lorentz and collisional forces. However it is known that particle speed decreases monotonically, as $1/v^2$. It is also known (from MacKinnon and Craig (1991)) how the distribution of particle pitch angles should evolve with time. The 3D stochastic code should reproduce this behaviour. The cosine of the pitch angle μ must therefore be calculated. This can be done using

$$\mu = \frac{v_z}{v}. \quad (5.53)$$

The resulting distributions for μ can be seen in figure 5.2, which compares the distribution of μ values at $t = 0.18$ as calculated from integrating 5.51 using the stochastic RK4, as calculated exactly using Legendre polynomials, and as calculated by using Euler integration to integrate 5.10. All three solutions agree closely. The slowing down of one electron can be seen in figure 5.3, which compares the change in speed of an electron as calculated by

integrating the set of equations 5.51 using the stochastic RK4 with the speed of an electron as calculated using $v = (1 - 3t)^{1/3}$ (MacKinnon and Craig (1991)).

It is known that v evolves deterministically, but here random quantities are added to the components of \mathbf{v} . I therefore wish to be sure that the particle still slows down monotonically. Speeds are normalised to the initial speed (v_0), distances are normalised to $(v_0^4 n_\beta m_e^2)/(4\pi e^4 \lambda)$ and times are normalised to $(v_0^3 n_\beta m_e^2)/(4\pi e^4 \lambda)$.

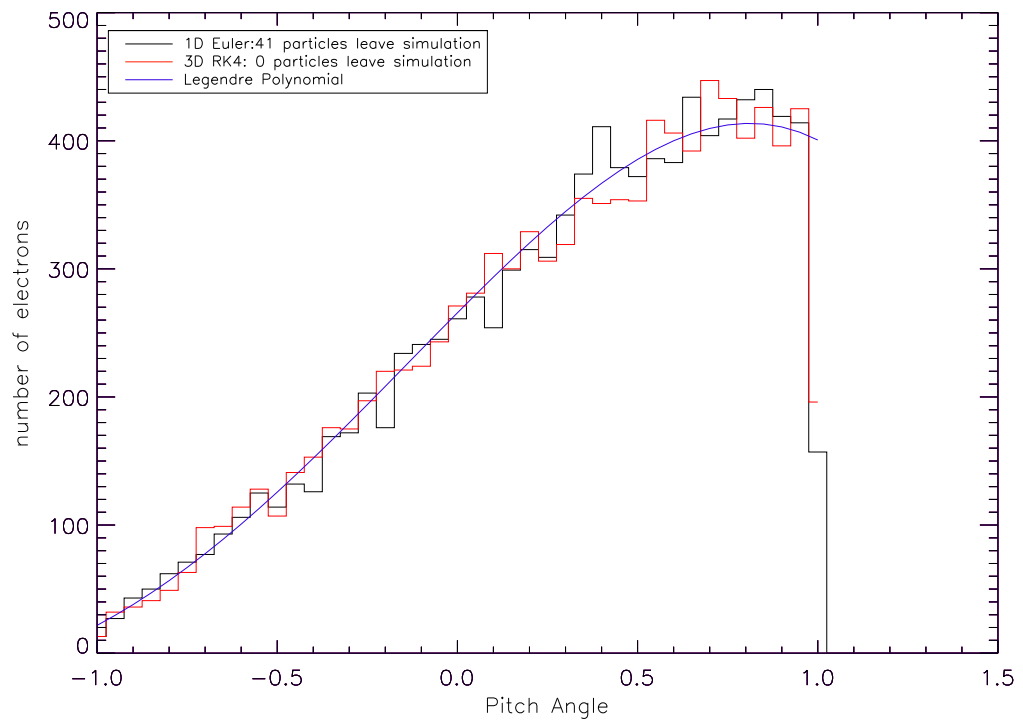


Figure 5.2: Comparison of stochastic RK4 integrating a set of 6 equations to determine the velocity components of the particles, Euler integration of the same solution reduced to one equation, evaluating the pitch angle of the particle only ; and the exact solution evaluated using Legendre polynomials, $t=0.18$. All three solutions agree closely.

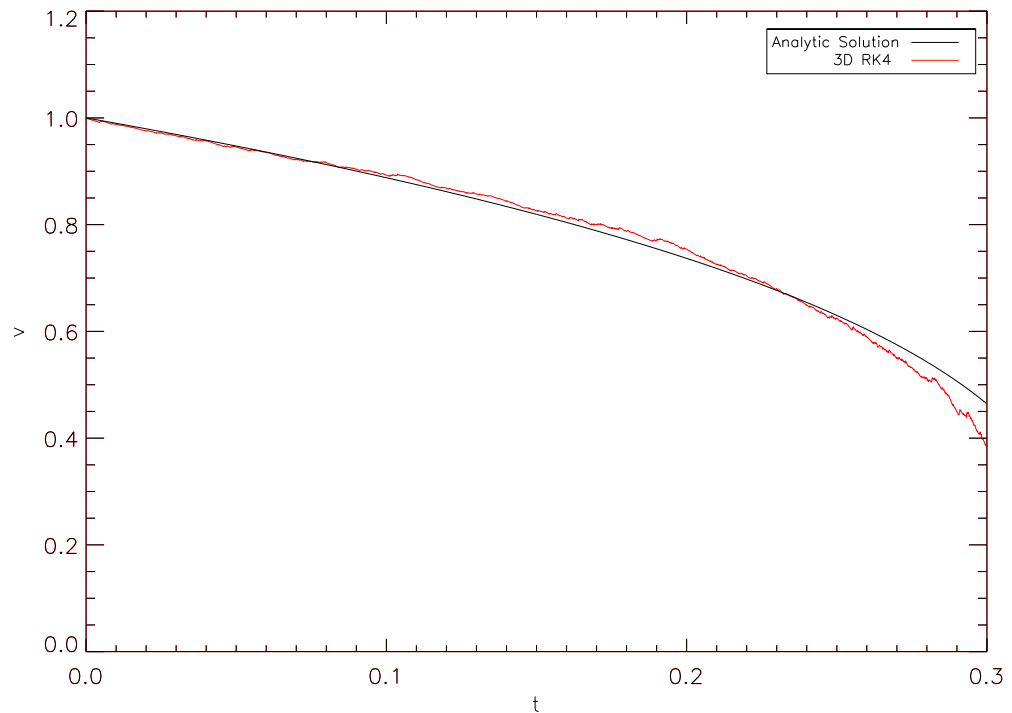


Figure 5.3: Comparison of the calculation of the slowing down of one electron calculated using stochastic RK4 integrating a set of 6 equations and by evaluating the analytic solution of MacKinnon and Craig (1991). The two solutions agree closely for the stepsize shown, which is 0.0001.

The effect of choosing a different stepsize was also investigated. Figure 5.4 shows that the slowing down of an individual particle is very sensitive to the choice of stepsize if the particle is followed using the stochastic RK4 method. It is known (e.g. Press *et al.* (1992)) that the error associated with RK4 is $O(h^5)$, where h is the stepsize being used. When the particle's trajectory is calculated analytically in the manner of MacKinnon and Craig (1991), stepsize is not as important. The analytical and numerical solutions diverge, particularly at higher t because the analytical solution is exact, whereas the numerical solution has an error associated with it. These errors accumulate over the time of the simulation, and so the solutions begin to diverge.

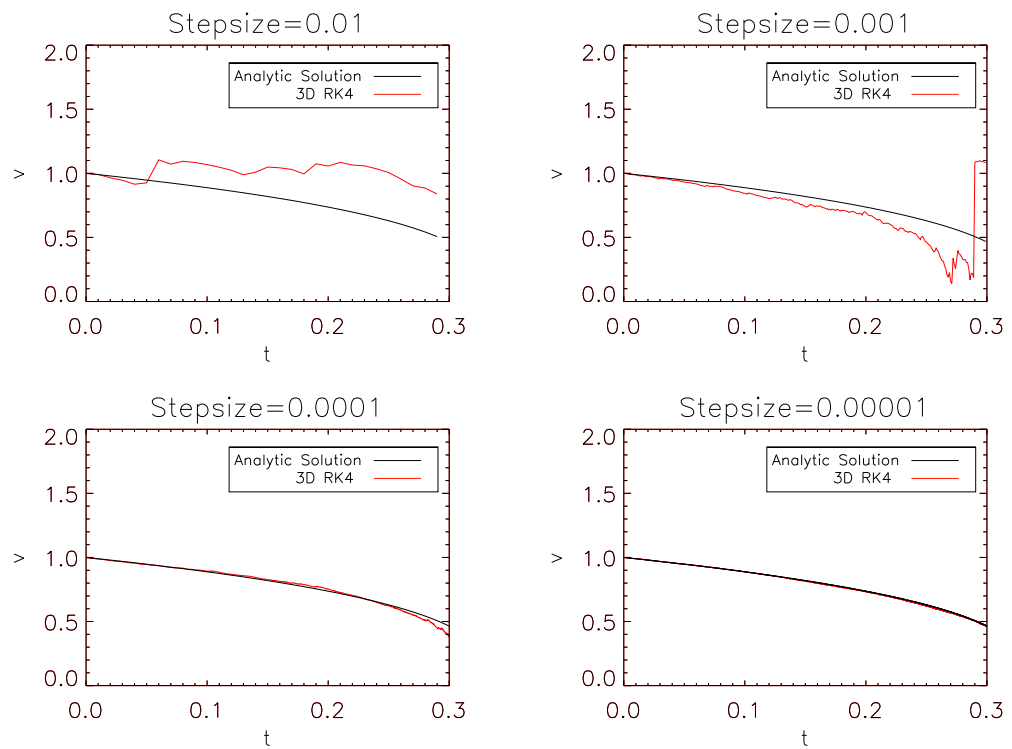


Figure 5.4: Comparison of the calculation of the slowing down of one electron calculated using stochastic RK4 integrating a set of 6 equations and by evaluating the analytic solution of MacKinnon and Craig (1991). The two solutions agree more closely as the stepsize is decreased.

Although the choice of stepsize has a significant effect on the slowing down of an individual particle, it does not greatly affect the overall distribution of the particles' pitch angles. The distribution of particle pitch angles at $t = 0.3$ for stepsizes 0.01 (figure 5.5), 0.001 (figure 5.6), 0.0001 (figure 5.7) and 0.00001 (figure 5.8) can be seen below.

It can be seen that decreasing the stepsize does not have a great effect on the overall distribution when the pitch angles are evaluated using velocity components that are calculated using RK4. In fact, the effect of stepsize is much greater on the distribution where the pitch angle was calculated directly using Euler integration as in MacKinnon and Craig (1991). Using a smaller stepsize meant that fewer particles left the simulation (i.e. fewer particles attained non-physical pitch angles), and the solution was closer to that given by the Legendre polynomial solution and the RK4 solution.

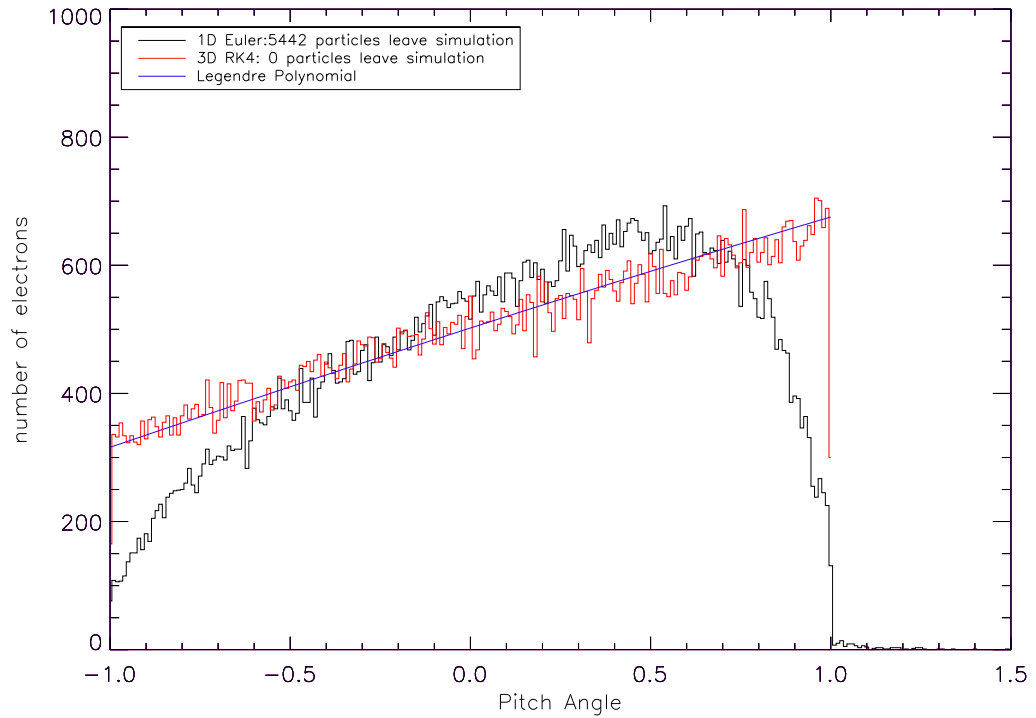


Figure 5.5: Comparison of stochastic RK4 integrating a set of 6 equations to determine the velocity components of 100 000 particles, Euler integration of the same solution reduced to one equation, evaluating the pitch angle of the particle only ; and the exact solution evaluated using Legendre polynomials, $t=0.3$. The stepsize used was 0.01 for both numerical integration methods.

5.8 Cross-Field Scattering

It is well known that particles can diffuse across field lines in magnetised plasmas (e.g. Galloway, Helander, and MacKinnon (2006)). In order for cross-field diffusion to happen, there must be some kind of stochastic process involved. If the field lines themselves are tangled or subject to stochastic fluctuations (e.g. Rechester and Rosenbluth (1978)), particles can diffuse across the field. Tangled field lines have been observed by the TRACE (transition region and coronal explorer) satellite; an example of such tangled field lines can be seen in figure 5.9.

Particle collisions can give rise to diffusion across the magnetic field. It was therefore thought that the stochastic RK4 method could be used to simulate cross-field scattering. In order to test this, a simulation was constructed which considered a single electron starting with velocity in the x direction only, moving through a magnetic field $B_x = 1G, B_y = B_z = 0$, with no electric field present.

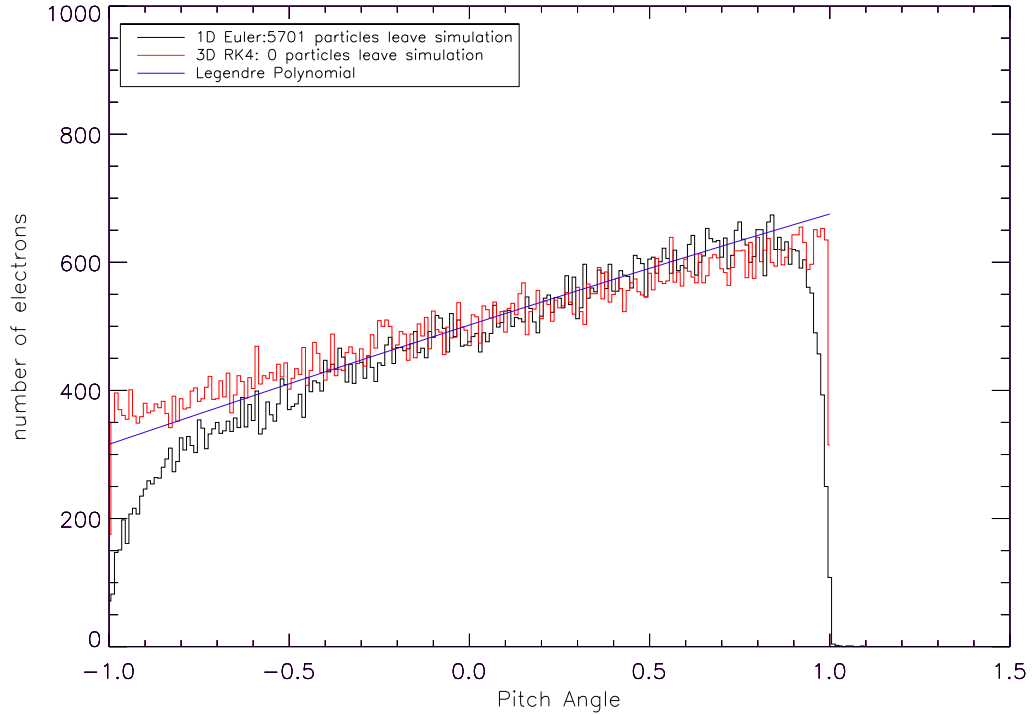


Figure 5.6: Comparison of stochastic RK4 integrating a set of 6 equations to determine the velocity components of 100 000 particles, Euler integration of the same solution reduced to one equation, evaluating the pitch angle of the particle only ; and the exact solution evaluated using Legendre polynomials, $t=0.3$. The stepsize used was 0.001 for both numerical integration methods.

5.8.1 Equations of Motion

The equations of motion of a test particle in electric and magnetic fields are given in (4.3). When the slowing down terms given in (5.51) are introduced, (4.3) is re-written for electrons moving in a fully ionised hydrogen plasma. Recall that collisional scattering is introduced by integrating these equations using the stochastic RK4. For equations (5.55a) to (5.55c), no noise is added. For equations (5.55d) to (5.55f), the noise term given in equation (5.49) is used. For this simulation times are normalised to the electron gyroperiod, speeds to the initial speed of the particle, and mass to the electron rest mass. The non-relativistic electron gyrofrequency is given by (in c.g.s units):

$$\omega_{ce} = eB/m_e c = 1.76 \times 10^7 \text{Brad/s} \quad (5.54)$$

Therefore when $B = 1G$, the electron gyroperiod is $3.57 \times 10^{-7} s$. Using the above set of normalisations, and adding the magnetic field term, (5.51) is written as:

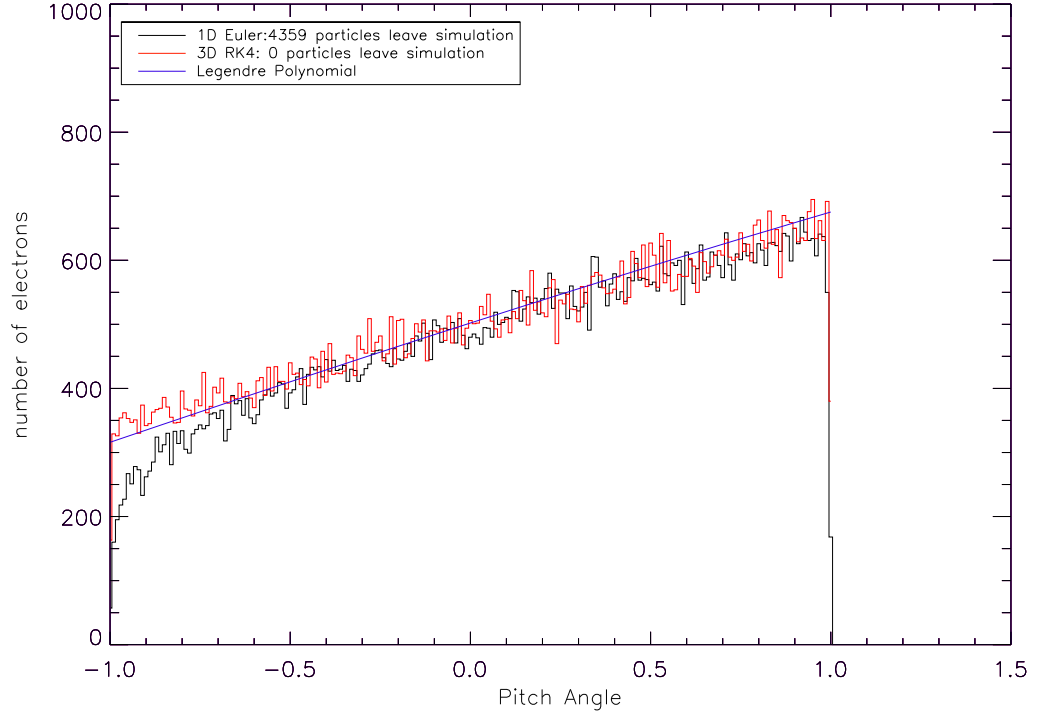


Figure 5.7: Comparison of stochastic RK4 integrating a set of 6 equations to determine the velocity components of 100 000 particles, Euler integration of the same solution reduced to one equation, evaluating the pitch angle of the particle only ; and the exact solution evaluated using Legendre polynomials, $t=0.3$. The stepsize used was 0.0001 for both numerical integration methods.

$$\frac{dx}{dt} = v_x \quad (5.55a)$$

$$\frac{dy}{dt} = v_y \quad (5.55b)$$

$$\frac{dz}{dt} = v_z \quad (5.55c)$$

$$m_e \frac{dv_x}{dt} = -3 \frac{\tilde{K} v_x}{v^3} + ((\tilde{K} \Delta t \mathbf{D})^{1/2} \mathbf{W})_x \quad (5.55d)$$

$$m_e \frac{dv_y}{dt} = -2\pi B_x v_z - 3 \frac{\tilde{K} v_y}{v^3} + ((\tilde{K} \Delta t \mathbf{D})^{1/2} \mathbf{W})_y \quad (5.55e)$$

$$m_e \frac{dv_z}{dt} = 2\pi B_x v_y - 3 \frac{\tilde{K} v_z}{v^3} + ((\tilde{K} \Delta t \mathbf{D})^{1/2} \mathbf{W})_z \quad (5.55f)$$

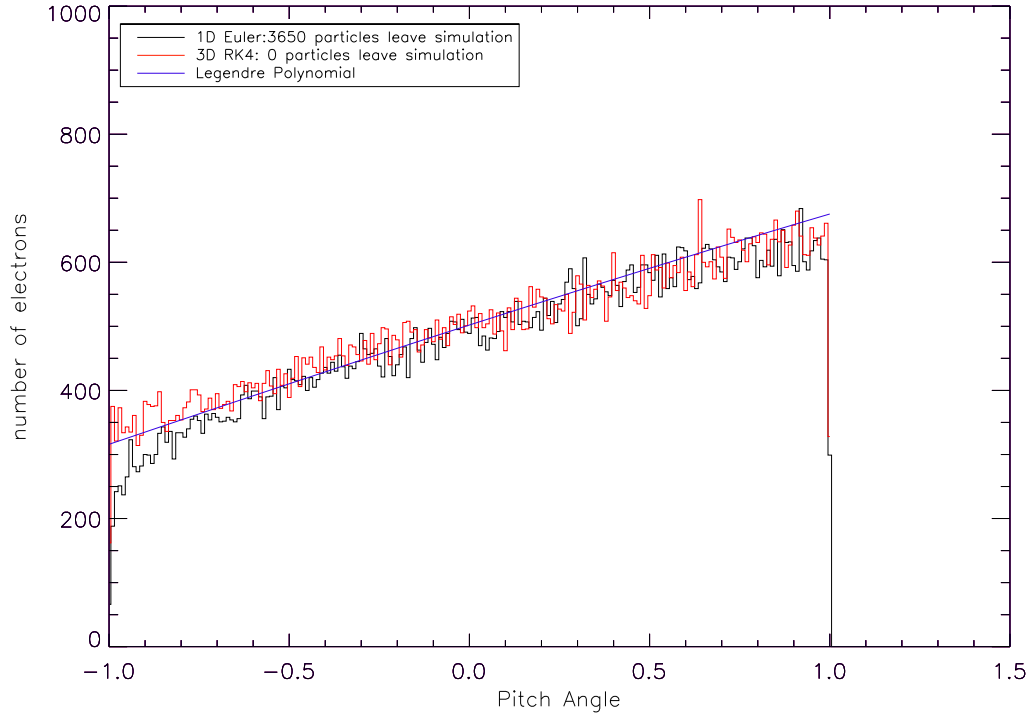


Figure 5.8: Comparison of stochastic RK4 integrating a set of 6 equations to determine the velocity components of 100 000 particles, Euler integration of the same solution reduced to one equation, evaluating the pitch angle of the particle only ; and the exact solution evaluated using Legendre polynomials, $t=0.3$. The stepsize used was 0.00001 for both numerical integration methods.

Here, the factor $K^{\alpha/\beta}$ is made dimensionless, so that

$$\tilde{K} = \frac{AK^{\alpha/\beta}\tau}{v_0}. \quad (5.56)$$

The normalising time is τ (in this case, the particle gyroperiod), and v_0 is the normalising speed (in this case, the initial speed, $0.1c$). A factor A was introduced, which is the ratio of the gyroperiod and the collision time. This was used to scale the slowing down and scattering terms. This can be considered to be analogous to altering the density of the plasma that the particle is moving through, which of course leads to changes in the slowing down rate and scattering frequency of the particles.

All electrons are started at position $x = y = 0$. They are also given the same velocities, $0.06c$ in the x direction, $0.06c$ in the y direction and $0.05c$ in the z direction. The ‘push’ in the y direction causes the particle to gyrate around the magnetic field in the absence of collisional scattering. Particles were followed until $t = 12.4$, which is the stopping time for



Figure 5.9: Tangled magnetic field lines in the solar corona as observed by TRACE (Galloway, Helander, and MacKinnon (2006)). The far left panel shows an example of regular, ordered coronal loops. The middle and right hand panels show more tangled, disordered loops. Galloway, Helander, and MacKinnon (2006) proposed a relationship between the random walk of scattered particles and diffusion across the field lines as a result of this macroscopic tangling.

electrons if $A = 1$. The monotonic slowing down of one electron can be seen in figure 5.10. The slowing down of the particle is smooth, and monotonic, as expected.

Figure 5.11 shows how an electron's trajectory is altered from simple gyromotion for increasing values of \tilde{K} , i.e. when more collisional scattering and slowing down is added. As the size of A (and therefore \tilde{K}) is increased, the particle's trajectory begins to change from simple gyromotion. When $A = 1$, the particle's trajectory is substantially altered, due to change in direction and increased deceleration, the particle does not travel as far in the x direction.

Figure 5.12 shows the y position of 10 000 electrons every half a gyroperiod in the cases $A=0$, 0.01, 0.1 and 1. All electrons began the simulation at $x = y = 0$. For low values of A , (i.e. for less pitch angle scattering), the peak of the distribution depends mostly on the electron position as it spirals around the field. At smaller A , particles cluster around distinct points at each half-gyroperiod. With increasing A , particles spread out in the y -direction as time increases, so that their positions are not primarily determined by gyromotion. Histograms were plotted at $t = 0, 0.5\tau, 1.\tau, 1.5\tau \dots 12\tau, 12.5\tau$, where τ is one gyroperiod. Each histogram is plotted in a different colour. Colours closer to black represent earlier times, colours closer

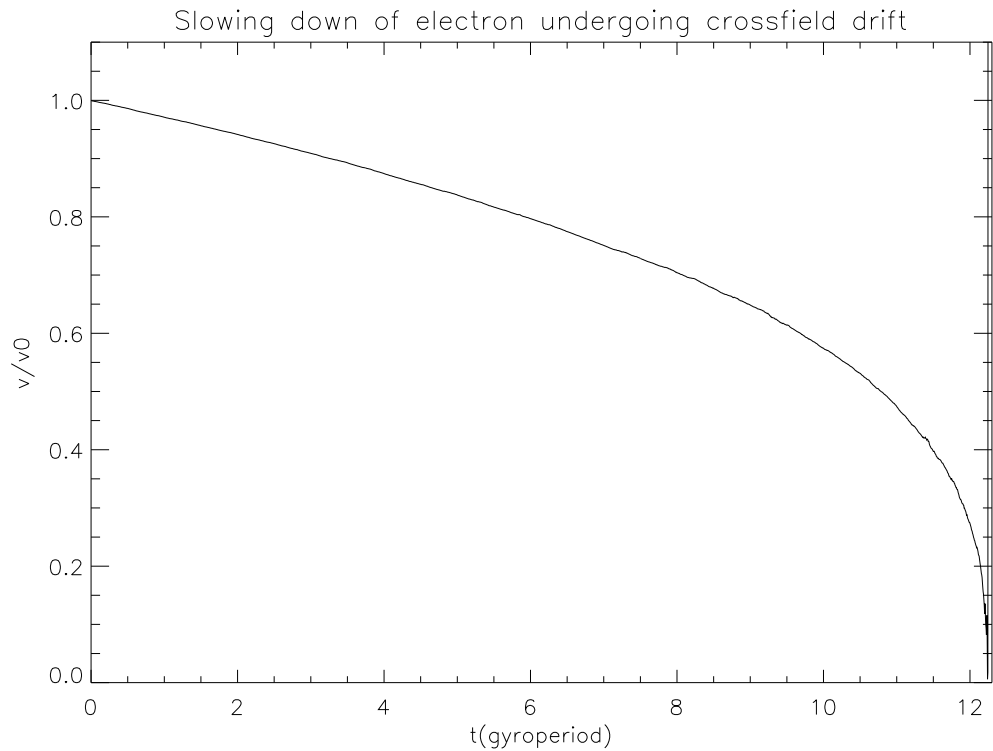


Figure 5.10: Slowing down of one electron in the case $A = 1$. There is no electric field, and the magnetic field is 1G in the x direction only

to red represent later times. A total of 24 histograms were plotted for each value of A , one for each half-gyroperiod.

It can be seen that the peak of each distribution deviates more and more from its expected position as the simulation progresses. The position of the peak of the distribution is plotted for successive gyroperiods in figure 5.13, which shows that the displacement of the peak of the distribution varies linearly with time. For the initial conditions $A = 1$, $B = B_x = 1G$, $v_0=0.1c$ and $n = 1. \times 10^{14}cm^{-3}$ (this high density was chosen to give a short slowing-down time, which could be quickly simulated), the electrons drift across the field at the rate of $\approx 2 \times 10^7 cms^{-1}$.

Figure 5.14 shows the average displacement of the distribution in z . As in figure 5.13, the displacement of the peak varies linearly with time, at approximately the same rate as the displacement in y .

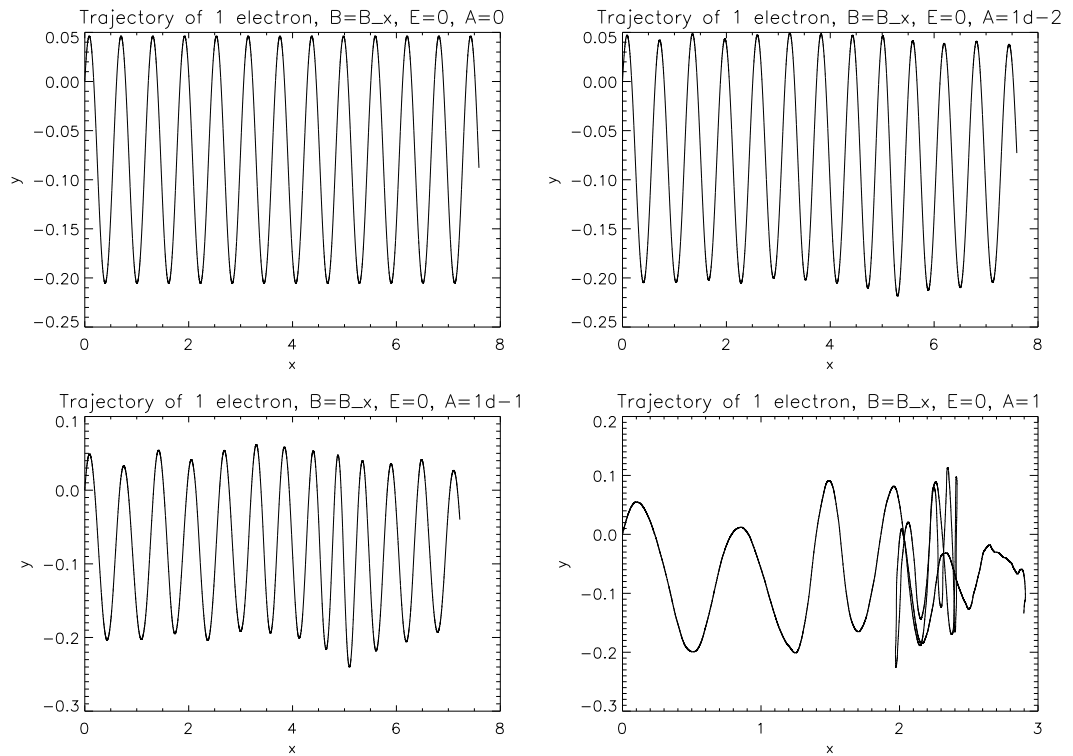


Figure 5.11: Electron trajectory in the cases $A=0, 10^{-2}, 10^{-1}$ and 1. There is no electric field, and the magnetic field is 1G in the x direction only

5.8.2 Perpendicular Diffusion Coefficient

It should now be possible to construct a coefficient to describe the diffusion of the particles across the magnetic field. It is known that the perpendicular diffusion coefficient (D_{\perp}) in a thermal plasma is (Helander and Sigmar (2002))

$$D_{\perp} \approx \frac{\rho^2}{\tau}, \quad (5.57)$$

where ρ is the particle's gyroradius and τ is its collision time. This expression is normally given for thermal particles; I assume it can be extended to nonthermal particles. The gyroradius is given by

$$\rho = \frac{v(1 - \mu^2)^{1/2}}{eB/mc}, \quad (5.58)$$

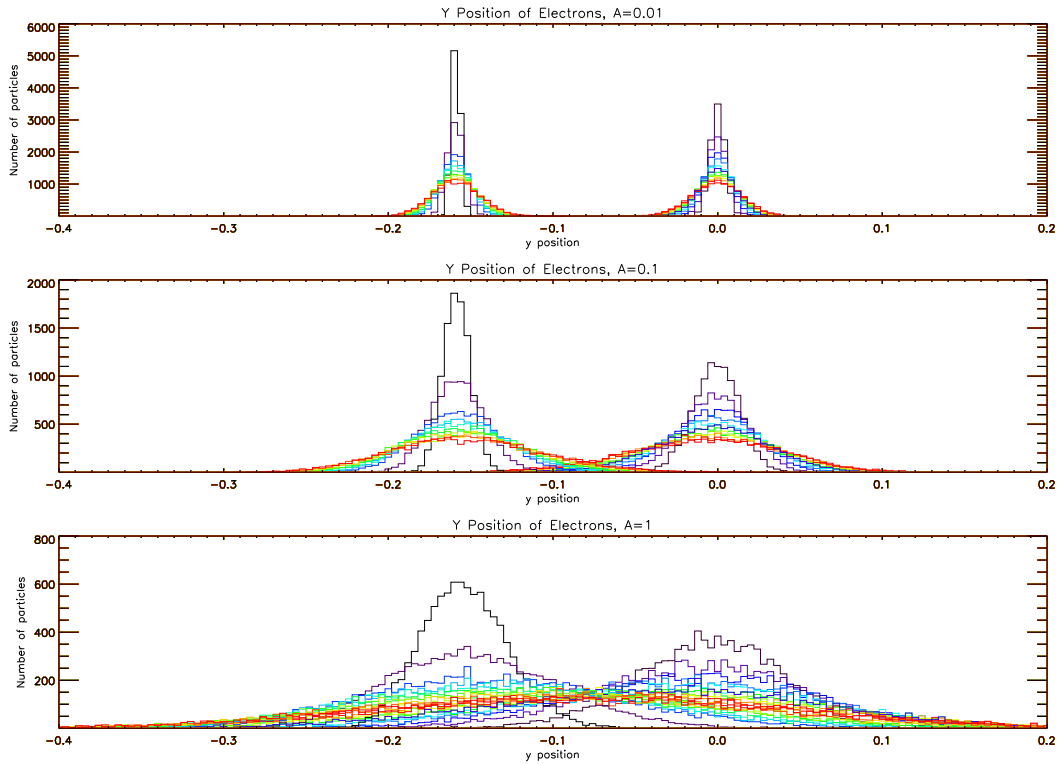


Figure 5.12: Distribution of y position at every half a gyroperiod for different amplitudes of slowing down and scattering terms, i.e. histograms were plotted at $t = 0, 0.5\tau, 1\tau, 1.5\tau \dots 12\tau, 12.5\tau$, where τ is one gyroperiod. Each histogram is plotted in a different colour. Colours closer to black represent earlier times, colours closer to red represent later times.

where μ is the cosine of the particle's pitch angle. τ is taken to be equal to the energy loss time, which is the same as the collisional scattering time for suprathermal electrons. Therefore

$$\tau = \frac{v}{|dv/dt|} \quad (5.59)$$

and since

$$\frac{dv}{dt} = -\frac{4\pi e^4 \Lambda n_e}{m_e^2} \frac{1}{v^2}, \quad (5.60)$$

this gives

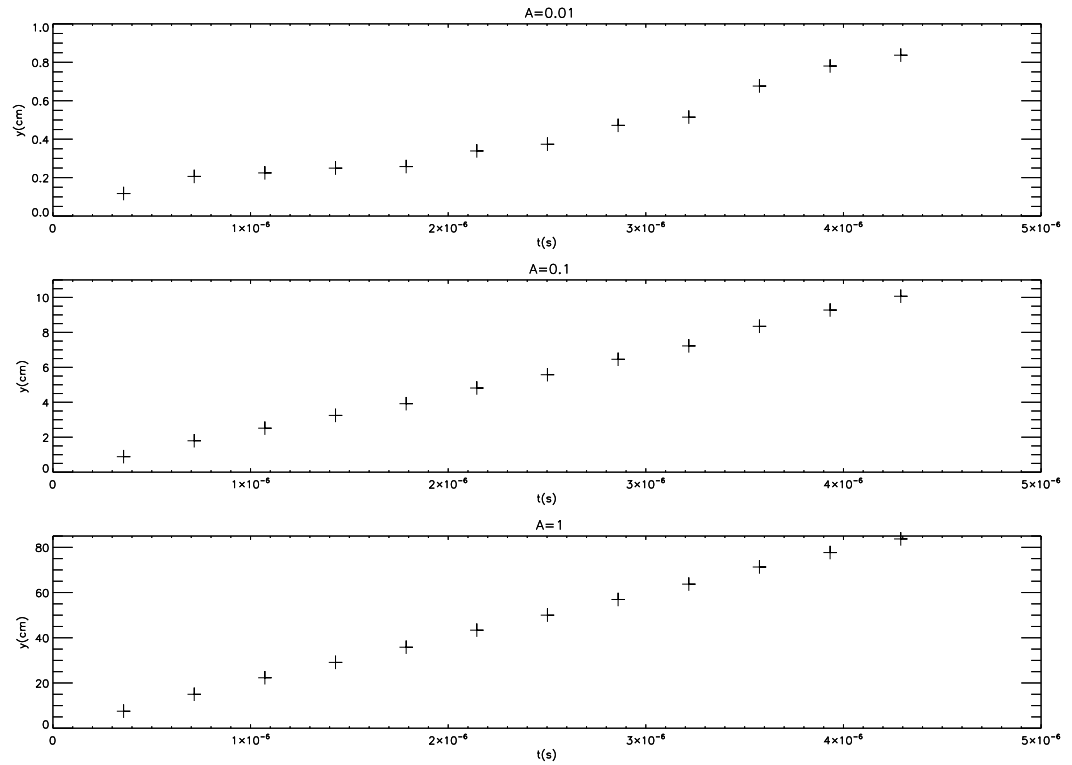


Figure 5.13: Change in the mean y position of the electron distribution with time for different amplitudes of slowing down and scattering terms. The mean y position was plotted every gyroperiod, and the mean y position in the absence of scattering should be zero at the times plotted.

$$\tau = \frac{m_e^2}{4\pi e^4 \Lambda n_e} v^3, \quad (5.61)$$

therefore

$$D_{\perp} \approx \frac{4\pi e^2 \Lambda n_e c^2 (1 - \mu^2)}{B^2} \frac{1}{v} cm^2 s^{-1}. \quad (5.62)$$

Fixing $A = 1$, $v_0 = 0.1c$, $B = 1G$, I can examine the effect of varying the density of the medium in which the electrons move. The diffusion in y for different densities can be seen in figure 5.15 which shows that the amount of diffusion is directly proportional to the density of the medium.

Let us now keep the density fixed (at $1 \times 10^{14} cm^{-3}$), keep a magnetic field of 1G, and vary the value of v_0 . The diffusion in y for different values of v_0 can be seen in figure 5.16. This figure shows that the amount of diffusion is inversely proportional to v_0 .

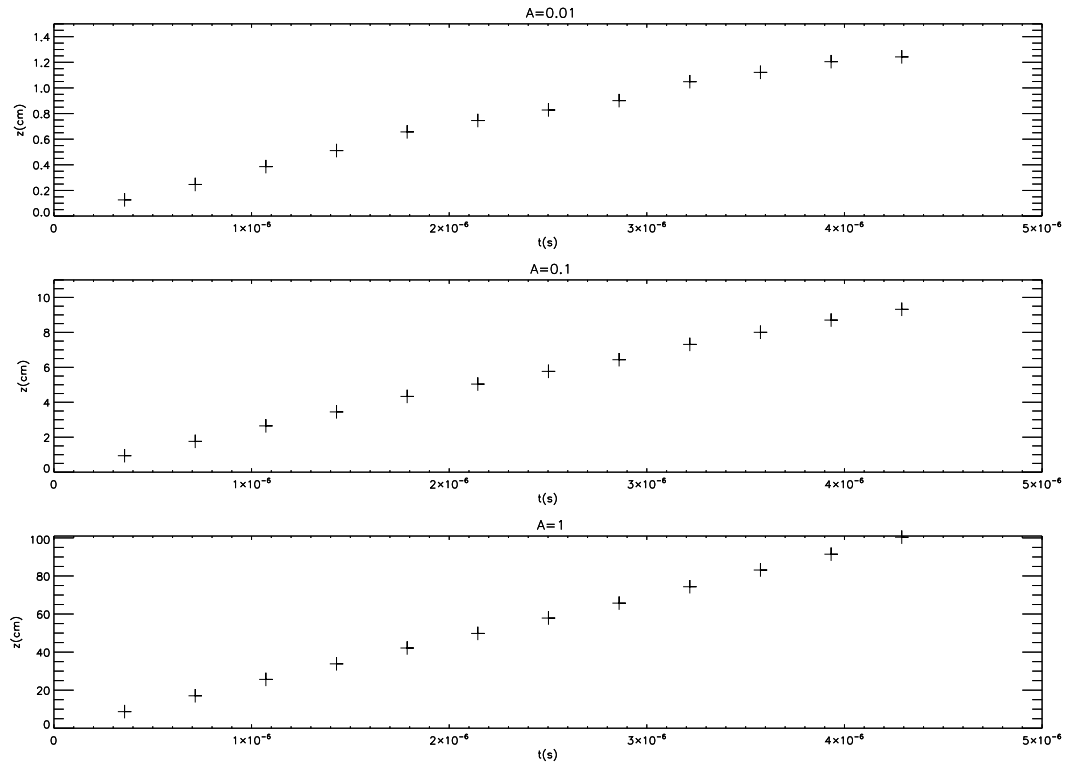


Figure 5.14: Change in the mean z position of the electron distribution with time for different amplitudes of slowing down and scattering terms. The mean z position was plotted every gyroperiod, and the mean z position in the absence of scattering should be zero at the times plotted.

Finally, let us keep the density fixed (at $1 \times 10^{14} \text{ cm}^{-3}$), fix $v_0 = 0.1c$, and vary the value of B . The diffusion in y for different values of B can be seen in figure 5.17, which shows that the amount of diffusion is inversely proportional to B^2 .

So, the change in a particle's position due to scattering is indeed proportional to

$$\Delta y^2 \propto \frac{n}{vB^2}, \quad (5.63)$$

therefore

$$D_{\perp} = \frac{4\pi e^2 \Lambda n_e c^2 (1 - \mu^2)}{B^2 v} \text{ cm}^2 \text{ s}^{-1}. \quad (5.64)$$

Figure 5.18 shows the value of the variance of y with time at successive gyroperiods, as well as the diffusion calculated using:

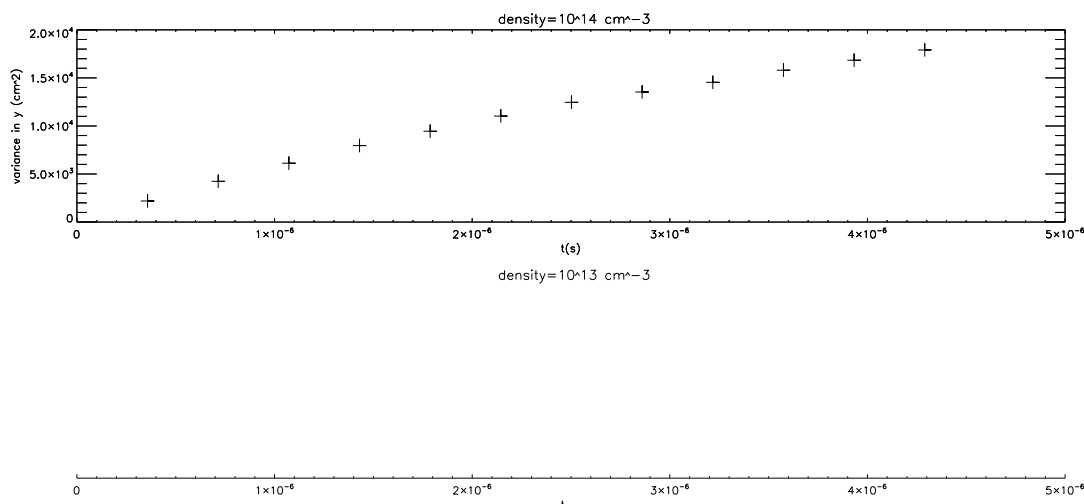


Figure 5.15: Change in y with time for different densities. The variance of y was plotted every gyroperiod.

$$\Delta y^2 = 2D_{\perp}t \quad (5.65)$$

It can be seen that the two methods agree reasonably well. The factor 2 in equation 5.65 was added as it was empirically found to be present. It would therefore be possible to follow a particle's behaviour using only the 1D equations for change in μ and v , and calculating the diffusion of the particles in space by using the diffusion coefficient.

5.9 Collisional Scattering At An X-Type Neutral Point

How do outcomes for the electrons I considered in section 4.2.6 change if collisional pitch-angle scattering and energy loss is also included? On the one hand, particles will lose energy to collisions. On the other hand collisional scattering may lead to electrons encountering the non-adiabatic region more frequently. Which effect will be more important? In the following section, the dimensionless units of chapter 4 are used.

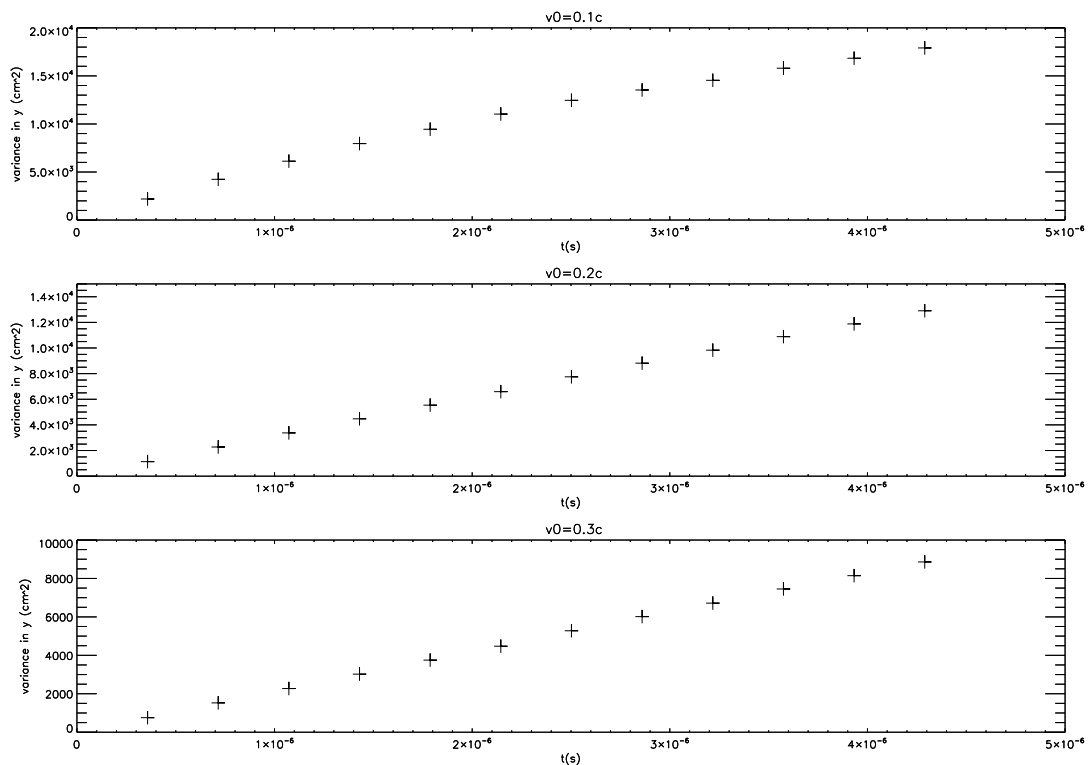


Figure 5.16: Change in y with time for different values of v_0 . The variance of y was plotted every gyroperiod.

5.9.1 The Dreicer Field

When considering collisional scattering, the velocity of the electrons must be taken into account. If electrons have speed less than the thermal velocity, collisions happen with almost constant frequency, increasing in number as the thermal velocity is approached. If an electron is moving faster than the thermal velocity, the collision frequency scales as $1/v^2$, so collisions become less frequent as the electron's speed increases (see e.g. Rozelot, Klein, and Vial (2000), Trubnikov (1965)).

Since electron energy loss rate decreases with energy, there is a critical electron energy for which energy gain from electric field is greater than energy loss from collisions. Electrons above this critical energy can be freely accelerated out of the thermal distribution by the electric field. The Dreicer field is the strength of electric field for which this critical energy equals the thermal energy, i.e. all electrons in the plasma can be freely accelerated. The speed at which collisions become less important as known as the runaway speed and is given by (e.g. Holman (1985))

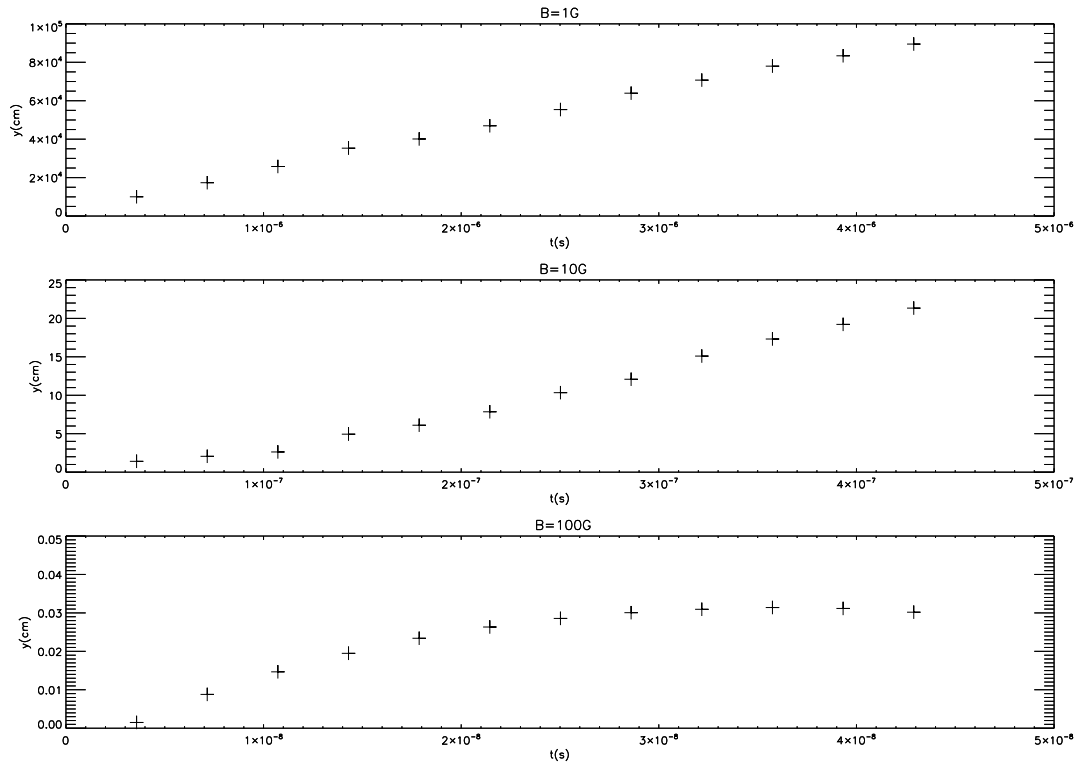


Figure 5.17: Change in y with time for different values of B . The variance of y was plotted every gyroperiod.

$$v_r = v_{T_e} \left(\frac{E_D}{E} \right)^{1/2}. \quad (5.66)$$

v_{T_e} is the thermal speed of the electrons, which is given by

$$v_{T_e} = \left(\frac{k_B T}{m_e} \right)^{1/2}. \quad (5.67)$$

The electric field strength E_D is the Dreicer field, which is given by (e.g. Holman (1985))

$$E_D = \frac{e\Lambda}{\lambda_D} = 2.33 \times 10^{-8} \left(\frac{n}{10^9 \text{ cm}^{-3}} \right) \left(\frac{T}{10^7 \text{ K}} \right)^{-1} \left(\frac{\Lambda}{23.2} \right) \text{ statvoltcm}^{-1}, \quad (5.68)$$

where Λ is the Coulomb logarithm, λ_D is the Debye length, and T is the plasma temperature. For the plasma being considered ($T = 1.4 \times 10^7 \text{ K}$, $n = 10^{10} \text{ cm}^{-3}$, $\Lambda = 25$), the Dreicer field is $1.8 \times 10^{-7} \text{ statvoltcm}^{-1}$, which is $5.4 \times 10^{-3} \text{ V/m}$. The electric field applied in these simulations is 10^{-3} in dimensionless units, which is 3.9 V/m for electrons.

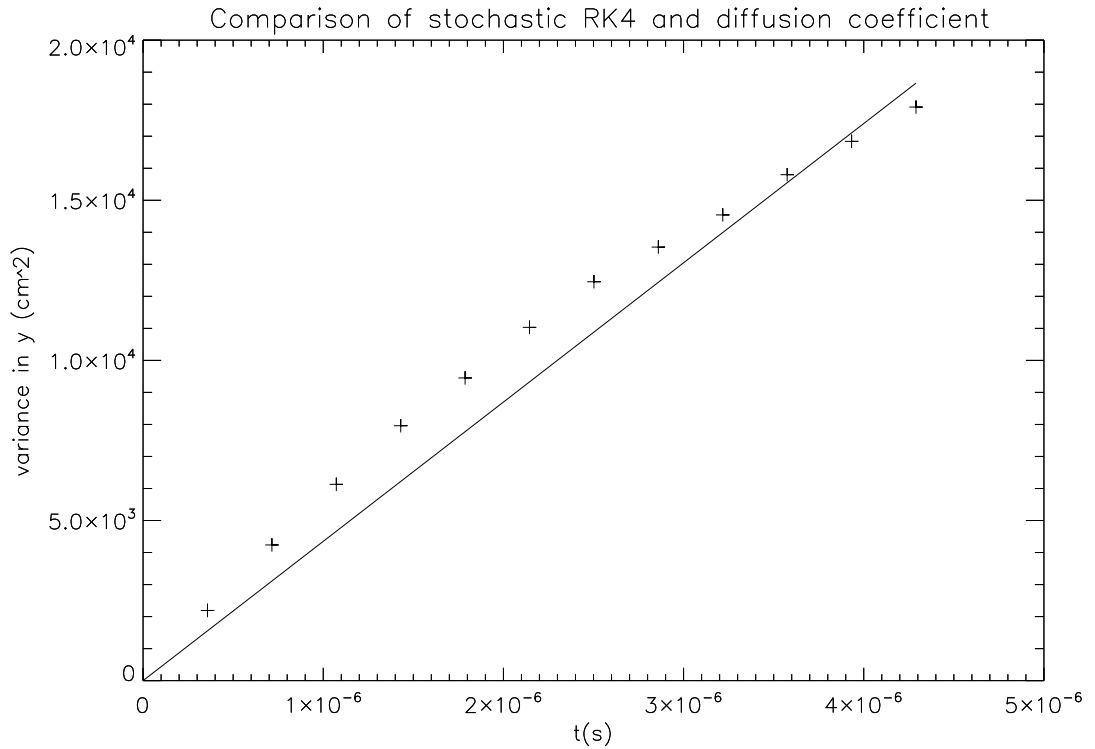


Figure 5.18: Change in the variance of y with time. The variance of y was plotted every gyroperiod, and is marked with a cross. The solid line is the average displacement as calculated using the diffusion coefficient, D , averaged over the number of electrons being considered (10 000 in this simulation).

For the plasma being considered, v_{T_e} is $1.5 \times 10^7 \text{ m s}^{-1}$. This gives a runaway speed of $5.6 \times 10^5 \text{ m s}^{-1}$ for $E=0.001$, which in my units is a speed of 1.9×10^{-3} . This means that all of the electrons in the distribution are 'runaway' electrons, and can be accelerated out of a thermal distribution.

5.9.2 Equations of Motion

Recall the set of equations 5.51, and add the appropriate electric and magnetic field terms for an unperturbed X-type neutral point. This gives, for an electron moving in a fully ionised hydrogen plasma:

$$\frac{dx}{dt} = v_x \quad (5.69a)$$

$$\frac{dy}{dt} = v_y \quad (5.69b)$$

$$\frac{dz}{dt} = v_z \quad (5.69c)$$

$$m_e \frac{dv_x}{dt} = B_y v_z - 3 \frac{\tilde{K} v_x}{v^3} + ((\tilde{K} \Delta t \mathbf{D})^{1/2} \mathbf{W})_x \quad (5.69d)$$

$$m_e \frac{dv_y}{dt} = -B_x v_z - 3 \frac{\tilde{K} v_y}{v^3} + ((\tilde{K} \Delta t \mathbf{D})^{1/2} \mathbf{W})_y \quad (5.69e)$$

$$m_e \frac{dv_z}{dt} = -(E + (B_y v_x - B_x v_y)) - 3 \frac{\tilde{K} v_z}{v^3} + ((\tilde{K} \Delta t \mathbf{D})^{1/2} \mathbf{W})_z. \quad (5.69f)$$

Once again, \tilde{K} is K expressed in the appropriate dimensionless units. In this case

$$\tilde{K} = \frac{K t_e}{c^3}. \quad (5.70)$$

I will integrate the set of equations 5.69 taking into account collisional scattering for case 1 (constant electric field in the z-direction, and an unperturbed X-type neutral point as the magnetic field). Once again, the scattering is introduced through the stochastic integrator, rather than by the inclusion of scattering terms in the equations of motion.

The slowing-down time was calculated using (MacKinnon and Craig (1991)) $v = (1 - 3t)^{1/3}$. It is important to note that this equation is in the units of MacKinnon and Craig, where speed is normalised to the initial speed of the particle, and time is normalised to $(v_0^3 n_\beta m_e^2) / (4\pi e^4 \lambda)$. Electrons were chosen to all start the simulation with the same velocity, $0.07c$, which is an energy of 1.23 keV. The simulation ran for $0.015s$, which is equivalent to the electron stopping time. To concentrate on the influence of collisions on the acceleration process I adopted a mono-energetic initial electron distribution. Electrons were released within the volume $0 \leq x \leq 1, 0 \leq y \leq 1$. In the case that no electric field is present, the particles should slow down monotonically, This can be seen in figure 5.19. The slowing down in this figure is slightly disappointing, as it is noisier than might be expected from the well-behaved test problem studied at the start of this chapter.

The slowing down can be made more uniform if a sufficiently small stepsize is taken. This can be seen in figure 5.20, which shows the slowing down of 5 electrons with identical starting conditions. Their trajectories were integrated using stepsizes of 0.01, 0.001 and 0.0001. It can be seen that the slowing down of the 5 electrons begins to look more similar as a smaller stepsize is taken. As the stepsize decreases, the rate of energy loss becomes smoother, and there are no gains in energy, as would be expected.

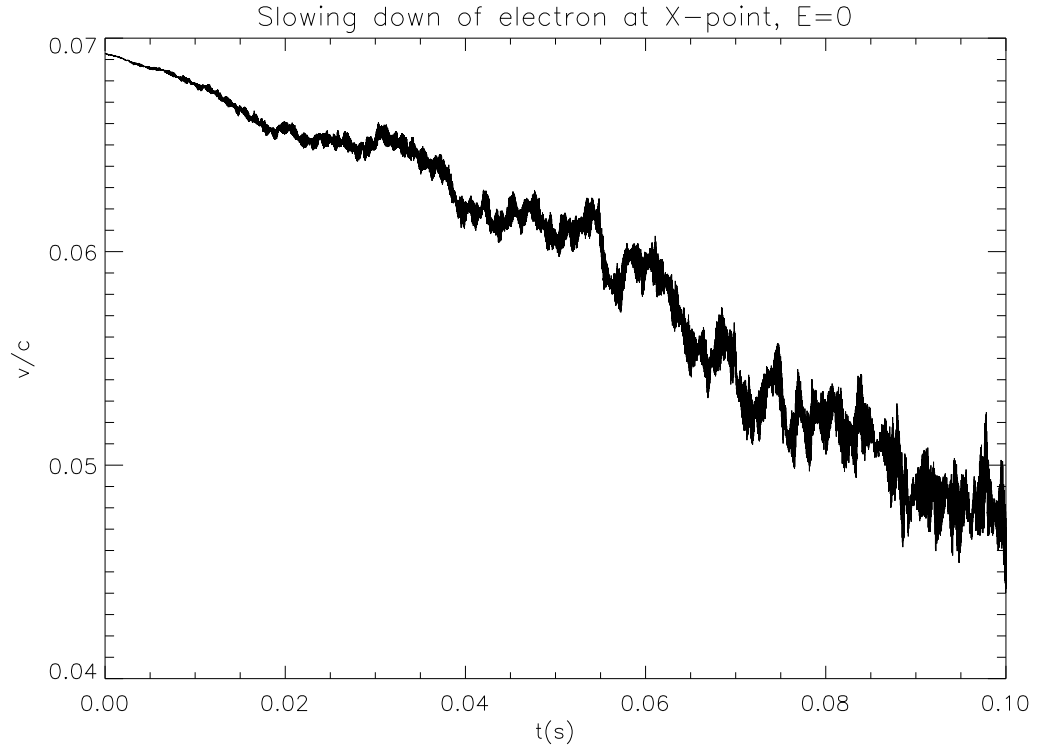


Figure 5.19: Slowing down of one electron at an X-type neutral point. A stepsize of 0.001 was used here. The electric field has magnitude 0. The slowing down in this figure is slightly disappointing, as it is noisier than might be expected from the well-behaved test problem studied at the start of this chapter. This is due to numerical issues which will be avoided by considering the problem in spherical polar coordinates.

5.10 Drift & Diffusion in Polar Co-ordinates

I do not wish to take a stepsize smaller than 0.001, as this would cause the computation time of the simulations to be increased to an impractical extent. I therefore decided to re-cast the equations of motion for an electron in polar co-ordinates. I am interested in the variation of the particle's velocity, azimuthal angle (θ), and pitch angle (ϕ). The equations of motion for an electron in polar co-ordinates (in the absence of any drift and diffusion terms) are written as follows:

$$\frac{dx}{dt} = v_x = v \sin(\phi) \cos(\theta) \quad (5.71a)$$

$$\frac{dy}{dt} = v_y = v \sin(\phi) \sin(\theta) \quad (5.71b)$$

$$\frac{dz}{dt} = v_z = v \cos(\phi) \quad (5.71c)$$

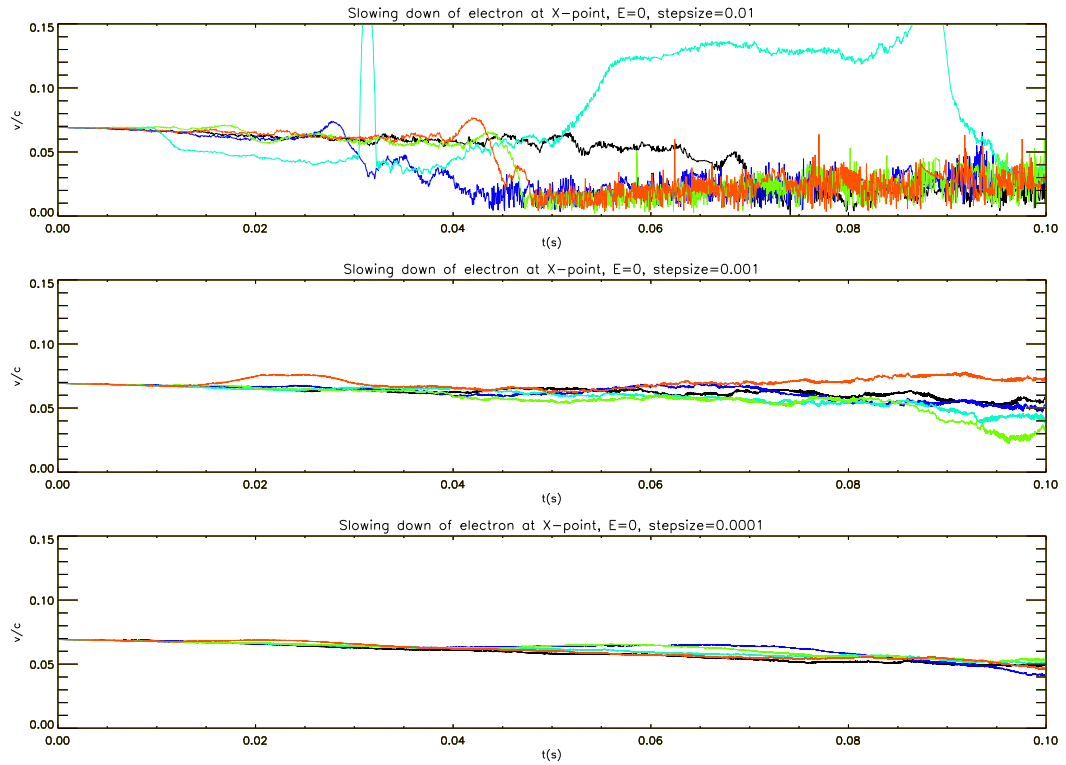


Figure 5.20: Slowing down of 5 electrons with identical starting conditions, including collisional scattering. Three different stepsizes were used. There is no electric field present.

$$\frac{dv}{dt} = \frac{q}{m_e} \frac{\mathbf{E} \cdot \mathbf{v}}{v} = \frac{q}{m_e} E \cos(\phi) \quad (5.71d)$$

$$\frac{d\theta}{dt} = \frac{q}{m_e} (\cot(\phi)(\cos(\theta)B_x + \sin(\theta)B_y)) \quad (5.71e)$$

$$\frac{d\phi}{dt} = \frac{q}{m_e} (E * \sin\phi/v) + (B_y \cos(\theta) - B_x \sin(\theta)) \quad (5.71f)$$

Changing variables from v_x, v_y, v_z to v, μ, θ , the stochastic differential equations governing the motion of one electron are given by

$$\frac{dx}{dt} = v \sin(\phi) \cos(\theta) \quad (5.72a)$$

$$\frac{dy}{dt} = v \sin(\phi) \sin(\theta) \quad (5.72b)$$

$$\frac{dz}{dt} = v \cos(\phi) \quad (5.72c)$$

$$\frac{dv}{dt} = \frac{q}{m_e} E \cos(\phi) - \frac{\tilde{D}}{v^2} \quad (5.72d)$$

$$\frac{d\theta}{dt} = \frac{q}{m_e}(\cot(\phi)(\cos(\theta)B_x + \sin(\theta)B_y)) + \left(\frac{\tilde{D}}{v^3 \sin^2(\phi)}\right)^{1/2} r \quad (5.72e)$$

$$\frac{d\phi}{dt} = \frac{E \sin(\phi)}{v} + (B_y \cos(\theta) - B_x \sin(\theta)) - \frac{2\tilde{D} \cos(\phi)}{v^3} + \left(\frac{\tilde{D}(\sin^2(\phi))}{v^3}\right)^{1/2} r \quad (5.72f)$$

where r is a random variable. The slowing down of one electron in the absence of any electric field can be seen in figure 5.21, which shows the required smooth, monotonic slowing down.

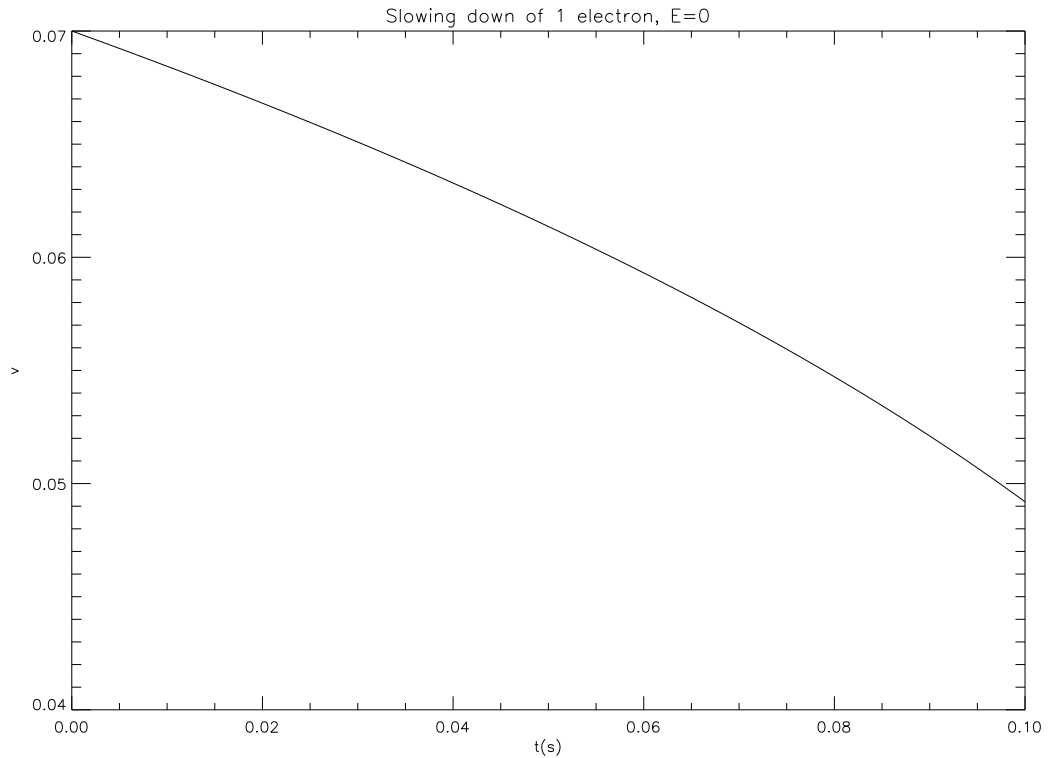


Figure 5.21: Slowing down of one electron at an X-type neutral point. A stepsize of 0.001 was used here. The electric field has magnitude 0.

Application to X-Type Neutral Point

Now that the appropriate equations of motion in polar co-ordinates have been obtained, the consequences of electron drift and diffusion at an X-type neutral point can be investigated. I initially considered particles being accelerated in an electric field, $E=0.001$ for my dimensionless units. The effects on particle trajectories can be seen in figure 5.22. It can be seen that adding collisional scattering and slowing down causes the trajectories of the particles to change, as would be expected. The particles change direction more frequently, and so cross the non-adiabatic region more often.

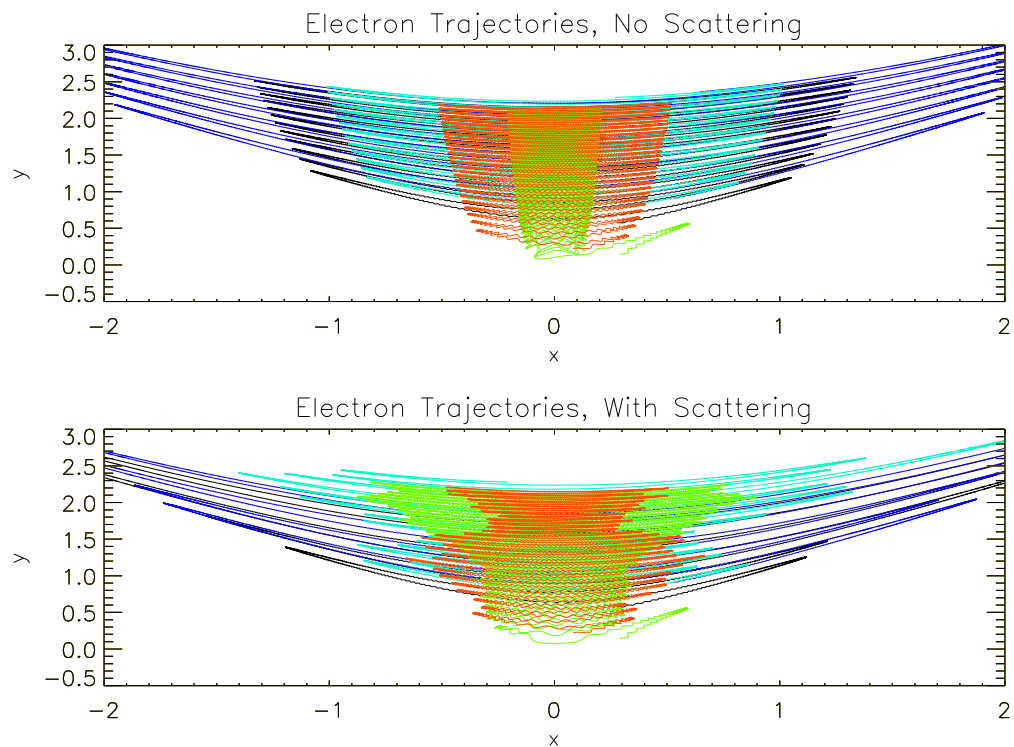


Figure 5.22: Trajectories of 5 electrons for case 1, integrated with and without the addition of collisional scattering. The sample has identical starting conditions for both sets of electrons. The electric field has magnitude 0.001 in our dimensionless units.

The effect that collisional scattering has on particle energies can be seen in figure 5.23. The density of the plasma being considered here is 10^{10}cm^{-3} . This density was chosen as it is a reasonable density for the solar corona, and it is high enough to show clearly the effect of the addition of collisions. The particles were followed until their theoretical stopping time, for such a density, 0.015s. The particles begin with an energy such that $\log_{10}(En_{\text{initial}}) = -2.9$. Most particles remain at this energy in both cases. In the absence of collisional scattering, some particles are accelerated by the electric field. If collisional scattering is added, some particles are accelerated, but some are decelerated. The maximum energy achieved is the same in both cases, although more particles achieve this energy in the absence of collisions.

However, one must bear in mind that if only collisional energy loss was included, the electrons which undergo collisional scattering should have stopped completely at $t = 0.015\text{s}$. The fact that they have not stopped means that they are being re-energised by the electric field. This is due to the fact that adding collisional scattering causes the particles to change direction more often, meaning that they cross the non-adiabatic region more often, thus gaining more energy.

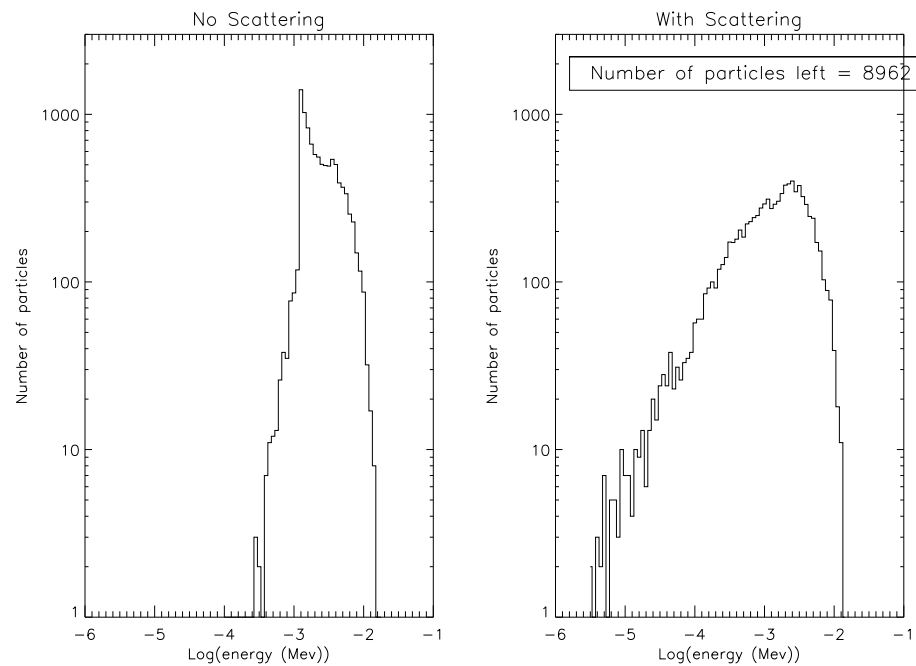


Figure 5.23: Energies at $t=0.015s$ for 10000 electrons whose trajectories have been integrated without the addition of collisional scattering (left) and with collisional scattering (right). The electric field has magnitude 0.001 in our dimensionless units.

Figures 5.24 and 5.25 show the energy distributions for electrons if $E=0.0001$ and $E = 10^{-5}$. As the electric field decreases, it can be seen that lower energies are achieved, both with and without collisional scattering. However, once again, the electrons undergoing collisions should have lost all of their energy in this time.

For these simulations, a particle is considered to have lost all of its energy if its energy is less than $5.11 \times 10^{-3}eV$ (this value was chosen as our simulations normalised energy to the electron rest mass energy, and the simulation was found to become unstable if the particle energy fell below 10^{-7} in these units). It can be seen that the amount of particles left with energy greater than $5.11 \times 10^{-3}eV$ decreases with decreasing electric field. Interestingly, for the cases shown in figures 5.24 and 5.25, the distributions when collisions are included are comprised of a lower energy peak and a higher energy peak. I suggest that the lower energy peak is caused by electrons that have gained just enough energy to remain above the cut-off energy, but which have generally been slowing down. The higher energy peak is caused by electrons which have been accelerated. This is not seen for a higher electric field (figure 5.23) as this field is high enough to accelerate the majority of the electrons in the distribution.

What happens if a sub-Dreicer field is applied to the electrons? The Dreicer field for an electron density of $10^{10}cm^{-3}$ and temperature 1.4×10^7 K is 5.4×10^{-3} V/m. If a field

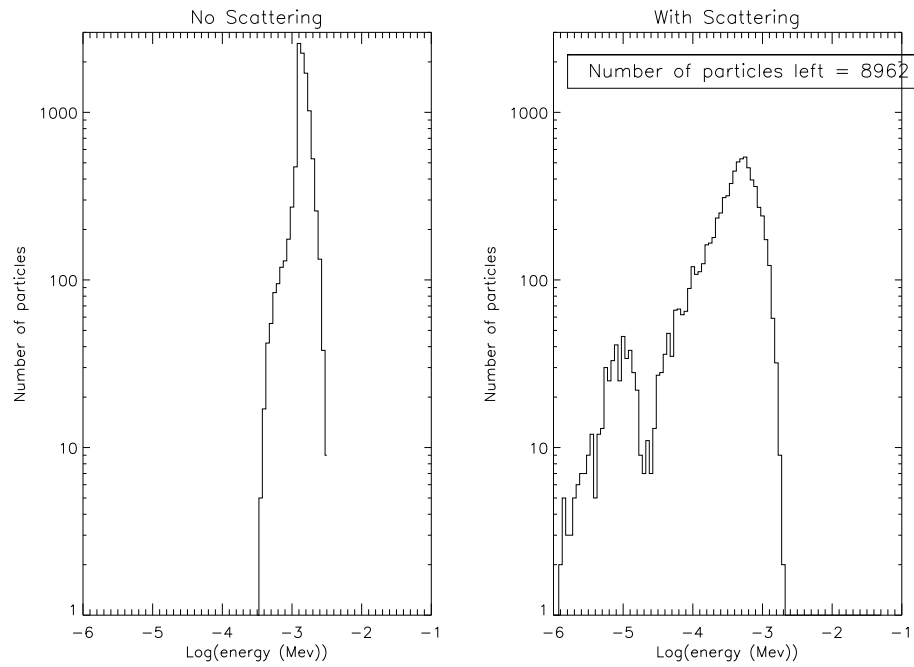


Figure 5.24: Energies at $t = 0.015s$ for 10000 electrons whose trajectories have been integrated without the addition of collisional scattering (left) and with collisional scattering (right). The electric field has magnitude 0.0001 in our dimensionless units.

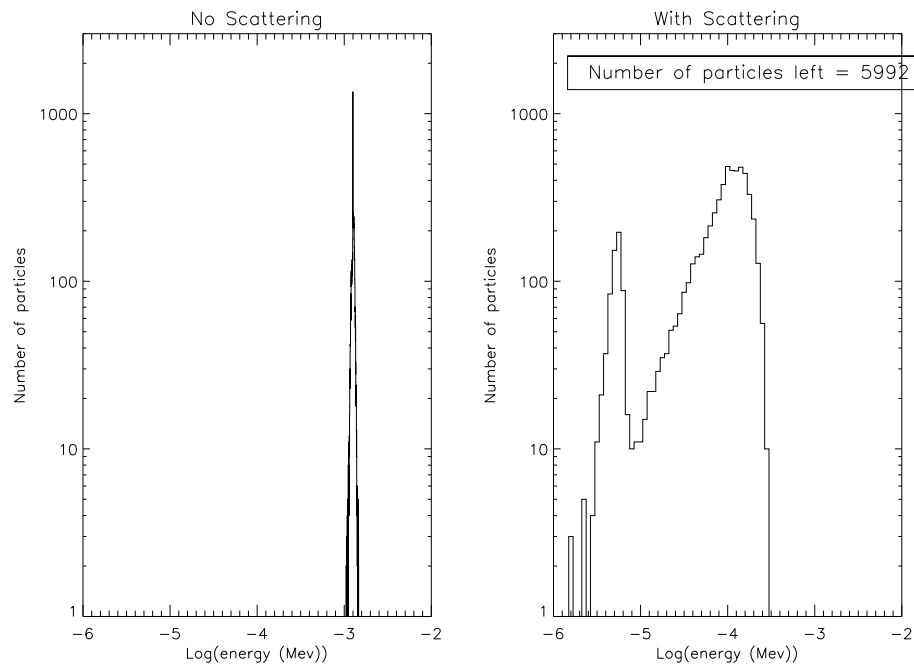


Figure 5.25: Energies at $t = 0.015s$ for 10000 electrons whose trajectories have been integrated without the addition of collisional scattering (left) and with collisional scattering (right). The electric field has magnitude 10^{-5} in our dimensionless units.

of 10^{-7} in our units is applied, that is equivalent to 3.9×10^{-4} V/m, so the electrons will experience a sub-Dreicer field. Electrons in a field of this magnitude have a runaway speed of

$5.7 \times 10^7 \text{ms}^{-1}$, which is 0.18 in our units, meaning the electrons are initially travelling below the runaway speed, and collisions will be more important. The effect of the sub-Dreicer field on electrons which both do and do not undergo collisional scattering can be seen in figure 5.26.

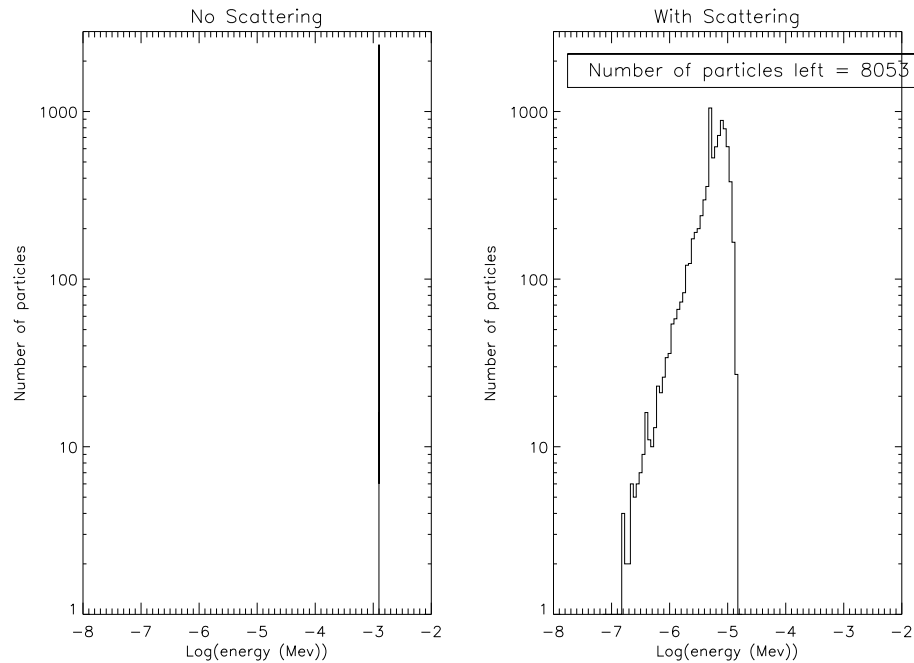


Figure 5.26: Energies at $t = 0.015\text{s}$ for 10000 electrons whose trajectories have been integrated without the addition of collisional scattering (left) and with collisional scattering (right). The electric field has magnitude 10^{-7} in our dimensionless units.

It can be seen that when electrons in such a low field do not undergo collisional scattering, their energy does not change. The electric field is too low to accelerate the electrons. However, if the particles undergo collisional scattering they lose energy, but they do not all lose all of their energy. If the electric field is less than the Dreicer field, collisions become more important, and more particles are left with energies greater than $5.11 \times 10^{-3} \text{eV}$ after the expected stopping time than are found for a small super-Dreicer field.

5.10.1 The Relativistic Case

Recall that the set of equations of motion used above is not valid in the relativistic case. However, using the arguments set forth in section 5.6, I can write a set of relativistic equations of the form:

$$\frac{dx}{dt} = v \sin(\phi) \sin(\theta) \quad (5.73a)$$

$$\frac{dy}{dt} = v \cos(\phi) \quad (5.73b)$$

$$\frac{dz}{dt} = v \cos(\phi) \quad (5.73c)$$

$$\frac{dv}{dt} = \frac{q}{m_e} E \cos(\phi) - \frac{1}{\gamma^3} \frac{\tilde{D}}{v^2} \quad (5.73d)$$

$$\frac{d\theta}{dt} = \frac{q}{m_e} (\cot(\phi)(\cos(\theta)B_x + \sin(\theta)B_y)) + \left(\frac{\tilde{D}}{v^3 \sin^2(\phi)} \right)^{1/2} r \quad (5.73e)$$

$$\frac{d\phi}{dt} = \frac{E \sin(\phi)}{v} + (B_y \cos(\theta) - B_x \sin(\theta)) - \frac{3 + \gamma}{4\gamma^2} \frac{2\tilde{D} \cos(\phi)}{v^3} + \left(\frac{3 + \gamma}{4\gamma^2} \frac{\tilde{D}(\sin^2(\phi))}{v^3} \right)^{1/2} r \quad (5.73f)$$

5.10.2 Application to X-Type Neutral Point

In order to investigate the consequences of collisions for relativistic electrons, electrons were started with an energy of 65keV. Energies of greater than around 160keV are too high for simulations to model the collisional behaviour of particles in a non-relativistic manner (Leach and Petrosian (1981)). Therefore if these particles are accelerated by more than 2.5 times their original energy, the calculations will need to be relativistic in order to be accurate. In order to reduce the simulation time, I have increased the plasma density here to 10^{12}cm^{-3} , which gives a stopping time for 65 keV electrons of 0.04s.

The energy distributions for relativistic particles, with and without the inclusion of collisional scattering can be seen in figure 5.27. The inclusion of collisional scattering does not make any difference to the energy distribution of the electrons if they start the simulation at high energies. This is also true for a much smaller electric field ($E = 1 \times 10^{-7}$), as can be seen in figure 5.28.

Figures 5.27 and 5.28 reproduce the quantitative results of the non-relativistic case. Collisions cause electrons to achieve a greater spread of energies if the electric field is relatively large. If the electric field is relatively small, particles simply lose energy due to collisions. In both cases, particles remain at higher energies than would be expected, as they are energised by the electric field.

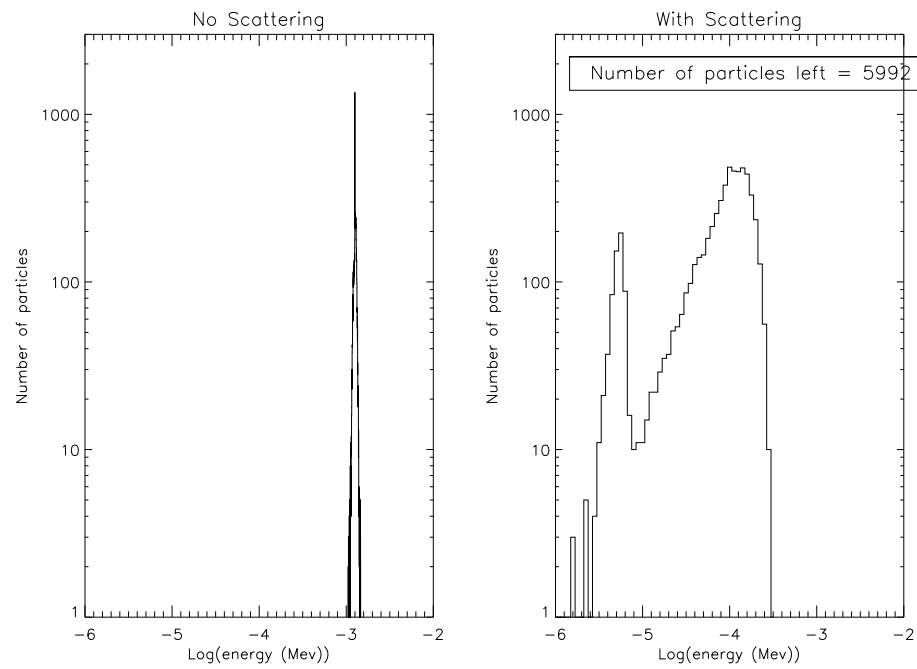


Figure 5.27: Energies at $t = 0.04s$ for 10000 electrons whose trajectories have been integrated without the addition of collisional scattering (left) and with collisional scattering (right), using the relativistic expressions for collisional scattering and collisional energy loss. The electric field has magnitude 0.001 in our dimensionless units.

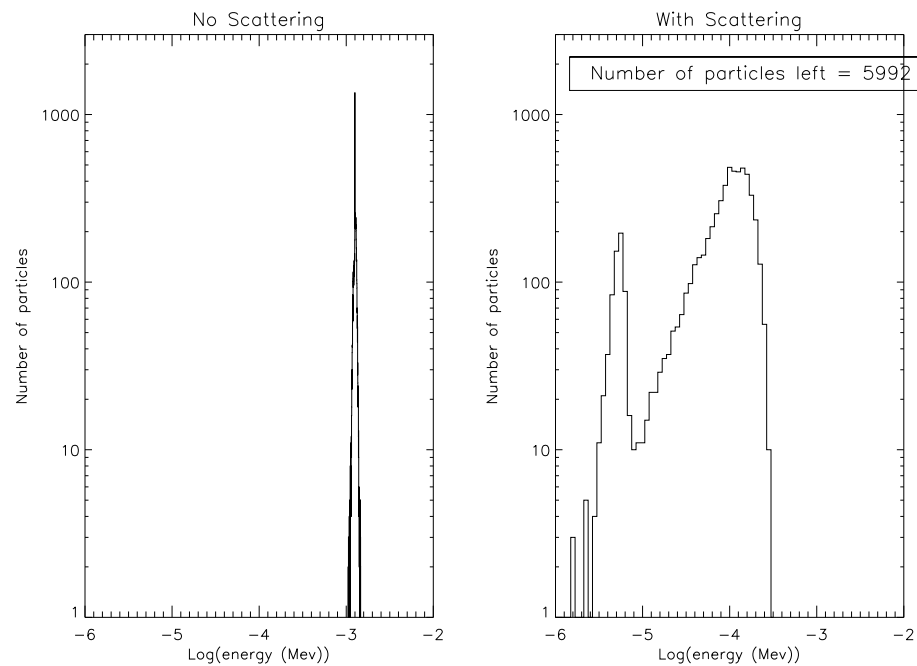


Figure 5.28: Energies at $t = 0.04s$ for 10000 electrons whose trajectories have been integrated without the addition of collisional scattering (left) and with collisional scattering (right), using the relativistic expressions for collisional scattering and energy loss. The electric field has magnitude 1×10^{-7} in our dimensionless units.

5.11 Conclusion

In this chapter, I have developed a method for including collisions in the calculation of particle trajectories. This method was developed by extending the stochastic RK2 method of Honeycutt (1992) to an RK4 method, which was then tested using the problem of collisional scattering in an unmagnetised plasma, as studied in MacKinnon and Craig (1991). The stochastic integrator performed better than the Euler integration used in MacKinnon and Craig (1991) for this 1D problem. The integrator was then extended for use in 3D calculations, with the drift and diffusion terms calculated using the method outlined in Trubnikov (1965). This method also performed well when used to find a solution to the test problem.

With confidence in the integration method, I then used the stochastic RK4 integrator to follow electrons gyrating around a constant magnetic field directed along the x axis, in the absence of an electric field. Increasing the magnitude of the drift and diffusion terms caused the electrons to drift across the field. An analytical expression for this drift was then obtained.

Finally, the stochastic integrator was used to add collisions to particle trajectories at an X-type neutral point. The addition of collisions causes the particles to lose energy, but because the particles are scattered in pitch angle, they return to the neutral point and are energised by the electric field. Therefore, even though the particles are followed for one stopping time, some of them still have energy. The amount of particles left with energy greater than $5.11 \times 10^{-3} eV$ decreases with decreasing electric field. However, if the electric field is less than the Dreicer field, collisions become more important, and more particles are left with energies greater than $5.11 \times 10^{-3} eV$ after the expected stopping time than are found for a small super-Dreicer field.

For relativistic electrons, collisions caused electrons to achieve a greater spread of energies if the electric field was relatively large. If the electric field was relatively small, particles simply lost energy. This is a quantitative reproduction of the results for the non-relativistic case.

I have shown that in the presence of an electric field, electrons that undergo collisions will still be energetic after their expected stopping time. These energised electrons will continue to produce Bremsstrahlung radiation, and could potentially produce a visible HXR source in the solar corona.

6. Conclusions and Future Work

What you do in this world is a matter of no consequence. The question is what can you make people believe you have done.

Sherlock Holmes, *A Study In Scarlet*

This thesis has focused on the behaviour of particles in different forms of electric and magnetic fields, both with and without the inclusion of collisional scattering. Such behaviour has been explored in the context of magnetic reconnection regions in solar flares, and for cross field drift in magnetised plasmas.

6.1 Noisy Electric & Magnetic Fields

The main body of this work has dealt with creating a simulation in which particles move in a magnetic field based on a perturbed X-type neutral point, and also in a noisy electric field which was created via a superposition of cold plasma eigenmodes. A large amount of time during this project has been devoted to developing the computational method used to calculate the hypergeometric function quickly and accurately. Calculating the eigenmodes of the hypergeometric function via integrating the hypergeometric differential equation (e.g. Press *et al.* (1992)) proved to take an excessive amount of time computationally when superpositions of many modes were required. Instead, an analytic continuation of the summation for the hypergeometric function was used. Analytic continuation methods are used to extend the region in which a particular analytic function can be used. In this case, the hypergeometric function can be represented as the summation of a series of terms in the region $z < 1$. However, outside of this region, this series no longer converges. Analytic continuation solves this problem, allowing us to continue representing the hypergeometric function as a series.

This was found to reproduce the results of Press *et al.* (1992), and the computation time was decreased by several orders of magnitude.

Adding many eigenmode oscillations caused the X-type neutral point to be dramatically changed and a complex magnetic field containing many smaller X- and O-type nulls was produced. An accompanying noisy electric field was also created, in the z -direction only. This work follows particles in the presence of a 2D magnetic field. A third component B_z of the equilibrium field would modify the structure of E and B , but Hamilton *et al.* (2005) show that a regime of sufficiently small B_z exists in which the resulting modifications are negligible for particle acceleration purposes. Larger B_z would result in reduced reconnection rate (and thus electric fields) as well as introducing time-dependent structure in the z direction, a more complex situation which I do not investigate here. The addition of a non-zero B_z component merely increases the efficiency of the acceleration, as particles tend to stay within the current sheet (see also Litvinenko (1996)). This means that the energies gained by particles in these simulations are likely to be at the lower end of the energy range that could be achieved with a 3D geometry.

Various physical effects would result from relaxing the 2D, cold plasma model. Gruszecki *et al.* (2011) show that non-linear effects become important as waves propagate towards the null, at a distance determined by plasma beta and the amplitude of the disturbance. Departures from azimuthal symmetry occur along with localised current spikes, all of which would have implications for accelerated particles. The plasma beta here is identically zero, which minimises these effects although they could become important in a more realistic treatment.

6.1.1 Consequences for Protons

Protons and electrons were released into these fields, and their behaviour was studied. Protons were easier to study since their greater mass means that the normalising timescale was greater. It was found that as more eigenmodes were added, the acceleration region became more efficient. This is due to the creation of a larger non-adiabatic region, and the fact that particles become trapped within this region. Adding more perturbative modes also causes particle pitch angles to vary more often, meaning that particles in the noisy fields undergo a kind of non-resonant pitch angle scattering. They change direction more often, which may lead them to crossing the non-adiabatic region more frequently. The smaller nulls that are created by a superposition of modes could also be sites for particle acceleration.

While there have been many studies of test particle acceleration in reconnection regions, the small volume involved in these regions is a problem if the large numbers of particles apparently accelerated in flares are to be accounted for. The effects described here open up the possibility of a much larger volume being involved in particle acceleration.

The effect of varying the distribution of the amplitude of the eigenmode oscillations was also investigated. It was found that letting the amplitude of the eigenmodes fall off as $a_0 k^{-5/3}$ (where k is the wavenumber of the mode, and a_0 is an arbitrary amplitude) produced a smaller total disturbance than for a flat spectrum of modes. The fields created by such a disturbance produced a high energy tail of particles which was much smoother and more regular in character than that produced by a flat spectrum of modes for the same a_0 .

Finally, the effect of varying the inertial resistivity was studied. It was found that decreasing resistivity caused protons to become more highly energised. Decreasing resistivity leads to changes in the formation of the small-scale nulls, so that more such nulls are created away from the very centre of the region. Since there are more sites of particle acceleration, particles can become more highly energised. Decreasing the value of the resistivity also causes the electric field to become less noisy. However, particles are still accelerated to higher energies in this less noisy field. It can therefore be concluded that it is not the noisier electric field that causes particles to become more energised as more perturbations are added in cases 1-5. Rather, it is the changes in the topology of the magnetic field, and the creation of more nulls, which are the sites of particle acceleration.

6.1.2 Consequences for electrons

It was more difficult to study electrons as their normalising timescale was much shorter due to their smaller mass, and smaller time steps had to be used to resolve the behaviour of the particles. In order to compensate for this, the normalising length scale for protons was changed to ten times the particle's gyroradius at the system boundary, rather than simply the gyroradius at the system boundary, as it was for protons. The electron mass was also increased to $10m_e$. This improved the computation time but still meant that electrons were only followed for a tenth of the time of protons. The masses of the test particles are still much less than those of ions and I expect major differences between electrons and ion to be revealed by these calculations.

It was found that the magnetic and electric fields of case 1 caused the electron distribution to gain energy as a whole (i.e. the plasma was heated). When eigenmode oscillations were added, this heating did not occur, but instead the addition of a superposition of eigenmode

oscillations caused the distribution to develop a high energy nonthermal tail. Again these effects appear to be due to the trapping of particles within the non-adiabatic region. Recall also that many smaller nulls are formed when more perturbative modes are added to the magnetic field.

I also calculated the X-ray spectra that would be produced by thin-target bremsstrahlung from the energy distributions of electrons calculated in chapter 4. It was found that adding more modes produced X-ray spectra that were similar in character to those that are observed: the spectra are comprised of both thermal and non-thermal photons. It is of course difficult to make quantitative statements here; the idealised nature of the simulations mean that the electron distributions are merely illustrative of those that may be found when some of the conditions are relaxed (for example, the introduction of a B_z component to the magnetic field). However, the fact that the X-ray spectra produced are qualitatively comparable to those which are observed is encouraging.

In integrating the trajectories for protons and in particular in integrating the electron trajectories for a superposition of modes, a major difficulty was the length of time taken for the simulations to run. The simulations took a long time to run as the gyromotion of the individual particles was being resolved at all times. The simulations could be sped up if the gyromotion was only followed within the non-adiabatic region. At larger r , I could merely follow the guiding centre of the particle's motion. This is much quicker to calculate as the equations of motion are much simpler. However, a difficulty arises in matching the calculations at the boundary between the two regimes. If the information about the v_x , v_y and v_z components of the particle's velocity was not preserved, these would have to be inferred in order to have detailed information about particle dynamics near the null. Calculating these quantities accurately (and quickly enough that the computation time saved by using the guiding centre approach further from the null is not negated) will be an important issue to be resolved.

6.2 Collisional Scattering

In order to model collisional scattering of particles, a stochastic Runge-Kutta integrator was developed, in the manner of Honeycutt (1992). This integrator was seen to reproduce the results of MacKinnon and Craig (1991) when tackling the same problem. The stochastic RK4 method was found to reproduce the distribution of particle pitch angles, and in fact performed better than the method of MacKinnon and Craig (1991) at later times. The monotonic slowing down of electrons was also well modelled.

With confidence in the stochastic RK4 established, I used this method to model cross field drift. Electrons were followed in the presence of a magnetic field in the x-direction only. It was found that adding more collisional scattering causes the particles to drift across the field, disrupting their usual gyromotion. An analytical diffusion coefficient was obtained, and the drift across the field lines predicted by this matched well with the results obtained when particle trajectories were integrated using a stochastic integration method. This gave us further confidence in the accuracy of the stochastic integrator. In this case, the monotonic slowing down of particles was also well modelled.

Stochastic RK4 was also used to add collisional scattering to electrons at an X-type neutral point. It was found that adding collisional scattering caused particles to achieve a greater spread of energies, and to remain energised after their theoretical collisional stopping time. As the size of the electric field is decreased, fewer electrons remain energised after one stopping time, if the electric field is above the Dreicer field value. If the electric field is below the Dreicer value, more particles remain energised, although because the magnitude of the field is necessarily small, they do not achieve high energies.

This is because electrons in a field greater than the Dreicer field are ‘runaway’ electrons, i.e. they are less affected by collisions, and so they are less likely to have their direction changed by a collision. Collisions merely cause such particles to lose energy. For electrons in a sub-Dreicer electric field, collisions are more important. Therefore the trajectories of these particles are more likely to be altered, meaning that they cross the neutral point more times than particles that do not undergo collisional scattering. When particles cross the neutral point, they gain energy. Therefore particles which undergo collisional scattering in the presence of a sub-Dreicer electric field will gain more energy than those which do not undergo collisions (for small electric fields). The correct expressions to describe the collisions of relativistic electrons were also derived.

The fact that energetic electrons are still seen is interesting as these electrons will be producing Bremsstrahlung radiation for longer than one might expect if only their collisional stopping time is considered. With high enough electric fields, these electrons could produce a coronal HXR source. The highest electric field I used for electrons was $3.9V/m$. Electric fields as high as $1kV/m$ have been observed in solar flares (Gorbachev and Somov (1989)). It is therefore possible that electrons could be emitting HXR via collisional Bremsstrahlung, and yet remain energised for times much longer than their stopping time.

The stochastic integrator performed slightly disappointingly in this case when it came to modelling the slowing down of the particles. Although the form of the slowing down is still

correct, the slowing down does not happen smoothly, but rather noisily. This is interesting since this did not occur in the other two problems studied, which suggests that the 'noisy slowing down' is a result of the set-up of this problem. I speculate that since the drift and diffusion terms in the stochastic integration algorithm are calculated from the v_x , v_y and v_z of the particles, large changes in these quantities near the null could cause anomalously high drift and diffusion terms, which could lead to the 'noisy slowing down' seen in this work. This problem was avoided by switching to a polar co-ordinate system, which recovered the expected monotonic slowing down.

6.3 Future Work

In order to better investigate the dynamics of electrons, faster codes should be developed. One way in which the speed at which particle trajectories are calculated could be increased is by parallelizing the code. Currently the time-scales associated with electron transport mean that such simulations are computationally expensive, and run for impractical lengths of time. Developing fast numerical integration methods, or finding quickly evaluated, analytical expressions which describe the turbulent fields in which the particles move would be a crucial part of this work. Once these rapid simulations are created, they could be applied to problems involving turbulent magnetic fields in a variety of astrophysical contexts.

In this work, I followed the orbit of each test particle individually, integrating the entire orbit for one particle before moving on to calculating the orbit for the next particle. The only way to integrate the trajectories of many particles quickly was to start several runs at once. This is a reasonably good method of decreasing the simulation time, but there are clever ways of doing this that make better use of the processing power available to us. If I was to rewrite the code for integrating particle orbits so that the behaviour of all of the particles was followed simultaneously (i.e. take one timestep, evaluate all quantities of interest for all of the particles in the simulation, and then take the next timestep), then I could parallelise the code. Running a process in parallel means that instead of the processor doing each of its required tasks in sequence, several processors are used to perform several tasks at once. The amount by which this could speed up the processing time is given by Amdahl's law (Amdahl (1967)), which states

$$T_{inc} = \frac{1}{r_s + \frac{r_p}{n}} \quad (6.1)$$

where r_s is the fraction of the code that has not been parallelised, r_p is the fraction of the code that has been parallelised, and n is the number of processors available. T_{inc} is the factor by which the running code of the time could be shortened. This means that if I was to rewrite the code so that half of it is in parallel, by running this job on 16 processors I could cut the running time of the code in half. If I was able to make 95% of our code parallel, our running time on 16 processors would be a tenth of that of a serial code.

Of course, it is possible to speed up calculations by making the calculations themselves simpler, and therefore quicker to evaluate. If one moves to a guiding centre approximation, the equations of motion are much simpler. The cross-field diffusion coefficient I developed will allow guiding centre studies of electron dynamics, in systems with a guide field. Such systems allow the use of a guiding centre everywhere (Wood and Neukirch (2005)). If the diffusion in pitch angle and the diffusion across the field can be modelled, then one can model all changes in the orbit of particles, whilst using simpler equations of motion, which will be able to be evaluated more quickly.

Numerical methods for stochastic differential equations have poorer convergence properties than similar methods for ordinary differential equations, as was illustrated by the small step-size needed to accurately follow the monotonic slowing down of particles. While my adoption of Honeycutt's (1992) stochastic RK4 method provided a good description of pitch-angle scattering, future work should investigate more sophisticated variants of stochastic RK4 methods, e.g. as described in Burrage and Burrage (1999), in order to improve the accuracy of the integrator.

I speculate that the stochastic RK4 integrator does not model the slowing down of an electron at the X-type neutral point accurately because the particles are not tightly tied to the magnetic field lines when they encounter the null point. This means that v_x , v_y and v_z can vary by large amounts as the particle gains energy in this region. Since the drift and diffusion terms are dependent on v_x , v_y and v_z , these changes may cause the drift and diffusion terms to vary inappropriately. A more accurate approach was achieved by recasting the problem in a polar coordinate system.

The stochastic RK4 integrator was also used to model cross field drift. In the problem studied in this work, the consequences for particles are simple; particles drift across the field lines as they undergo collisions. If the field lines were not simple straight field lines, but were instead tangled (as has been observed in the solar corona, see section 5.8), then diffusion across these field lines could have interesting consequences for particle dynamics. Diffusion across the tangled magnetic field will cause particles to travel to different spatial locations

than they would be able to reach by diffusing across straight field lines, since they would be able to follow these tangled field lines to locations that they could not access via drift alone.

I am also interested in determining how magnetic field topology influences turbulent interactions, and how the turbulent interactions can change magnetic field topology. I have already studied weak turbulence at an x-type neutral point, but I am also interested in simulating particle dynamics in fields such as the Arnold-Beltrami-Childress field, which is an example of a deterministically chaotic flow. Could such a flow be used in modelling turbulent flows in the solar corona or solar wind? Previous work on the ABC field has focussed on more generalised models of turbulent flows; it would be interesting to see if such flows could be applied in astrophysical contexts.

Bibliography

- Abramowitz, M., Stegun, I.A.: 1965, *Handbook of mathematical functions with formulas, graphs, and mathematical tables*.
- Alexandrova, O., Saur, J., Lacombe, C., Mangeney, A., Mitchell, J., Schwartz, S.J., Robert, P.: 2009, Universality of Solar-Wind Turbulent Spectrum from MHD to Electron Scales. *Physical Review Letters* **103**(16), 165003–+. doi:10.1103/PhysRevLett.103.165003.
- Amdahl, G.M.: 1967, Validity of the single processor approach to achieving large scale computing capabilities. In: *Proceedings of the April 18-20, 1967, spring joint computer conference, AFIPS '67 (Spring)*, ACM, New York, NY, USA, 483–485. doi:http://doi.acm.org/10.1145/1465482.1465560. http://doi.acm.org/10.1145/1465482.1465560.
- Aschwanden, M.J.: 2001, An Evaluation of Coronal Heating Models for Active Regions Based on Yohkoh, SOHO, and TRACE Observations. *Astronomy and Astrophysics Reviews* **560**, 1035–1044. doi:10.1086/323064.
- Aschwanden, M.J.: 2004a, *Physics of the Solar Corona. An Introduction*, Praxis Publishing Ltd, ???.
- Aschwanden, M.J.: 2004b, Pulsed Particle Injection in a Reconnection-Driven Dynamic Trap Model in Solar Flares. *Astronomy and Astrophysics Reviews* **608**, 554–561. doi:10.1086/392494.
- Aschwanden, M.J., Benz, A.O.: 1997, Electron Densities in Solar Flare Loops, Chromospheric Evaporation Upflows, and Acceleration Sites. *Astronomy and Astrophysics Reviews* **480**, 825. doi:10.1086/303995.
- Aschwanden, M.J., Nightingale, R.W.: 2005, Elementary Loop Structures in the Solar Corona Analyzed from TRACE Triple-Filter Images. *Astronomy and Astrophysics Reviews* **633**, 499–517. doi:10.1086/452630.

- Aschwanden, M.J., Fletcher, L., Schrijver, C.J., Alexander, D.: 1999, Coronal Loop Oscillations Observed with the Transition Region and Coronal Explorer. *Astronomy and Astrophysics Reviews* **520**, 880–894. doi:10.1086/307502.
- Benz, A.O.: 2002, *Plasma astrophysics: Kinetic processes in solar and stellar coronae*, 2nd edn., *Astrophysics and Space Science Library* **279**, Kluwer, Dordrecht, Netherlands; Boston, U.S.A..
- Benz, A.O.: 2008, Flare observations. *Living Reviews in Solar Physics* **5**(1). <http://www.livingreviews.org/lrsp-2008-1>.
- Berger, T.E., Title, A.M.: 1996, On the Dynamics of Small-Scale Solar Magnetic Elements. *Astronomy and Astrophysics Reviews* **463**, 365. doi:10.1086/177250.
- Birn, J., Priest, E.R.: 2007, *Reconnection of magnetic fields : magnetohydrodynamics and collisionless theory and observations*.
- Blasi, P., Gabici, S., Brunetti, G.: 2007, Gamma Rays from Clusters of Galaxies. *International Journal of Modern Physics A* **22**, 681–706. doi:10.1142/S0217751X0703529X.
- Brown, J.C.: 1971, The Deduction of Energy Spectra of Non-Thermal Electrons in Flares from the Observed Dynamic Spectra of Hard X-Ray Bursts. *Sol.Phys.* **18**, 489–502. doi:10.1007/BF00149070.
- Brown, J.C., Turkmani, R., Kontar, E.P., MacKinnon, A.L., Vlahos, L.: 2009, Local re-acceleration and a modified thick target model of solar flare electrons. *Astron. Astrophys.* **508**, 993–1000. doi:10.1051/0004-6361/200913145.
- Browning, P.K., Dalla, S., Peters, D., Smith, J.: 2010, Scaling of particle acceleration in 3D reconnection at null points. *Astron. Astrophys.* **520**, A105. doi:10.1051/0004-6361/201014964.
- Bulanov, S.V., Syrovatskii, S.I.: 1980, MHD oscillations and waves near a magnetic null line. *Soviet Journal of Plasma Physics* **6**, 1205–1218.
- Burge, C.A., Petkaki, P., MacKinnon, A.L.: 2012, Particle Acceleration in the Presence of Weak Turbulence at an X-Type Neutral Point. *Solar Phys.*, 65. doi:10.1007/s11207-012-9963-2.
- Burrage, K., Burrage, P.M.: 1999, High strong order methods for non-commutative stochastic ordinary differential equation systems and the Magnus formula. *Physica D Nonlinear Phenomena* **133**, 34–48. doi:10.1016/S0167-2789(99)00097-4.

- Chen, F.F., Torreblanca, H.: 1984, *Introduction to plasma physics and controlled fusion, 2nd edition*.
- Cho, J., Lazarian, A., Vishniac, E.T.: 2002, Simulations of Magnetohydrodynamic Turbulence in a Strongly Magnetized Medium. *Astronomy and Astrophysics Reviews* **564**, 291–301. doi:10.1086/324186.
- Craig, I.J., Watson, P.G.: 1992, Fast dynamic reconnection at X-type neutral points. *ApJ* **393**, 385–395. doi:10.1086/171512.
- Craig, I.J.D., McClymont, A.N.: 1991, Dynamic magnetic reconnection at an X-type neutral point. *ApJ Letters* **371**, L41–L44. doi:10.1086/185997.
- Craig, I.J.D., McClymont, A.N.: 1993, Linear theory of fast reconnection at an X-type neutral point. *ApJ* **405**, 207–215. doi:10.1086/172354.
- Craig, I.J.D., Heerikhuisen, J., Watson, P.G.: 2003, Hall current effects in dynamic magnetic reconnection solutions. *Physics of Plasmas* **10**, 3120–3130. doi:10.1063/1.1590980.
- Cranmer, S.R., van Ballegoijen, A.A.: 2003, Alfvénic Turbulence in the Extended Solar Corona: Kinetic Effects and Proton Heating. *Astronomy and Astrophysics Reviews* **594**, 573–591. doi:10.1086/376777.
- Dalla, S., Browning, P.K.: 2005, Particle acceleration at a three-dimensional reconnection site in the solar corona. *Astron. Astrophys.* **436**, 1103–1111. doi:10.1051/0004-6361:20042589.
- Dalla, S., Browning, P.K.: 2008, Particle trajectories and acceleration during 3D fan reconnection. *Astron. Astrophys.* **491**, 289–295. doi:10.1051/0004-6361:200809771.
- De Moortel, I., Ireland, J., Walsh, R.W.: 2000, Observation of oscillations in coronal loops. *Astron. Astrophys.* **355**, L23–L26.
- De Moortel, I., Ireland, J., Hood, A.W., Walsh, R.W.: 2002, The detection of 3 & 5 min period oscillations in coronal loops. *Astron. Astrophys.* **387**, L13–L16. doi:10.1051/0004-6361:20020436.
- Fitzpatrick, R.: 1993, Interaction of tearing modes with external structures in cylindrical geometry (plasma). *Nuclear Fusion* **33**, 1049–1084. doi:10.1088/0029-5515/33/7/108.
- Fletcher, L.: 1995, On the generation of loop-top impulsive hard X-ray sources. *Astron. Astrophys.* **303**, L9.

- Fletcher, L., Martens, P.C.H.: 1998, A Model for Hard X-Ray Emission from the Top of Flaring Loops. *Astronomy and Astrophysics Reviews* **505**, 418–431. doi:10.1086/306137.
- Fletcher, L., Petkaki, P.: 1997, Particle Acceleration and Transport in Reconnecting Plasmas. *Solar Phys.* **172**, 267–270.
- Foukal, P., Little, R., Gilliam, L.: 1987, Paschen-line Stark-broadening as an electric field diagnostic in erupting prominences. *Solar Phys.* **114**, 65–73.
- Frisch, U.: 1995, *Turbulence. The legacy of A. N. Kolmogorov.*
- Furth, H.P., Killeen, J., Rosenbluth, M.N.: 1963, Finite-Resistivity Instabilities of a Sheet Pinch. *Phys. Fluids* **6**, 459–484. doi:10.1063/1.1706761.
- Galloway, R.K., Helander, P., MacKinnon, A.L.: 2006, Cross-Field Diffusion of Electrons in Tangled Magnetic Fields and Implications for Coronal Fine Structure. *Astronomy and Astrophysics Reviews* **646**, 615–624. doi:10.1086/504699.
- Gardiner, C.W.: 1985, *Handbook of stochastic methods: for physics, chemistry and the natural sciences, Springer series in synergetics*, Springer, Berlin.
- Georgoulis, M.K., Rust, D.M., Bernasconi, P.N., Schmieder, B.: 2002, Statistics, Morphology, and Energetics of Ellerman Bombs. *Astronomy and Astrophysics Reviews* **575**, 506–528. doi:10.1086/341195.
- Goldreich, P., Sridhar, S.: 1995, Toward a theory of interstellar turbulence. 2: Strong alfvénic turbulence. *Astronomy and Astrophysics Reviews* **438**, 763–775. doi:10.1086/175121.
- Goldstein, M.L., Roberts, D.A., Matthaeus, W.H.: 1995, Magnetohydrodynamic Turbulence In The Solar Wind. *Annual Review of Astronomy and Astrophysics* **33**, 283–326. doi:10.1146/annurev.aa.33.090195.001435.
- Gorbachev, V.S., Somov, B.V.: 1989, Solar Flares of 1980NOV5 as the Result of Magnetic Reconnection at a Separator. *Soviet Ast* **33**, 57.
- Gordovskyy, M., Browning, P.K.: 2011, Particle Acceleration by Magnetic Reconnection in a Twisted Coronal Loop. *Astronomy and Astrophysics Reviews* **729**, 101. doi:10.1088/0004-637X/729/2/101.
- Gordovskyy, M., Browning, P.K., Vekstein, G.E.: 2010a, Particle acceleration in a transient magnetic reconnection event. *Astron. Astrophys.* **519**, A21. doi:10.1051/0004-6361/200913569.

- Gordovskyy, M., Browning, P.K., Vekstein, G.E.: 2010b, Particle Acceleration in Fragmenting Periodic Reconnecting Current Sheets in Solar Flares. *Astronomy and Astrophysics Reviews* **720**, 1603 – 1611. doi:10.1088/0004-637X/720/2/1603.
- Gruszecki, M., Vasheghani Farahani, S., Nakariakov, V.M., Arber, T.D.: 2011, Magnetoacoustic shock formation near a magnetic null point. *Astron. Astrophys.* **531**, A63. doi:10.1051/0004-6361/201116753.
- Guo, J.-N., Büchner, J., Otto, A., Santos, J., Marsch, E., Gan, W.-Q.: 2010, Is the 3-D magnetic null point with a convective electric field an efficient particle accelerator? *Astron. Astrophys.* **513**, A73. doi:10.1051/0004-6361/200913321.
- Hamilton, B., McClements, K.G., Fletcher, L., Thyagaraja, A.: 2003, Field-Guided Proton Acceleration at Reconnecting x-Points in Flares. *Solar Phys.* **214**, 339 – 352.
- Hamilton, B., Fletcher, L., McClements, K.G., Thyagaraja, A.: 2005, Electron Acceleration at Reconnecting X-Points in Solar Flares. *Astronomy and Astrophysics Reviews* **625**, 496 – 505. doi:10.1086/430100.
- Hannah, I.G.: 2005,. PhD thesis, University of Glasgow.
- Hassam, A.B.: 1992, Reconnection of stressed magnetic fields. *ApJ* **399**, 159 – 163. doi:10.1086/171911.
- Haug, E.: 1997, On the use of nonrelativistic bremsstrahlung cross sections in astrophysics. *Astron. Astrophys.* **326**, 417 – 418.
- Helander, P., Sigmar, D.J.: 2002, *Collisional transport in magnetized plasmas*.
- Heyvaerts, J., Priest, E.R., Rust, D.M.: 1977, An emerging flux model for the solar flare phenomenon. *Astronomy and Astrophysics Reviews* **216**, 123 – 137. doi:10.1086/155453.
- Hillas, A.M.: 2005, TOPICAL REVIEW: Can diffusive shock acceleration in supernova remnants account for high-energy galactic cosmic rays? *Journal of Physics G Nuclear Physics* **31**, 95. doi:10.1088/0954-3899/31/5/R02.
- Holman, G.D.: 1985, Acceleration of runaway electrons and Joule heating in solar flares. *Astronomy and Astrophysics Reviews* **293**, 584 – 594. doi:10.1086/163263.
- Honeycutt, R.L.: 1992, Stochastic runge-kutta algorithms. i. white noise. *Phys. Rev. A* **45**(2), 600 – 603. doi:10.1103/PhysRevA.45.600.
- Iroshnikov, P.S.: 1963, Turbulence of a Conducting Fluid in a Strong Magnetic Field. *Astronomicheskij Zhurnal* **40**, 742.

- Jackson, J.D.: 1965, Peripheral Production and Decay Correlations of Resonances. *Reviews of Modern Physics* **37**, 484–500. doi:10.1103/RevModPhys.37.484.
- Jones, C.A., Thompson, M.J., Tobias, S.M.: 2010, The Solar Dynamo. *Space Sci. Rev.* **152**, 591–616. doi:10.1007/s11214-009-9579-5.
- Kanbach, G., Bertsch, D.L., Fichtel, C.E., Hartman, R.C., Hunter, S.D., Kniffen, D.A., Kwok, P.W., Lin, Y.C., Mattox, J.R., Mayer-Hasselwander, H.A.: 1993, Detection of a long-duration solar gamma-ray flare on June 11, 1991 with EGRET on COMPTON-GRO. *Astron. Astrophys. Suppl.* **97**, 349–353.
- Karlický, M., Bárta, M.: 2006, X-Ray Loop-Top Source Generated by Processes in a Flare Collapsing Trap. *Astronomy and Astrophysics Reviews* **647**, 1472–1479. doi:10.1086/505460.
- Kolmogorov, A.: 1941, The Local Structure of Turbulence in Incompressible Viscous Fluid for Very Large Reynolds' Numbers. *Akademiia Nauk SSSR Doklady* **30**, 301–305.
- Kraichnan, R.H.: 1965, Inertial-Range Spectrum of Hydromagnetic Turbulence. *Physics of Fluids* **8**, 1385–1387. doi:10.1063/1.1761412.
- Krucker, S., Battaglia, M., Cargill, P.J., Fletcher, L., Hudson, H.S., MacKinnon, A.L., Masuda, S., Sui, L., Tomczak, M., Veronig, A.L., Vlahos, L., White, S.M.: 2008a, Hard X-ray emission from the solar corona. *Astrophys. J.* **16**, 155–208. doi:10.1007/s00159-008-0014-9.
- Krucker, S., Battaglia, M., Cargill, P.J., Fletcher, L., Hudson, H.S., MacKinnon, A.L., Masuda, S., Sui, L., Tomczak, M., Veronig, A.L., Vlahos, L., White, S.M.: 2008b, Hard X-ray emission from the solar corona. *Astronomy and Astrophysics* **16**, 155–208. doi:10.1007/s00159-008-0014-9.
- Leach, J., Petrosian, V.: 1981, Impulsive phase of solar flares. I - Characteristics of high energy electrons. *Astronomy and Astrophysics Reviews* **251**, 781–791. doi:10.1086/159521.
- Lin, R.P., Schwartz, R.A., Pelling, R.M., Hurley, K.C.: 1981, A new component of hard X-rays in solar flares. *Astrophys. J. Lett.* **251**, L109–L114. doi:10.1086/183704.
- Lin, R.P., Krucker, S., Hurford, G.J., Smith, D.M., Hudson, H.S., Holman, G.D., Schwartz, R.A., Dennis, B.R., Share, G.H., Murphy, R.J., Emslie, A.G., Johns-Krull, C., Vilmer, N.: 2003, RHESSI Observations of Particle Acceleration and Energy Release in an Intense Solar Gamma-Ray Line Flare. *Astrophys. J. Lett.* **595**, L69–L76. doi:10.1086/378932.

- Litvinenko, Y.E.: 1996, Particle Acceleration in Reconnecting Current Sheets with a Nonzero Magnetic Field. *Astronomy and Astrophysics Reviews* **462**, 997. doi:10.1086/177213.
- Litvinenko, Y.E.: 2003, Particle Acceleration by a Time-Varying Electric Field in Merging Magnetic Fields. *Solar Phys.* **216**, 189–203. doi:10.1023/A:1026143310271.
- Litvinenko, Y.E.: 2006, Three-dimensional fan magnetic reconnection and particle acceleration in the solar corona. *Astron. Astrophys.* **452**, 1069–1074. doi:10.1051/0004-6361:20054324.
- Liu, C., Wang, H.: 2009, Reconnection Electric Field and Hardness of X-Ray Emission of Solar Flares. *Astrophys. J. Lett.* **696**, L27–L31. doi:10.1088/0004-637X/696/1/L27.
- Liu, W., Petrosian, V., Dennis, B.R., Jiang, Y.W.: 2008, Double Coronal Hard and Soft X-Ray Source Observed by RHESSI: Evidence for Magnetic Reconnection and Particle Acceleration in Solar Flares. *Astronomy and Astrophysics Reviews* **676**, 704–716. doi:10.1086/527538.
- MacKinnon, A.L., Craig, I.J.D.: 1991, Stochastic simulation of fast particle diffusive transport. *Astronomy and Astrophysics* **251**, 693–699.
- Martens, P.C.H.: 1988, The generation of proton beams in two-ribbon flares. *Astrophys. J. Lett.* **330**, L131–L133. doi:10.1086/185220.
- Masuda, S., Kosugi, T., Hara, H., Tsuneta, S., Ogawara, Y.: 1994a, A loop-top hard X-ray source in a compact solar flare as evidence for magnetic reconnection. *Nature* **371**, 495–497. doi:10.1038/371495a0.
- Masuda, S., Kosugi, T., Hara, H., Tsuneta, S., Ogawara, Y.: 1994b, A loop-top hard X-ray source in a compact solar flare as evidence for magnetic reconnection. *Nature* **371**, 495–497. doi:10.1038/371495a0.
- Matthaeus, W.H., Goldstein, M.L.: 1982, Measurement of the rugged invariants of magnetohydrodynamic turbulence in the solar wind. *J. Geophys. Res.* **87**, 6011–6028. doi:10.1029/JA087iA08p06011.
- McClements, K.G., Shah, N., Thyagaraja, A.: 2006, The coupling of shear and fast Alfvén waves at a magnetic X-point. *Journal of Plasma Physics* **72**, 571–585. doi:10.1017/S0022377805004277.

- McLaughlin, J.A., Hood, A.W., de Moortel, I.: 2011, Review Article: MHD Wave Propagation Near Coronal Null Points of Magnetic Fields. *Space Sci. Rev.* **158**, 205–236. doi:10.1007/s11214-010-9654-y.
- Miller, J.A., Cargill, P.J., Emslie, A.G., Holman, G.D., Dennis, B.R., LaRosa, T.N., Winglee, R.M., Benka, S.G., Tsuneta, S.: 1997a, Critical issues for understanding particle acceleration in impulsive solar flares. *Journal of Geophysical Research* **102**, 14631–14660. doi:10.1029/97JA00976.
- Miller, J.A., Cargill, P.J., Emslie, A.G., Holman, G.D., Dennis, B.R., LaRosa, T.N., Winglee, R.M., Benka, S.G., Tsuneta, S.: 1997b, Critical issues for understanding particle acceleration in impulsive solar flares. *Journal of Geophysical Research* **102**, 14631–14660. doi:10.1029/97JA00976.
- Ott, E.: 2002, *Chaos in Dynamical Systems - 2nd Edition*. doi:10.2277/0521811961.
- Pariat, E., Aulanier, G., Schmieder, B., Georgoulis, M.K., Rust, D.M., Bernasconi, P.N.: 2004, Resistive Emergence of Undulatory Flux Tubes. *Astronomy and Astrophysics Reviews* **614**, 1099–1112. doi:10.1086/423891.
- Park, B.T., Petrosian, V., Schwartz, R.A.: 1997, Stochastic Acceleration and Photon Emission in Electron-dominated Solar Flares. *Astronomy and Astrophysics Reviews* **489**, 358. doi:10.1086/304753.
- Parker, E.N.: 1957, Sweet's Mechanism for Merging Magnetic Fields in Conducting Fluids. *J. Geophys. Res.* **62**, 509–520. doi:10.1029/JZ062i004p00509.
- Parker, E.N.: 1963, The Solar-Flare Phenomenon and the Theory of Reconnection and Annihilation of Magnetic Fields. *ApJ* **8**, 177–+. doi:10.1086/190087.
- Petkaki, P.: 1996,. PhD thesis, University of Glasgow.
- Petkaki, P., Freeman, M.P.: 2008, Nonlinear Dependence of Anomalous Ion-Acoustic Resistivity on Electron Drift Velocity. *Astronomy and Astrophysics Reviews* **686**, 686–693. doi:10.1086/590654.
- Petkaki, P., MacKinnon, A.L.: 1997, Particle Acceleration in Dynamical Collisionless Reconnection. *Sol.Phys.* **172**, 279–286.
- Petkaki, P., MacKinnon, A.L.: 2007, Particle acceleration by fluctuating electric fields at a magnetic field null point. *Astron. Astrophys.* **472**, 623–632.

- Petkaki, P., MacKinnon, A.L.: 2011, Acceleration of charged particles by fluctuating and steady electric fields in a X-type magnetic field. *Advances in Space Research* **48**, 884–898. doi:10.1016/j.asr.2011.04.019.
- Petrosian, V., Liu, S.: 2004, Stochastic Acceleration of Electrons and Protons. I. Acceleration by Parallel-Propagating Waves. *Astronomy and Astrophysics Reviews* **610**, 550–571. doi:10.1086/421486.
- Petschek, H.E.: 1964a, Magnetic Field Annihilation. *NASA Special Publication* **50**, 425–+.
- Petschek, H.E.: 1964b, Magnetic Field Annihilation. *NASA Special Publication* **50**, 425–+.
- Press, W.H., Teukolsky, S.A., Vetterling, W.T., Flannery, B.P.: 1992, *Numerical recipes in FORTRAN. The art of scientific computing.*
- Priest, E., Forbes, T.: 2000, *Magnetic Reconnection.*
- Rechester, A.B., Rosenbluth, M.N.: 1978, Electron heat transport in a tokamak with destroyed magnetic surfaces. *Phys. Rev. Lett.* **40**, 38–41. doi:10.1103/PhysRevLett.40.38. <http://link.aps.org/doi/10.1103/PhysRevLett.40.38>.
- Rozelot, J.P., Klein, L., Vial, J.-C. (eds.): 2000, *Transport and Energy Conversion in the Heliosphere, Lecture Notes in Physics, Berlin Springer Verlag* **553**.
- Schrijver, C.J., Siscoe, G.L.: 2010, *Heliophysics: Space Storms and Radiation: Causes and Effects*, Cambridge University Press, ???.
- Somov, B.V., Oreshina, I.V., Kovalenko, I.A.: 2008, Magnetic reconnection, electric field, and particle acceleration in the July 14, 2000 solar flare. *Astronomy Letters* **34**, 327–336. doi:10.1134/S1063773708050058.
- Speiser, T.W.: 1965, Particle Trajectories in Model Current Sheets, 1, Analytical Solutions. *J. Geophys. Res.* **70**, 4219–4226. doi:10.1029/JZ070i017p04219.
- Speiser, T.W.: 1970, Conductivity without collisions or noise. *Planetary Space Science* **18**, 613. doi:10.1016/0032-0633(70)90136-4.
- Strauss, H.R.: 1976, Nonlinear, three-dimensional magnetohydrodynamics of noncircular tokamaks. *Physics of Fluids* **19**, 134–140. doi:10.1063/1.861310.
- Sturrock, P.A., Kaufman, P., Moore, R.L., Smith, D.F.: 1984, Energy release in solar flares. *Solar Phys.* **94**, 341–357. doi:10.1007/BF00151322.

- Sweet, P.A.: 1958a, The Neutral Point Theory of Solar Flares. In: B. Lehnert (ed.) *Electromagnetic Phenomena in Cosmical Physics, IAU Symposium* **6**, 123–+.
- Sweet, P.A.: 1958b, The Neutral Point Theory of Solar Flares. In: B. Lehnert (ed.) *Electromagnetic Phenomena in Cosmical Physics, IAU Symposium* **6**, 123–+.
- Torres, D.F., Romero, G.E., Dame, T.M., Combi, J.A., Butt, Y.M.: 2003, Supernova remnants and γ -ray sources. *Physical Review Letters* **382**, 303–380. doi:10.1016/S0370-1573(03)00201-1.
- Trubnikov, B.A.: 1965, Particle Interactions in a Fully Ionized Plasma. *Reviews of Plasma Physics* **1**, 105–+.
- Tsuneta, S.: 1996, Structure and Dynamics of Magnetic Reconnection in a Solar Flare. *Astronomy and Astrophysics Reviews* **456**, 840. doi:10.1086/176701.
- Tsuneta, S., Hara, H., Shimizu, T., Acton, L.W., Strong, K.T., Hudson, H.S., Ogawara, Y.: 1992, Observation of a solar flare at the limb with the YOHKOH Soft X-ray Telescope. *Publications of the Astronomical Society of Japan* **44**, L63–L69.
- Turkmani, R., Cargill, P.J., Galsgaard, K., Vlahos, L., Isliker, H.: 2006, Particle acceleration in stochastic current sheets in stressed coronal active regions. *Astronomy and Astrophysics* **449**, 749–757. doi:10.1051/0004-6361:20053548.
- Van Hollebeke, M.A.I., Ma Sung, L.S., McDonald, F.B.: 1975, The variation of solar proton energy spectra and size distribution with heliolongitude. *Solar Phys.* **41**, 189–223. doi:10.1007/BF00152967.
- Vekstein, G.E., Browning, P.K.: 1997, Electric-drift generated trajectories and particle acceleration in collisionless magnetic reconnection. *Physics of Plasmas* **4**, 2261–2268. doi:10.1063/1.872555.
- Verwichte, E., Aschwanden, M.J., Van Doorsselaere, T., Foullon, C., Nakariakov, V.M.: 2009, Seismology of a large solar coronal loop from euvi/stereo observations of its transverse oscillation. *Astronomy and Astrophysics Reviews* **698**, 397–404. doi:10.1088/0004-637X/698/1/397.
- Vilmer, N., MacKinnon, A.L., Hurford, G.J.: 2011, Properties of Energetic Ions in the Solar Atmosphere from γ -Ray and Neutron Observations. *Space Sci. Rev.* **159**, 167–224. doi:10.1007/s11214-010-9728-x.

- Vilmer, N., MacKinnon, A.L., Trotter, G., Barat, C.: 2003, High energy particles accelerated during the large solar flare of 1990 May 24: X/ γ -ray observations. *Astron. Astrophys.* **412**, 865 – 874. doi:10.1051/0004-6361:20031488.
- Vlahos, L., Krucker, S., Cargill, P.: 2009, The Solar Flare: A Strongly Turbulent Particle Accelerator. In: P. Cargill & L. Vlahos (ed.) *Turbulence in Space Plasmas, Lecture Notes in Physics, Berlin Springer Verlag* **778**, 157.
- Waelbroeck, F.L.: 1989, Current sheets and nonlinear growth of the $m=1$ kink-tearing mode. *Physics of Fluids B* **1**, 2372 – 2380. doi:10.1063/1.859172.
- Wang, R., Wang, J.: 2006, Spectra and solar energetic protons over 20 GeV in Bastille Day event. *Astroparticle Physics* **25**, 41 – 46. doi:10.1016/j.astropartphys.2005.11.002.
- White, S.M., Benz, A.O., Christe, S., Fárnik, F., Kundu, M.R., Mann, G., Ning, Z., Raulin, J.-P., Silva-Válio, A.V.R., Saint-Hilaire, P., Vilmer, N., Warmuth, A.: 2011, The Relationship Between Solar Radio and Hard X-ray Emission. *Space Sci. Rev.* **159**, 225 – 261. doi:10.1007/s11214-010-9708-1.
- Wood, P., Neukirch, T.: 2005, Electron Acceleration in Reconnecting Current Sheets. *Solar Phys.* **226**, 73 – 95. doi:10.1007/s11207-005-5686-y.
- Zharkova, V.V., Agapitov, O.V.: 2009, The effect of magnetic topology on particle acceleration in a three-dimensional reconnecting current sheet: a test-particle approach. *Journal of Plasma Physics* **75**, 159. doi:10.1017/S002237780800771X.
- Zweibel, E.G., Yamada, M.: 2009, Magnetic Reconnection in Astrophysical and Laboratory Plasmas. *Annual Review of Astron. and Astrophys.* **47**, 291 – 332. doi:10.1146/annurev-astro-082708-101726.